The University Of Sheffield.

Wind-induced Fatigue Behaviour of Connections for Plug-in System using Prefabricated Timber Panels

Ying Liu

170119023

A thesis submitted in partial fulfilment of the requirements for the degree of

Doctor of Philosophy

The University of Sheffield

School of Architecture

Submission Date 30/11/2021

Acknowledgements

Firstly, I would like to thank my supervisor Dr Wen-Shao Chang. His innovative understanding of timber structure laid the foundation for this research topic, and his supervision helped me one step closer to being an independent researcher. Additionally, I gained more practical experience and knowledge of civil engineering, and the cross-disciplinary research approach broadened my horizon.

Thanks to Dr Maurizio Guadagnini for helping me with the experiment plan in the laboratory. Mr Kieran Nash and Mr Kieren O Howarth helped prepare the concrete specimen and provided me a place for sample assembly. During the Covid-19 lockdown period, they helped me store my testing specimens properly. Mr Kieren O Howarth also got the machines working. In the material workshop, Mr Stuart Moran gave me the benefit of his skill and experience to help me assemble my samples and prepare stencils for the DIC test. Without their help, I could not finish my research smoothly.

I am grateful that my parents and grandma supported me with tuition fees and love and gentle guidance in my life. Finally, I would like to thank my cat, Pancake, who provided me with spiritual support and made me not feel lonely during research, especially during the pandemic of covid-19.

Abstract

Timber has become one of the popular choices as a sustainable building material, and with the increase in timber building height, the problem caused by wind load becomes remarkable. Most research focused on the ultimate structure performance under wind load or vibration under cyclic shear force due to dynamic wind load. However, a lack of research on the serviceability of timber wall connections under out-of-panel load caused by dynamic wind pressure may lead to underestimating damage to timber structures. Therefore, this study investigates the fatigue performance of connections for plug-in timber panels under out-of-panel cyclic load caused by wind.

The study first developed a new method to design loading sequences for a lab test, to analyse the joint fatigue behaviour under wind load. This research focused on the angle bracket connection system with fasteners. Compared with the testing sequences from other building codes, the newly developed process is more logical and can save testing time.

The high-cycle fatigue testing results proved that wind load could degrade stiffness of timber wall joint with an angle bracket system but did not cause the connection system failure or material damage. Additionally, with the increase in building height, stiffness reduction increased. The angle bracket connecting system can connect timber and concrete but selecting the angle bracket type is essential. Different connecting details were tested. The results demonstrate that changing nail pattern or angle bracket size can influence the cyclic fatigue performance of timber wall joints.

By applying the digital image correlation (DIC), this study indicates that the cyclic loading mainly affects the mechanical properties of joints by affecting the embedment of fasteners rather than the strain of the angle bracket.

This study then extended the investigation to the life-cycle environmental impact of timber building. Results pointed out that neglecting the energy or material used for joint timber maintenance can cause at least 20% underestimating the embodied carbon.

Contents

List of Tables

List of Figures

Declaration

I, Acknowledgement the author, confirm that the thesis is my own work. I am aware of the University's Guidance on the Use of Unfair Means (www.sheffield.ac.uk/ssid/unfair-means). This work has not been previously presented for an award at this or any other university.

Chapter 1. Introduction

1.1 Background and motivation

As a new solution to global warming, engineered timber such as Cross-laminated timber (CLT), glue-laminated timber (GLT), and Laminated Veneer Lumber (LVL) have constructed new building projects, of which the height has grown from 29 metres in 2009 to 85.4 metres in 2019. Completed in Norway on 14 March 2019, the MJØSTÅRNET (Figure 1-2) has become the tallest timber building worldwide. This building is built with a CLT core and frames with GLT. Another 84-metre timber building, HoHo Tower in Vienna, was completed in 2017 and had a hybrid system that combines concrete core and CLT. Compared with the concrete and steel buildings, the higher strength to weight and stiffness to weight ratio of timber buildings indicates a potential for continuous increase in height.

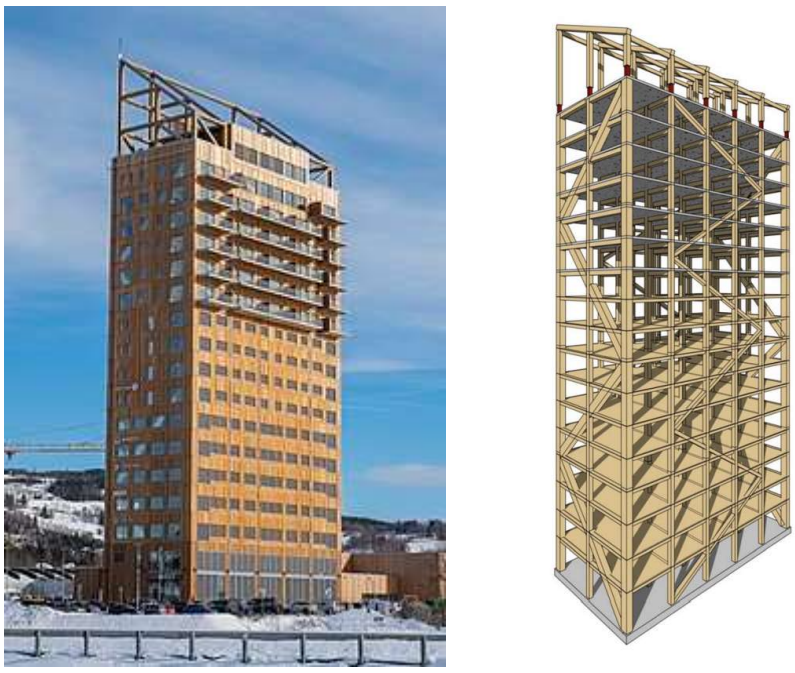

Figure 1-1: Mjøstårnet by Voll Arkitekter in Brumunddal, Norway (Dezeen,2019)

Because timber belongs to lightweight structural materials, wind vibration problems will occur once the building exceeds a certain height, which means in some cases, the whole structure mass of timber building may not be sufficient against heavy wind load. The concrete floor slabs between levels 12 and 18 are used in MJØSTÅRNET to add building

mass for resisting wind forces. Adding building mass and installing a damping system has been beneficial in reducing the structural vibration of the whole structure, which means that wind action design is an essential part of the tall timber structure design. Even within the wind action design, the wind still provides dynamic loading on the building systems due to the wind speed fluctuation that may cause excessive vibrations. Research and timber building design codes focused on the ultimate building performance by preventing failure caused by the extreme load. Besides, two other risks could lead to long-term excessive vibration: first, the building would fail to comply with the serviceability limit; second, the fatigue damage can be accumulated on the connections or timber material. Consequently, the performance of the building will degrade, resulting in a strong influence on serviceability and reliability of performance of the dynamic properties of timber building structures.

The dynamic properties of timber structures have been analyzed in several projects, focusing on seismic behaviour. This research covered connections to the full-scale facilities using lab testing or finite element analyses. During full-scale tests, the timber shear walls performed like a rigid body, whereas the connections between different structural members provide flexibility (Popovski and Karacabeyli, 2012a.) It is confirmed that timber buildings' ductility and energy dissipation depend highly on the connections. Without building collapse being considered, the local failure can still happen in timber members near connections due to the factor of fatigue. Despite this, less research aims to determine the serviceability of timber wall connections in high-rise timber buildings under long-term wind load.

The assessment of serviceability and reliability of high-rise timber buildings is conducted with the support of wind tunnel tests and FE modelling. The serviceability performance under wind load is influenced by the design of timber connections and can further affect the occupation comfort, maintenance frequency of non-structural elements and building operation. There is one question about that fact: how do timber connections in tall buildings perform when subjected to long-term cyclic loading due to wind excitation? This question is particularly relevant to those connections that connect the façade panels and the main structures. Engineers need this knowledge to design robust and reliable tall timber buildings. Additionally, with the advance of hybrid timber building systems, the combination of

frames of different construction materials with plug-in timber panel walls has become a meaningful way to promote the development of timber building height, which makes the design of the joint between the wall panel and the frame even more critical.

The cyclic loading test is the most direct way to analyse the fatigue behaviour of timber building connections. One essential premise of the research joint under cyclic wind load is to provide a load protocol that can reflect wind load characteristics. However, the review shows that most testing suggestions are based on the research on roof claddings other than timber wall panels, and the currently available protocols remain too complex or time-consuming.

The motivation of this study is to address the insufficient understanding of the wind-induced fatigue behaviour in timber connection in a plug-in panel system in tall timber buildings. The aims of the study include three aspects: first, to develop a repeatable cyclic testing process for timber wall connections that can reflect the performance under wind load; second, to apply the lab test with the newly designed loading protocol to study the behaviour of timber joints; last but not least, using lifecycle assessment to analyse whether the degradation of timber connection will influence the energy and CO2 efficiency when considering the maintenance of timber building.

1.2 Objectives and scope

This study starts from the following research questions:

1. How do timber wall connections perform under the wind load?

2. What are the existing wind load protocols, and how to develop a new testing method based on the timber wall behaviour?

3. How do the timber wall joints perform under different scenarios, i.e., different loading protocols, building heights, and connection types?

4. Will the maintenance of timber buildings caused by connection fatigue damage change the life cycle energy consumption and environmental impact?

To answer these research questions, the elementary purposes of this research are:

- To propose a reliable assessment loading protocol to evaluate the long-term behaviour of timber connections under wind load circumstances.
- Test the fatigue behaviour of timber connections with different boundary conditions in a plug-in system under wind-induced excitation.
- To evaluate the life-cycle energy consumption and environmental impact when connection maintenance is considered.

The objectives of this thesis are:

- To evaluate the existing wind-induced cyclic test method from different building codes and understand the dynamic wind simulation mechanism.
- To collect enough wind data and simulate the wind gust wind velocity under different return periods following the extreme wind pressure prediction method.
- To figure out the vibration amplitude of timber wall by applying finite element analysis method with the predicted wind velocity as input data and combining the existing building code to develop a new wind load fatigue behaviour test protocol.
- To examine the factor influencing the fatigue behaviour of timber in-fill wall systems under different conditions:
    - To compare the performance under different loading protocol
    - To validate the effect of varying building height
    - To test the influence of different connection details
- To calculate the life-cycle energy consumption and CO_2 emissions considering wall fatigue life and connection replacement

The outline of this thesis is organized according to these objectives.

This research investigates the fatigue behaviour of in-fill timber wall systems in high-rise timber buildings and conducts a life-cycle assessment of wall and connection fatigue, which requires a research object of timber buildings higher than 10 meters. Furthermore, this

research focused on the along-wind performance of timber building wall connections. Thus the influence of cross-wind load is omitted. This research selected one city as a criterion to collect wind data, thus predicting and simulating the extreme wind pressure on timber buildings with collected data. The influence of wind season and direction are not involved.

The engineered timber products are the sole focus in the vibration simulation, and experimental test, where the angle bracket fastened with nails is used in the connections, as is usually used in practice. The test includes the life cycle assessment, the energy consumption of wall connections, and environmental impact, but connectors between other structural parts are not.

1.3 Thesis outline

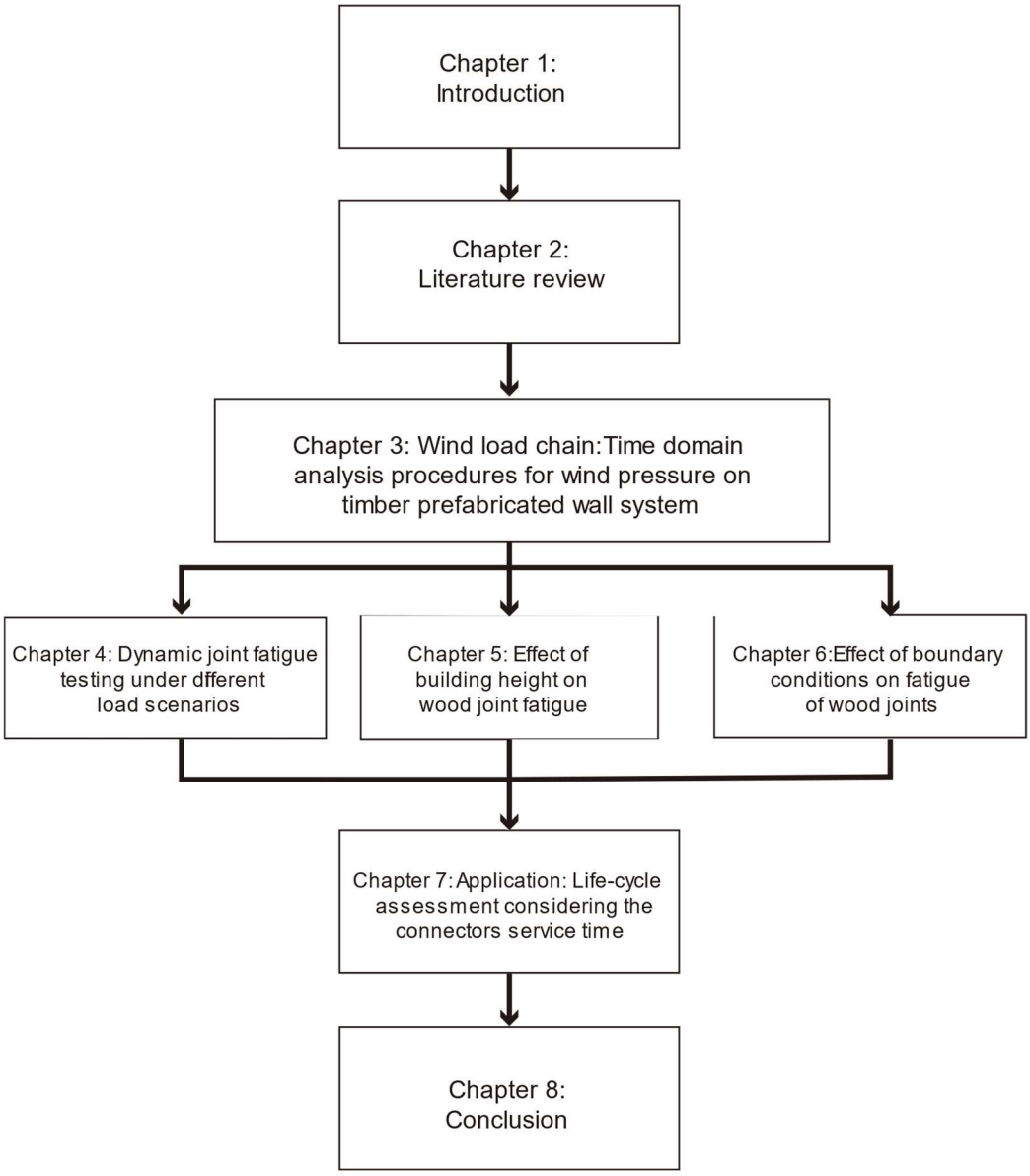

Figure 1-2: Structure of the thesis

This thesis comprises eight parts. Chapter 1 introduces the research background and motivation, in which the research object and scope are clarified. The thesis outline is displaced subsequently.

In Chapter 2, the development of timber building from ancient to modern timber structures and illustrates the promotion of engineered timber material have been reviewed, where the review of current rise timber building and related research indicates the challenge from wind load may influence the increase of timber building height. Introducing the in-fill panel system and its connection system used in current timber building design shows the

challenge and advantages. This chapter also reviews the basic theory of wind-induced vibration and recent research on timber building fatigue behaviour under wind load.

What is first introduced in Chapter 3 is the available methods to evaluate the wind pressure on buildings and selected the CFD method for this study. Subsequently, what is presented in this chapter is the dynamic wind pressure simulation progress on the timber wall system, including the data collection, extreme wind prediction, and wind spectrum simulation. The wind velocity simulation results are used in finite element coupled analysis to determine the timber wall behaviour under dynamic wind pressure; before that, the sensitivity study of the FE analysis is also expressed.

Chapters 4, 5, and 6 describe the experimental test results of timber connections under cyclic load integrated from Chapter 3. In Chapter 4, the displacement data recorded from chapter 3 and the Rainflow counting method to develop a new cyclic testing protocol were combined. The cyclic behaviour and stiffness residual of timber connections under the new testing protocol has been compared with the other three protocols from different building codes to evaluate the feasibility of the newly designed method.

Chapter 5 applied the new testing protocol design process to develop the loading sequences for joints at different building heights. Then, this chapter analyzed the joint behaviour under cyclic test and stiffness residual after cyclic load. The DIC method is applied in this Chapter to assess the angle bracket and timber component strain.

A new loading protocol to test the fatigue behaviour of timber joints with different connector details is applied in Chapter 6. This chapter applies the DIC method to compare timber components and connectors' strain or relative movement. The study variables include change of angle bracket type, change of nail pattern and change of connection boundary.

Considering the reduction of stiffness after the long-term wind load, it may be necessary for a timber building to have proper maintenance. In Chapter 7, the author introduced one application method of research findings from previous chapters. This chapter assessed the lifecycle environmental impact and energy consumption of a timber building under different maintenance scenarios, and the comparison results were presented between concrete-based buildings and timber frame buildings.

Chapter 2. Literature review

2.1 Developments and challenges in timber construction

2.1.1 Traditional and modern wooden buildings

Before the invention of reinforced concrete, wood-frame buildings were one of the most popular building types. Especially in ancient China, wood was widely used for residential, commercial or religious buildings (Lam et al., 2008, Langenbach, 2008). The Yingxian Pagoda, located in Shanxi Province, China, is the tallest ancient wood-frame building at 67.3 m. Built-in 1056 AD, the Yingxian Pagoda has experienced eight magnitudes 6 or higher earthquakes in 1000 years (Lam et al., 2008). Buildings constructed primarily of wood are also found in other parts of the world. The Great Buddha Hall at Todaiji Temple in Japan, 57 m by 50.4 m in plan and 48.6 m in height, is considered the largest ancient timber structure in the world (Langenbach, 2008). Compared to Western countries, traditional Chinese timber structures have unique characteristics in terms of construction techniques (Fang et al., 2001, Zhang et al., 2011). Dou gong and Tenon Joint are essential components of the structure and serve as connections between different elements (Figure 2-1). Metal reinforcements are not used in these structures (Zhang et al., 2011). It was noted that this semi-rigid connection is flexible in lateral cycling tests, and energy is dissipated through friction between the tenons(Fang et al., 2001, Zhang et al., 2011, Che et al., 2006, Li and Qin, 2005). In different experimental tests, the damping ratio of the monolithic structure ranged from 3% to 5%, which indicates that this construction technique performs better than other structures in earthquakes (Zhang et al., 2011). Finite element simulations have also been applied to analyze the dynamic behaviour of traditional Chinese wood-frame buildings under wind loads, and the results show that the most significant displacements occur at the roof (Han et al., 2021). Han (Han et al., 2021)also noted that current wind load codes in China are inadequate in analyzing wind-induced vibrations in ancient wood structures. In addition, thermal performance studies have shown that ancient Chinese hall-type timber-frame buildings can provide a relatively moderate temperature in summer (Xu et al., 2016). However, limitations of these traditional buildings have emerged.

Due to the lightweight construction and tongue and groove flexibility, these buildings are sensitive to wind loads (Han et al., 2021), limiting their development into modern high-rise residential buildings. In addition, these buildings do not perform as well thermally in winter as in summer (Xu et al., 2016).

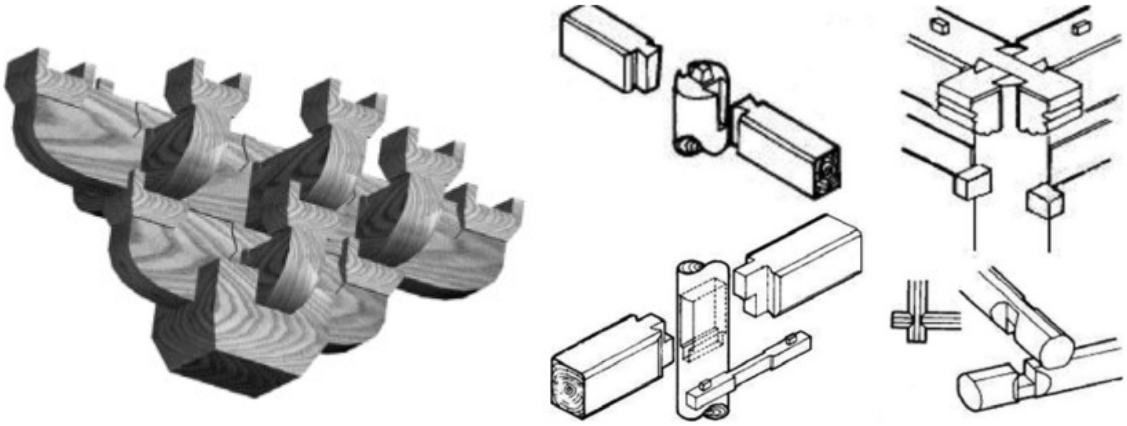

Figure 2-1: Example of Dou gong and Tenon Joint (Zhang et al., 2011)

Studies point out that there is a great potential to reduce environmental impacts, as the construction industry contributes up to 40% of energy consumption and greenhouse gas emissions (Shao et al., 2014); (Ruuska and Häkkinen) (UNE, 2018). With the development of mineral-based building materials, reinforced concrete is widely used in construction (Brandner et al., 2016). However, the construction industry has also started to adopt decarbonisation techniques to mitigate climatic conditions and save energy. Wood as a natural and sustainable material is once again one of the options to reduce energy consumption in buildings, and with the development of new engineered woods such as cross-laminated timber (CLT), glulam laminated timber (glulam), and laminated veneer lumber (LVL), the mechanical properties of wood as building components have been improved. Due to better thermal properties, including lower thermal conductivity and lower thermal mass, wood panels are advantageous in improving building insulation, reducing energy consumption during the operational phase and providing a better temperature environment (Bellamy and Mackenzie, 1999).

In addition, the carbon sequestration capacity of wood allows for 50% of its growth to be achieved by absorbing carbon dioxide from the atmosphere (Harris, 2005). When a forest is under sustainable management, cutting and planting new trees ensures the efficiency of the carbon cycle, as the rate of carbon dioxide absorption decreases as the age of the trees

(Sposito and Scalisi, 2019). In addition, at the end of its life cycle, wood can provide about six times more energy as a biofuel than planting and maintenance (Harris, 2004, Sposito and Scalisi, 2019). As a construction material, engineered timber panels are often prefabricated, minimising assembly time and construction waste (Zhou et al., 2017). Furthermore, Börjesson (Börjesson and Gustavsson, 2000)states that up to 10% of the wood can be recycled for other products after demolition.

The structural form of modern timber-frame buildings varies with the purpose, and the development trend is to achieve higher floors or larger spans (Li et al., 2020). Although different in detail from architecture, modern wood-frame building systems can be divided into three parts: heavy frame buildings, deck buildings, and timber grill shell buildings (Figure 2-2) (Smith and Frangi, 2008, Harris and Buildings, 2011). Heavy frame timber frame buildings have a skeleton of massive engineered timber posts and timber beams decorated with different wall panels depending on the need for vertical load bearing, horizontal stability and thermal or acoustic insulation (Thelandersson and Larsen, 2003). This structure is usually built as a dwelling and is suitable for 6-5 storeys (Thelandersson and Larsen, 2003, Smith and Frangi, 2008). Combining timber beams and columns with a structural core is usually suitable for taller buildings (Harte and Maintenance, 2017). The platform type is simpler to design and install than the former and is now typically used in mid-rise and high-rise residential buildings (Grasser, 2015). Cross-laminated timber (CLT) panels are usually used in the decking style. In this style, the floor and foundation serve as a platform for the next floor, and the walls can resist all types of loads (Harte and Maintenance, 2017, Shahnewaz, 2018, Shahnewaz et al., 2019). However, dead loads increase with the height of the building, further increasing the burden on the ground floor walls, resulting in a limitation of this type of rising (Harte and Maintenance, 2017). Unlike the two previously mentioned styles, mesh shell construction is mainly used in public buildings. The development of digital design tools and CNC machines has provided opportunities for timber buildings to be more creative with their shapes (Kuzman and Sandberg, 2016). This structure type facilitates the provision of large spans and more visually striking spaces but requires more design and construction skills (Harris and Buildings, 2011).

Figure 2-2: Different modern timber structures: heavy-frame (left), platform(middle), Grid-shell (right).

2.1.2 Development of engineered timber

Wood has a high strength-to-density ratio (Table 1), which gives it an advantage over concrete buildings in reducing the overall structural weight (Thelandersson and Larsen, 2003, STA, 2003). Furthermore, as mentioned earlier, conventional timber structures perform well in seismic areas. However, as an anisotropic material, the strength and stiffness of wood are highly dependent on fibre orientation. In addition, the strength of wood decreases when knots appear between the stem and the branches (Thelandersson and Larsen, 2003).

Engineered timber is a wood product in which several layers of veneer are bound together in different sequences using glue or nails according to structural requirements (Thelandersson and Larsen, 2003). Trees are debarked and cut into desired shapes after harvesting, and these veneers need to be dried and graded before glueing (Sun et al., 2020). These manufacturing processes reduce and disperse surface defects and obtain more reliable structural quality (Sun et al., 2020, Thelandersson and Larsen, 2003). A study comparing the flexural strength of 286 mm Parallel Strand Lumber showed a 50% increase in load capacity (Thelandersson and Larsen, 2003).

Table 1 Strength to density ratio of different materials(Thelandersson and Larsen, 2003).

Material	*Density kg/m²*	*Strength Mpa*	*Strength to Density Ratio 10^{-3} Mpa·m³/kg*
Structural steel	7800	400-1000	50-130
Aluminium	2700	100-300	40-110
Concrete	2300	30-120	13-50
Clear Softwood (Tension)	400-600	40-200	100-300
Structural Timber	400-600	15-40	30-80

There are different engineered timber products for different building types and building components. Including parallel strand board (PSL), laminated strand lumber (LSL), and laminated veneer lumber (LVL), most engineered timber products are made from thin veneers ranging in thickness from 2.4 mm to 4.8 mm. These products are often made into wood I-beams to replace beams or columns in solid wood sawed light frame buildings (Thelandersson and Larsen, 2003). In addition, oriented strand board (OSB) made from wood chips has been invented. Although OSB is unsuitable for structural members, it performs better than traditional timber sawn into the short-span top or edge panels in resisting shear and bending loads (Thelandersson and Larsen, 2003). Heavy engineered timbers, including Glue-laminated timber (GLT) and cross-laminated timber (CLT), are among the most popular modern timber building design branches.

(1) Glue-laminated timber (GLT)

The use of glulam timber dates back more than a century. Evidence shows that some structural elements of railway bridges in England, Scotland and Sweden were built in the 18th century (Riberholt, 2007, Lehringer et al., 2014). In contrast, the GLT, now referred to, was patented by Otto Hetzer in 1906 (Ong, 2015, Thelandersson and Larsen, 2003). GLT is made by laminating softwood boards in grain parallel to their length (Figure 2-3). A board is typically 40-50 mm thick, or thinner if required, and 1-2 m long, meaning that raw material for GLT can be harvested from smaller trees. The flexibility in size makes

GLT suitable for different building elements, from straight beams and columns to large span arches (Ong, 2015).

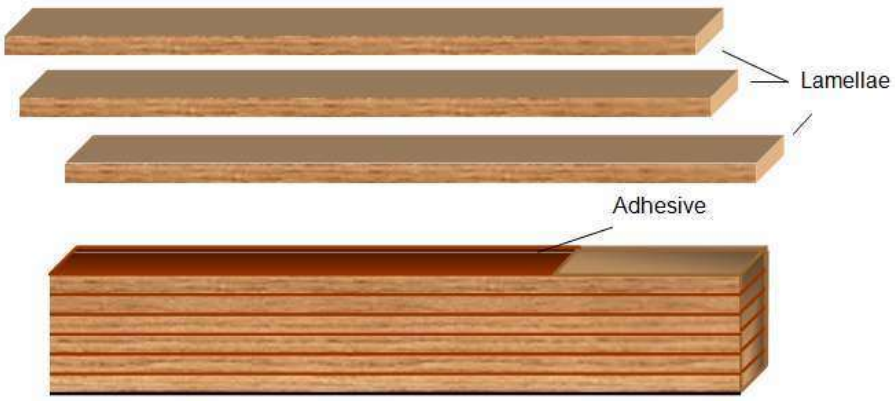

Figure 2-3: Laminating form for GLT (Zangiácomo et al., 2017)

GLTs also have the advantage of increased stiffness and strength, and their load-bearing capacity can be further increased by using near-surface mounting techniques compounded with fibre-reinforced polymers (FRPs) (Sun et al., 2020, Ong, 2015). Researchers have applied various materials, including carbon or glass fibres, steel, and bamboo, to reinforce GLTs (Dorey and Cheng, 1996, Micelli et al., 2005, Guan et al., 2005, De Luca et al., 2012, Echavarria et al., 2012). Compared to unreinforced GLT, reinforced GLT showed improved ductility and increased strength over stiffness in bending tests (De Luca et al., 2012, Issa et al., 2005, Sun et al., 2020, Wang et al., 2017). Studies have pointed out that FPR has an advantage over metals in improving tensile strength (Martin et al., 2000). Carbon FRP performs better than glass in improving mechanical properties in bending (Sun et al., 2020). Adding a layer of reinforcement to the tensile surface of GLT beams instead of multi-layered wood panels can improve mechanical properties while reducing material costs (Ong, 2015).

Recent research on GLT aims to build high-rise or large-span buildings that sustainably produce GLT and protect or repair GLT structures (Ong, 2015). The properties of adhesives strongly affect the strength of GLT in wet environments; therefore, some researchers have focused on the technology of adhesives (Moody et al., 1999, Serrano et al., 2014). Furthermore, many studies focus on the non-destructive GLT structures (Teder and Wang, 2013, Neuenschwander et al., 2013), which may be helpful in the future rehabilitation of GLT structures.

(2) Cross Laminated Timber (CLT)

Invented decades ago in Switzerland and Austria, CLT was another large engineered timber product widely used in modern timber construction (Van De Kuilen et al., 2011, Harris, 2015). Each layer in CLT is laminated with a 90-degree grain (Figure 2-4), finally forming a maximum 500 mm thick plank (Liang et al., 2020, Gagnon and Pirvu, 2011). The out-of-plane strength and stiffness of CLT are improved compared to GLT because the material is bi-directional along the grain (Sun et al., 2020, Lehmann et al., 2011, Harris, 2005). Such prefabricated panels can be used as floors, walls or roofs of buildings and provide a low-dust, low-noise and low-waste site. Harris (Harris, 2015, Gagnon and Pirvu, 2011)states that another benefit in practice is reducing construction time and that some buildings are erected in weeks. In addition, CLT has the advantage of a longer fire resistance period compared to steel structures (Frangi and Fontana, 2005, Bochicchio et al., 2008, Lehmann, 2012). These advantages have made CLT popular in medium and high-rise buildings (Wells, 2011). There are already buildings using CLT, and a study of the Forté apartment building in Melbourne showed the potential to reduce energy consumption and CO_2 emissions during the construction phase (Durlinger et al., 2013). In addition, by controlling the number of layers or thickness of CLT, the range of strengths can be controlled to accommodate different building levels or components, further reducing construction costs (Harris, 2015).

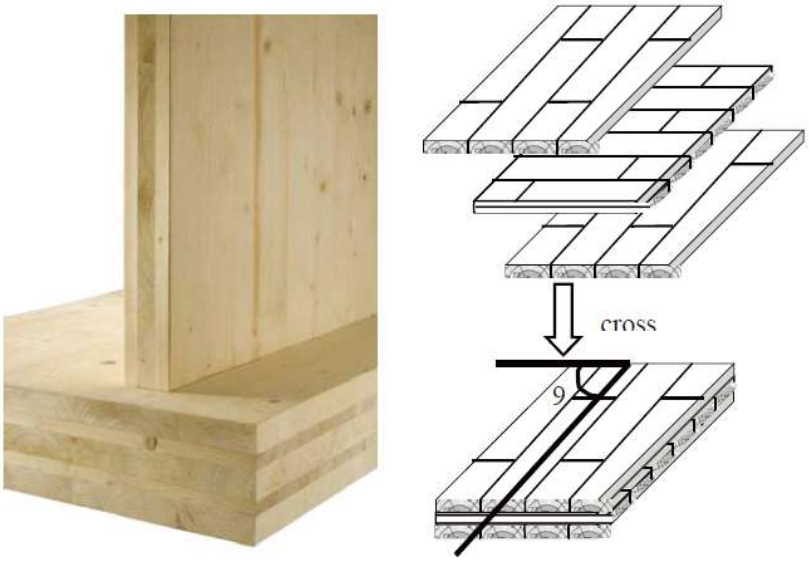

Figure 2-4: Picture of Crosse laminated Timber (Van De Kuilen et al., 2011)

To further improve the out-of-plane mechanical properties, researchers have focused on the performance of hybrid CLT produced with soft and hardwood (Sun et al., 2020). Sun (Sun et al., 2020)concluded that shear resistance is higher for hardwood or hybrid CLT than for pure softwood CLT. Composite CLT with other engineered and conventional woods can outperform conventional CLT in terms of flexural and shear resistance (Wang et al., 2017, Wang et al., 2015, Davids et al., 2017). There is also the potential to reduce material consumption by using optimized CLT panel design strategies (Mayencourt and Mueller, Stanić et al., 2016).

CLT production capacity has proliferated, especially in Europe (Brandner et al., 2016, Grasser, 2015, Larasatie et al.). Between 2012 and 2019, global annual production grows from 500,000 m^3 to 1.44 million m^3 (Brandner et al., 2016, Muszynski et al., 2020). However, challenges remain in developing large CLT buildings, such as fire safety restrictions in some countries, concerns about durability, maintenance, and even acceptance by the public (Lehmann et al., 2011). Protection from insects, high humidity environments, and acoustics can also be an issue (Gereke et al., 2010, Lehmann, 2012). Furthermore, Brandner Brandner et al. (2016) suggest that optimizing the connection system can further improve CLT utilization.

2.1.3 Developments and challenges in high-rise timber frame construction

1) High-rise wooden buildings

In recent years, timber buildings have shifted from multi-story (up to 9 stories) to high-rise construction. Figures 2-5 show the increased height of timber buildings in recent years. With the completion of the mjøsa tower in Norway, the maximum height of a modern building is now 85.5 m. In addition, the Hoho Wien in Vienna, completed in 2019, has the highest number of storeys. However, the quest to increase the height of timber buildings has never stopped. Researchers believe there is potential for developing timber skyscrapers because naturally growing trees can reach 150 meters, exceeding the cantilever limit of many manufactured materials (Sposito and Scalisi, 2019, Smith and Frangi, 2008).

London's Oakwood House, a skyscraper design, is under development (Foster and Ramage, 2017) and will be over 300 meters tall.

Figure 2-5: Timber building heights development

Modern high-rise timber buildings are buildings where the primary building material is timber products. Therefore, the high-rise timber buildings mentioned in Figure 2-5 can be classified as pure and composite timber structures. Foster (Foster et al., 2016)provides a more detailed classification of the different high-rise timber structural systems, as shown in Figure 2-6.

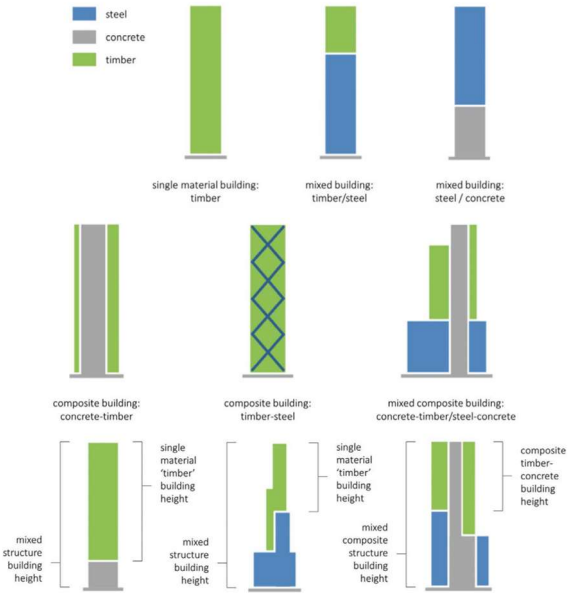

Figure 2-6: Building type classification (Foster et al., 2017)

The CLT platform system and heavy timber frame with CLT wall panels can be considered single-material timber buildings (Gagnon et al., 2013). Stadhaus is one of the tallest CLT platform buildings, with all components made of wood panels except the foundation (Wells, 2011). The study noted that the structural design of the CLT platform building could be easily calculated following the Eurocode 5 guidance (Wells, 2011). Feedback from the occupation showed that the building was satisfactory structural, acoustic and thermal performance (Wells, 2011). The Forté building was made entirely of CLT panels and erected on a concrete base (Figure 2-7) (KOTWICA and KRZOSEK, 2018). This building system provides a new paradigm for modular construction, and construction time can be saved by up to 50% due to less assembly process than reinforced concrete systems (Crespell and Gagnon, 2010). As load-bearing walls, the thickness of the CLT slab increases with the load-bearing requirements. Therefore, the thickness of the underlying CLT wall increases with the total number of stories (Schmidt et al., 2013). A design example by TRADA (TRADA, 2009) shows that it is safe to construct a 12-story CLT deck building by calculating the ultimate limit states and serviceability limit States following Eurocode 5 (BS EN 1995-1-1: 2004 and the National Annex)(Schmidt et al., 2013). Well (2011) argues that the system's height could be increased to 15 storeys by increasing the strength of the connections. Therefore, one of the limitations of the CLT platform building is the connection between the different components.

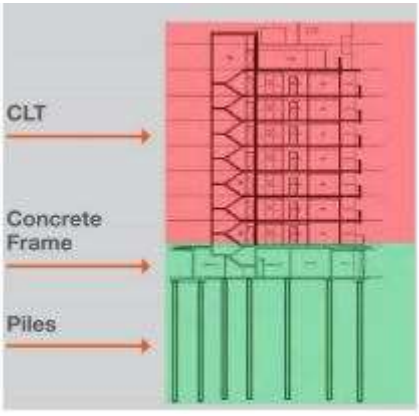

Figure 2-7: Structure of Forté Building (KOTWICA and KRZOSEK, 2018)

Thus, applying a post-and-beam framing system allows for a broader range of building types for a single timber material. The Wood Innovation and Design Center (WIDC), an eight-story office building, is one such structure (Figure 2-8). The entire building consists of engineered timber products, including GLT and LVL columns, PSL beams, and CLT

walls and floors (Danzig, 2011). First of all, the benefit of this structural system is the reduction in the size of the structural components, which provides more space for human activities (Wells, 2011). In addition, the stiffness of this system becomes higher by reducing the connections between floors compared to the deck system (Danzig, 2011). Other post-and-beam structures are being developed for pure wood buildings, such as 475west 18 in New York (Robinson et al., 2016)and the "Wooden Tower" in Chicago (Skidmore and Merrill, 2013). However, finite element dynamic response studies of high-rise timber buildings based on the "Wooden Tower" design have shown that wind has a more significant effect on peak acceleration in high-rise timber buildings than in multi-story buildings (Abeysekera and Malaga Chuquitaype, 2015). Abeysekera (Abeysekera and Malaga Chuquitaype, 2015) also noted that even with a 5% increase in damping ratio, the vibration condition of high-rise wood-frame buildings may still fail to meet suitability criteria. Another study on a 22-storey pure wood frame building also noted that the fundamental frequency is 0.6 Hz, resulting in high peak accelerations at the top floor considering the lightweight properties (Johansson et al., 2016).

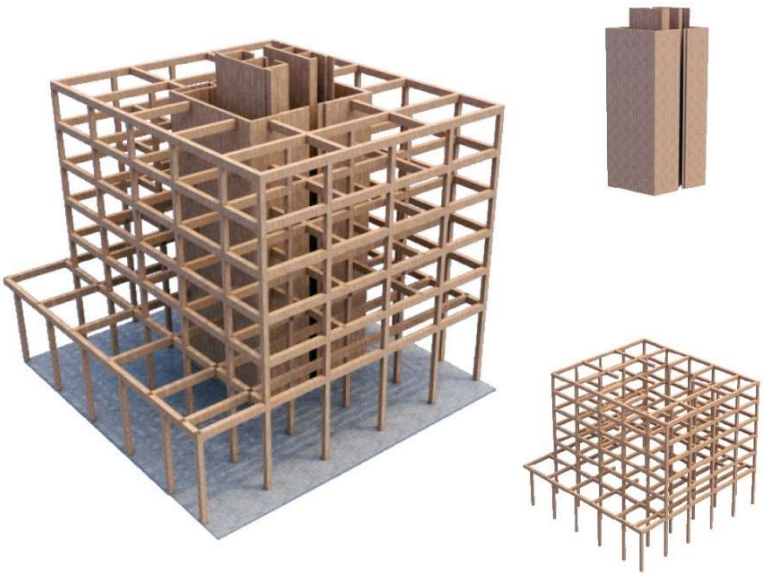

Figure 2-8: Structure of WIDC (GEORGE, 2015)

In practice, most high-rise timber buildings are composite structures. Of these, wood and concrete and wood-steel construction are typical applications. In the case of timber-concrete buildings, there are two forms: timber cores with concrete floors and concrete

cores with timber columns and beams (Figure 2-9). The Treet Building and the Mjøsa Building in Norway consist of a timber frame and core plus several floors of concrete slabs.

The Treet residential building is a modular structure with 6 and 10 floors of concrete slabs serving as a foundation for four floors of timber modules (Abrahamsen and Malo, 2014). Adding concrete floor slabs increases the mass of the whole building, which improves the wind-induced behaviour. The study showed that the peak acceleration at the top floor was still higher than expected within acceptable limits (Bjertnæs and Malo, 2014). The Mjøsa building replaced the wooden floor with concrete above the 12th floor. In addition, since floors 12 to 18 are apartments, concrete floor slabs also enhance sound insulation (Abrahamsen, 2017).

Brock Commons (Staub-French et al., 2021) and Hoho Wien (Hanuliak and Hartman, 2021) use a second type: concrete core and timber frame. In both buildings, the primary function of the concrete core is to resist lateral forces from wind and earthquakes (Moudgil, 2017, Hanuliak and Hartman, 2021). For Brock Commons, a concrete core was based on local codes (Moudgil, 2017). One study analyzed the feasibility of replacing concrete cores with wood cores at Brock Commons and noted that LVL is more suitable than CLT but requires careful design (Moudgil, 2017). The potential for designing skyscrapers by combining the two types was analyzed (Figure 2-10) (Van De Kuilen et al., 2011). Concrete cores can improve the stability of the structure, while concrete slabs can be used as a foundation for the wooden elements above (Van De Kuilen et al., 2011). In addition, floors with concrete floors can provide fire and emergency partition spaces (Van De Kuilen et al., 2011). In addition to the hybrid building systems mentioned above, hybrid timber components have also been designed, such as composite timber-concrete floors (TCC) (Dias et al., 2016, Ceccotti, 1995, Ahmadi and Saka, 1993). Studies have pointed out that TCC performs better than CLT flooring in seismic and flexural resistance and is more suitable for high-rise and large-span buildings (Mai et al., 2018). TCC floors also outperform CTL in acoustic performance (Zhang et al., 2020). Dias (Dias et al., 2016) stated that the advantages of TCC systems can further contribute to the development of timber construction.

Figure 2-9: Timber-concrete hybrid building: timber frame with a concrete slab(left)(Malo et al., 2016), timber frame with concrete core (right) (https://www.naturallywood.com/resource/introduction-to-brock-commons-tallwood-house-ubc-tall-wood-building/)

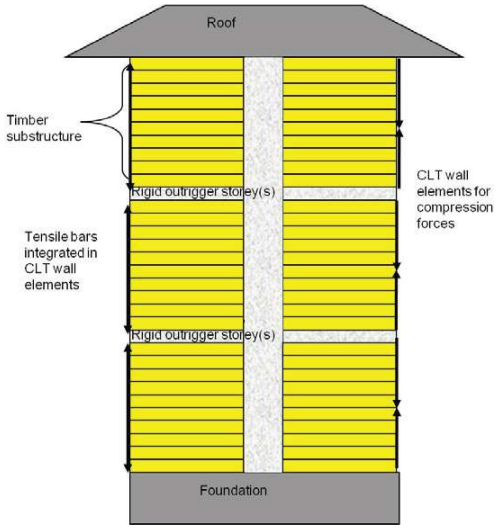

Figure 2-10:Concept of the combination of two timber-concrete systems

Currently, hybrid wood-steel structures are in the research and design phase. Research directions include steel frames with timber infill panels (Li et al., 2019a, Li et al., 2019b, Li et al., 2019c, Tesfamariam et al., 2014, Bezabeh et al., 2016, Sullivan, 2012, Baker et al., 2014), timber-steel trusses (Gilbert and Erochko, 2019) timber cores with steel connection beams (Zhang et al., 2017, Zhang et al., 2015, Zhang et al., 2016) and timber-hybrid floors or beams (Loss and Frangi, 2017, Loss et al., 2018, Hassanieh et al., 2017, Hassanieh et al., 2016). Studies of timber floors combined with steel beams have shown that yielding capacity can be improved, and stiffness and strength can be adjusted as required (Loss et al., 2018). Loss (Loss et al., 2018) state that TCC and TSC floors do not

need to be cast on-site and are relatively light. In addition to composite structural members, research into new structural combinations offers additional opportunities for high-rise timber buildings. Green and Karsh proposed the concept of the forest through trees (FFTT) (Green and d Karsh, 2012). In the FFTT design, a large timber core is connected to GLT columns and beams through steel beams, allowing the building to reach 12 storeys in height according to the British Columbia building code (Figure 2-11) (Green and d Karsh, 2012).

Studies of the seismic behaviour of this structure have shown that the maximum inter-story drift rate is about 1.1% lower than the building code limit (Fairhurst et al., 2014). The ductility of the structure is improved, and the safety of the CLT core under cyclic loading after steel beam failure can be ensured by a proper layout arrangement (Zhang et al., 2017, Zhang et al., 2016). Zhang (Zhang et al., 2016) concluded that the seismic performance of the FFTT system is better for buildings with higher floors, but the problem of wind-induced vibration may become significant. The study tested another way of combining steel and timber beams: bending resisting braces (BRB) (Figure 2-12) attached to external timber beams and columns (Gilbert and Erochko, 2019, Miller et al., 2021). Simulation results show that the system drifts 10% less than the building specified during earthquakes (Miller et al., 2021). In addition, laboratory test results support that the structure can maintain a safe relative drift rate of 4.4% under wind loads (Gilbert and Erochko, 2019). The current study focused on 7-story buildings and higher levels that require further analysis (Gilbert and Erochko, 2019).

Steel seismic frames with timber infill walls (SMRF) are another hybrid approach (Figure 2-13), and after static analysis (Dickof et al., 2014, Dickof, 2013), analysed their dynamic behaviour under cyclic loading. Tesfamariam (Tesfamariam et al., 2014)tested different floors with different seismic behaviour of steel frames with filling criteria. He noted that in the absence of a CLT infill, the drift rate might exceed the use limit and the value decreases as the number of infill increases. In terms of the hysteresis damping ratio, simulations show that the value is closely related to the stiffness ratio of the wall to the frame (Li et al., 2019c, Bezabeh et al., 2016). Bezabeh (Bezabeh et al., 2016)argues that the hysteresis damping is more related to the spatial relationship between the panel and the frame rather than the thickness or strength of the panel. In addition, Li (Li et al., 2019d) noted that the method of connection between the frame and the panels might affect the seismic behaviour of the

system. Although research on hybrid wood-steel systems is still in its early stages, these analyses provide a new direction for high-rise wood-frame buildings due to building code restrictions on the height of wood structures. In addition, the wind load behaviour of this system could be a direction for further research.

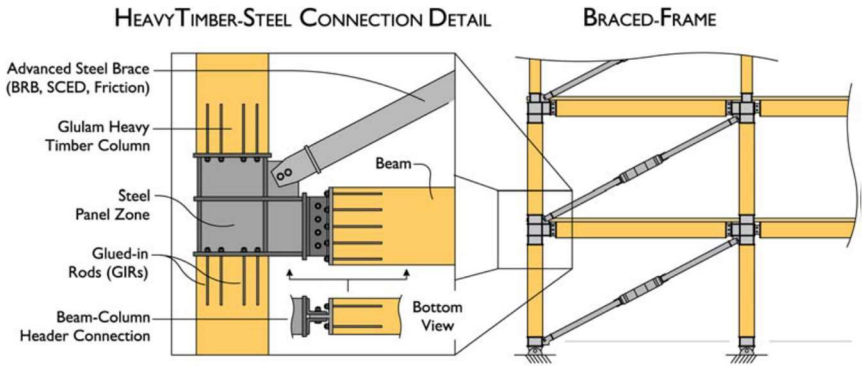

Figure 2-11: Illustration of FFTT system(Zhang et al., 2016)

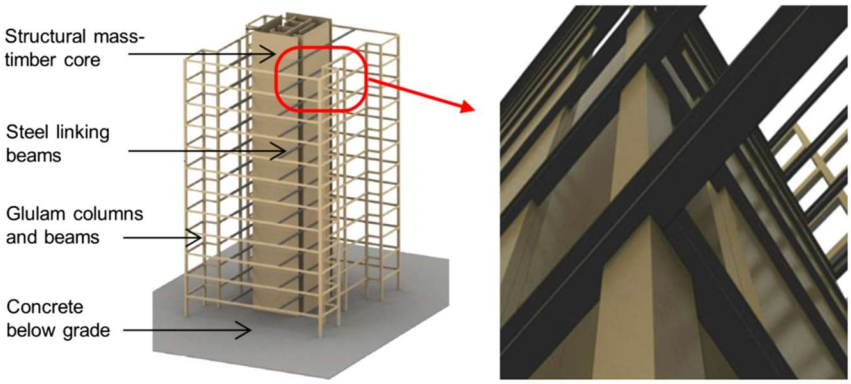

Figure 2-12: Illustration of Timber-BRBs system (Miller et al., 2021)

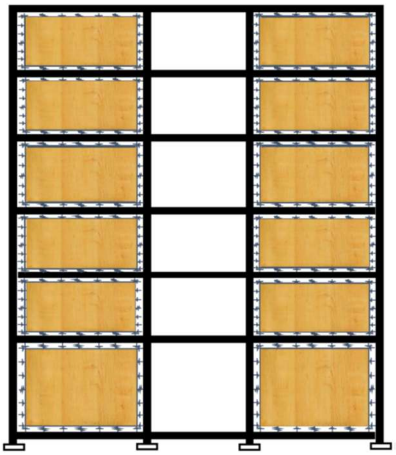

Figure 2-13: Illustration of Steel frame and timber in-fill panel system (Bezabeh et al., 2016)

1) The challenge of wooden construction

Replacing mineral-based materials building with pure timber construction increases the structure deflection. Studies have shown that deflection may increase by about 17% compared to replacing a reinforced concrete building with a timber envelope, and deflection values may be as high as 68% with a timber core (Hanuliak and Hartman, 2021). Wind resistance becomes critical as the building becomes more resistant to wind.

In addition, the connections between different structural members may be another challenge. Due to the anisotropic material properties, the load path will significantly depend on the choice of the connection system (Foster and Ramage, 2017). Reynolds (Reynolds et al., 2011)states that dynamic wind loads may affect the service life of the connections as the building height increases. Currently, connections in CLT walls are often point-like and non-linear, making the joints crucial in timber structures, as they may dictate the strength of the structure, which means the overall behaviour and member sizes will generally be determined performance of connectors rather than by the strength of the member. Therefore, analysing the performance of dowl-type connection models by simplifying them as the linear model is not adequate. Beander (2016) recommended that further research focus on the load-bearing capacity of the applied connection technique and timber member performance.

2.2 In-fill panel system

Infill panel systems are buildings constructed with load-bearing framing and infill wall panels. The reinforced concrete frame with masonry infill panels or structural infill walls is a popular type (Figure 2-14) (Chaker and Cherifati, 1999). Such systems have expanded with the development of engineered timber and prefabricated wood walls. As previously mentioned, wood posts and beam-framed buildings with infill wood walls have been constructed. Research continues to investigate wood walls infilled in different frames such as RC and steel frames. Sustersic et al. (Sustersic and Dujic, 2014) analyzed the feasibility of retrofitting existing masonry-infused RC framed buildings with wood walls. This study evaluated the seismic behaviour of RC frames with timber walls and RC frames with

masonry infill walls covered by CLT panels. Figure 2-15 shows the angle bracket connections for the first system. The results show that by replacing the masonry walls with CLT panels, the seismic performance can be improved by up to 90%, and adding more angle brackets can improve even more. Also, laboratory tests showed that the strength of the reinforced masonry walls using CLT panels increased and that the CLT panels kept the entire structure safe even when the masonry walls were damaged by seismic loads (Sustersic and Dujic, 2014).

The previous section presented those studies on steel frames with timber infill (Dickof et al., 2014, Dickof, 2013, Tesfamariam et al., 2014). Most studies chose the same connection system shown in Figure 2-16 but with different types of angle brackets. The researchers also evaluated several other connection methods (Loss et al., 2016a, Loss et al., 2016b, Asiz and Smith, 2011). Asiz (Asiz and Smith, 2011), by connecting the mechanical properties of the CLT and steel frame with screw fasteners, concluded that the results varied with the length, number, and distance of the fasteners. Loss (Loss et al., 2016a) tested different connection systems for steel-wood hybrid infill system components, where self-tapping screws were mainly used. He recommends the connection of the CLT wall and steel beam in Figure 2-17.

Research on infill panel systems has facilitated the development of high-rise wood-frame buildings and the application of modular construction (Ferdous et al., 2019). For example, in addition to acting as beams and columns, steel can be used in modular framing to fill prefabricated wall panels (Lawson et al., 2014). With the previously mentioned research experience, timber panels could be one of the options. Concrete modular frames with prefabricated timber panels are another economic combination for high load-bearing structures (Ferdous et al., 2019).

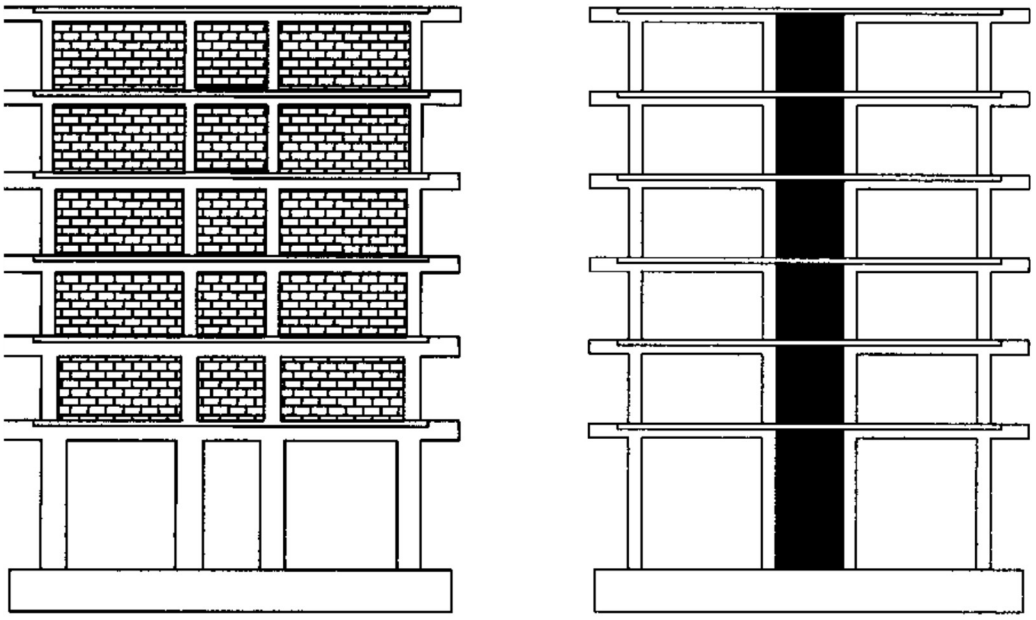

Figure 2-15: Reinforce concrete frame with infill walls (Lu, 2002)

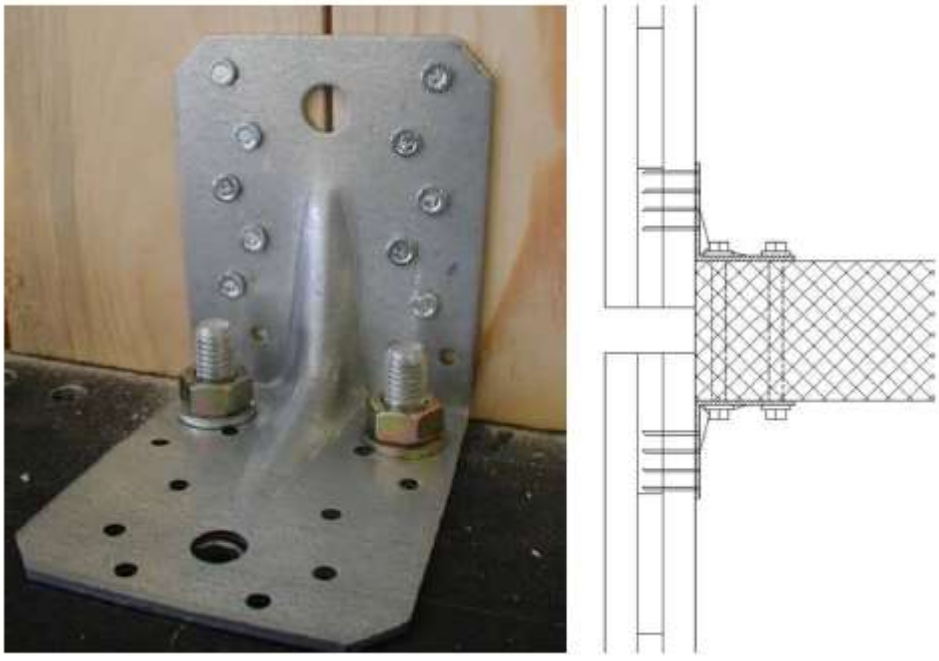

Figure 2-16: connection type in concrete frame with in-fill timber wall system.

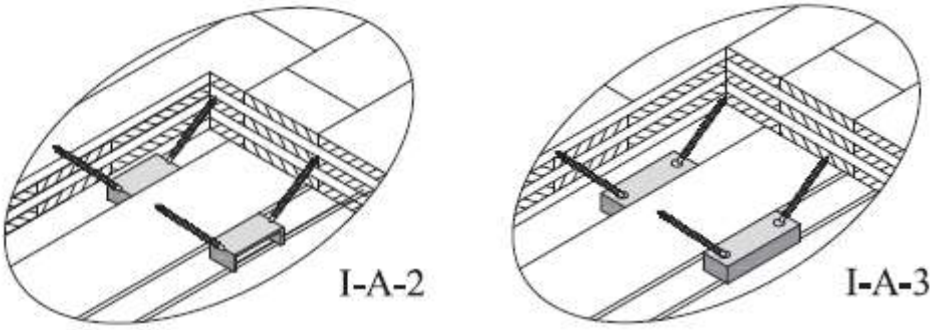

Figure 2-17: connection with self-tapping screw for a steel frame with CLT infills

2.3 Wind-induced fatigue behaviour of timber buildings

2.2.1 Wind-induced vibration

Depending on the source of the wind load, the structural response can be classified. Wind-induced responses may be caused by dynamic wind pressure or the aeroelastic forces of structural motion. The focus of this study is on the former.

- Along-wind response: caused by fluctuations in wind pressure
- Crosswind reaction: caused by alternating vortex shedding

These two reactions overlap in tall buildings, but the codes specify separate calculations. In addition, torsional reactions may also occur due to the asymmetry of some structures.

1) Methods of analysis of wind-induced reactions

The basic process for analyzing the wind response is shown in Figure 2-18. There are several methods to estimate the along-wind response, which help design tall buildings to reduce the risk of wind. The main link between wind and response estimation is the Equivalent Static Wind Load (ESWL) proposed by Davenport in 1967 (Davenport, 1967). In this theory, the practical peak loads can be divided into average loads, fluctuating quasi-static loads, and loads that cause resonant responses (Holmes, 2015b). Average loads are obtained from local data records and are not significantly influenced by turbulence. Fluctuating quasi-static loads are dynamic but lower frequency loads that do not cause

resonance. The internal forces of the structure in the first mode are considered to be the loads that cause resonant responses. Davenport applied Buffeting theory to civil engineering based on his theory, providing the gust loading factor (GLF) method and introducing the concept of gust factor to calculate the peak ESWL. The value of the gust factor is the ratio of the maximum displacement of the structure to the average displacement. This method is now applied in North American building codes (ASCE, 2017, (NRC)). However, Kareem argues that the gust coefficients in the GLF based on the displacement response of the first mode are not representative of the ESWL of the other modes (Kareem et al., 2003). The inertial wind load (IWL) method was developed based on the GLF method and related the gust coefficients to the structure's mass distribution, dynamic properties, and height. The method was applied to wind load regulations in China (China, 2012). The load-response correlation (LRC) method is another analytical method that originated from Kasperski's (1992) study of the wind response of low-rise industrial buildings (Kasperski et al., 1992, Kasperski, 1992). This method uses the correlation coefficient between the wind load and the structure's response at any point as a coefficient of ESWL to obtain the most unfavourable distribution. This method considers the correlation between the applied loads and the structure's response but is rarely applied in codes because its accuracy is related to the specific spatial distribution and the accuracy of the wind pressure data (Chen and Kareem, 2005). By comparing the response of the top and bottom of the structure, Zhou et al. (Zhou et al., 2000, Zhou et al., 2017)found significant positional differences in the results calculated by existing methods. Therefore, they developed a Gust factor algorithm based on the base moment called Moment Gust Loading Factor (MGLF) method. The moment data for MGLF can be obtained from wind tunnel tests to calculate ESWL, and this method is also accepted by ASCE (Alinejad and Kang, 2020). The Gust Load Envelope (GLE) method was developed by Chen and Kareem (Chen and Kareem, 2005). In contrast to the conventional gust factor method, the load distribution of this method depends on the external fluctuating winds rather than the mean winds. Compared to the LRC method, the GLE method yields a simpler load distribution and is more conducive to engineering applications (Chen and Kareem, 2005).

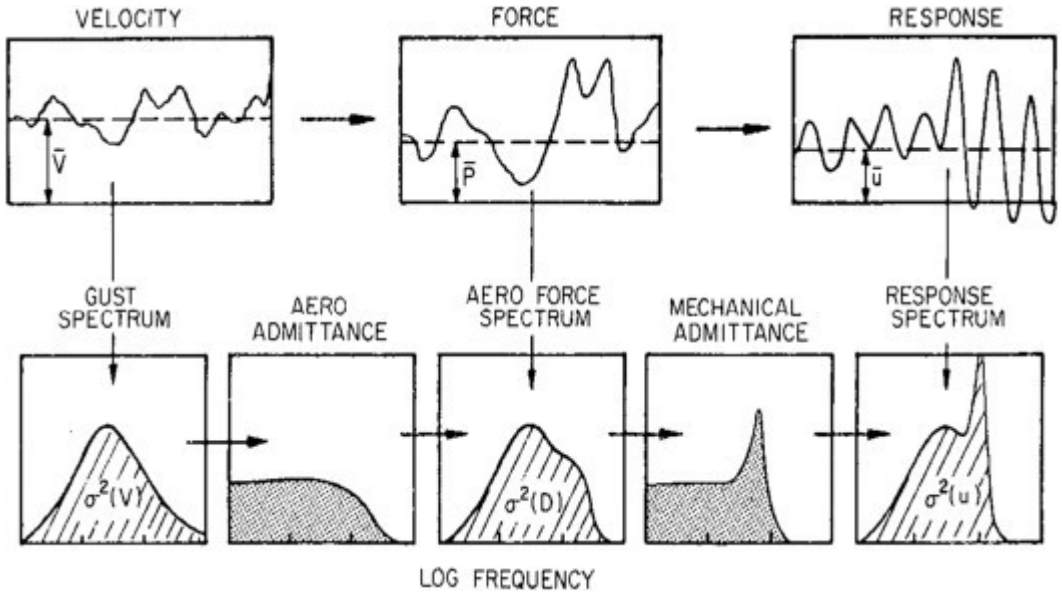

Figure 2-18: Approaches to the wind responses of structures (Isyumov, 2012)

The numerical simulation methods described above provide a method for studying wind engineering and contribute to developing wind-resistant design codes. In addition, field measurements, wind tunnel tests, and computerized fluid dynamics (CFD) simulations provide more advanced methods for studying the wind dynamics of tall buildings. The latter two methods are presented in Chapter 3.

2) Wind response in wooden buildings

Studies of low-rise lightweight wood-frame buildings have shown that wood-frame buildings are vulnerable to high winds, especially the connections between roofs and walls(Guha and Kopp, 2014, Henderson et al., 2013, Chowdhury et al., 2013). Most buildings smaller than 40 m are considered rigid, and the effects of dynamic wind loads can be neglected (Abrahamsen et al., 2020). However, even in bulk, timber buildings are flexible and less stiff than other building modes and may be sensitive to wind loads due to low-frequency vibrations (Abrahamsen et al., 2020, Reynolds et al., 2011, Lazzarini et al., 2021). Therefore, wind-resistant design is already a challenging part of the process, even if the existing mass timber structures are far from the height of conventional high-rise buildings.

Therefore, researchers started to study the wind behaviour of existing and simulated wooden buildings regarding this challenge. Based on Eurocode 1, Reynolds (Reynolds et al., 2011) analyzed the wind performance of a 20-story wooden building and indicated that the acceleration could meet the use limits by increasing the building's fundamental frequency or increasing the damping ratio. In addition, laboratory test results showed that the connections' service life varies with the dynamic load's duration and magnitude. This implies that the whole structure is as important as the connections when considering the wind load behaviour of a wooden building. Chapman et al. (Chapman et al., 2012)designed a 30-story wooden structure and analyzed its wind-induced behaviour. The building had a maximum drift rate of 0.07% and an inter-story drift rate of 0.1% under wind loads, which met safety requirements. However, Champman (Chapman et al., 2012) noted that the actual value could be higher due to the flexibility of the neglected connections during the analysis. In terms of dynamic response, this study found that damping ratios for CLT buildings are unpredictable and noted the need for studies on completed wood buildings (Chapman et al., 2012).

A study of the 'wooden tower' (Skidmore and Merrill, 2013)analysed the vibration frequencies of the first mode in different directions and concluded that this proposed 42-storey building might not be at risk from the wind. However, detailed vibration performance, such as acceleration, was not analyzed (Felicita, 2021). Another study on the existing wooden building "Treet" showed (Bjertnæs and Malo, 2014) that the natural frequencies of the modules were higher than the natural frequencies of the overall structure, a result that further guided the design of the connection between the modules and the frame. Furthermore, the peak acceleration at the top floor was 0.051 m/s2, below the serviceable limit. Feldmann et al. (Feldmann et al., 2016) selected four wooden buildings in Germany for field measurements. The results showed that the wind-induced performance varied between building types and that the use of Eurocode1 allows the assessment of the drift performance of wooden buildings but is not sufficient for dynamic performance assessment. They also suggest that the temporal multi-meter method is better than the frequency multi-meter method when analyzing windborne vibrations of wooden structures.

Considering the suitability of different buildings, Bezabeh et al. (Bezabeh et al., 2020) performed wind tunnel tests on a 40-story wooden building model. They concluded that the

exposed wind field conditions, damping ratio, and building height affect wind-induced performance. The results show that the vibration conditions appear to be significantly influenced by crosswinds and demonstrate the feasibility of applying CFD to study wind-induced responses of wooden buildings. However, according to the evaluation of the NBCC ((NRCC), 2012), compliance with wooden buildings is also related to how they are used. Lazzarini (Lazzarini et al., 2021) used a CFD model and analysed the comfort level of Mjøstårnet under wind loads.

The above study exposes key issues regarding wind-induced responses to tall timber buildings. First, every material is subject to fatigue due to wind loading, but steel and concrete are not as onerous as timber. Second, wind-induced behaviour between timber structural components can affect the deflection and service life of the entire structure. Furthermore, current assessments of the wind-induced performance of timber buildings are based on traditional provisions for mineral-based construction, which may result in a lack of the required accuracy (Bezabeh et al., 2020, Feldmann et al., 2016). Finally, wind-induced properties such as damping ratios and natural frequencies remain unpredictable and diverse. Therefore, on-site measurements of existing timber buildings to create a database will help guide the design of high-rise buildings.

2.2.2 Fatigue and creep in timber structures

1) Fatigue analysis

Fatigue of materials or structures is the mechanism by which they fail or crack before their ultimate strength after cyclic loading (Lalanne, 2014). There are three main components to analyzing the fatigue behaviour of a structure: repetitive actions, stresses, and material properties (Lalanne, 2014, Haroon, 2019). Fatigue behaviour is influenced by the periodic loads' amplitude, sequence, and frequency. Different methods to assess fatigue behaviour include low-cycle fatigue analysis, S-N curve testing, and crack assessment. The S-N curve is the most popular method (Figure 2-19) (Lalanne, 2014).

After cyclic lab tests, the S-N curve is plotted based on the stress (S) and the number of cycles (N) that cause failure at that stress value(Haroon, 2019) according to the following equation:

$$NS^m = K \tag{2.1}$$

Where: K is a constant depending on material properties.

This analysis involves converting random amplitude stresses into different consistent stress sets and applying the Palmger-Miner rule (Equation 2.2) for cumulative damage analysis.

$$\sum \left(\frac{n_i}{N_i}\right) = 1 \tag{2.2}$$

The average stress and the R-ratio are two other key concepts in fatigue analysis (Figure 2-20). The S-N curve is considered standard when the average stress level is zero, while for non-zero average stresses, the Goodman diagram is applied (Figure 2-19). Among other things, the equation of the Goodman diagram and the relationship between the two methods are as follows:

$$\sigma_{al} = \frac{\sigma_{max} - \sigma_{min}}{2} \tag{2.3}$$

$$\sigma_{meam} = \frac{\sigma_{max} + \sigma_{min}}{2} \tag{2.4}$$

$$\sigma_{eff} = \sigma_{al}\left(\frac{\sigma_u}{\sigma_u - \sigma_{meam}}\right) \tag{2.5}$$

Where: σ_{al} is the alternating stress, σ_{mean} is the mean stress, σ_u is the ultimate strength, σ_{eff} is the effective stress. The effective stress can be applied to the standard S-N curve (Haroon, 2019).

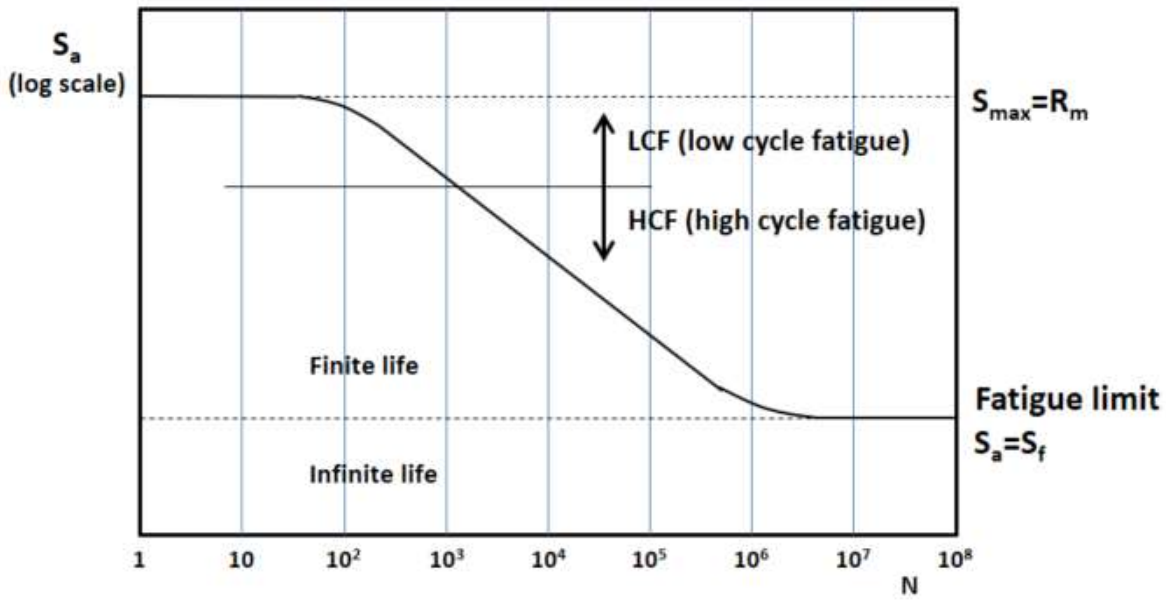

Figure 2-19: Typical S-N Curve for fatigue assessment (https://www.fatec-engineering.com/2018/02/20/description-of-a-s-n-curve/)

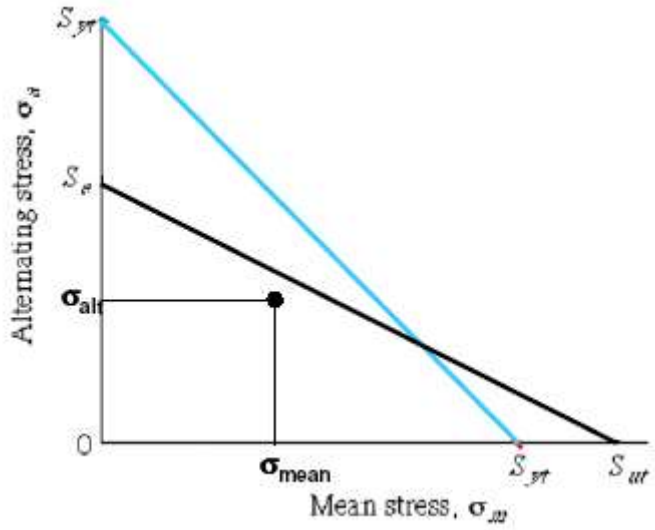

Figure 2-20: Typical Goodman line (https://www.engineersedge.com/fatigue/modified_godman_fatugue_curve.htm)

Wind-induced fatigue refers to the accumulation of damage due to structural vibrations caused by wind speed fluctuations, which may lead to failure or collapse (Repetto and Solari, 2001). Naturally, wind stresses are random and difficult to estimate, but following the (Dowling, 1971, Miner, 1945) rule, the accumulated damage due to random amplitude loads can be calculated (Dowling, 1971, Miner, 1945). Due to the randomness, wind fatigue loads can be classified as a narrow band, wide band, high cycle and low cycle loads, in

which wide and narrow are frequency ranges and high and low are cycle ranges. There are two methods to analyze wind load fatigue: frequency domain and time domain (Repetto and Solari, 2001). The frequency-domain approach combines stochastic dynamics and Davenport's concept of wind spectrum to calculate the cumulative damage caused by the possibility of wind load fluctuations at different mean wind speeds (Petrov and Aerodynamics, 1998, Mikitarenko et al., 1998). This method is accurate but complex to apply in practice (Repetto and Solari, 2001). In contrast, the time domain method is simple to operate by recording loads from wind tunnel tests and then calculating the total damage using the cycle counting method (Gu et al., 1999, Van Staalduinen and et al., 1993). However, this method requires much data collection from laboratory or computational tests (Repetto and Solari, 2001).

1) Fatigue and creep of wood materials

Wood is considered a viscoelastic material in which the duration of loading (DOL) significantly affects the mechanical resistance properties (Reynolds, 2013, Köhler and Faber, 2003). Therefore, this effect can cause cumulative creep or fatigue during long-term loading.

The creep behaviour of wood has been studied in several experiments under long-term constant loading, and Figure 2-21 shows an example of creep deformation of wood. The behaviour can be modelled for linear viscoelastic materials by applying the Burgers model (Figure 2-22) (Burgers and plasticity, 1935, Morlier, 1994). Displacement increases when a load is applied and decreases with time after the load is removed. By connecting a series of elastic springs and viscous dampers in parallel, a linear formulation of stress, strain, and time can be derived to obtain a creep curve (Bodig and Jayne, 1993). Reynolds (Reynolds, 2013)states that the Burgers model assumes a constant deformation rate under load, but for wood, the deformation rate varies with time variation. Other studies have highlighted that the linear model applies to wood at lower stress levels, temperature and moisture content (Bach, 1966, Schniewind and Technology, 1968, Whale, 1989).

The relationship between peak stress levels and DOL is plotted as a Madison curve, which is accepted as a design limit by the structural code for wood (Figure 2-23) (Wood, 1960). Madison's static creep behaviour does not consider the effect of fatigue behaviour (Smith

et al., 2003). One experimental result showed that cyclic fatigue caused more serious damage than statistical creep (Kohara and Okuyama, 1992). However, another study concluded that static creep tests resulted in higher deformation than high cyclic fatigue tests. These results may indicate that wood's creep and fatigue behaviour varies from species to species (Smith et al., 2003) and imply that separate analyses of creep and fatigue properties are needed when considering the mechanical behaviour of wood.

Tests under cyclic loading of wood showed that fatigue limits exist in wood materials and that moisture content affects their fatigue behaviour. The researchers also analyzed the effect of loading characteristics on the fatigue behaviour of wood. First, the shape of the waveform affects the accumulation of damage, and the results showed that square waveforms, with the highest peak stress rates and peak stress durations, may cause the greatest damage than triangular or sinusoidal waves (Okuyama et al., 1984, Gong and Smith, 2005). Secondly, the effect of a loading sequence from high to low is more significant than that of low to high. (Gong and Smith, 2000), a comment supported by Whale's previous cyclic creep tests (Whale, 1989). Furthermore, reversal (via zero) load cycling is more detrimental than non-reversal cycling, with an R ratio equal to -1 being the worst case (Tsai and Ansell, 1990) (Bonfield and Ansell, 1991). However, these results on wood materials are not representative of the behaviour of wood structures or wood joints (Smith et al., 2003)

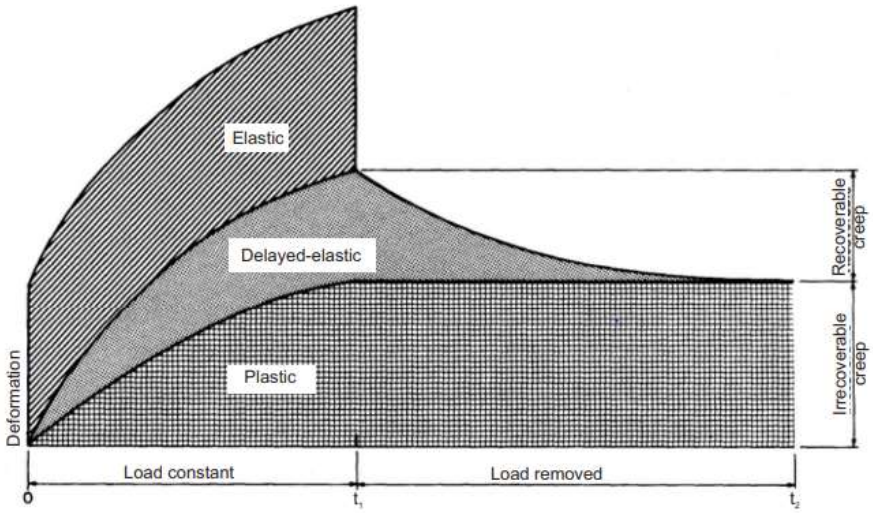

Figure 2-21: Creep curves of timber material (Reynolds, 2013)

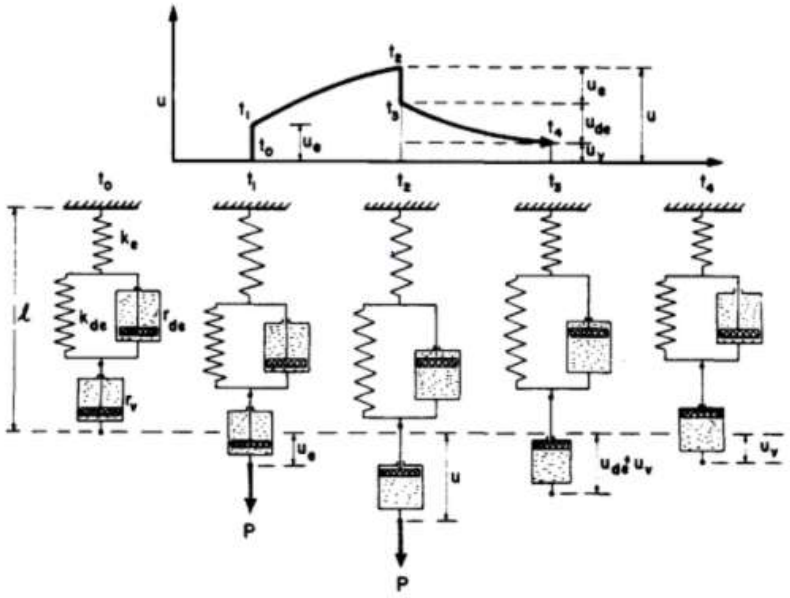

Figure 2-22: Burgers model for linear viscoelastic material (Morlier, 1994)

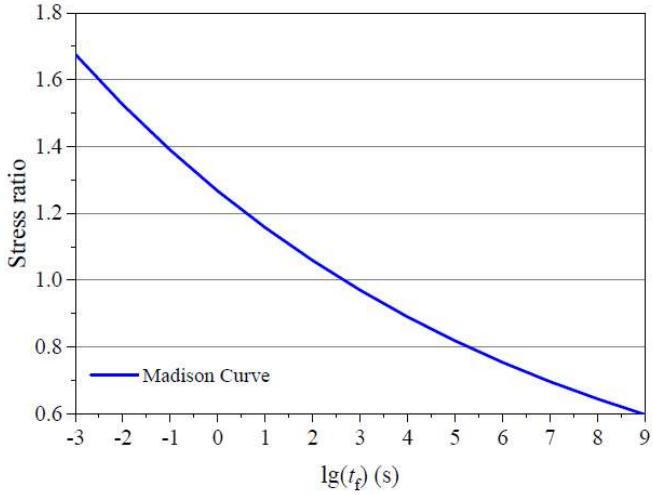

Figure 2-23： Madison curve (Wu et al., 2021)

2) Connection fatigue

Connection systems for wood construction are complex and diverse. This section reviews only the fatigue behaviour of connections with angular brackets shown in Figure 2-16, as this type of connection is commonly used in wood wall and wood infill panel systems.

Many researchers have tested the behaviour of wall panels anchored with different angle brackets under seismic loading. Figure 2-24 shows a typical test setup where combined lateral and longitudinal forces can be applied. Popovski et al. (Popovski et al., 2010)

(Popovski and Karacabeyli, 2012a) noted that in laboratory tests, wooden walls behaved as rigid bodies with displacements contributed mainly by the joints. The results also suggest that the choice of fastener type affects resistance performance, with nails performing better than screws at higher stress levels and ring nails providing more resistance to withdrawal compared to screw nails but slightly reducing the ductility of the system (Popovski and Karacabeyli, 2012a). The researchers also suggested that hoops (Figure 2-25) could improve the system's seismic behaviour, but using long screws is not recommended because it reduces the ductility of the system (Popovski and Karacabeyli, 2012a). Angle braces' strength varies with shape, size, and reinforcement conditions (Tomasi and Smith, 2015). The experimental results also indicate that the combination of fastener type, nailing pattern, and angle bracket shape affect the system's performance. After cyclic testing, the level of strength reduction for the angle bracket with reinforcement (Figure 2-26) appeared to be lower than for similarly shaped angle brackets (Tomasi and Smith, 2015). The equivalent damping ratios ranged from 10% to 20%, with no significant relationship to the geometry (Tomasi and Smith, 2015). Tomasi (Tomasi and Smith, 2015) concluded that the fatigue behaviour of connections with angle brackets is nonlinear and complex. Therefore, it is recommended that this system be evaluated by laboratory testing rather than predicted by simulation. Gastric (Gavric et al., 2015a) provided a numerical prediction model, but the resistance properties of the system were lower than the laboratory test results, possibly due to neglecting the tensile and shear capacity of the connection.

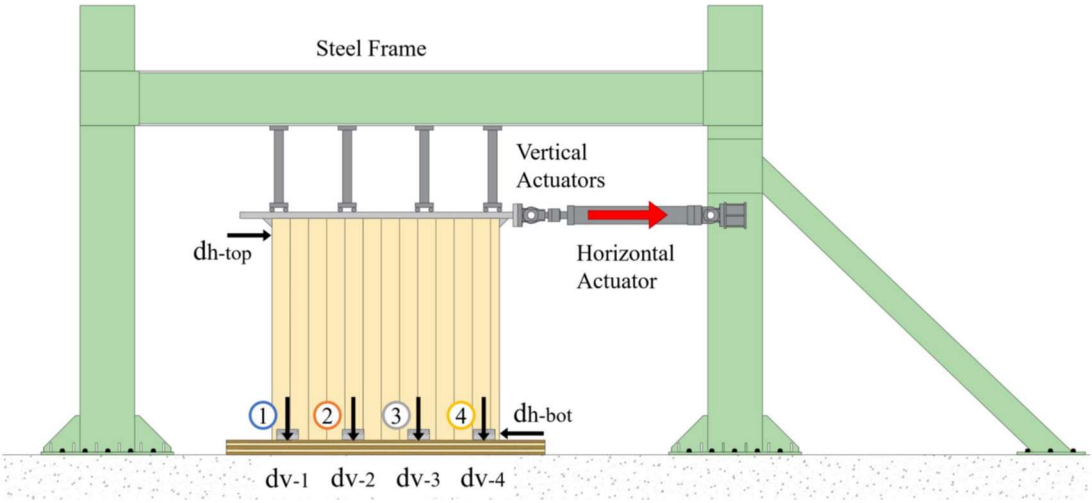

Figure 2-24: Cyclic shear force testing set up for timber panel with angle bracket(D'Arenzo et al., 2021)

Figure 2-25:Hold-down(Gavric et al., 2015a)

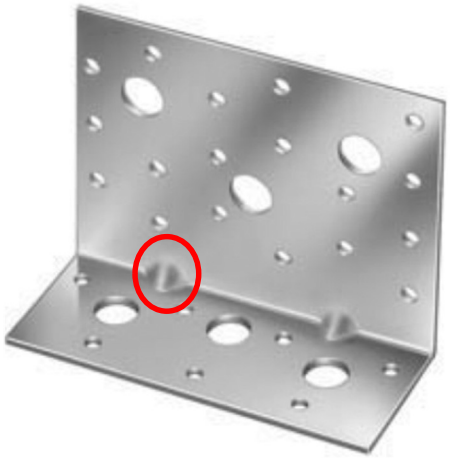

Figure 2-26:Angle bracket with reinforced ribs (Liu and Lam, 2018)

Several researchers (Liu and Lam, 2018 , Shen et al., 2021) have also used reduced cyclic tests. Shen et al. (Shen et al., 2021) did cyclic shear and tensile tests, respectively and applied different methods to find the yield point of this joint system. This study showed that the equivalent energy elastic-plastic (EEEP) results were not as accurate as of the Yasumura and Kawai (Y&K) method and also pointed out that the cumulative damage due to cyclic loading should not be neglected even at low-stress levels (Shen et al., 2021). Liu and Lam (Liu and Lam, 2018) performed a test on a CLT plate with a reduced specimen of a CLT plate with an angle bracket applied coupled constant tension and cyclic shear and noted that the coupled tension reduces the shear capacity of the joint.

All the studies mentioned above have focused on the cyclic response of timber connections with angle bracing to shear or common shear. These studies aimed to figure out the seismic behaviour of such connection systems rather than the wind-induced vibration behaviour. No studies give the exact choice or arrangement of angles, and numerical models for strength prediction are still under development. Therefore, most recommendations are to maintain the connection's shear and ductility.

2.4 Conclusion

The chapter begins with a review of studies of ancient timber-frame buildings that show their advantages in terms of seismic resistance and disadvantages in terms of wind and insulation performance, which limited their development as superior residential buildings. Secondly, a review of the development of engineered timber materials suggests reasons for the resurgence in the popularity of timber construction. In particular, the invention of CLT and GLT has led to significant improvements in structural and thermal properties compared to traditional sawn timber, which has contributed to the removal of height restrictions on timber construction. The current trend in developing timber frame construction is towards taller and larger spans to accommodate a broader range of building types. This chapter, therefore, further reviews the development of high-rise timber buildings. The maximum height of a modern timber building is 85.5m. Although the height is not significant when compared to concrete or steel buildings. With the development of hybrid timber structures, there is potential to increase their height. In addition, a review of in-fill panel systems suggests that the development of tall timber or modular buildings could be improved by combining timber panels with the framing of various building materials.

Wind-induced joint fatigue is one of the important issues in high-rise timber buildings. However, the challenges of high-rise timber buildings are also illustrated, the most important of which is the increase in wind resistance required as the height of the building increases. Therefore, this section also reviews the research on the wind-induced behaviour of wooden buildings. However, in reviewing the fatigue behaviour of timber panels with angle-frame connection systems, the authors found that most current research has focused on the effects of flashing loads rather than wind pressure.

Chapter 3. Wind Load Chains: Time domain analysis procedure for wind pressures on wooden prefabricated wall systems

3.1 Introduction

The review of the technological development of timber frame construction in Chapter 2 shows that as the height of timber frame buildings increases, it encounters several challenges, particularly wind-induced vibrations that may affect the suitability of lightweight structures or lead to fatigue or even structural failure (Constantinescu et al., 2018; Zhu et al., 2020). Therefore, this chapter aims to clarify the vibration of timber walls under wind pressure and prepare for the next chapter to develop a new laboratory test method to assess the fatigue effects of wind on timber infill panel connections. The steps to evaluate the impact of wind pressure on wood walls include 1) collecting wind load data, 2) using the collected wind field data to study the wind pressure characteristics, and 3) analyzing the dynamic response of the structure under wind load

This chapter begins with reviewing methods for assessing wind pressure in buildings. The wind load chain is then proposed to develop a new assessment method to evaluate the effect of wind on the fatigue behaviour of timber infill panel connections. Therefore, the first step is to collect weather and climate data for the selected cities. In this study, climate data were obtained from the CWB Observation Data Query System (CODis) in the Taiwan area (2020), and Taipei City was selected as the reference city. Secondly, CFD model simulation analysis was conducted to determine wind pressure's effect on wood infill panels and their response and deflection characteristics.

Extreme wind velocity predictions were made using the wind velocities from 2002 to 2018 in Taipei City without considering the wind direction. In this study, CFD simulations were applied to determine the response of buildings to wind velocity because this method requires only computer conditions and is cheaper than wind tunnel tests. Although calibration may be needed in the future, CFD is still a good option for analyzing the early stages of design progress. CFD simulations were used to analyze the vibration behaviour

of different wood wall panels under different boundary conditions for the final purpose. The data were analyzed, including wall deflection and acceleration with time.

3.2 Methods for assessing wind pressure

There are several different research methods applied to assess wind pressure in timber buildings, such as the Equivalent Static Wind Load (ESWL) process (Bezabeh et al., 2018; Edskär and Lidelöw, 2019; Heiduschke et al., 2008; Edskär, 2019), field monitoring (Zisis et al., 2011;Reynolds et al., 2014) and wind tunnel test (Bezabeh et al., 2018;Guha and Kopp, 2014; Zisis and Stathopoulos, 2012; Bezabeh et al., 2020;Dao Thang and van de Lindt John, 201;Morrison and Kopp, 2011). Computational fluid dynamics (CFD) simulations are also a method for studying wind pressure in tall buildings. The basis behind these methods is the wind load chain established by Davenport in 1961. The Davenport wind load chain is a framework that guides the study of wind action on buildings. Researchers can apply it to the entire structure, building elements, or around the building to study wind-induced deflection, occupant comfort, and even the landscape layout around the building (Isyumov, 2012). To apply the Davenport wind load chain, the following four key components need to be identified (Davenport, 1961a; Holmes, 2015d; Isyumov, 2012))

- Wind climate: use the correct statistics to describe the wind conditions, including wind velocity and direction characteristics.
- Aerodynamic shape factors: identify the reference building shape and any features that may cause wind-induced vibrations.
- Local wind direction: specify the exposure conditions of the building, including the shedding and height of the terrain.
- Design criteria: develop criteria to assess the results of wind action.

Most building codes are based on wind load chains. Table 2 shows the equations used in different building codes to calculate the wind action on buildings.

Table 2:The calculation formulas for wind action in different building codes (Holmes, 2015a)

Country	*Code*	*Velocity*	*Dynamic pressure*	*Building pressure/ force*
International	Iso 4354(Standardization, 2009)	$V_{site} = V_{ref} C_{exp}$	$q_{site} = \frac{1}{2}\rho(V_{site})^2$	$p = q_{site} C_p C_{dyn}$
Europe/British	Eurocode 1:part 1-4 (Institution, 2005)	$V_b = C_{dir} C_{season} V_{b,0}$	$q_p(z) = \frac{1}{2} C_e(z) \rho {V_b}^2$	$w_e = q_p(z) C_{pe}$
America	ASCE 7 (Engineers, 2017)	V	$q_z = \frac{1}{2}\rho K_Z K_{zt} K_d V^2 I$	$p = q(GC_P)$
Japan	AIJ(Japan, 2015)	$U_H = U_O K_D E_H K_{rW}$	$q_H = \frac{1}{2}\rho {U_H}^2$	$W_f = q_H C_f G_f A^a$
Australia/New Zealand	AS/NZS1170.2 (Society, 2012)	$V_{sit,\beta} = V M_d M_{(z,cat)} M_s M_t$	$q_Z = \frac{1}{2}\rho_{air} {V_{des,\theta}}^2$	$p = q_z C_{fig} C_{dyn}$
China	GB 50009-2012 (China, 2012)	$u(z) = u_0 (\frac{z}{z_0})^{\alpha}$	$w_0 = \frac{1}{2}\rho {v_0}^2$	$w_k = \beta_z \mu_z \mu_s w_0$

These provisions show how the quasi-steady-state wind action on a building is calculated. Most of the equations, although they appear to differ from each other, include the key elements in the wind load chain: quasi-steady-state or dynamic coefficients (*Cp, Cpe, Cf, βz, Cdyn*), shape (Cfig, μs) and height factor (z). However, these codes are concerned with the suitability of the building structure rather than the building envelope.

Wind load regulations are a technical guide to building practice, not a state-of-the-art for wind-sensitive buildings (Irwin et al., 2013). They can only be used as a reference when performing dynamic-wind response analysis on buildings. Therefore, wind tunnel tests are applied to study unique structures and materials. Bezabeh (2018a) used wind tunnel tests to obtain the dynamic pressure of the designed CLT building and then calculated the ESWL to check the limit state of the structural design under wind loads. In addition, the dynamic response of the building under simulated wind loads can also be simulated in a wind tunnel laboratory (Bezabeh et al., 2020).

BRERWULF (Cook et al., 1988)is another wind tunnel device for testing the wind pressure of building elements, especially roofs. This type of equipment can give more detailed tests. Nevertheless, those full-scale wind tunnel tests can only calculate the response of the whole structure, and it is challenging to observe detailed properties such as joint strength or nail rigidity. Inspired by BRERWULF, Kopp (2010) developed a new system called Pressure Load Actuators (PLAs) for analyzing building cladding performance under wind loads. Several comprehensive tests have used PLAs to investigate building connection behaviour

and low building performance under realistic wind loads Kopp et al. 2012; Henderson et al. 2013; Shen et al. 2017; Zisis and Stathopoulos 2012), and this device can also be applied to local scale tests (Morrison and Kopp, 2011). However, both wind tunnel tests and PLA tests are costly.

CFD techniques have evolved with the development of computational wind engineering (CWE), providing a new approach to analysing wind and building interactions (Huang et al., 2007). Cochran (Cochran and Derickson, 2011)states that although calibration between wind tunnel and CFD models is critical, the calibration importance will decrease with the development of CWE techniques. CFD techniques encounter several problems due to the complexity of the hydrodynamics around structures, which include 1) different turbulence scales, 2) large Reynolds numbers, and 3) sharp edges of structures (Holmes, 2015a; Huang et al., 2007), etc. Tamura (2008)emphasizes that collecting more data from both physical and CFD models is essential to making CFD an independent simulation tool in the construction field is crucial. Many studies have shown the potential of using CFD to predict the average pressure of buildings (Baines, 1963; Zu and Lam, 2018; Daniels et al., 2013). Marie's research (Thordal et al., 2020a; Thordal et al., 2020b) attempted to develop a standard CFD setup program to obtain a more accurate simulation of the wind action on buildings. Their results showed that it is possible to use CFD to predict façade pressure and structural response. As a computer-based simulation technique, CFD is an excellent method for predicting early design stages at a low cost (Swaddiwudhipong and Khan, 2002).

3.3 Methodology

3.3.1 Dynamic wind velocity simulation

Wind data collection

To analyze the wind loads on a building, estimating the extreme wind velocities at the site is crucial. Van der Hoven (1957) demonstrated that fluctuations in random winds should be observed over a large time scale. In addition, the average wind load velocity varies from year to year. In the Code for Structural Design Loads of Buildings (GB 50009-2012), the wind pressures in Taipei are 0.4 kN/m^2, 0.7 kN/m^2 and 0.85 kN/m^2 for a 1 to 10-year return

period, 1 to 50 years return period and 1 to 100 years return period. These values are updated based on the data before 2008 and can be used as input parameters for building wind action analysis. However, data on long-term fluctuations are required to determine the wind velocity probabilities for selected return periods (Harris, 1982). Typically, data collection takes up to 10 to 20 years to estimate a 50-year return period ((Palutikof et al., 1999). Therefore, this study collects and analyzes data from CODis to provide hourly mean and gust wind velocities from 2000 to 2020 to obtain more recent data and provide more definitive advances in extreme wind velocity simulations.

The author has written a Matlab program to collect data from CODis' website (https://e-service.cwb.gov.tw/HistoryDataQuery/index.jsp). The collection period is from 2000 to 2018. There are 157,680 data points, which include: the hourly 10-minute average wind velocity and the passenger wind velocity of the Taipei station in Taiwan from 2000 to 2018. The station is located at an elevation of 5.3 meters. Several years have missing data, ranging from 2.55% to 0.15% for mean wind velocity and 0.67% to 0.15% for gusts. Figure 3-1 shows the annual mean and gust wind velocities from 2000 to 2018, and Table 3 lists the missing data for mean and gust wind velocities for different years. Missing data are ignored as the percentage of missing data is not high. The recommendations suggest that storm type affects wind load simulation results (Holmes, 2015a). However, the average wind velocities for the other months shown in Figures 3-2 indicate no significant seasonal effect on wind velocities for the selected cities. Cook suggested that wind direction should be included in the estimates (Cook, 1983; Cook and Miller, 1999). However, this study did not consider this factor at this stage.

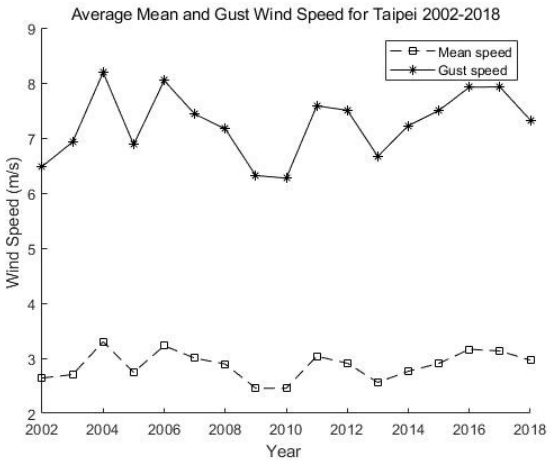

Figure 3-1: Average mean and gust wind speed from 2002 to 2018 (CODis)

Table 3: Missing data for wind velocity collection

Year	*Missing data (Mean)*	*Missing data (Gust)*
2000	93	0
2001	155	0
2002	279	0
2003	589	31
2004	155	0
2005	434	0
2006	279	0
2007	310	0
2008	496	0
2009	217	0
2010	187	0
2011	109	0
2012	93	0
2013	0	0
2014	31	0
2015	31	0
2016	62	0
2017	0	155
2018	0	0

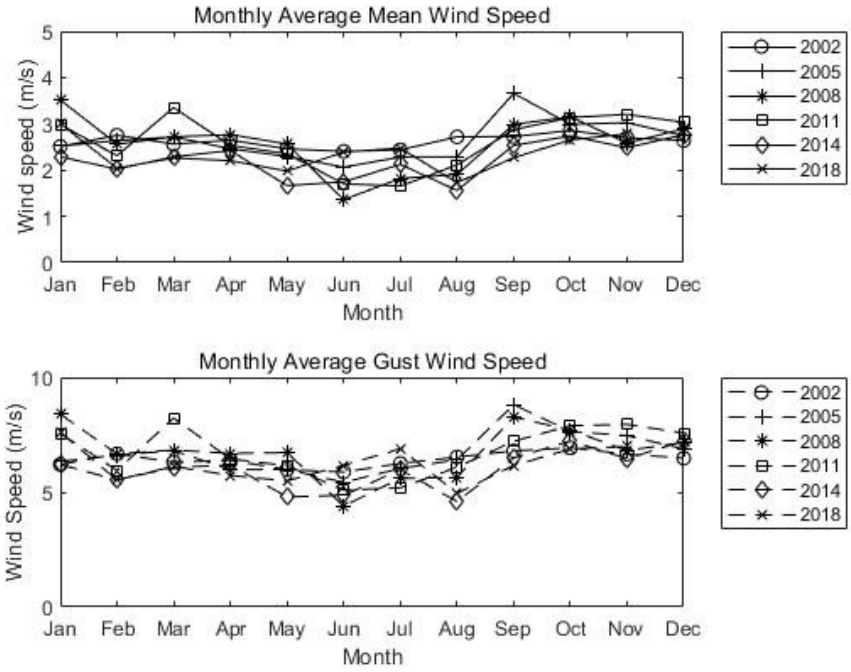

Figure 3-2: Wind monthly average mean and gust wind speed in selected years

Methods for estimating extreme winds

Using extreme value analysis theory can fit the maximum value of a sample of size n into three types of distributions (Fisher and Tippett, 1928). (Von Mises, 1936, Falk and Marohn, 1993)suggested that the use of generalized extreme value (GEV) distributions can simplify three types of distributions, Gumbel type (Type I), Fréchet type (Type II), and Weibull type (Type III) (Figure 3-3). The Weibull method was first introduced into the field of wind velocity estimation by Lundtang Petersen et al. (1981). The process was subsequently reviewed by Conradsen (1984). Initially, researchers usually used the Weibull distribution method to estimate extreme wind velocities. Walshaw's study tested wind velocity series using the Weibull type and showed that the wind velocity distribution fit this type well (Walshaw, 1994). Hosking noted that in his study, the likelihood test for his data rejected the distribution type when k = 0 (Hosking, 1984). Lecher (Lechner et al., 1992)and Simiu (Simiu and Heckert, 1996)considered the type III distribution applicable to most of the data series collected in their study. The Weibull method is more suitable for prediction due to the upper limit of wind velocity (Palutikof et al., 1999; Holmes, 2015c; Perrin et al., 2006). However, its accuracy is challenged, considering that annual extremes have little effect on the Weibull distribution (Abild et al., 1992b). Studies (Simiu and Scanlan, 1986)both

Walshaw (Walshaw, 1994)and Simiu (Simiu and Scanlan, 1986)show that for the same return period, extreme wind velocities estimated with type III are smaller than those with type I estimated are smaller. This may be because the annual extremes are more independent than the hourly extremes (Perrin et al., 2006). Therefore, the method developed by Gumbel (Tocher, 1955)is preferred. Studies have shown that Type I is suitable for extreme wind estimation in temperate regions (Abild et al., 1992a; Cook, 1986; Gusclla, 1991, Ross, 1987)).

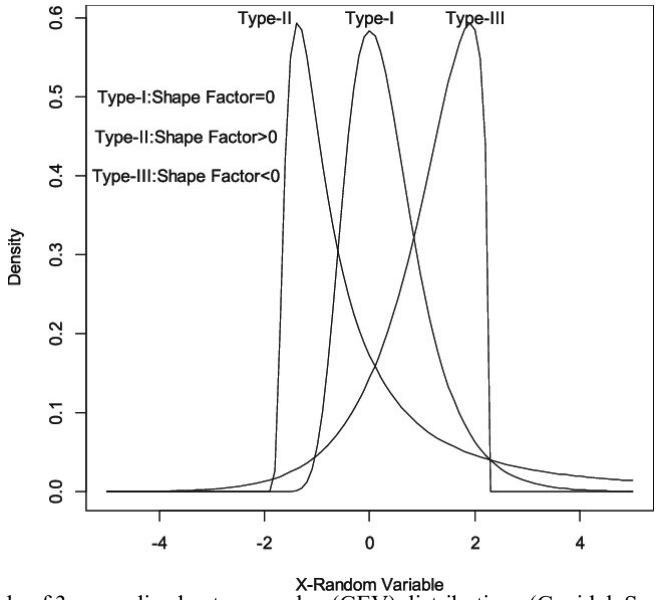

Figure 3-3:an example of 3 generalized extreme value (GEV) distributions (Gavidel, Saeed & Jeremy, 2017).

The cumulative distribution functions for the three different types of GEV are:

$$F_U(U) = \begin{cases} exp\left\{-\left[1-\dfrac{k(U-\mu)}{\alpha}\right]^{\frac{1}{k}}\right\} \ldots\ldots\ldots\ldots k \neq 0 \\ \exp\left\{-\exp\left[-\dfrac{(U-\mu)}{\alpha}\right]\right\} \ldots\ldots\ldots\ldots\ldots k = 0 \end{cases} \quad 3.1$$

Where: k is the shape factor, α is the scale factor, and μ is the location parameter. The values of k are negative and positive for Type II and Type III distributions; for Type I, the value of k is 0. The value of U is the annual maximum wind velocity.

The cumulative distribution function for $F_U(U)$ with density is:

$$f_U(U) = \begin{cases} \frac{k}{\alpha}\left(\frac{U-\mu}{\alpha}\right)^{k-1} \exp\left\{-\left(\frac{U-\mu}{\alpha}\right)\right\} \dots\dots\dots\dots\dots\dots\dots\dots k \neq 0 \\ \frac{1}{\alpha}\exp\left(-\frac{U-\mu}{\alpha}\right)\exp\left[-\exp\left(\frac{U-\mu}{\alpha}\right)\right] \dots\dots\dots\dots\dots k = 0 \end{cases} \quad 3.2$$

The relationship between GEV and the regression period is:

$$T = \frac{1}{1 - F_U(U)} \quad 3.3$$

Where: T is the return period.

Combination of Equations 3.1 and 3.3:

$$U = \begin{cases} \mu + \frac{\alpha}{k}\left\{1 - \left[-\ln\left(1-\frac{1}{T}\right)\right]^k\right\} \dots\dots\dots\dots\dots\dots\ k \neq 0 \\ \mu - \alpha \ln\left[-\ln\left(1-\frac{1}{T}\right)\right] \dots\dots\dots\dots\dots\dots\dots\dots k = 0 \end{cases} \quad 3.4$$

The next step is to find out the parameters of the GVE, and the method applicable to Type I is shown below:

We define y as a reduced variable, and the relationship between y and U is:

$$U = \alpha y + \mu \quad 3.5$$

Therefore to figure out the value for α and μ, we need to plot U against y. Combine the functions 3.1 and 3.5:

$$y_{Gumbel} = -\ln\{-ln[F_U(U_m)]\} \quad 3.6$$

Where: y_{Gumbel} is the Gumbel reduced variate. $F_U(U_m)$ for this function refer to the probability that yearly maxima are less than U. To estimate $F_U(U_m)$, the following formula is recommended:

$$F_U(U_m) = \frac{m}{N+1} \quad 3.7$$

Additionally, there is a particular function for removing bias(Gringorten, 1963):

$$F_U(U_m) = \frac{m - 0.44}{N + 0.12} \qquad 3.8$$

The process to figure out m and N is based on the following steps:

1. Pick up the maxima from annual hourly wind velocity data
2. Sort those maxima from smallest to largest:1,2,…m…to N.
3. Substitute the numbers into the formula above.

Apart from the GVE method, the generalised Pareto distribution (GPD) method, also known as the peaks-over-threshold(POT) method, has been developed in recent years(Davison and Smith, 1990, Holmes and Moriarty, 1999, Lechner et al., 1992). This method solved the problem that, when the storm occurred, the GVE Type I method could only extract one maximum value in each calendar year.

The cumulative distribution function for this method is :

$$f(U) = \begin{cases} 1 - \left[1 - \frac{k}{\alpha}(U - u_0)\right]^{\frac{1}{k}} \dots\dots\dots\dots k \neq 0 \\ 1 - \exp\left[-\frac{(U - u_0)}{\alpha}\right] \dots\dots\dots\dots\dots k = 0 \end{cases} \qquad 3.9$$

Where: k is the shape parameter, α is the scale parameter, and u_0 is the selected threshold.

The equation U-u_0 in the function above is the exceedance. the value λ is introduced, which refers to the exceedance rate, to estimate the quantiles:

$$\lambda = \frac{\mathrm{n}}{\mathrm{M}} \qquad 3.10$$

Where: n is the number of times that exceed the limitation u_0, M is the number of years recorded.

Combination the functions 3.3, 3.9 and 3.10, we get the function for estimating the extreme wind velocity for a specific return period(Abild et al., 1992a) :

$$U_R = \begin{cases} u_0 + \frac{\alpha}{k}[1 - (\lambda \mathrm{T})^{-k}] \dots \dots \dots \dots k \neq 0 \\ u_0 + \alpha \ln(\lambda \mathrm{T}) \dots \dots \dots \dots \dots \dots \dots \mathrm{k} = 0 \end{cases} \quad 3.11$$

The probability weight moments (PWMs) method is used for parameters estimation:

The first three PWM are given by(Palutikof et al., 1999):

$$b_0 = \overline{U} \quad 3.12a$$

$$b_1 = \sum_{j=1}^{n-1} \frac{(n-j)U_j}{n(n-1)} \quad 3.12b$$

$$b_2 = \sum_{j=1}^{n-2} \frac{(n-j)(n-j-1)U_j}{n(n-1)(n-2)} \quad 3.12c$$

The equation for the GPD parameter estimation:

$$\hat{k} = \frac{b_0}{2b_1 - b_0} - 2 \quad 3.13$$

$$\hat{\alpha} = (1 + \hat{k})b_0 \quad 3.14$$

The choice of statistical model for the collected data may determine the certainty of the estimates. In addition, the calculation of the GEV or GPD distribution parameters may also affect the accuracy. Therefore, it is recommended to calculate standard errors (SE) to check the accuracy of the parameters and quantification (Palutikof et al., 1999, Abild et al., 1992b). When k = 0, the SE equation for GEV is given by:

$$SE[U] = [\frac{\alpha^2}{n}(0.608Z^2 - 0.514Z + 1.109]^{\frac{1}{2}} \quad 3.15$$

Where n is the sample size and:

$$Z = \ln\left[-ln\left(1-\frac{1}{T}\right)\right] \quad 3.16$$

The GPD is:

$$SE[U] = \left(\frac{\alpha^2}{n}\{1+[ln(\lambda T)]^2\}\right)^{\frac{1}{2}} \quad 3.17$$

As previous research shows, the results from Type II GVE were significantly higher than realistic and not suitable for building design purposes (Simiu et al., 1978). Therefore, only Type I and Type III were applied in this study. This chapter shows how extreme wind velocities are compared and determined in numerical simulations of fluctuating wind velocity time series.

Numerical simulation of fluctuating wind velocity time series

1) The theoretical basis for wind load simulation

Fluctuating winds are manifested mainly by causing wind vibrations in building structures. Numerical simulation of time series of fluctuating wind velocities is suitable for calculating the wind forces on structures. Based on observations and long-term developments, several general static wind models have been defined, such as mean wind, wind spectrum and wind profile (Kareem et al., 2019)). However, there are challenges in modelling fluctuating wind velocities. Therefore, parametric models such as time-varying mean winds, time-frequency wind spectra, and vertical wind profiles are still developing (Kareem et al., 2019). There are also several different methods for numerical simulation of fluctuating wind velocities, such as harmonic superposition (Rice, 1944), linear filtering (Iannuzzi and Spinelli, 1987; Iwatani, 1982), wavelet analysis (Kitagawa and Nomura, 2003; Yamada and Ohkitani, 1991), and the inverse fast Fourier transform (IFFT) method (Cebon, 1993)

Firstly, understanding wind by knowing the basic characteristics of the time-varying wind is essential. Assuming that both time and space together make up the wind field at a point (x,y,z), and then the wind velocity $\overline{U}(x,y,z,t)$ can be defined by:

$$\overline{U}(x,y,z,t) = U(x,y,z,t) + u(x,y,z,t) \quad 3.18$$

Where: $U(x, y, z, t)$ is the static mean wind velocity and $u(x, y, z, t)$ is the non-stationary wind velocity.

Finding extreme static mean wind velocities or gusts for the simulation has been described in 3.2.2 U. Various types of terrain and height above the ground also affect the mean wind velocity. The relationship between mean wind velocity and tropical rainforest follows the logarithmic law.:

$$U = \frac{u_*}{k_a} \ln\left(\frac{z}{z_0}\right) \tag{3.19}$$

Where: u_* is the friction velocity (not physical velocity); k_a is the von Karman's constant, and k≈0.14; z is the height from the ground and z_0 is roughness length.

The function for mean wind influenced by heigh above ground is given by:

$$\frac{U}{U_{10}} = \left(\frac{z}{10}\right)^a \tag{3.20}$$

Where: a is the index of the wind profile, which varies with the terrain type. u_{10} is the wind velocity at 10 m height.

Before simulating fluctuating winds, it is essential to determine their characteristics, including the wind spectrum, turbulence intensity, turbulence integration length scale, and spatial correlation. The wind spectrum describes the frequency of change of the fluctuating wind velocity and is given by the following equation.:

$$\sigma_u^2 = \int_0^\infty S_u(n) dn \tag{3.21}$$

Where: σ_u^2 is the square standard deviation, representing the velocity changing frequency; $S_u(n)$ is the spectral density for fluctuating wind u(x,y,z,t). Researchers developed several parametric forms for $S_u(n)$, Davenport spectrum, which Davenport designed in 1961 based on his observation(Davenport, 1961), for example:

$$S_u(n) = \frac{4k{U_{10}}^2 x^2}{n(1+x^2)^{\frac{4}{3}}} \tag{3.22}$$

Where: n is the frequency for fluctuation wind velocity; k is the roughness coefficient; and:

$$x = \frac{1200n}{U_{10}} \tag{3.23}$$

The (Davenport, 1961)is obtained by observing and recording the actual wind field and then applying the Fourier transform to create an expression (Davenport, 1961). Another type of spectrum uses filters to record wind velocities and draw power spectrum curves from which spectral expressions are made ((von Kármán, 1948, Harris, 1968), and the)Carman spectrum is an example:

$$S_u(n) = \frac{4x\sigma_u^2 L_u^2}{\left[1 + 70.8x^2 L_u^{x\,2}\right]^{\frac{5}{6}}} \tag{3.24}$$

Where:

$$x = \frac{n}{U} \tag{3.25}$$

σ_u^2 is the root-mean-square value of fluctuating along-wind velocity, and the equation is given by:

$$\sigma_u = \{\frac{1}{T\int_0^T [\bar{U}(t) - U]^2 dt}\}^{\frac{1}{2}} \tag{3.26}$$

L_u^x is the along-wind turbulence integral-length scale, which varies with the roughness and height from the ground. The expression is:

$$\mathrm{L_u^x} = \frac{\mathrm{U(z)}}{\sigma_u^2 \int_0^{+\infty} R_u(\tau) d\tau} \tag{3.27}$$

Where: $R_u(\tau)$ is the correlation function of time-series fluctuating wind velocity.

In addition, turbulence intensity is another parameter used to describe fluctuating winds, which shows the intensity of wind velocity variations. Its expression is given by:

$$I_u = \frac{\sigma_u}{U(logitudinal)} \tag{3.28(a)}$$

$$I_v = \frac{\sigma_v}{U(lateral)} \qquad 3.28(b)$$

$$I_w = \frac{\sigma_w}{U(vertical)} \qquad 3.28(c)$$

He(He, 2006) pointed out the relationship between along-wind turbulence intensity (I_u), the roughness length (z_0) and the wind profile index (α) with the following equation:

$$I_u(z) = 1.5\alpha\left(\frac{z_0}{10}\right)^{-1.7\alpha} \qquad 3.29$$

2) Simulation method of single point fluctuating wind velocity

The four previously mentioned numerical simulation methods are all based on understanding the parameter mentioned above concepts. The time-series distribution of wind velocity in homogeneous isotropic turbulence can be considered a Gaussian stochastic process (Berg et al., 2016; Ott and Mann, 2005; Wilczek et al., 2011). When extreme non-stationary data in the initial phase are neglected, researchers use steady-state Gaussian stochastic processes to model wind velocities with time-series fluctuations (Sun, 2007). For example, the harmonic superposition and linear filter methods are usually chosen (Spanos and Zeldin, 1998; Deodatis, 1996).In 1944, Rice (1944) developed the basic concept of harmonic superposition. Researchers subsequently developed the constant amplitude wave superposition (CAWS) and weighted amplitude wave superposition (WAWS) methods and used these methods to model multidimensional Gaussian stochastic processes (Shinozuka, 1971; Shinozuka and Jan, 1972; Grigoriu, 1993). The algorithms of this approach are intuitive and straightforward and have a rigorous mathematical basis. However, this method models the stochastic process based on a sequence of cosine functions. Therefore, as the dimensionality increases, many operations are required for each frequency, leading to inefficiency (Li, 2005; Sun, 2007). In addition, this approach ignores time dependence (Cheng et al., 2016). Therefore, researchers prefer linear filtering methods (Iannuzzi and Spinelli, 1987; Mignolet and Spanos, 1992; Spanos and Mignolet, 1992. such simulation advances include auto-regressive (AR) models, moving average (MA) models, auto-regressive moving average (ARMA) models, etc. This method is widely used for stochastic and time series oscillatory analysis because it is less computationally intensive, fast and efficient (Sun, 2007). However, the algorithms of this method are complex and may face

accuracy challenges (Cheng et al., 2016). Therefore, it is crucial to determine the autoregressive order of the AR model prior to simulation (Rossi et al., 2004). Based on the purpose of this study, the AR model was used.

The principle of the AR model is that a computer generates Gaussian random numbers with zero mean and then applies them to a given wind power spectrum to produce a time series of fluctuating wind velocities. The fluctuating wind velocity is time-dependent, and the values between time intervals can be predicted by linear interpolation. Thus, it can be described as a linear function of the previous time-history velocity u(t) of an independent stochastic process at time t. Computing real random numbers may face slow speed, low efficiency and large storage space problems. Therefore, researchers use recursive mathematical formulas to generate pseudo-random sequences of various probability distributions. Different development environments provide different functions and methods for generating random numbers; this study used the Mersenne Twister method, the default algorithm for Matlab (Matsumoto and Nishimura, 1998). Random number generators provided by using function libraries of computer languages are an easy way to obtain such numbers.

The second step is to substitute the random series of time into a linear function of the wind velocity time history of fluctuating winds Eq.:

$$u(t) = \sum_{k=1}^{p} \varphi_k u(t - k\Delta t) + N(t) \qquad 3.30$$

Where: φ_k is the Autoregressive coefficient; p is the order of the AR model, which needs to be determined in the next step; Δt is a manually set time step. N(t) is the random independent process generated at step one.

Multiply the above 3.30 on both left and right sides by u(t-jΔt):

$$u(t - j\Delta t)u(t) = [\sum_{k=1}^{p} \varphi_k u(t - k\Delta t)]u(t - j\Delta t) + N(t)\, u\,(t - j\Delta t) \qquad 3.31$$

Where: j = 1,2,3……p.

Take the mathematical expectation of function 3.31 on both sides at the same time and combine the properties of the autocorrelation function:

$$R(\tau) = E[x(t)x(t+\tau)] \tag{3.32}$$

Where: τ is the time difference. Furthermore, for this AR model, the autocorrelation function can be written as:

$$R(j\Delta t) = E[u(t)u(t-j\Delta t)] \tag{3.33}$$

Because the N(t) is independent random series with a 0 mean value, thus can be ignored. Then, the relationship between R(jΔt) and φ_k is:

$$R(j\Delta t) = \sum_{k=1}^{p} \varphi_k R[\,(j-k)\Delta t] \tag{3.34}$$

Therefore, the value φ_k can be determined according to the following formula:

$$\begin{cases} R(\Delta t) = \sum_{k=1}^{p} \varphi_k R[\,(1-k)\Delta t] \\ R(2\Delta t) = \sum_{k=1}^{p} \varphi_k R[\,(2-k)\Delta t] \\ R(\mathrm{j}\Delta t) = \sum_{k=1}^{p} \varphi_k R[\,(j-k)\Delta t] \end{cases} \tag{3.35}$$

According to the Wiener-Khinchin theorem, the autocorrelation function of Ru(jΔt) at time jΔt is shown as:

$$R_u(t) = \int_0^{\infty} S_u(n)\cos(2\pi nt)\,dn \tag{3.36}$$

The autocorrelation order of the AR model is a decisive factor in the accuracy and efficiency of the entire calculation process. Too small an order will result in fast computation but low accuracy. However, too large an order may reduce the computational efficiency of the AR model. Therefore, the third step before the final simulation is to

determine the order of autocorrelation. In this paper, the proposed residual square minimization method is used to determine the order of the model (Sun, 2007). The sum of squares of the residual errors of the AR model is defined as:

$$e^2(t) = \sum_{k=1}^{p} [\varphi_k u(t - k\Delta t) - u(t)]^2 \quad 3.37$$

The square of the residual error is calculated from the first order, gradually increasing the order until there is no significant change in quantity between the two models, and then the smaller model is chosen as the final model to simulate fluctuating wind velocities.

3.3.2 Finite element model framework for CFD

1) CFD Basics

The development of CFD based on the Navier-Stokes (N-S) equations began in the 1970s with the aim of computer simulation of aerodynamic drag by the finite element method ((Zhu et al., 2020; Oberkampf et al., 2004; Cummings et al., 2015, Witherden et al., 2017). The expression of the N-S equations is based on the mass, momentum and energy conservation principles (White and Corfield, 2006). The continuity equation comes from the state of the mass conservation principle, i.e., there is no mass difference between the inlet and outlet flows throughout the system.:

$$\frac{\partial \rho}{\partial t} + \rho(\nabla \cdot v) = 0 \quad 3.38$$

Where: ρ is density, v is the velocity vector and the gradient operator. For incompressible fluid whose density is assumed to be constant, the mass conservation equation can be simplified as follows:

$$\nabla \cdot u = 0 \quad 3.39$$

The momentum conservation equation comes from Newton's Second Law:

$$F = m \cdot a \quad 3.40$$

Where: F is the external force, a is the acceleration, and m is the mass. Therefore, for the Newtonian fluid, the momentum conservation equation is:

$$\underbrace{\frac{\partial u}{\partial t}}_{momentum} = \underbrace{(u \cdot \nabla)u}_{mass\ force} - \underbrace{\frac{1}{\rho}\nabla p}_{surface\ force} + \underbrace{\frac{f}{\rho}}_{body\ force} + \underbrace{\nu\nabla^2 u}_{viscous\ force} \qquad 3.41$$

Regarding equation 3.39, equation 3.41 for incompressible fluid can be simplified as:

$$\frac{\partial u}{\partial t} + (u \cdot \nabla)u = -\frac{1}{\rho}\nabla p + \nu\nabla^2 u \qquad 3.38$$

Where: u is the fluid velocity vector; p is the fluid pressure; ρ is the fluid density; υ is the kinematic viscosity, and ∇2 is the Laplace operator.

Studies have shown that CFD models are a reasonable choice from a civil engineering perspective, as higher energy vortices are the main cause of the dynamic response of structures; therefore, not all flow characteristics need to be clarified (Romanowski, 1996, Dowell and Hall, 2001). Fluid information, such as velocity and pressure fields, can be clarified by solving the N-S equations. However, researchers have pointed out the limitations of direct computer solution equations for natural irregular flows (Argyropoulos and Markatos, 2015, Hanjalic, 2004.

Three models are usually available for CFD analysis in different commercial or open-source programs. The main difference is the turbulence part (Lorenzon et al., 2017). The first one is the direct numerical simulation (DNS) model, which solves the equations directly and captures simultaneously, even up to Kolmogorov, the scale of the fluid dissipation length and, more importantly, the fluid period to obtain the mean fluctuations (Lorenzon et al., 2017). This model yields more accurate fluid characteristics and does not require creating a new turbulence model. However, this model requires high grid resolution, resulting in high computational demands and is unsuitable for regions with high Reynolds numbers (Franke et al., 2004). Another model with reduced computational demands is the Large Eddy Simulation (LES) model, which captures a small flow area with only a basic grid resolution (Sagaut, 2006). A spatial filter separates large and small eddies in this model, and only large eddies are simulated numerically. In the case of small eddies, the turbulence

model is applied. As a result, small-scale effects will appear in the momentum equation's sub-filter stresses and boundary terms (Ghosal and Moin, 1995).

Rodi (1997)pointed out the advantages of this model in solving complex, unsteady processes when large eddies severely affect fluid transport. LES can now simulate the flow around structures of different shapes because of the development of computational techniques (Rodi, 1997). The third is the Reynolds Averaged Navier-Stokes (RANS) model, which has been commonly used in wind engineering in recent years (Franke et al., 2004; Rodi, 1997). The turbulence model of RANS follows the concept of Reynolds stress, where the turbulence fluctuates around the mean and affects the mean flow (Franke et al., 2004). This time-dependent model averages all the flow variables with different turbulence models, where the K-ε vortex viscous turbulence model is commonly applied. (Lorenzon et al., 2017.

2) Recommendations on the definition of computational models

Three components need to be taken care of when building a geometric simulation model for CFD simulations: the domain size, the details of the buffer body, and the boundary conditions. The size of the computational domain can be measured by the blocking rate, which should be limited to less than 3% (Baetke et al., 1990):

$$Blocking\ Rate = \frac{A_s}{A_d} \tag{3.39}$$

Where: A_s is the maximum cross-sectional area of the structure, and A_d is the cross-sectional domain area.

Hall (1997) recommends that the distance from the building to the inlet, lateral and top boundaries should be at least five times the height away from the building. For some physical wind tunnel simulations, the distance can be 300 m around the buffer (Franke et al., 2004). In addition, to allow the flow behind the buffer to develop sufficiently until it disappears, the outflow boundary should be located at least 15H behind the building (Hall, 1997.

The level of detail in the interaction between buffers and wind flow patterns is large and depends on the research interest. It is difficult to model all the obstacles affecting the fluids

for a city-scale simulation. Therefore, a canopy model was introduced to represent the surface roughness of the neighbourhood ((Tominaga and Stathopoulos, 2013; Mochida et al., 2008)). In CFD simulations, obstacles around buildings are usually created when descending to the building level. For example, An (An et al., 2013)set the observed structure in the centre of a low-rise building to analyze the effect of obstacles. The obstacle was built as a square block of size 5.6 H by 5.6 H. Frank (Franke et al., 2004)also suggests that the details of the central building should be modelled when the dimensions exceed 1 m. For example, when the roof is the object of study, modelling roof details is more important than the surrounding obstructions. However, inlet turbulence can be ignored when modelling some significant obstructions between the inlet boundary and the observed structure, as these can generate the necessary turbulence (Cochran and Derickson, 2011).

Some inlet flow parameters such as flow direction, velocity profile, and physical and turbulent properties of the flow need to be checked before simulation. The boundary conditions represent the effects of the environment surrounding the computational domain and include inlet and outlet boundaries and wall conditions. The inlet boundary refers to a uniform or profiled flow on the inlet surface, and the outlet boundary refers to flow leaving the outlet surface (Franke et al., 2004). At the outlet boundary, the derivatives of all flow variables are forced to vanish, corresponding to a fully developed flow. The convection results are usually set to zero at the boundary surface, and the exit boundary and the quantity are determined according to the flow direction (Tu et al., 2018). The combination of inlet velocity profile and constant pressure at the outlet boundary is commonly used in commercial schemes due to fast convergence and computational robustness (Tu et al., 2018).

In addition, the distance between the obstacle and the exit surface needs to be far enough. A minimum of ten times the building height behind the target building is recommended (Mochida et al., 2002, Shirasawa et al., 2003). Other boundary surfaces, such as the top and side, can be assumed to be walls or no-slip conditions. There is no relative velocity between the surface and the flow near the surface (Tu et al., 2018). In addition, the recommended blockage rate needs to be observed to ensure that the flow is parallel between the boundary and the obstacle surface (Franke et al., 2004). The results of the calculations depend heavily on the grid used for the discrete computational domain.

As mentioned earlier, mesh resolution can significantly affect the accuracy and efficiency of finite element simulations. Therefore, sufficiently fine and high-quality mesh resolution is needed to match the turbulence model to capture the flow and obstacle details (Franke et al., 2004). However, too small meshes in the computational domain may lead to inefficiencies and even difficulties in convergence. Therefore, it is important to maintain an accurate grid resolution in the region of interest. Furthermore, for untested regions, it is recommended that the mesh expansion ratio, i.e. the ratio of the size of the largest and smallest sectors in the domain, should be lower than 1.3. hexahedral shapes of the mesh are preferred over tetrahedra (Fadl and Karadelis, 2013). In addition, a hybrid form of the mesh can provide more accurate results than a pure tetrahedral mesh (Fothergill et al., 2002, Franke et al., 2004). Franke (Franke et al., 2004)also recommends a resolution of at least ten cells per cubic root of the building volume in building analysis. For other problems, mesh resolution sensitivity testing is required before simulation.

Description of the finite element model

1) Finite element models in Abaqus

In this study, CFD simulations were done using the commercial software Abaqus, which provides a basic Navier-Stokes equation solver for incompressible fluids and different turbulence models for turbulence that can simulate either laminar or turbulent flows (SIMULIA, 2014). The turbulence models in this software include Implicit Large-Eddy Simulation (ILES), Spalart-Allmaras (SA), k-ε RNG, k-ε realizable, and k-ε SST. ILES and Spalart-Allmaras models are frequently applied (Mandara et al., 2016) as an effective method to solve time-dependent models for high Reynolds number fluids and give reliable results (Fureby and Grinstein, 2002). In addition, the Spalart-Allmaras model in Abaqus based on the RANS program is more straightforward than ILES (Spalart and Allmaras, 1992). It provides accurate results at a lower resolution and computational cost (Franke et al., 2004).

Abaqus provides several built-in simulation engines for multiphysics field problems. The objective of this simulation is to understand wall vibrations under wind flow. Therefore, fluid-structure interaction programs are applied. These joint simulation programs combine Abaqus standard/explicit and Abaqus CFD to solve the interaction problem between

structure and flow. Both programs simultaneously compute and analyze the interaction behaviour of interacting surfaces of multiple models (Mandara et al., 2016a).

Figures 3-3 show that a building block can be considered as combining several single building block units. In this study, one of these units was selected for finite element simulation to understand the behaviour of permeable walls in fluids at the microscopic scale.

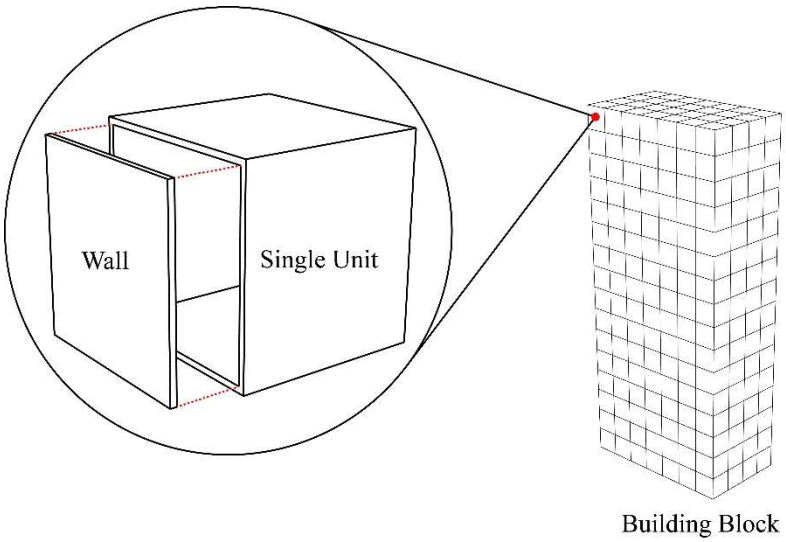

Figure-3-3: Finite element simulation research object

The simulation model in Abaqus FSI is divided into two parts. One is the structural domain, which represents a single building unit with interior infill walls. Figure 3-4 shows a simplified structural model. The wall panels measure 3m x 3m x 0.1m with Obstacle 1 behind them, representing the rest of the building unit's envelope. Because modelling the entire building increases the size of the wind domain, Obstacle 2 was designed as a simplified alternative for this simulation to reduce the computational requirements.

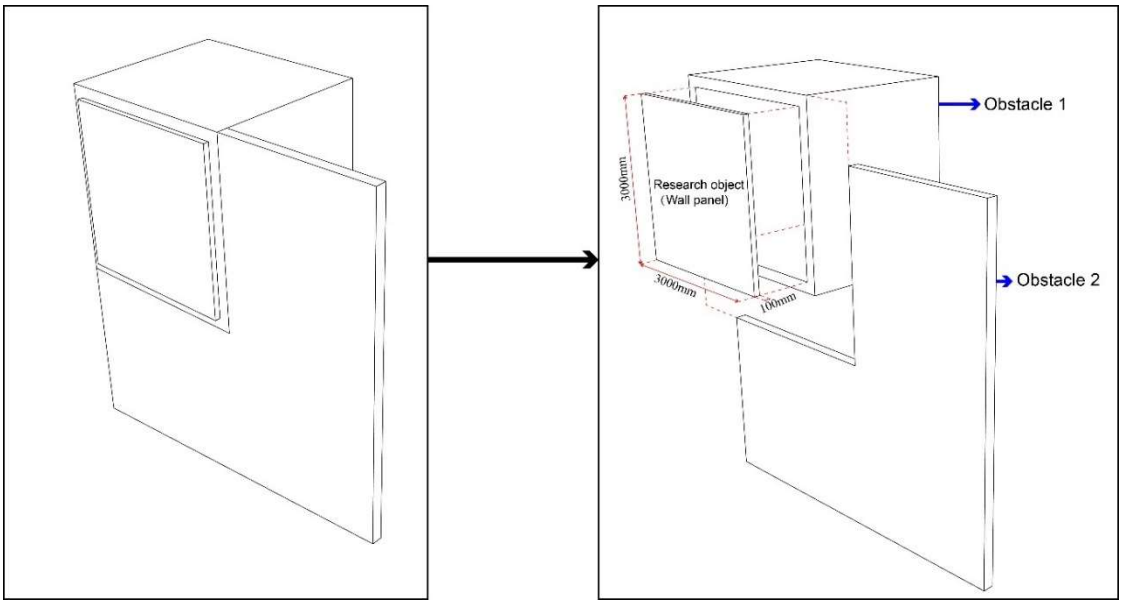

Figure 3-4: simplified structural model in Abaqus

In contrast to CLT, the material of the wall panels was assumed to be wood, and the tree species was chosen to be spruce, a common material for CLT (Xiong Yu et al., 2009). As an orthogonal material, the properties of wood vary with direction. The axes corresponding to the three directions are shown in Figure 3-5, where L is the grain direction, R is the texture direction, and T is the tangent direction.

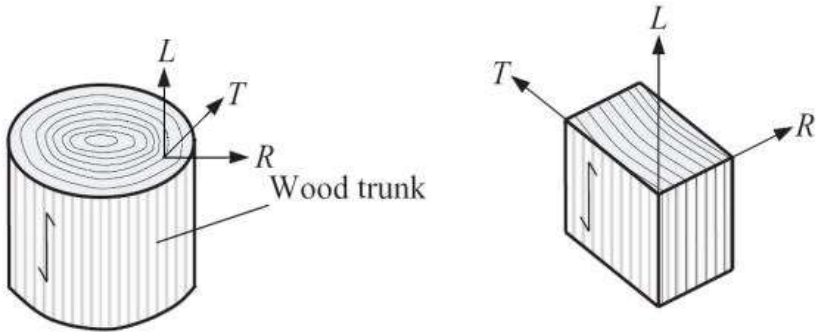

Figure 3-5: Coordinate axes for wood trunk and cut wood (Porteous and Kermani, 2013).

Table 4 shows the material properties entered into Abaqus. For the elastic properties, select the orthogonal engineering constants and set the material properties as shown in Figure 3-6, depending on the local coordinate system in Abaqus. The connections between wall panels are usually several angel brackets, secured with nosings or screws, so the edges of the walls are set up in Abaqus with a 6-degree-of-freedom fixed boundary condition of 50 mm every 200 mm (Figure 3-7). In addition, obstacles 1 and 2 are set up as 6-degree-of-freedom fixed conditions.

Table 4: Material properties used in the simulation analysis(Mirianon et al., 2008)

Notation	*Meaning*	*Value*	*Unit*
E_r	Elastic moduli in different directions	600	MPa
E_t		600	MPa
E_l		12000	MPa
v_{lt}	Poisson's ratios	0.015	-
v_{rt}		0.558	-
v_{lr}		0.038	-
G_{lt}	Shear moduli in different directions	700	MPa
G_{rt}		40	MPa
G_{lr}		700	MPa
ρ	Density	500	Kg/m^2

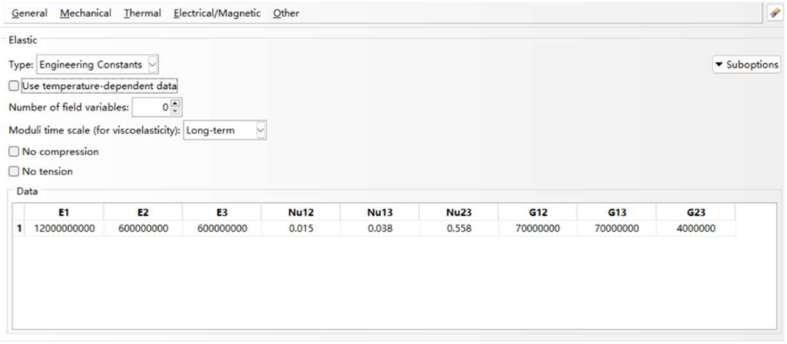

Figure 3-6: Elastic properties in Abaqus simulation

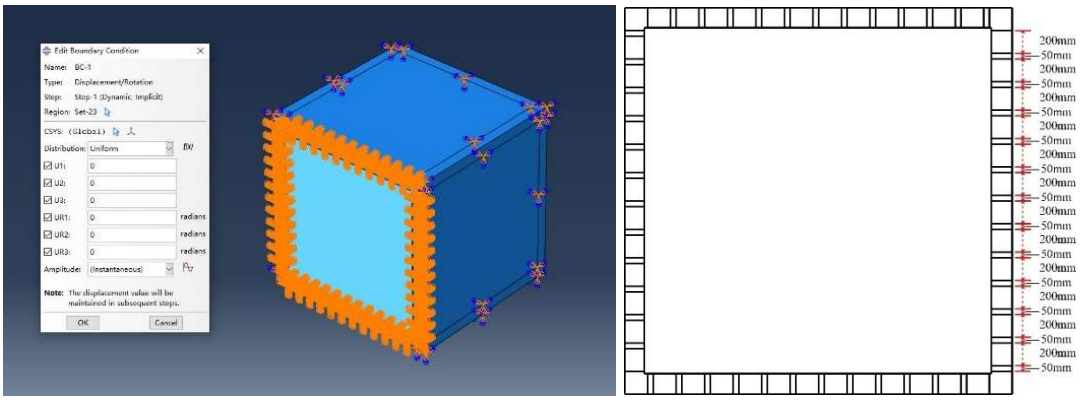

Figure 3-7: Boundary condition of the building unit

Figure 3-8 shows the wind field model in Abaqus. The size of the CFD domain was set to 50m x 50m x 50m, with the interactive building units located in the middle of the wind field, as recommended in Chapter 3.3.1. The wind velocity controls the inlet boundary, taken from Chapter 3.2. The outlet boundary was set to free outflow with a pressure of 0. The wall panel's outer surface and the fluid domain's inner surface has been assumed to be interaction regions (Figure 3-9). The other surfaces were assumed to have no sliding wall boundaries.

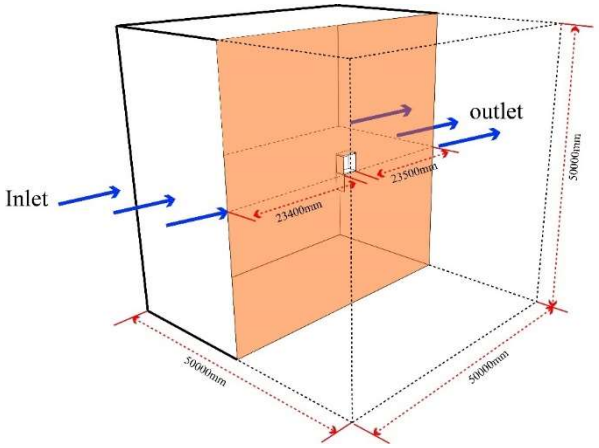

Figure 3-8: CFD model in Abaqus

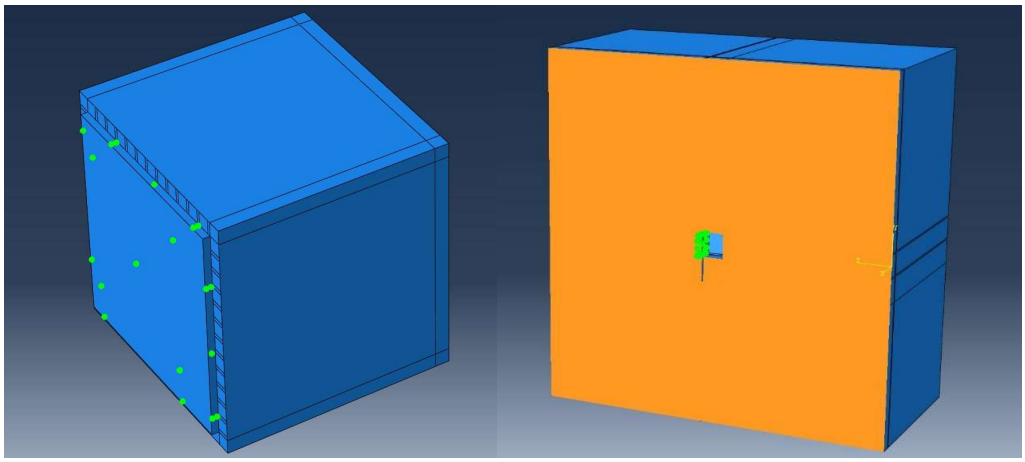

Figure 3-9: left is intersurface of the wall panel, and right is the wind field.

The structural model has meshed the wall section in a 0.1m x 0.1m hexagonal structure. Other elements not part of the interaction area are not as detailed as the wall section to reduce the computational requirements. Therefore, the total number of meshes for the structural model is 7932. In the CFD model, the target area meshes at 0.1m x 0.1m; for untested points, the mesh expansion is kept at about 1.2. the total number of meshes for the CFD model is 246,376. Figure 3-10 shows the meshes for the structure and CFD model. Verification checks, including mesh size checks, are performed in the next section

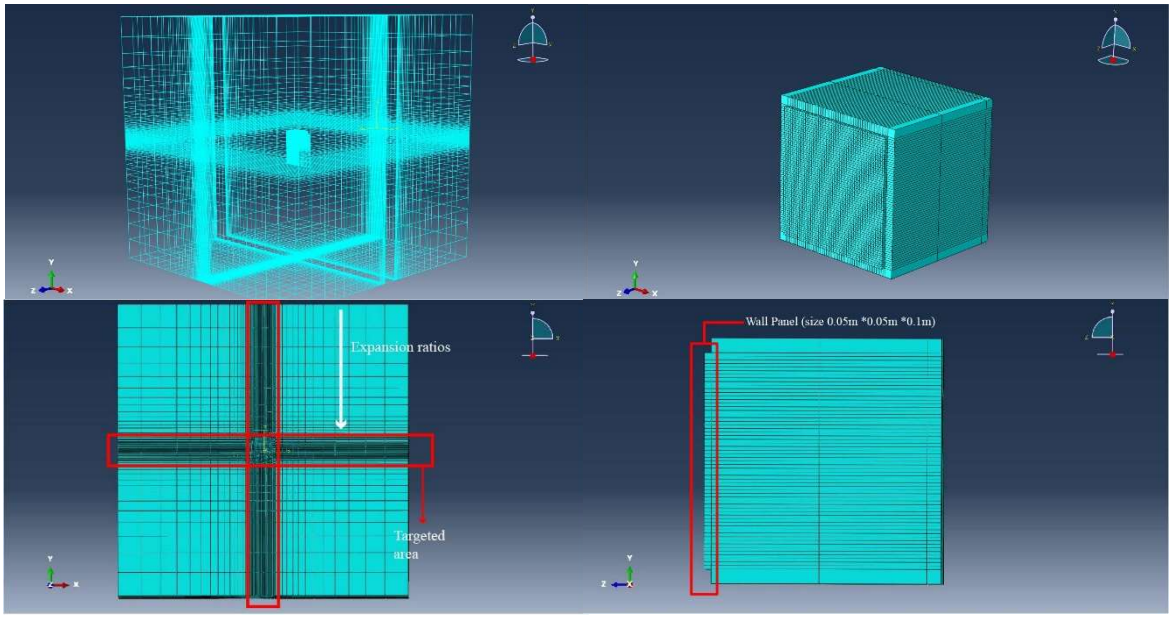

Figure 3-10: Mesh grid for CDF and building unit model.

2) Mesh sensitive check

Firstly, a smaller fluid domain is built to check the sensitivity of mesh grid size. The element sizes for the targeted area in the CFD model change from 0.2m to 0.04m, and the mesh grid size for the wall panel remains 0.1m. Two points are selected in each model, and data analysis is performed (Figure 3-11).

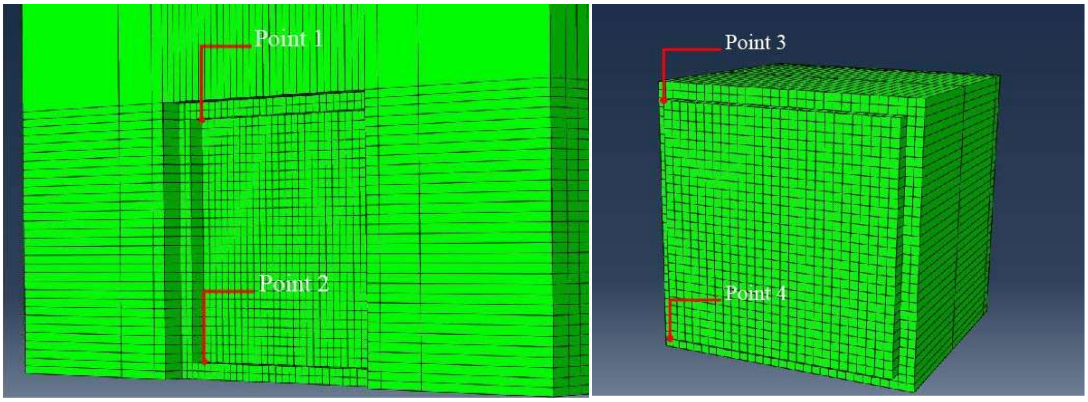

Figure 3-11: Point selection for mesh sensitive checking

Figure 3-12 shows that the pressure trends of poin1 and point2 in the CFD model for element sizes between 0.2m and 0.12m oscillate, and as the size decreases, the trends become stable but with different values. This indicates that the element size should be less than 0.12 m. However, the pressure values at point2 fluctuate sharply when the time step is between 1.8s and 2s. Therefore, Figure 3-13 shows the displacement at point 2 to aid in the future design of the grid dimensions. It shows no significant difference in the displacement values when the dimensions are between 0.11m and 0.04m.

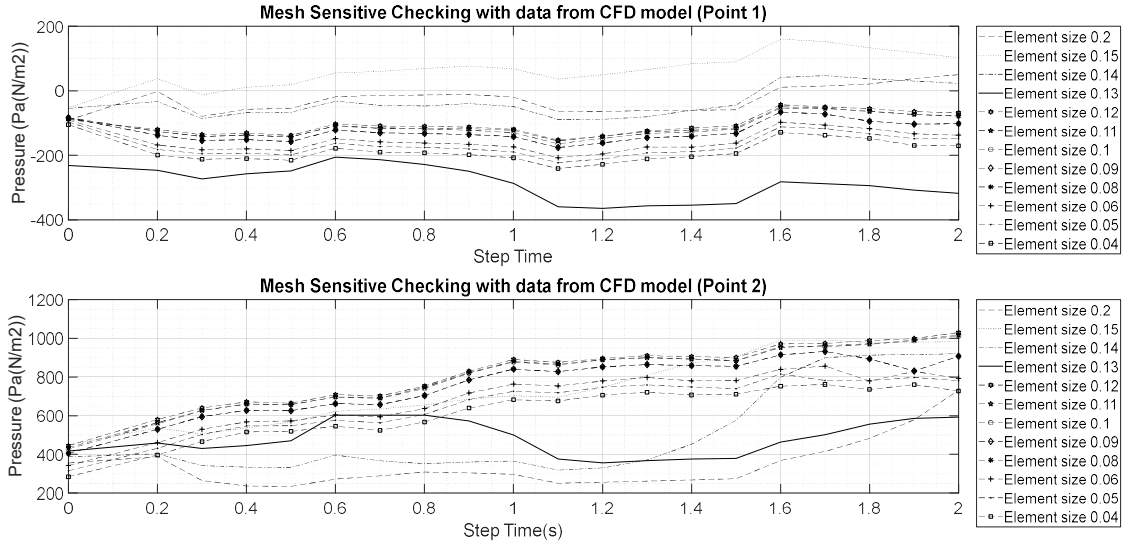

Figure 3-12: Wind pressure at point 1 and point 2

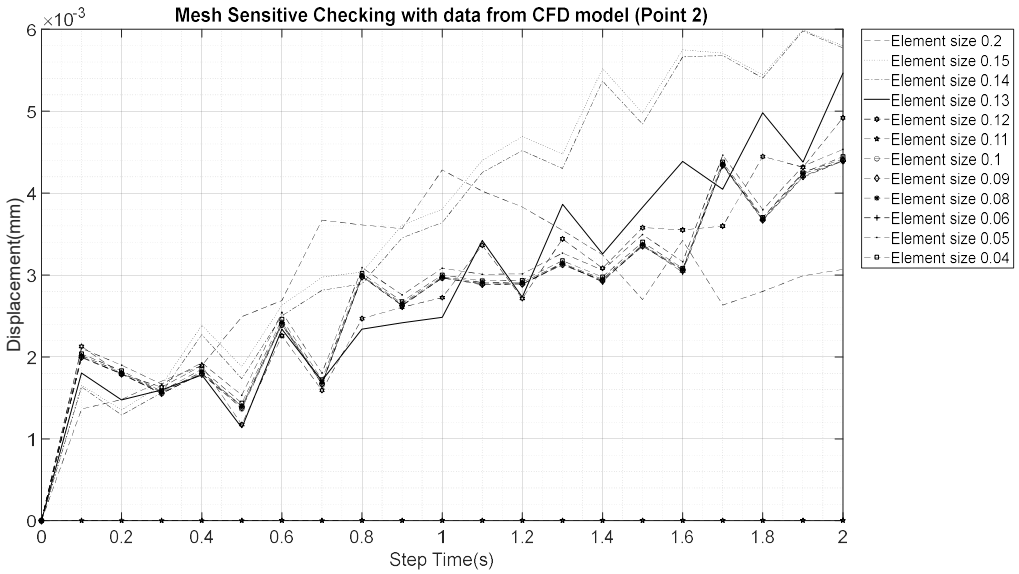

Figure 3-13: Displacements of Point 2 through step times

However, when the grid size decreases, the number of elements increases, and the running time increases. Therefore, an analysis of the running time and accuracy is required. Since this study focuses on coupled structural and fluid simulations, it is also critical to check the accuracy of the structural model. Figure 3-14 shows that the maximum and average displacement values become stable from a size of 0.11 m. When the grid size is reduced to 0.04m, the run time increases to 19 hours. The 0.1m size was chosen based on these analyses to make the simulation more efficient.

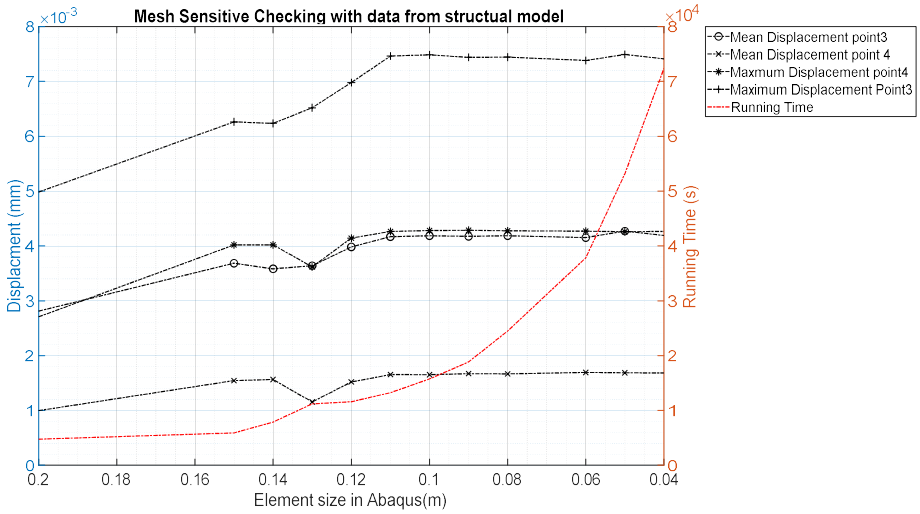

Figure 3-14: maximum and mean displacements at point 3 and point 4

3) Model validation

Validation of the CFD model is required to ensure quality control of the numerical results, determining if the numerical models are actual representations of the physical flow. This research validates the CFD model by firstly simulating the flow character in a Two-dimensional turbulent channel and compared with literature results from Kim et al. (Kim et al., 1987). The validation details are shown in Appendix A.

3.4 Results and discussion

3.4.1 Results of wind velocity time series

(1) Extreme wind velocity estimation

Figures 3-15 and 3-16 show the average wind velocity and gust wind velocity data collected for Taipei City from 2000 to 2018. There are 434696 data for average wind velocity and 438216 data for gust wind velocity. The following analysis has extracted the maximum mean wind velocity and gust wind velocity (Figure 3-17). First, a parametric analysis of the cumulative Weibull and Gumbel probability density functions was performed using Matlab (license number: 976008). The regression periods were then calculated from the results of the cumulative probability density functions.

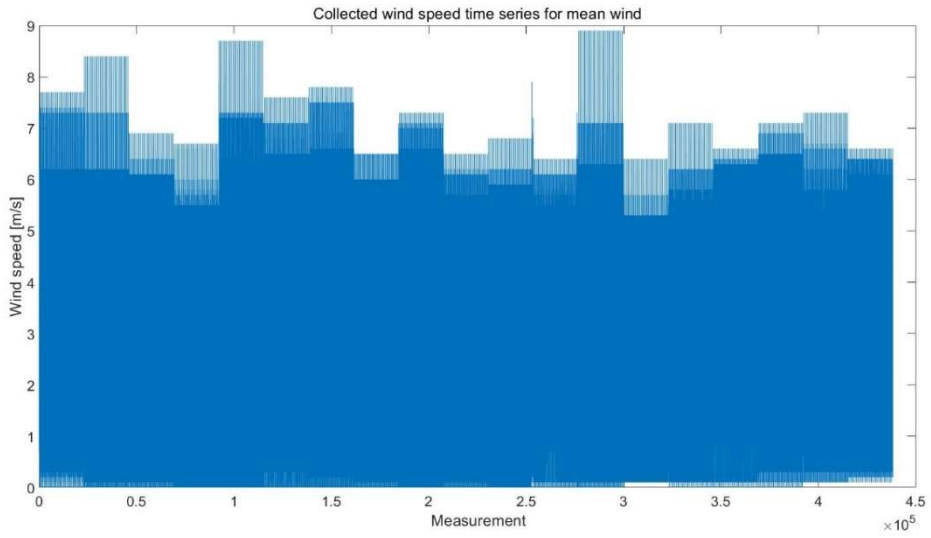

Figure 3-15: Collected mean wind velocity data

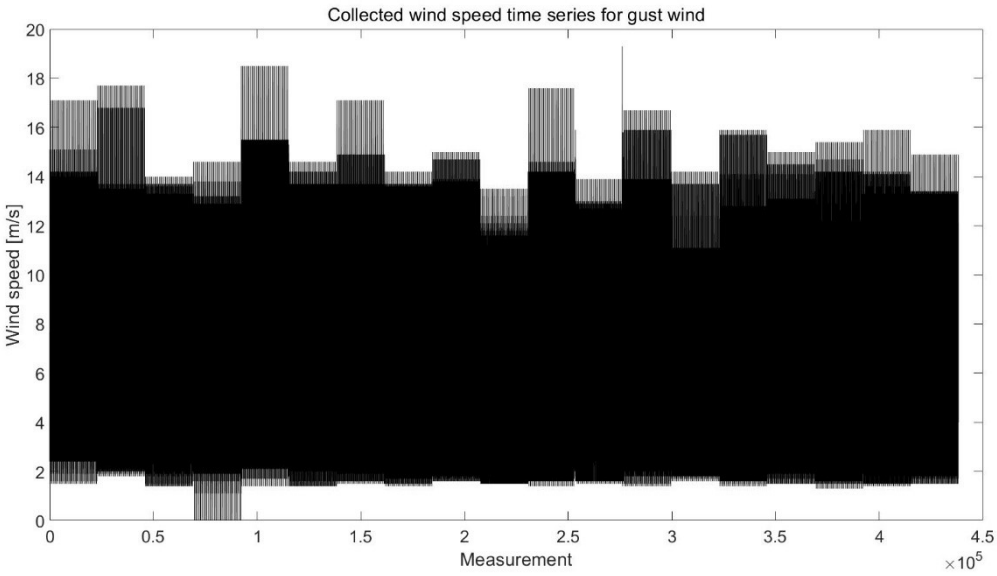

Figure 3-16: Collected gust wind velocity data

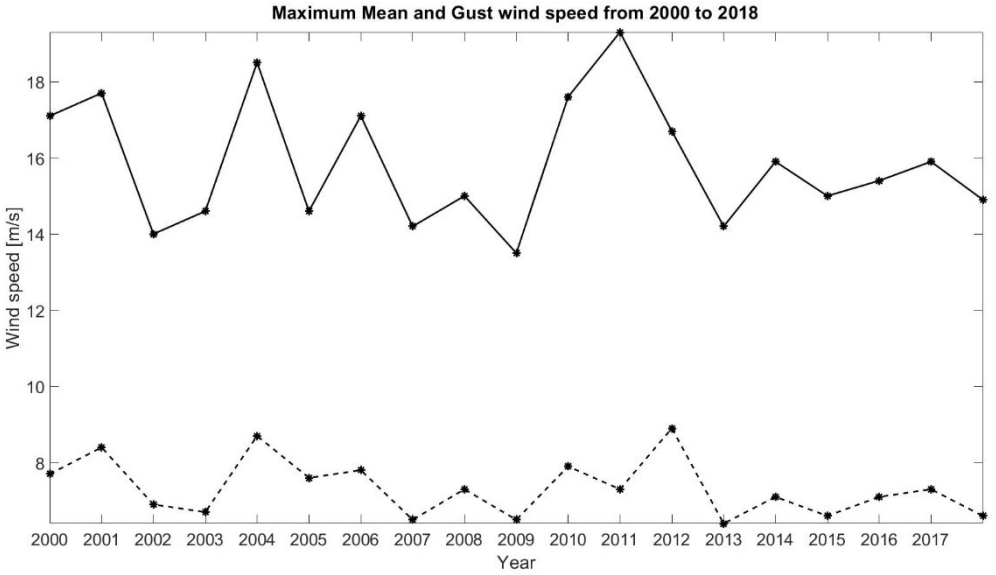

Figure 3-17: Extracted Maximum data from collected wind velocity

First, to check whether the maximum data fit the Weibull or Gumbel distributions, a probability plot was used in which each data was plotted with a marker symbol against a reference line representing the theoretical distribution. Figure 3-18 shows that data points appear along the reference line and that both the Weibull and Gumbel distributions fit these extracted data. In addition, an empirical cumulative distribution function was plotted and compared to the theoretical CDF on the exact plot. The results (Figure 3-19) also validate the feasibility of applying the Weibull and Gumbel distributions to these data.

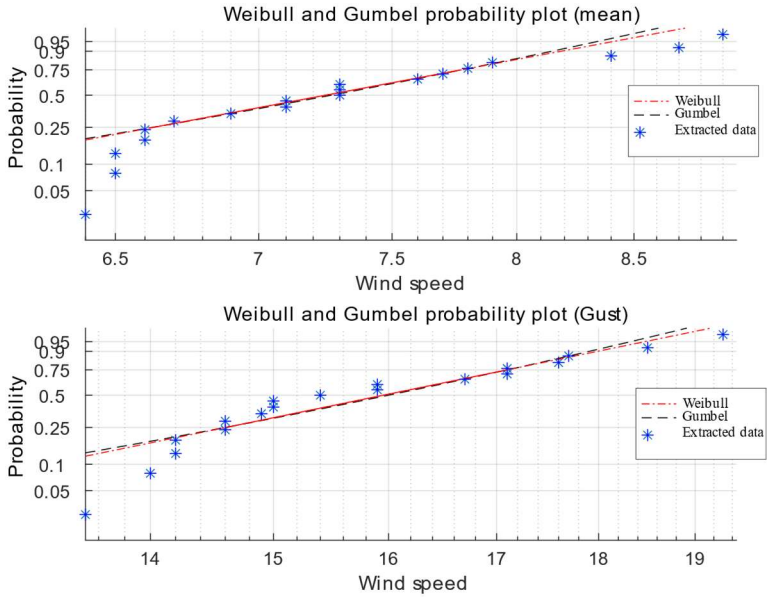

Figure 3-18: Probability plot for extracted data

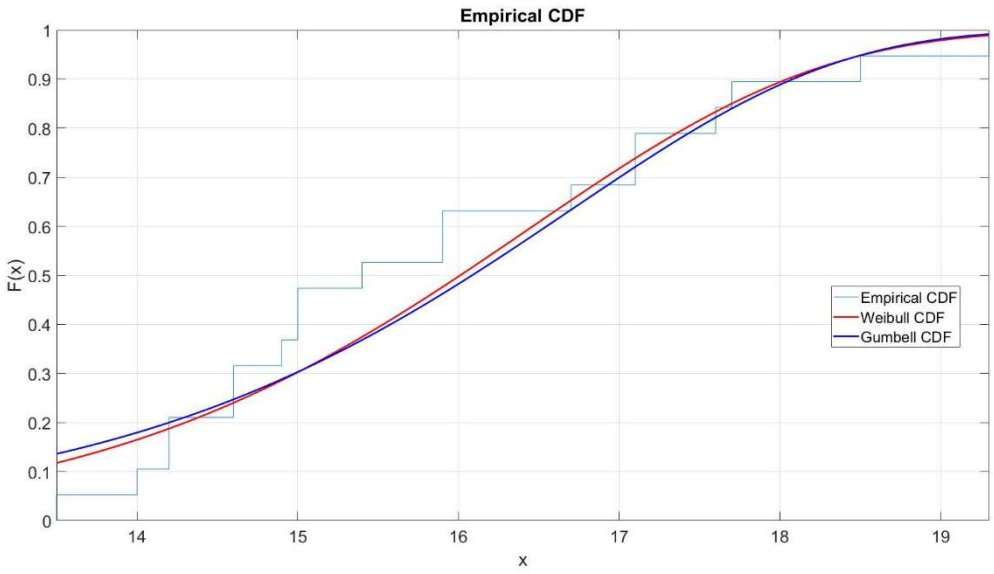

Figure 3-19:Comparation of Empirical CDF and theoretical CDF

Matlab was then used to calculate the parameters of these functions, and the one-sample Kolmogorov-Smirnov test was used to test the null hypothesis that the selected data came from a theoretical distribution with a 5% significance level. The results of the one-sample test (Table 5) failed to reject the null hypothesis at the default 5% significance level. Also, the standard error calculations in 3.2.2 were applied to check which distribution was better for these extracted data. This indicates that the distributions of the annual maximum mean and gust wind velocities for Taipei City can be expressed relatively accurately using the estimated parameters of the Weibull or Gumbel functions. Furthermore, when comparing

the standard errors of the Gumbel and Weibull distributions, there appears to be no significant difference, indicating that both methods can estimate the regression period.

Table 5: Results of parameter analysis and One-sample Kolmogorov-Smirnov test

Distribution Type	*k*(shape factor)*	*α* (scale factor)*	*μ*(location parameter)*	*p-value*	*SE (standard error)*
Gumbel Type (Type I) for mean velocity	0	0.78 [0.56, 1.08]	7.72 [7.35, 8.09]	0.4514	86.0
Weibull Type (Type III) for mean velocity	9.92 [7.15, 13.79]	7.68 [7.32, 8.06]		0.5328	86.8
Gumbel Type (Type I) for gust velocity	0	1.66 [1.20, 2.31]	16.69 [15.90, 17.49]	0.5794	402.5
Weibull Type (Type III) for gust velocity	10.04 [7.19, 14.00]	16.61 [15.83, 17.42]		0.5755	406.0
	* Confidence interval				

Therefore, the Weibull CDFs for annual maximum mean and gust wind velocities are:

$$\begin{cases} F_u(U_m) = 1 - exp\left[-\left(\frac{U_m}{7.68}\right)^{9.92}\right] \\ F_u(U_G) = 1 - exp\left[-\left(\frac{U_m}{16.61}\right)^{10.04}\right] \end{cases} \quad 3.41$$

Furthermore, The Gumbel CDFs can be written as:

$$\begin{cases} \mathrm{F_u(U_m)} = \exp\left[-\exp\left(-\frac{\mathrm{U_m} - 7.72}{0.78}\right)\right] \\ \mathrm{F_u(U_G)} = \exp\left[-\exp\left(-\frac{\mathrm{U_G} - 16.69}{1.66}\right)\right] \end{cases} \quad 3.42$$

Figure 3-20 shows the extracted wind velocity distribution with the linearized Weibull distribution from function 3.41. Figure 3-21 plots the results for PDFs and CDFs based on the above-estimated parameters. In the PDFs chart, the negative skewness level of the Gumbel method is higher than the Weibull method. The CDF curves indicated that the predicted data points for both groups closely follow the fitted normal distribution line. The Gumbel method returns a higher wind speed than the Weibull method at the same probability level. Thus, when the regression period is considered (Figure 3-22), the velocity results of the Gumbel method are substantially higher than those of the Weibull method for both mean and gust winds. In this study, the gust velocities for the different regression years in the Gumbel method were chosen as the extreme velocities for the next step.

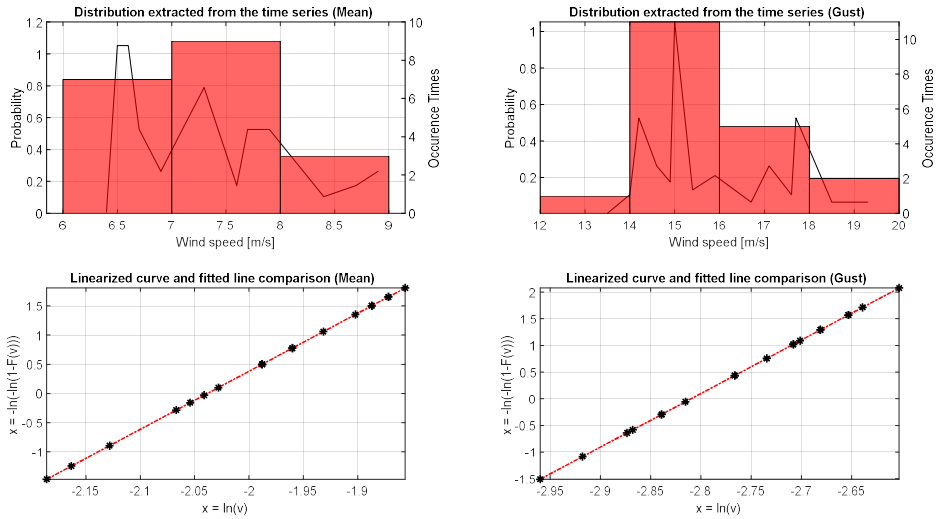

Figure 3-20: distribution of extracted wind velocity and the linearized Weibull distribution

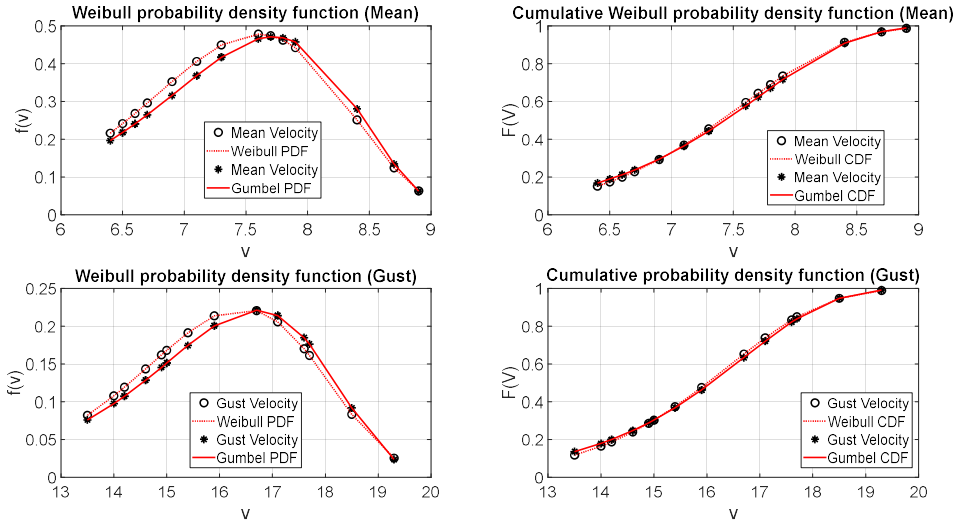

Figure 3-21: PDFs and CDFs for annual maximum mean and gust wind velocity

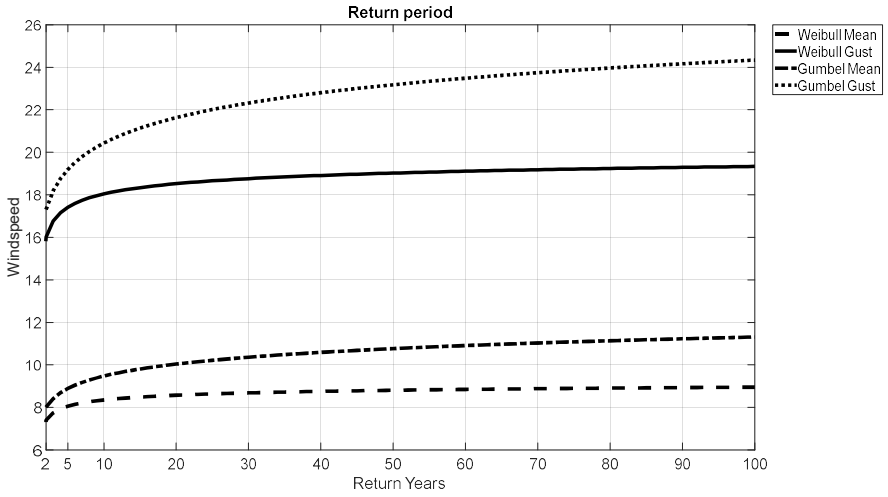

Figure 3-22: Return period estimation with extracted mean and gust wind velocities

(2) Time series simulation

This study uses the Davenport spectrum to model time-series wind velocities. The input means gust wind velocities were taken from the previous step, and a 50-year regression period was used. Additional information for this simulation is presented in Table 6.

Table 6:Basic information for fluctuated wind velocity simulation

Power Spectral Type	***Gust Wind speed***	***Return Period (years)***	***roughness coefficient * (k)***	***Time interval***	***Time***	***Order of AR model+***
Davenport spectrum	23.14 m/s	50 year	0.004	0.1s	1024s	5

** Recommendation from literature(Wang and Cui, 2002)*

+ Recommendation from literature(Cheng et al., 2016)

Autoregressive coefficient(φ_k)	**φ_1**	**φ_2**	**φ_3**	**φ_4**	**φ_5**
	0.8512	0.0121	0.0170	0.0269	0.0506

The fluctuating wind velocity is shown in Figure 3-23, which shows that the simulated wind velocity has good randomness. In addition, the time history curve was converted to the frequency domain. Figure 3-24 shows that the trend and magnitude between the simulated and target spectrum match, with only slight deviations at low frequencies. The following function is also used to quantify the difference between the two spectral densities.:

$$\beta = \frac{1}{n} abs(\sum_{i=1}^{n} \frac{S(n) - S'(n)}{S(n)}) \qquad \#3.43$$

S(n) is the target spectrum, and S'(n) is the simulated spectrum. β for this simulation equals 0.12.

This research only uses five-second time-series gust wind velocity wind for the next step. Figure 3-25 shows the relationship between wind velocity and height. From formula 3.20, the gust wind velocity at 10m, 30m, and 60m height in a 50-year return period for different heigh is shown in Figure 3-26.

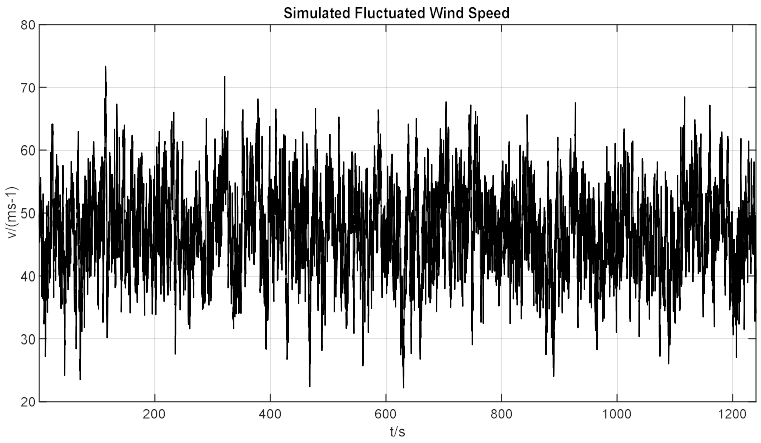

Figure 3-23: Simulated Fluctuated Wind Speed

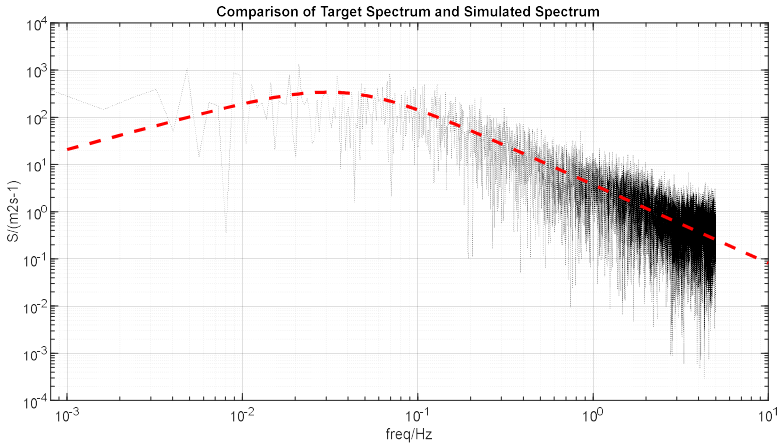

Figure 3-24: Comparison of Target Spectrum and Simulated Spectrum

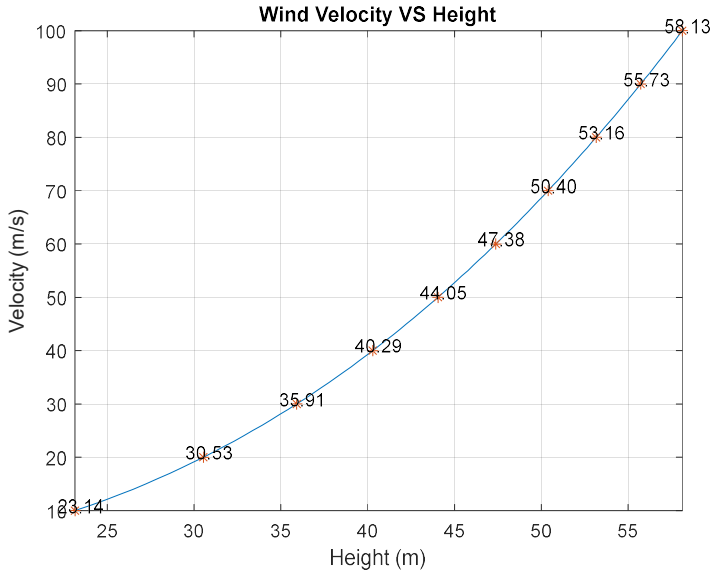

Figure 3-25: Wind velocity changing with height

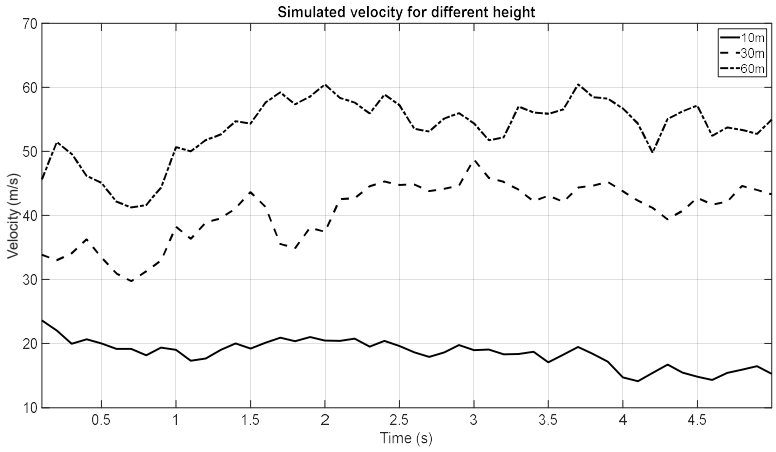

Figure 3-26 The wind velocity for the CFD co-simulation in Abaqus

3.4.2 Results of CFD co-simulation

In contrast to the limit state, the serviceability limit state is the non-destructive state. When the serviceability limit state is exceeded, localized damage, strength degradation and occupancy discomfort may occur (Kim et al., 2008, Lawrence, 2003). In addition, several structural safety factors, including frame stability and the robustness of the building envelope, can be affected by the use limit state (Lawrence, 2003). Deflection, acceleration and fatigue states under load may all affect the serviceability of a building. This section analyses wind load and acceleration deflections and compare them to code limits.

1) Displacement

Different building codes provide different methods for evaluating serviceability limit states. Most codes focus on structures, beams, or floors rather than non-structural members (Lawrence, 2003). Eurocode 5 only provides deflection limits for structural timber members (Table 7) (Porteous and Kermani, 2013). Eurocode 1 calculates the maximum usable displacements of different building elements under wind loads but does not specify limits (Institution, 2005). Similarly, the Chinese load code GB50009-2012 provides a method for calculating the limit state but does not mention the serviceable state ((China, 2012). Analyzing the wall channel displacements under CFD simulations and comparing them to the code may be possible to understand the serviceability performance.

Table 7: Deflection limitation from Eurocode

Use Classification	Deflection Limit
Roof beams (industrial)	L/180
Roof beams (commercial and institutional without plaster ceiling)	L/240
Roof beams (commercial and institutional with plaster ceiling)	L/360
Floor beams (ordinary usage)	L/360
Highway bridge stringers	L/200 to L/300
Railway bridge stringers	L/300 to L/400
$LL < 2.5\ kN/m^2$	L/480
$2.5\ kN/m^2 < LL < 4.0\ kN/m^2$	L/420
$LL > 4.0\ kN/m^2$	L/360

Figures 3-27 and 3-28 show the wind velocity and pressure fields at 30 m height from CFD simulations, respectively. As the pressure increases, the wind velocity decreases near the building block. It appears that the wind pressure is higher at the edge next to obstacle 1 than at the edge away from the obstacle

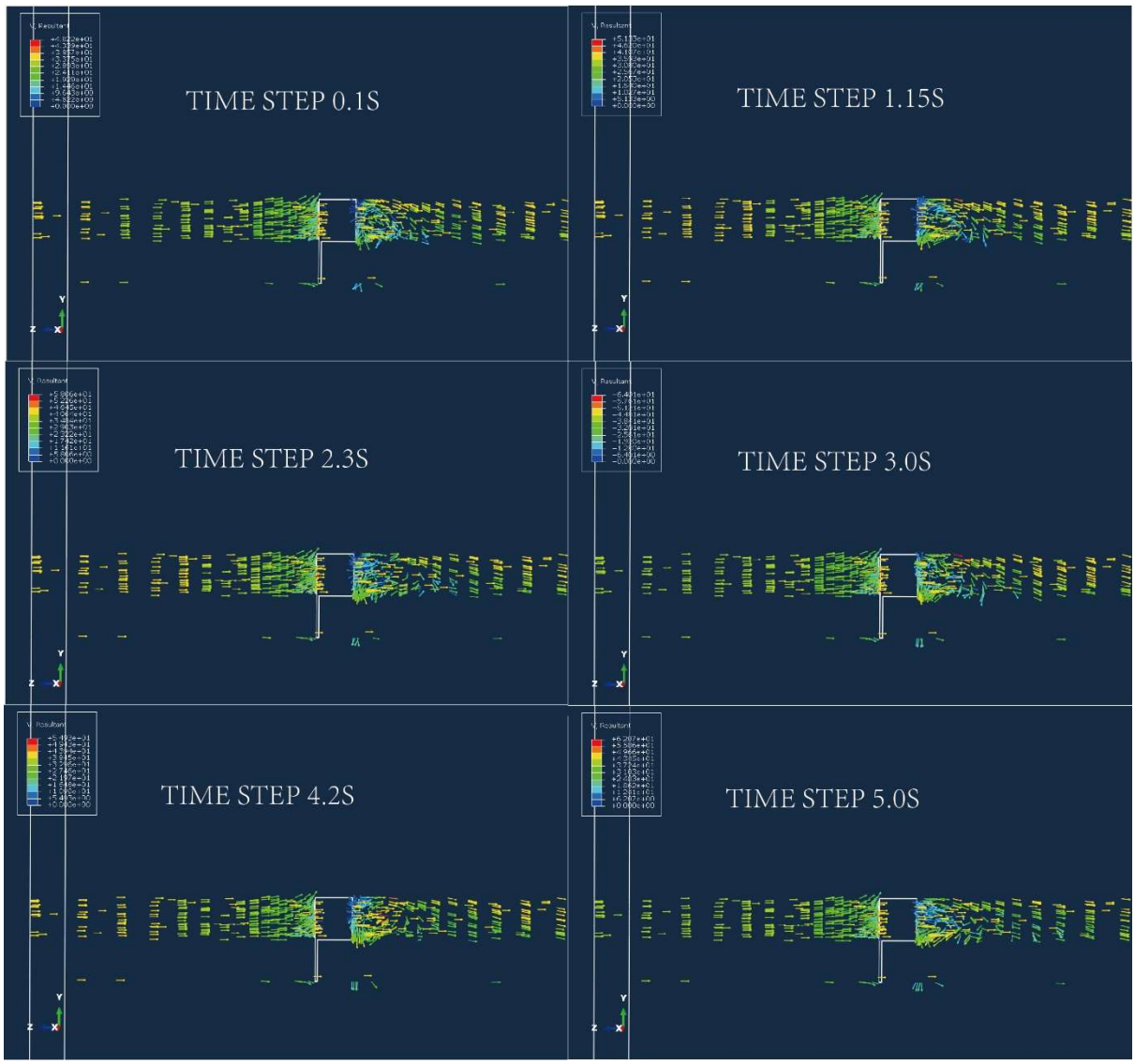

Figure 3-27: Wind filed for wind speed at 30m

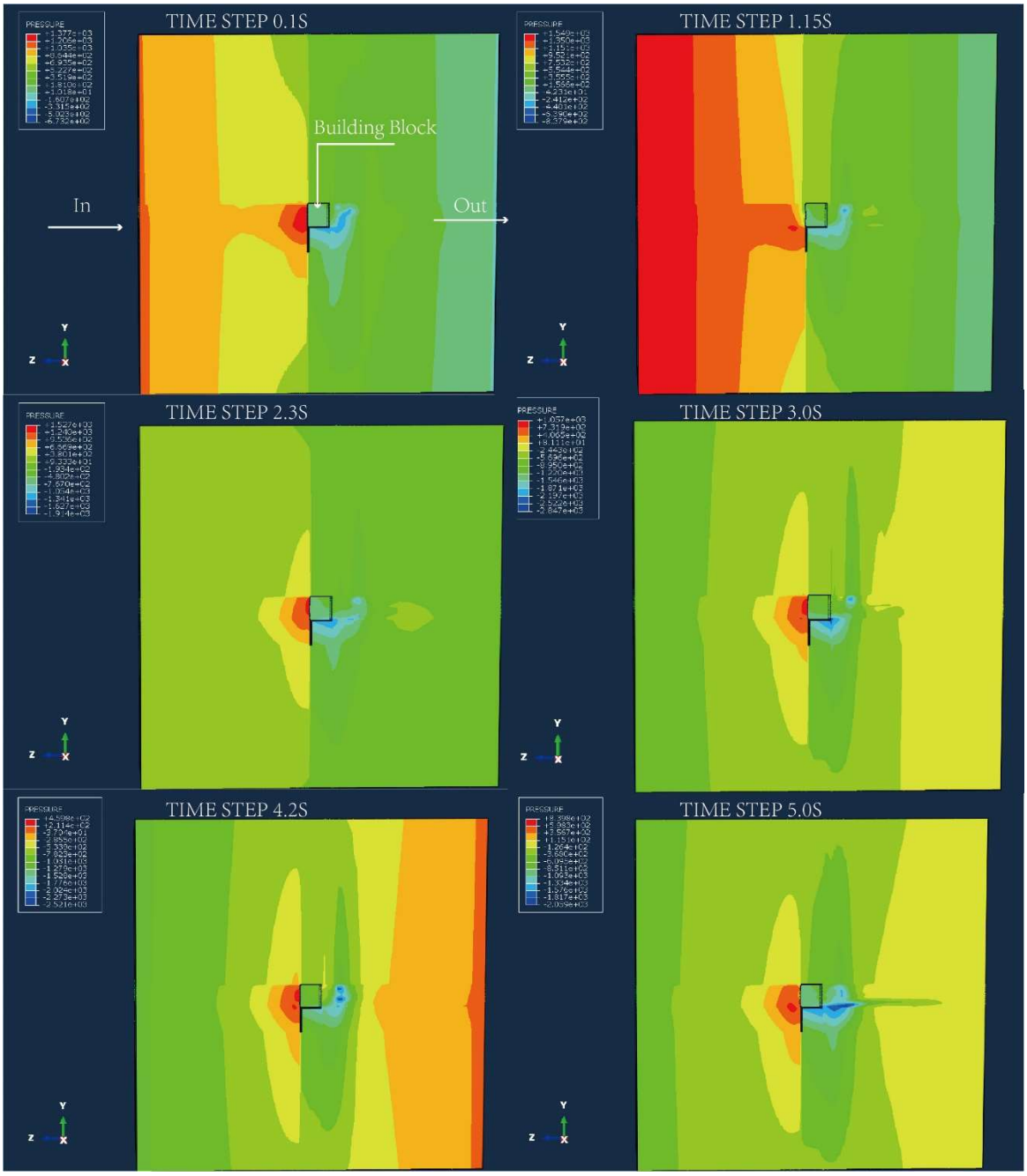

Figure 3-28: Pressure filed for wind speed at 30m

Thirteen points on the target wall (Figure 3-29) were selected for further analysis, and the range of displacements in 5s time steps is shown in Figure 3-30. The displacement range increases from the edge to the middle, both vertically and laterally. The maximum displacement at point M exceeds 120 mm. points 1, 6, 11, and 16 are near the fixed boundary and have relatively lower displacements than the other points, but slight vibrations can still be observed. Figure 3-31 shows the average, maximum and minimum values in the transverse and vertical directions. A numerical symmetry can be observed,

with the average and the maximum displacement in the positive direction occurring at point M. Combined with Figure 3-29, it can be concluded that the increased pressure in the vicinity of the obstacle influences the amplitude of the vibration.

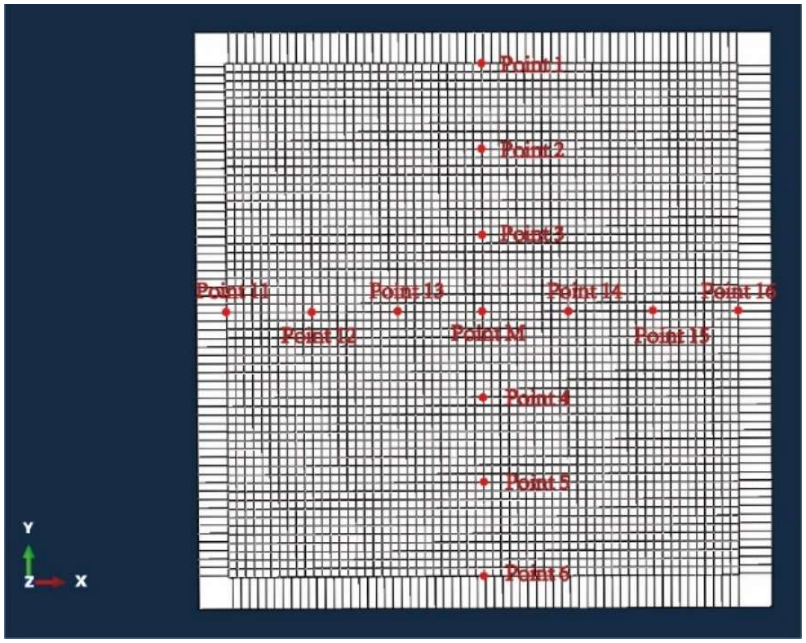

Figure 3-29: Point selected for analysing

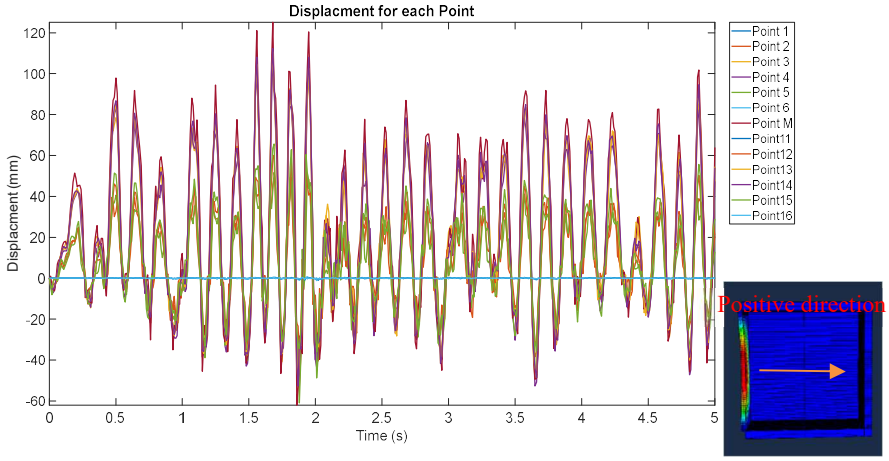

Figure 3-30: Cyclic Displacement of each Point

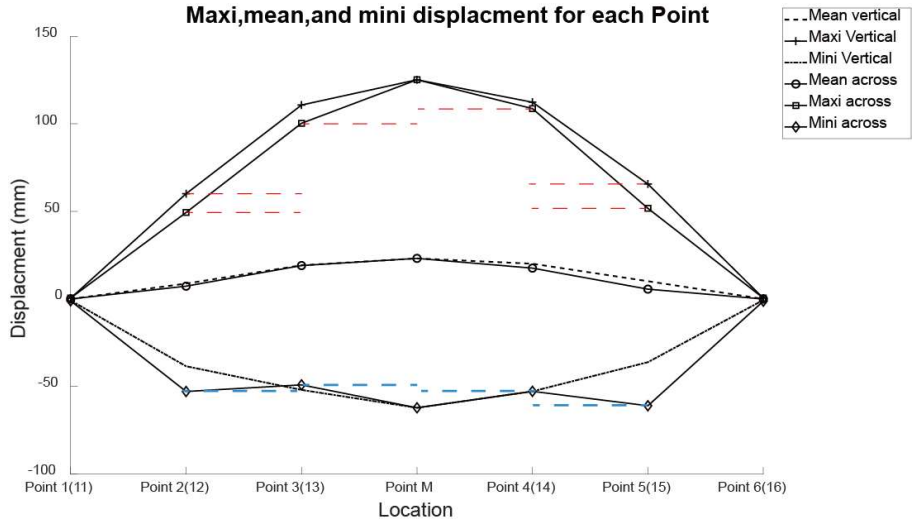

Figure 3-31: maxi, mini and mean displacement of each point

Figures 3-32 and 3-33 show vertical and cross-vibration patterns at different step times. Combining these two figures, the wall plate historically exhibited mainly the single degree of freedom vibrations. However, at 1.0s, 3.0s, and 3.5s, the vibrations exhibit multiple degrees of freedom. Further modal analysis may be required to analyze the vibration frequencies in the various modes.

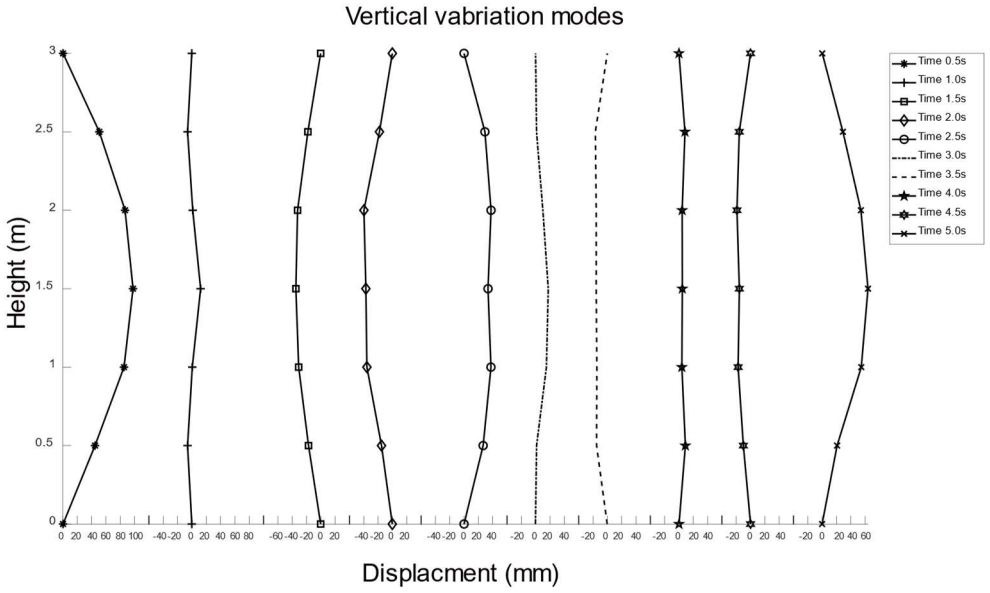

Figure 3-32: Vertical vibration modes at different step time

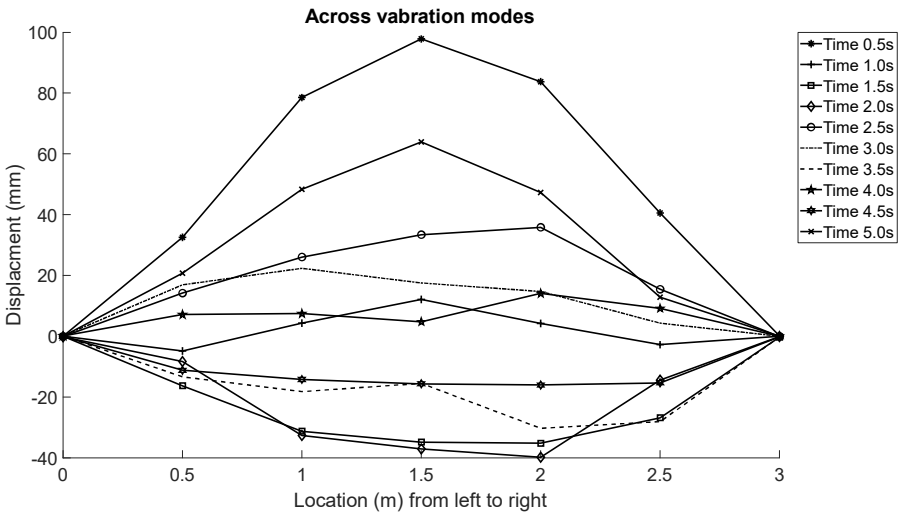

Figure 3-33: Across vibration modes at different step time

Three design codes, including Eurocode (Institution, 2005), ASCE 7-16 (ASCE, 2017), and GB50009-2012 (China, 2012), were selected for comparison with CFD simulations. According to Section 3.4.1, the basic mean wind velocity at 10 m under the 50-year return period is 23.14, and the calculated parameters for the wind velocity at 30 m are shown in Table 8.

Table 8: Wind force calculation for wind velocity at 30m

Parameter	***Design codes***		
	Eurocode	**ASCE7-16**	**GB50009-2012**
Basic velocity	23.14 m/s	23.14 m/s	23.14 m/s
Mean Wind velocity at 30m	18.44m/s	23.14 m/s	36 m/s
Equivalent static wind force	0.715 kN/m^2	0.77 kN /m^2	0.94 kN /m^2

From the CFD simulation results, it can be seen that the response of the target wall is symmetrical. Therefore, this study calculated the maximum displacements based on different wind tunnel codes by simplifying the wall to a two-point support structure. Figure 3-34 shows the maximum displacements for the simulated and code in the positive and negative directions. When comparing the maximum displacements in the positive direction, the simulated results agree well with the calculated results from the code. However, the simulated results are larger than the building code for the negative displacements because this study ignored the internal pressure when calculating the displacement based on regulations. In addition, the setting of the boundary conditions in Figure 3-7 may also affect

the displacements and cannot simply be considered as a two-point support structure. However, the specific effects of the boundaries may require more detailed modelling of the connections. Without careful connection design, the risk of damage to the walls or cladding may increase. It is worth noting that the maximum displacements already exceed the serviceability limit states in ASCE 7-16, where the rotation ratios of the walls should be within 1/400 and 1/600 or less than 10 mm.

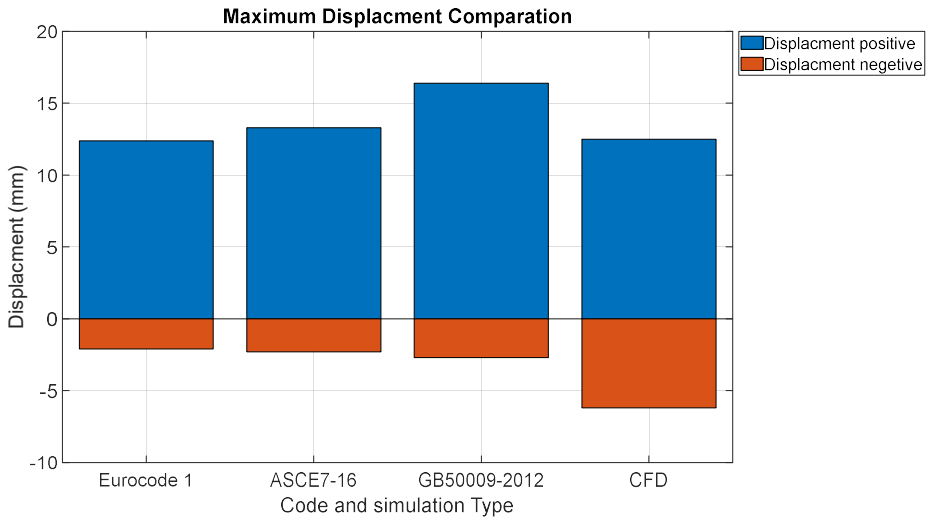

Figure 3-34: Maximum Displacement comparison

1) Acceleration

Building motion is another factor that influences building serviceability. Frequency weighted peak acceleration and root-mean-square acceleration are suggested to be used for structural vibration analysis(BSI, 2011). The function is as follows:

$$a_w = \left[\frac{1}{T}\int_0^T {a_w}^2(t)dt\right]^{\frac{1}{2}} \qquad 3.44$$

Where: $a_w(t)$ is the Frequency weighted acceleration transferred for time history acceleration in meters per second squared (m/s^2), T is the duration of the measurement in seconds

However, most studies have focused on the applicability limits to the entire building structure or floor. Chang (Chang, 1973)suggested comfort levels for different peak acceleration limits for tall buildings, see Table 9.

Table 9 Comfort levels of different peak acceleration limits

Peak acceleration	***Comfort Limit***
<0.5%g	Not Perceptibility
0.5% to 1.5%g	Threshold of Perceptibility
1.5% to 5.0%g	Annoying
5.0% to 15.0%g	Very Annoying
> 15%g	Intolerable

Where g is the acceleration of gravity equals 9.8m/s^2

ASCE 7-16 (ASCE, 2017)also states that acceleration should be less than 0.5%g for quiet operation. For floor slabs, the tolerance threshold is between 5% and 10%g. For traffic structures, the vertical and horizontal peak accelerations should be below 0.7 and 0.2 m/s^2 (Gulvanessian). However, the applicable acceleration limits for facades under wind loads are not specified. Eurocode 1 (Institution, 2005)provides a method for calculating the maximum acceleration of buildings and different elements under quasi-static wind loads. The previous research shows that the ASCE shows higher estimation results in the background and resonant response than Eurocode (Zhou et al, 2002). Considering the local climate condition, this research used Eurocode, which was applied in temperate locations, as a benchmark compared with the CFD simulation results. First, the natural frequencies of the first five vibration modes of the target wall panels were simulated in Abaqus. The fundamental frequency of 47.5 Hz was used for further calculations. The time-history acceleration at point M in the CFD simulation is shown in Figure 3-35(a), with peak accelerations up to 780 m/s^2 and average values of 141.5 m/s^2. Figures 3-35(c) and (d) respectively show the peak and R.M.S acceleration values. The wind force coefficient calculation is based on the free-standing wall (signboard) equation in Eurocode 1. Figure 3-36 shows that boundary conditions are different from the simulation (Figure 3-36), which leads to a lower structural stiffness than the simulation model, which may be why the simulation results are lower than the calculation in both peaks and R.M.S acceleration values. The method recommended by Eurocode is designed primarily for sensitive vibration structures, such as entire buildings, roofs, or bridges. Therefore, it may be relatively conservative to use it to calculate wall vibration accelerations. Although there are no code recommended serviceability limits for walls, when considering acceleration values between 0 and 10 Hz, it is clear that both calculated and simulated peaks are higher than 2m/s^2, which may increase the burden on the wall connections. Careful design of connections and analysis of acoustic issues may be a direction for further research.

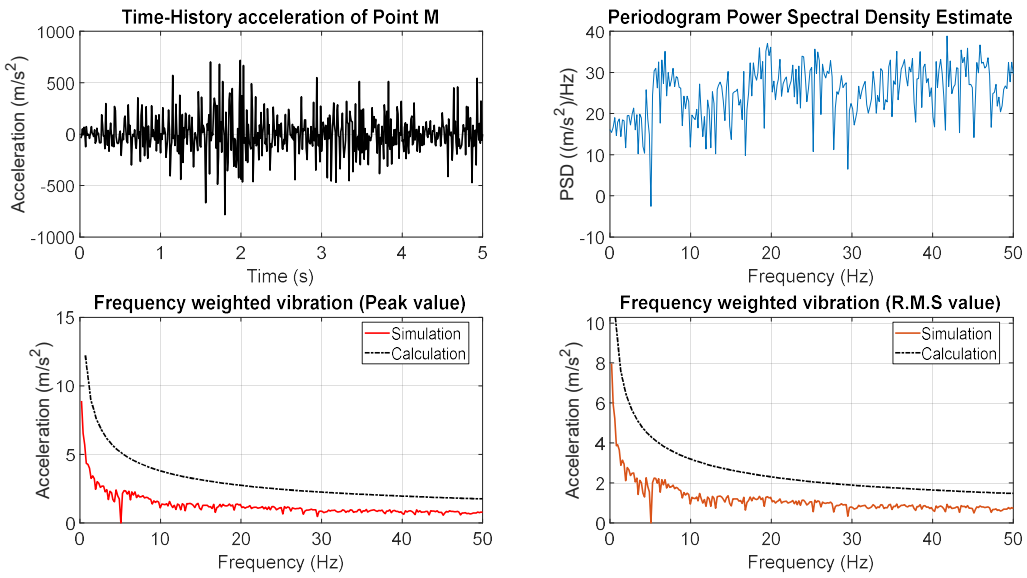

Figure 3-35: Acceleration analysis of Point M : (a)Time-History vibration,(b) PSD,(c) Peak acceleration, (d) R.M.S acceleration

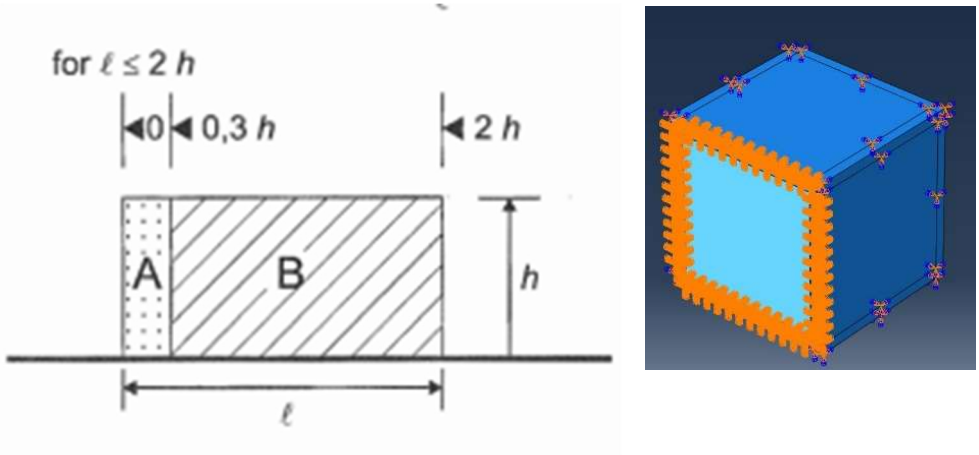

Figure 3-36: Boundary condition for calculation and simulation

3.5 Conclusion

Finally, this chapter investigates the wind-induced response of retaining walls in tall buildings by applying wind load chain theory to predict and simulate wind velocities in selected cities and then using the results in finite element simulations. First, the extreme wind velocity estimation methods and fluctuating wind velocity simulation are presented. The results show that the extreme wind velocities estimated by the Gumbel method are higher than the Weibull method. To simulate fluctuating wind velocities, the Davenport spectrum was used. However, the values of fluctuating velocities are affected by the roughness coefficient (k) and standard deviation (SD) of the input white noise. For this study, the SD was set to an empirical value of 1 (Yang, 2016). The SD of the final velocity results at 10 m, 30 m and 60 m ranged between 2.9 m/s and 4.8 m/s, which is close to the SD of the collected wind data (3.36 m/s). Field studies may be needed at different heights in the selected cities to obtain more accurate simulation results.

CFD simulations are then performed using the input velocity values from the previous steps. The model design is presented, and relatively reasonable wind field dimensions are determined based on validation checks. The simulation results show that the maximum deflection of the wall panels is within the limit compared to the code but exceeds the usable range. In terms of acceleration, the curve shows the value decrease with frequency for simulated and calculated results. However, peaks and R.M.S acceleration values for the midpoint of the simulated wall panel are lower than the calculated value and the gravitational acceleration, indicating that the connection boundary-setting significantly influences structural wind action. It is important to mention that there is no provision to indicate the hazard when the wall plate vibrates at too high a frequency but based on the simulation results, this component should not be ignored because the peak acceleration at lower frequencies is above most of the usable limits of other building elements.

In addition, this section is designed to establish an analytical process for testing the fatigue behaviour caused by connecting winds. Wind tunnel tests are usually used to obtain cyclic sequences for wind load cycling tests, but CFD simulations provide a more economical approach. A comparison of the simulation results with relevant regulations demonstrates that CFD is feasible in analyzing wind-induced behaviour of walls. Furthermore, this

method can be applied anywhere in the rest of the world when wind data is available. The results of CFD simulations are applied in the next chapter.

The CFD simulation results are applied in the next chapter to develop a new wind load cycle test sequence for joint fatigue behaviour analysis

Chapter 4. Dynamic joint fatigue testing under different load scenarios

4.1 Introduction

As introduced in Chapter 2, prefabricated engineering timber products such as Cross-laminated timber (CLT) and Glue-laminated timber (GLT) are widely used in high timber buildings. Due to high in-plane stiffness and linear elasticity, CLT panels are prone to brittle failure under shearing force (Fragiacomo et al., 2011). Therefore, connections in heavy timber constructions prove good mechanical properties under different types of loading and act as the ductile zones under seismic conditions (Izzi et al., 2018a, Karacabeyli and Douglas, 2013, Fragiacomo et al., 2011). Without proper design, structural members' connections may cause discontinuity in overall strength or stiffness, which may cause structural failure, especially during strong earthquakes or hurricanes(Mohammad et al., 2013). Consequently, connections play a crucial role in the success of multi-level timber structures.

The connection types for mass timber structures vary by location and material. Figure 4-1 shows four different places, including in-plane connections (A), corner connections (B) and wall-to-floor connections (C), and wall-to-foundation connections (D) (Mohammad et al., 2013). The fasteners type can vary even at the same location, such as long self-tapping screws and standard dowel-type fasteners (Figure 4-2) with wood screws, nails, bolts, and dowels and angle brackets with fasteners are commonly recommended (Karacabeyli and Douglas, 2013).

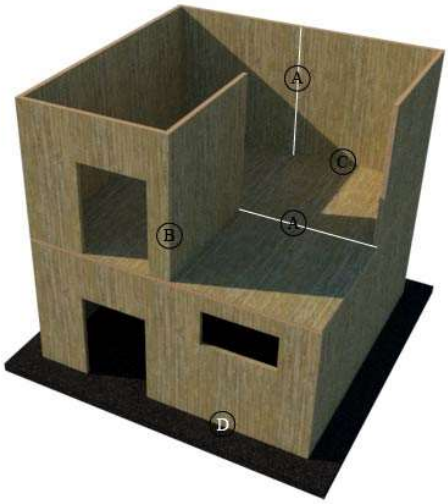

Figure 4-1*:* Location of the different connections

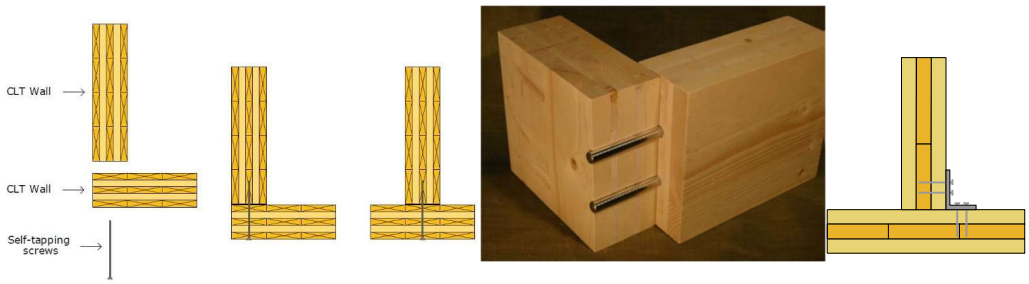

Figure 4-2 Self-tapping screws (left), dowel-type fasteners (middle) and angle bracket with fasteners(left) (Gagnon and Pirvu, 2011, Uibel and Blaß, 2007).

Additionally, the connection type for timber walls can be divided into two types according to its role: preventing sliding and shaking of the walls and preventing the sliding between continuous walls or floors (Polastri et al., 2017, Dietsch and Brandner, 2015, Porteous and Kemani, 2013). Hold-downs or angle brackets fastened with nails or screws are typically used in the first condition (Tomasi and Smith, 2015). Angle brackets (Figure 4-3) are made from 2 to 3 mm thickness pre-galvanized or stainless steel with holes for nails or screws and larger holes for bolts, and some products also have a reinforced rib between two plates (Gustafsson, 2019, ETAG015, 2012). The main benefit is the flexibility of connecting timber with different materials and directions (Figure 4-4).

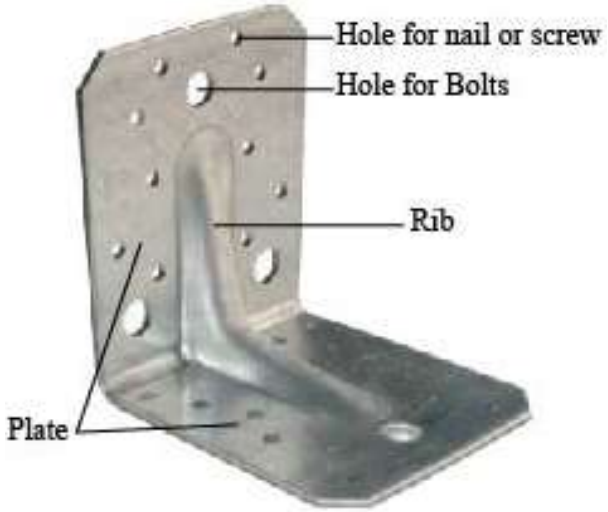

Figure 4-3: Photograph of the angle bracket

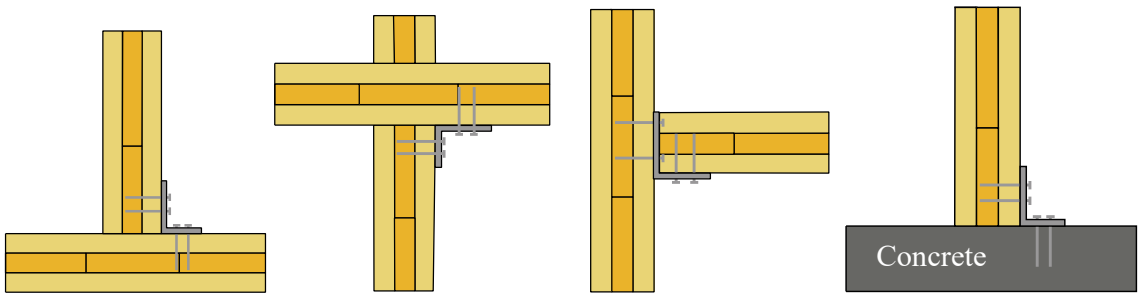

Figure 4-4: Different connection methods using corner brackets

Angel brackets with different geometry and fastener numbers have been tested under cyclic and monotonic shear or tension loads(Fragiacomo et al., 2011, Flatscher et al., 2015, Tomasi and Smith, 2015, Izzi et al., 2018b, Lauriola and Sandhaas, 2006, Gavric et al., 2014, Shahnewaz et al., 2018). Ceccotti (2006) and Pei (2013)pointed out that the angled layout strongly influences the whole connection system. Some oversize angle brackets and hold-downs are designed especially for heavy timber structures to resist the inertia loads generated during overloading. That lead to a stiff system (Lauriola and Sandhaas, 2006), and the connector plate may fail before any nail yields (Polastri et al., 2017). Some common failure modes are recognised because of incorrect design by research, such as withdrawal of the nails or pull-out of the anchoring bolts and tensile failure at the cross-section of the metal plates (Gavric et al., 2015b). The research recommended that when setting up angle brackets and fasteners, providing reasonable ductility by allowing the wall panel to rock in load paths is required to prevent failure of relatively rigid elements (wall panel) (Dujic et

al., 2006, Dujic et al., 2008, Popovski and Karacabeyli, 2012a, Gavric et al., 2015b). The angle brackets are commonly installed symmetrically on both sides of the wall in the shear forces testing (Pei et al., 2013, Gavric et al., 2015b). Installed only inside the building walls in practice which may lead to an asymmetrical loading condition (Polastri et al., 2017). Therefore, the design to prevent out-of-plane deformation is required.

Most research mentioned above focused on the mechanical behaviour of connectors with angle brackets between wall and foundation, and connections at conner between walls are rarely analysed. Additionally, more attention is paid to cyclic shear, tension, or combination of lateral and axial loading paths than pressure. That may be because those researches aim to study the ultimate limited state under extreme conditions.

This research applied the angle bracket fastened with nails as the connection. However, this study aims to analyse serviceability conditions under the out-of-plane force caused by wind; thus, the angle bracket is set on a single side. To understand the fatigue behaviour of in-fill panel connection under dynamic wind velocity, a new cyclic testing scheme was developed with the input wind data simulated from Chapter 3. Monotonic tests followed the cyclic tests to figure out the strength degradation. This testing scheme is compared with other methods from different codes for fatigue assessment under wind action.

4.2 Methods and materials

4.2.1 Cyclic assessment methods from Codes

Under cyclic loading, a material or structure may fail due to fatigue. Therefore, the first step in fatigue assessment is the loading description. Research on the sequence of wind pressure loading on buildings begins with the roof cladding of low-rise buildings. Researchers have noted that dramatic fluctuations in wind action can lead to the absence of roof cladding or fatigue failure of roof fasteners (Walker, 2010, Beck and Stevens, 1979, Henderson et al., 2010, Morgan and Beck, 1976). As a result, several building codes have developed fatigue resistance tests for roofs with different loading sequences. The Darwin Area Building Manual (DABM) recommends that roof systems should not fail after 10,000 cycles of 1.8 times the ultimate design load ((DRC), 1976). As this test is considered too severe (Mahendran and Station, 1993), another loading process called TR440,

recommended by Melbourne, is accepted by the Australian Wind Load Code ((SAA), 2018).TR440 has three load classes but has more cycles than DABM (Table 10). However, DABM is still used as the standard test code in northern Australia because some roofs can still be destroyed in Darwin even if they pass the TR440 test (Henderson et al., 2010, Mahendran and Station, 1993). To better represent the behaviour of cyclones, the Low-High-Low (L-H-L) test was later introduced in the Australian Building Code (Kathekeyan and Mahendran, 2018). The L-H-L method includes seven levels with a total cycle count of 10360 (Table 10). Considering that the first two codes are for cyclone-prone regions, the British Building Research Establishment (BRE) developed a loading procedure for temperate regions (Table 10). In North America, two test standards are widely used, FM4470 and UL580, controlled by time rather than the number of cycles (Table 10) (Baskaran and Lei, 1997). The benefit of FM testing is that it is time-saving and can be completed in less than 10 minutes. However, FM does not seem to represent fluctuations in wind action compared to other dynamic tests (Baskaran, 2002). Therefore, a new loading cycle procedure, called SIGDERS, was developed specifically for roofs in wind tunnel tests (Baskaran and Chen, 1998). This detailed method consists of eight sequences divided into two groups (Table 10).

In addition, in Europe, Gerhardt and Kramer recommended a testing procedure called Ueatc (Gerhardt et al., 1986). The test load consists of four steps, focusing on the design load of the fastener rather than the entire roof system (Table 10). However, this method is time-consuming, taking 3 hours to complete the first step and 138 hours for the entire process (Baskaran and Lei, 1997, Gerhardt et al., 1986). These proposals are studies of wind-induced roof fatigue, which may be because roofs are more vulnerable to damage in the wind than heavier brick or concrete walls. As the height of wood buildings increases, walls with lightweight wood materials also face fatigue under high winds. The previous studies have guided the design of loading sequences for wind fatigue of wood walls.

ASTM E2126 provided the standard method to analyse the fatigue life of connections with hold-down or angle brackets in terms of building walls. Those recommended methods in this standard focus on the performance under shear force without considering specific conditions such as seismic or heavy wind, but several suggestions are set up for cyclic testing. The actuator's displacement rate should fall between 1.0 and 63.5 mm/s to avoid

the inertial effects, and the rate should be within that 25.4 mm/min in the monotonic testing (ASTM, 2019).

This research selected DABM, TR440 and BRE as the standard loading sequences compared with the newly designed scheme. The displacement rate and setups have followed the recommendation from ASTM E2126

Table 10: Different cyclic wind-induced fatigue tests

Standard	DABM		TR440		BRE		FM4470		UL580	
	Percentage of design load	**Number of cycles**	**Percentage of design load**	**Number of cycles**	**Percentage of design load**	**Number of cycles**	**Pressure**	**Time**	**Pressure**	**Time**
	100	10000	62.5	8000	90	1	1400pa	1 min	-2330pa	5min
	-	-	75	2000	40	960	Increase 700pa per min	Until fail	1990pa	5min
	-	-	100	200	60	60			Cyclic 1160 to 2330 pa	60min
	-	-	-	-	50	240			-2710 pa	5min
	-	-	-	-	80	5			2330pa	5min
	-	-	-	-	70	14				
	180	1	200	1	100	1				

Standard	Ueatc		SIGDERS	
	Step 1		**Group 1**	
	Load: percentage of 300N per fastener	**Cycles**	**Percentage of design pressure**	**Cycles**
	40	500	25	400
	60	200	50	700
	80	5	70	200
	90	2	1	50
	100	1	**Group 2**	
	90	2	25-50	400
	80	5	25-75	400
	60	200	25-100	25
	40	500	50-100	25
	Step 2			
	Load：100N per fastener	200000		
	Step 3：repeat step 1			
	Step 4：repeat step 1 with a maximum load of 400N			

4.2.2 New assessment programme

1) New loading protocol design process

Firstly, time-series loading is required for the loading sequence reconstruction. Some researchers used wind tunnel pressure records for the loading sequence development(Baskaran and Chen, 1998). As mentioned before, this research uses the data from the Abaqus-CFD co-simulation as the time-history pressures for this new assessment method design.

Several ways to reconstruct the loading sequence include power spectral density, round-trip matrix, and cycle counting (Khosrovaneh and Dowling, 1990). Cycle counts can be changed by using different counting methods. The Rain Flow Counting (RFC) method is preferred for loading analysis and sequence construction (Potter and Watanabe, 1989, Bisping et al., 2014, Lee and Tjhung, 2012, Xu, 1995, Arıduru, 2004). The results of RFC are the period, range and average of the random load history extracted for further stress-strain analysis (Cheng and Broz, 1986). Although exact counting methods have been defined (which can be found in Cheng's review (Cheng et al., 2016, Cheng and Broz, 1986)), techniques for sequence reconstruction are not standardized. Amzallag (Amzallag et al., 1994)states that some periods can be ignored, and Baskaran (1998) chose 5% as the threshold in his study.

This study uses Matlab to do RFC for the stochastic time-history wind load cycle counts. After defining the return period (T), that this study focused on the 50-year return period, the construction of loading sequences is based on the following steps:

1. Identify extreme wind speeds (U) and return year (r) from 40% to 100%
2. Simulate dynamic wind load ($\overline{U}$)
3. Simulate time-history loads with CFD
4. Plot the displacement value (D) at a selected point
5. Apply RFC methods to count cycles (n) and amplitude (D)

6. Develop load sequences with displacement value and cyclic time

The first four steps are described in Chapter 3. Since the BRE (BRE, 1989) recommends that only loads exceeding 40% of the design load need to be tested, this study simulates extreme wind speeds from 40% to 100% based on the dynamic wind speed simulation method in Chapter 3. Reconstruction of load cycles should consider amplitude, load ratio and cycle length. Although (Khosrovaneh and Dowling, 1990) recommend testing the most important cycles in rain flow counts first, Sonsino states that the development of loading cycles can be determined by testing the machine (Sonsino, 2007). In this study, the maximum amplitudes of extreme velocities were selected from each rainfall count for different percentages, taking into account the testing time. The total number of time-history loading cycles was reconstructed according to the following function.

$$N_{C(i)} = n_{r(i)} * N_{r(i)} \tag{4.21}$$

Where: Nc is the loading cycles for the extreme wind velocity of 40% to 100%, nr is the number of occurrences of maximum amplitude from the rain flow counting, and Nr is the return times of extreme wind velocity of 40% to 100% in 50 years. Figure 4-5 shows the flow chart for the new loading protocol design process.

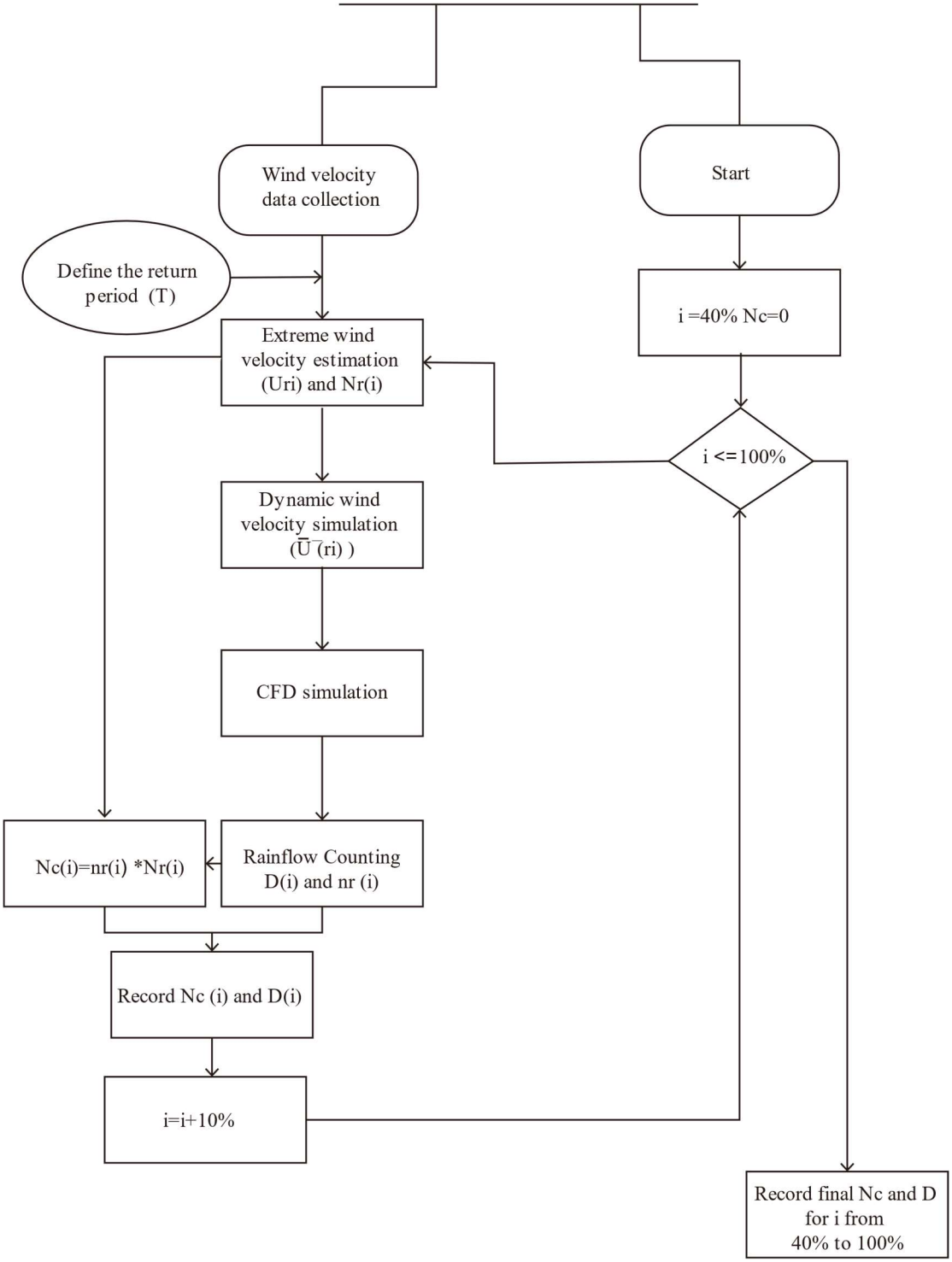

Figure 4-5: Flow chart for new loading protocol design

Return times over 50 years were calculated for the extreme wind velocity of 40% to 100%, which are used in the final sequence development (Table 11). Figure 4-6 shows the results of the dynamic wind speed simulations at 30 m height for CFD simulation.

Table 12: wind velocity and return period

Percentage of extreme velocity	***40%***	***50%***	***60%***	***70%***	***80%***	***90%***	***100%***
Velocity at 10m (m/s)	9	12	14	16	19	21	23
Return times in 50 years (N_r)	150	50	20	9	4	2	1
Velocity at 30m (m/s)	14	18	22	25	29	32	36

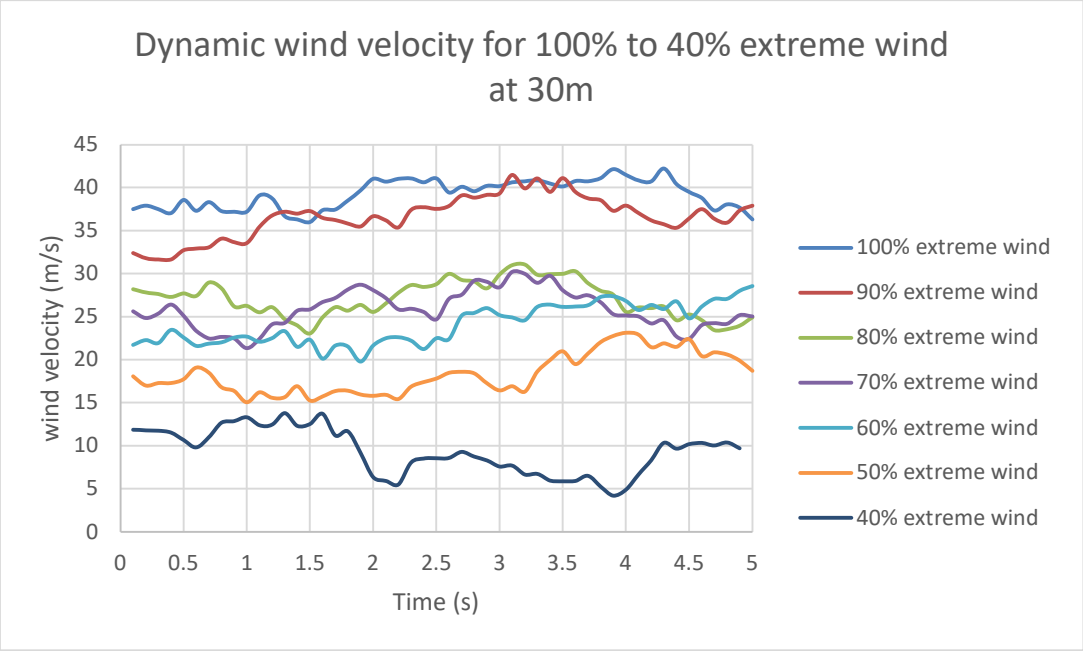

Figure 4-6: Dynamic wind velocity at 30m height

After CFD simulations, the points selected for further analysis are shown in Figure 4-7, and the FEM simulation displacement results for the selected points are shown in Figure 4-8. Since the laboratory tests are performed under displacement control, the time history displacement of the selected points is recorded for the next step. Then, rainfall statistics are done using Matlab. The cycle count results for calculated displacements at 36m/s and 14m/s wind speed are shown in Figure 4-9. The final load protocol from the newly designed method is shown in Table 12.

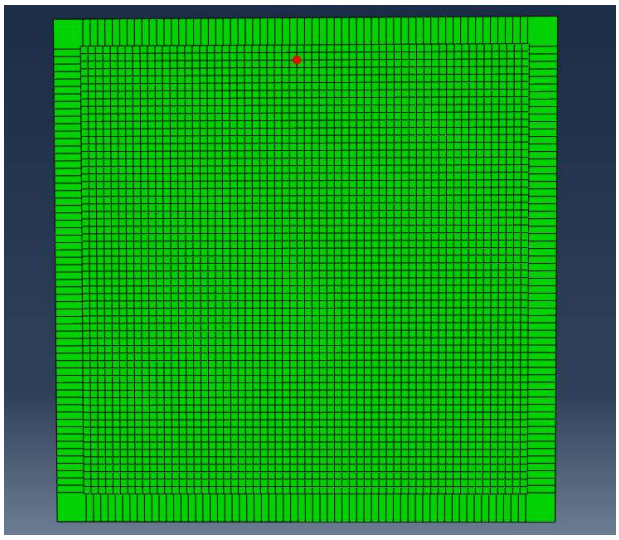

Figure 4-7: Point selection for analyses

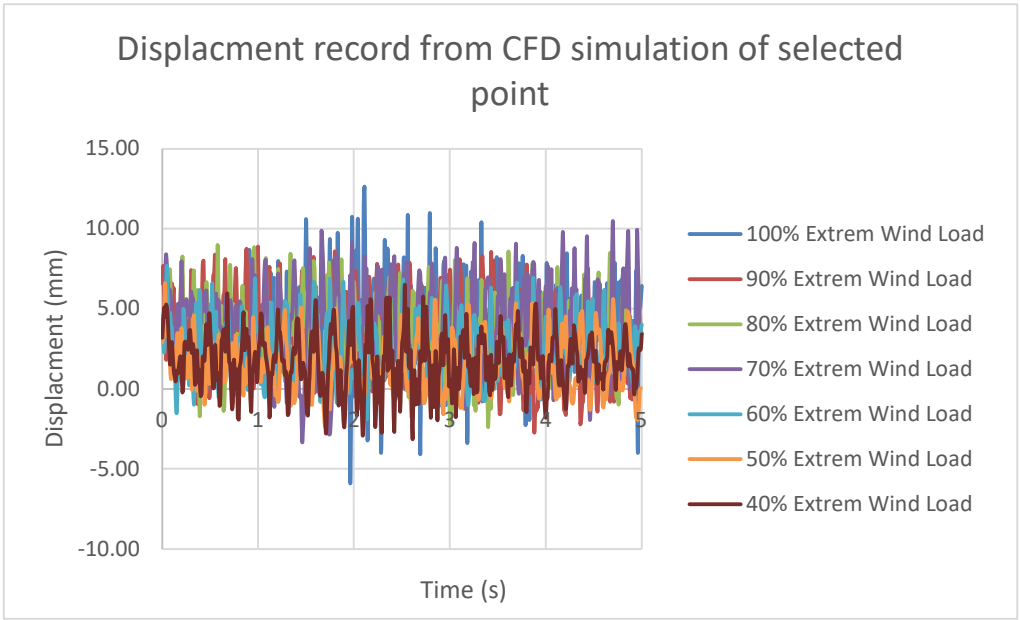

Figure 4-8:Displacement record from CFD simulation results

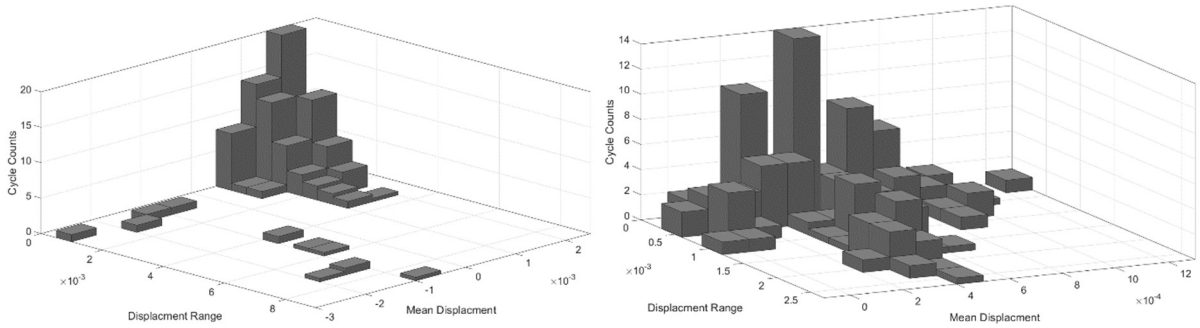

Figure 4-9:Rainfall statistics for 40% (left) and 100% (right) limiting speed percentages at 30 m height

Table 13:Loading sequences (New method)

Test Group name	***Cycles Displacment***				***Number of Cycles***
ARC3050 (apply five times)	0 to -9	-9 to 0	0 to 5	5 to 0	2
	0 to -9	-9 to 0	0 to 3	3 to 0	150
	0 to -8	-8 to 0	0 to 1	1 to 0	20
	0 to -7	-7 to 0	0 to 1	1 to 0	50
	0 to -11	-11 to 0	0 to 2	2 to 0	4
	0 to -9	-9 to 0	0 to 2	2 to 0	9
	0 to -12	-12 to 0	0 to 3	3 to 0	1

2) material and assemble

Considering the financial and machine constraints, the specimen design was simplified to Figure 4-10. Both edges of the foundation part were extended to fix the sample on the testing machine, which can prevent the whole sample rotation. However, this may lead to a difference from the actual practice, which is one limitation of the sample design. The system was assumed to be part of a beam supported at both forces analysis ends. The test material was a 4-ply (35-40-40-35 mm) plywood (GLT) made of spruce. The strength class achieved was GL24c, and its average density was 450 kg/m3 with a moisture content of 6.2%, following (BSI, 2009) recommendations of EN1380 (BSI, 2009). The boards are stored at a temperature of 20±2°C and relative humidity of 65±5%. Unlike CLT, the grain of the wood in GLT is parallel, making it a flexible shape. Therefore, GLT can be used as straight, curved, or arched load-bearing structures such as beams and columns and for floor or roof trim. The test specimens were attached with ABR 90 x 90 x 65 x 2.5 mm (ETA., 2021) type angle brackets, fastened with 4 x 60 mm CNA ring shank nails (ETA., 2019) following the fastening pattern in Figure 4-11. The dimensions of the test specimens are shown in Figures 4-12.

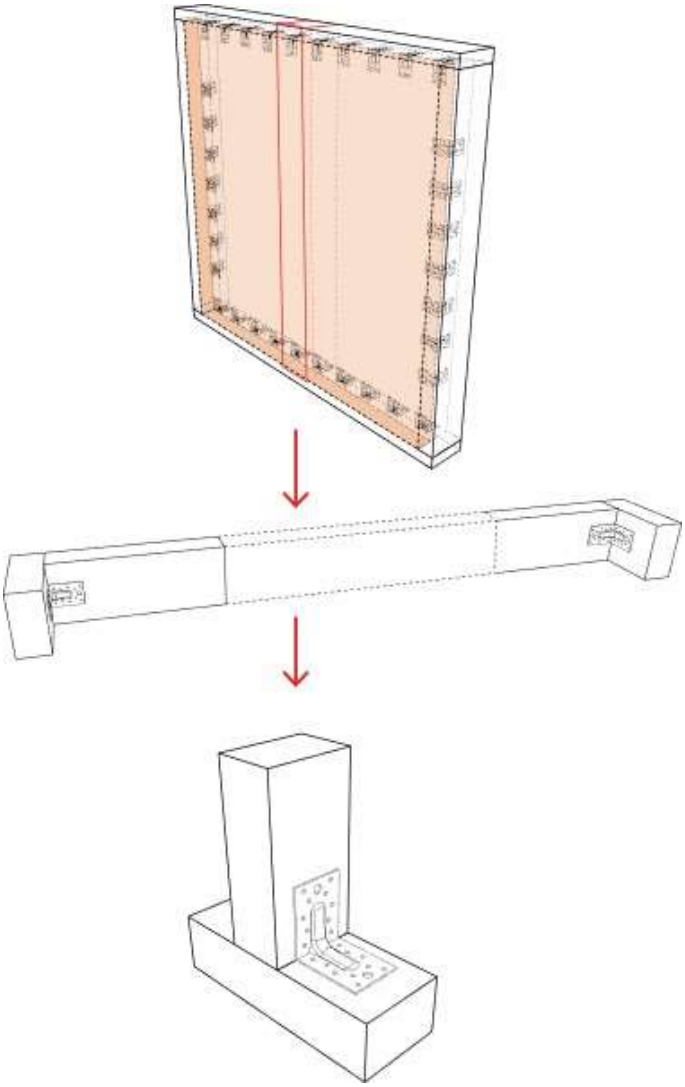

Figure 4-10: Specimen simplify

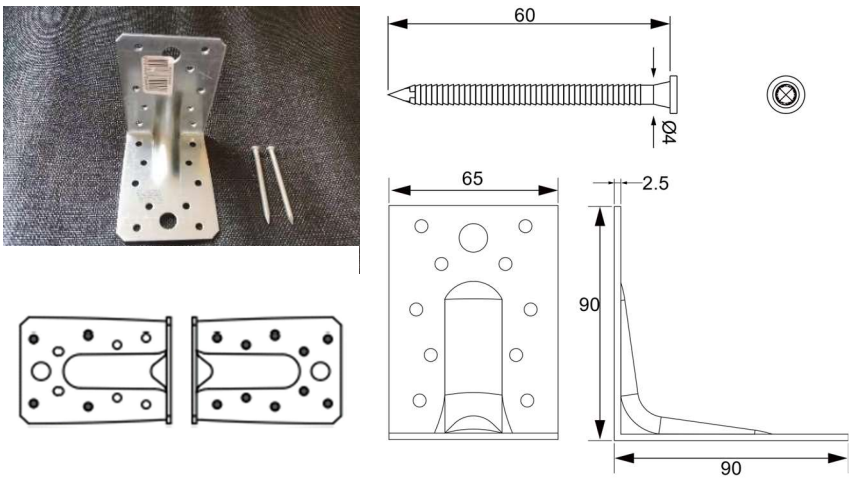

Figure 4-11: Mental connector and fasteners used in tests

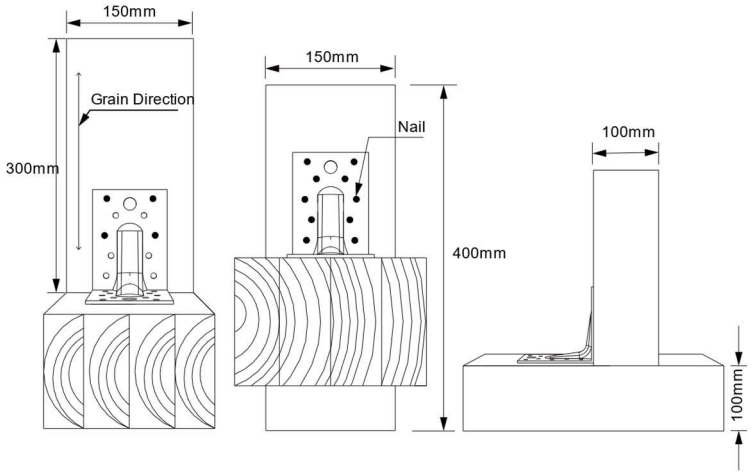

Figure 4-12: Dimensions of the specimen

3) Loading protocol

The purpose of the experimental test was to analyze the performance of the wall connection under cyclic loading and to compare the new load sequence with the DABM, TR440 and BRE codes. To run this test in the displacement domain protocol, the specimen's response to dynamic loads first needs to be calculated. The specimen is assumed to be a single degree of freedom system, and the following function gives the dynamic response under step loading.

$$x = Ae^{-\xi\omega_n t}\sin(\omega_d t + \phi) + \frac{F}{k} \tag{4.23}$$

Where:

$$\xi = \frac{c}{2\sqrt{km}} \tag{4.24}$$

$$\omega_d = \omega_n\sqrt{1-\xi^2} \tag{4.25}$$

$$\omega_n = \sqrt{\frac{k}{m}} \tag{4.26}$$

$$A = -\frac{F}{k\sqrt{1-\xi^2}} \tag{4.27}$$

$$= \frac{tan\phi}{\frac{\sqrt{1-\xi^2}}{\xi}} \quad 4.28$$

Where: c is the damping coefficient

For beams supported at both ends under uniform continuous distributed loads.

$$k = \frac{24\,E\,I}{q\,x\,(L^3 - 2\,L\,x^2 + x^3)} \quad 4.29$$

Where: E is Young's modulus, I is the moment of area, L is the length of the beam, and x is the length of the specimen.

If initially held at rest at a distance X from its equilibrium position and then released, the initial condition at t = 0 is x(0) = X (Williams, 2016). Thus, the undamped free vibration is.

$$\dot{x} = Xcos\omega_n t \quad 4.30$$

Thus, the adjusted displacement at wind pressure is.

$$\dot{X} = x + \dot{x} \quad 4.31$$

The design wind pressure for the 50-year return period is from GB50009-2012 (China, 2012). For Taipei City, the wind pressure value for 10 m height is 0.7 KN/m^2. The wind pressure (w_k) for the envelope can be calculated as the following function:

$$w_k = \beta_{gz}\mu_{st}\mu_z w_0 \quad 4.32$$

Where: β_{gz} is the gust factor at height z, μ_{st} is the local form factor,μ_z is the variation coefficient for different heights, w_0 is the wind pressure at 10m.Theresultfor$w_k$equals 0.94KN/m^{2}isshownin Figure 4-13, and the peak and valley are used to combine the test loading sequence. The loading protocol for BRE and DABM, TR440 is shown in Table 13. Figure 4-14 show the cyclic load curves for different loading protocols.

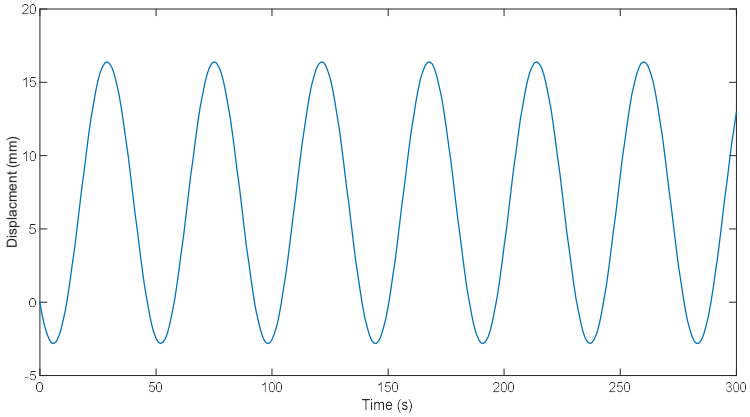

Figure 4-13: structure response under step load for wind pressure at 0.94 KN/m^2

Table 14 Loading sequences (BRE, DABM and TR440)

TEST GROUP NAME	DISPLACEMENT RANGE (MM)				CYCLES
BRE (APPLY FIVE TIMES)	0 to -15	-15 to 0	0 to 3	3 to 0	2
	0 to -6	-6 to 0	0 to 1	1 to 0	960
	0 to -10	-10 to 0	0 to 2	2 to 0	60
	0 to -8	-8 to 0	0 to 1	1 to 0	240
	0 to -13	-13 to 0	0 to 2	2 to 0	5
	0 to -12	-12 to 0	0 to 2	2 to 0	14
	0 to -16	-16 to 0	0 to 3	3 to 0	1
DABM	0 to -16	-16 to 0	0 to 3	3 to 0	10000
	0 to -29	-29 to 0	0 to 5	5 to 0	1
TR440	0 to -10	-10 to 0	0 to 2	2 to 0	8000
	0 to -12	-12 to 0	0 to 2	2 to 0	2000
	0 to -16	-16 to 0	0 to 3	3 to 0	200

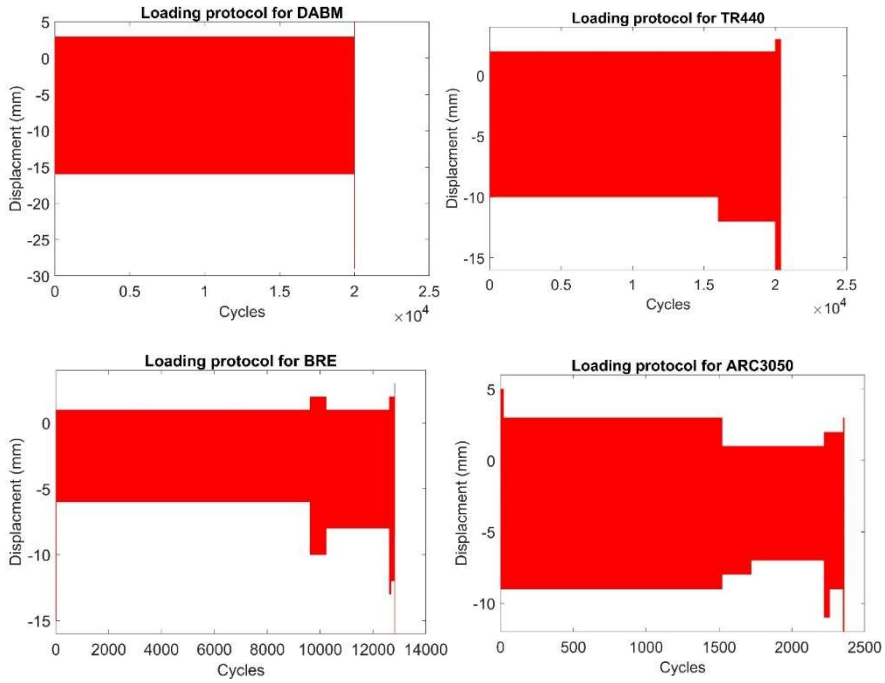

Figure 4-14: Loading protocol curve for 4 testing scenarios

(3) Testing setup

The Eland 50kN 200mm stroke tension and compression digital servo-hydraulic actuator perform cyclic and monotonic tests. The tests were performed at the heavy structures lab, University of Sheffield. The specimens were anchored to a steel foundation with steel sheets, and four linear variable differential transformers (LVDTs) with a range of 50mm were used to measure the displacement, as shown in Figure 4-15. The actuator is on the left side of the specimen facing the angle bracket and performs the out-of-plane load. The back of the angle bracket is defined as positive (Figure 4-16). The displacement ratio of the actuator is between 16-20 mm per second for cyclic loading and 0.2mm per second for monotonic loading stopped at 50mm displacement. Table 14 lists every physical test carried out in this study. For comparison, separate monotonic tests were first conducted in this study to understand the strength of this kind of structure.

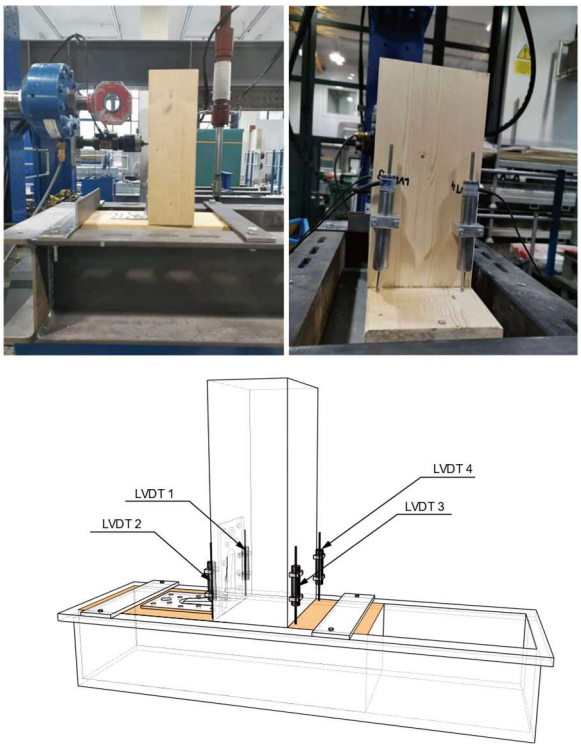

Figure 4-15: Specimen anchoring and LVDTs locations

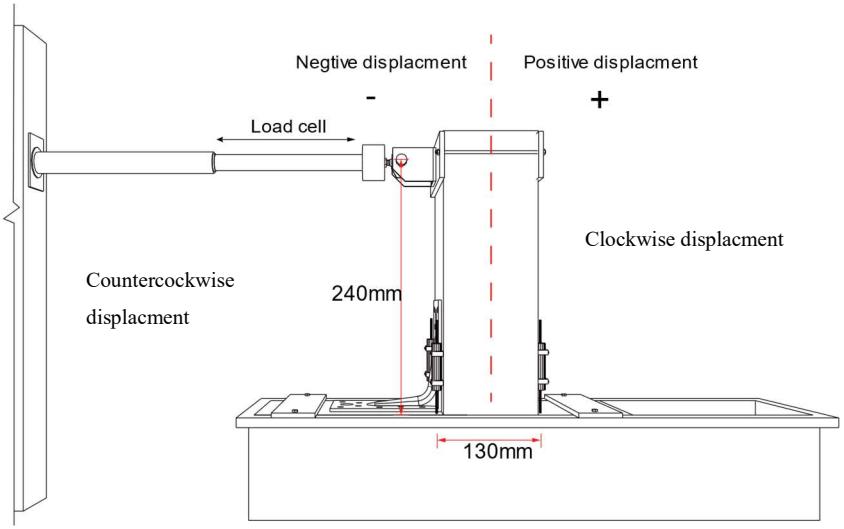

Figure 4-16: details of actuator setting up

Table 15: List of the testing schedule

Group	Description	Number of specimens	Angle bracket type
MOP	Monotonic test (Pull counterclockwise direction 50mm)	2	ABR90 × 90 × 65 ×2.5mm
MOpu	Monotonic test (Push clockwise direction 50mm)	2	ABR90 × 90 × 65 ×2.5mm
BRE	Loading protocol from BRE	2	ABR90 × 90 × 65 ×2.5mm
BREpu	Loading protocol from BRE (Push positive direction 50mm)	2	ABR90 × 90 × 65 ×2.5mm
TR440	Loading protocol from TR440	3	ABR90 × 90 × 65 ×2.5mm
DABM	Loading protocol from DABM	3	ABR90 × 90 × 65 ×2.5mm
ARC3050	Loading protocol from newly designed scheme	2	ABR90 × 90 × 65 ×2.5mm
ARC3050pu	Loading protocol from the newly designed scheme (Push positive direction 50mm)	2	ABR90 × 90 × 65 ×2.5mm

4.3 Results and discussion

4.3.2 Cyclic loading and fatigue behaviour

- **Group BRE**

The results, including strength impairment, ratio and energy dissipation during cyclic loading, were analysed according to EN 12512 (BSI, 2001). Figures 4-17 and 4-18 show the definitions of strength damage and equivalent viscous damping, and the equation for equivalent damping(ν_{eq}) is given below.

$$\nu_{eq} = \frac{E_d}{2\pi * E_q} \tag{4.36}$$

E_d is the energy dissipated per half cycle, and E_q is the available potential energy.

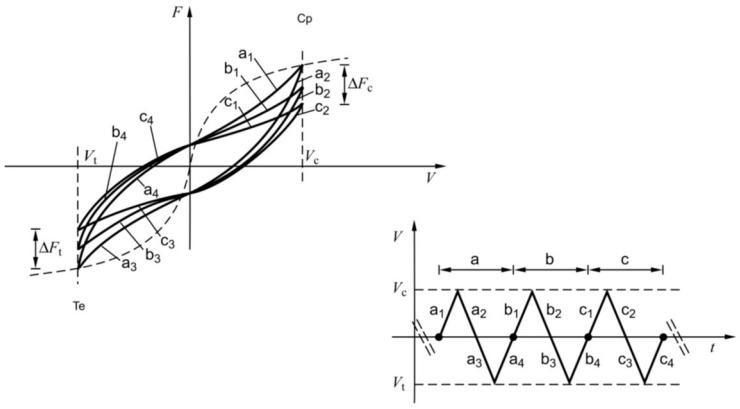

Figure 4-17: Illustration of impaired strength (BSI, 2001)

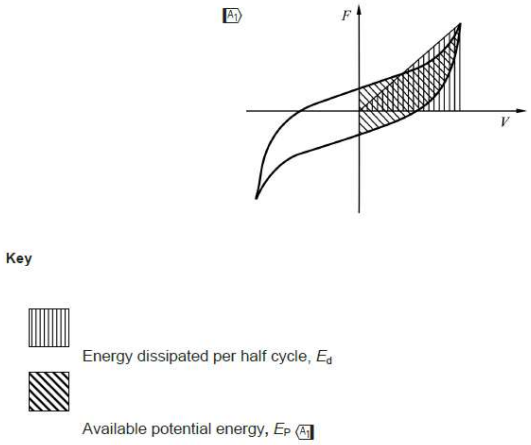

Figure 4-18:Graphical representation of energy dissipation (BSI, 2001)

Figure 4-19 shows all specimens' torque and rotation ratio curves. The results show differences between individual specimens, which may be due to differences in the manual assembly process. The resistance to clockwise torque is better than counterclockwise, which may be because the resistance to clockwise depends primarily on the angle bracket. However, counterclockwise, the fasteners may have contributed more to the resistance.

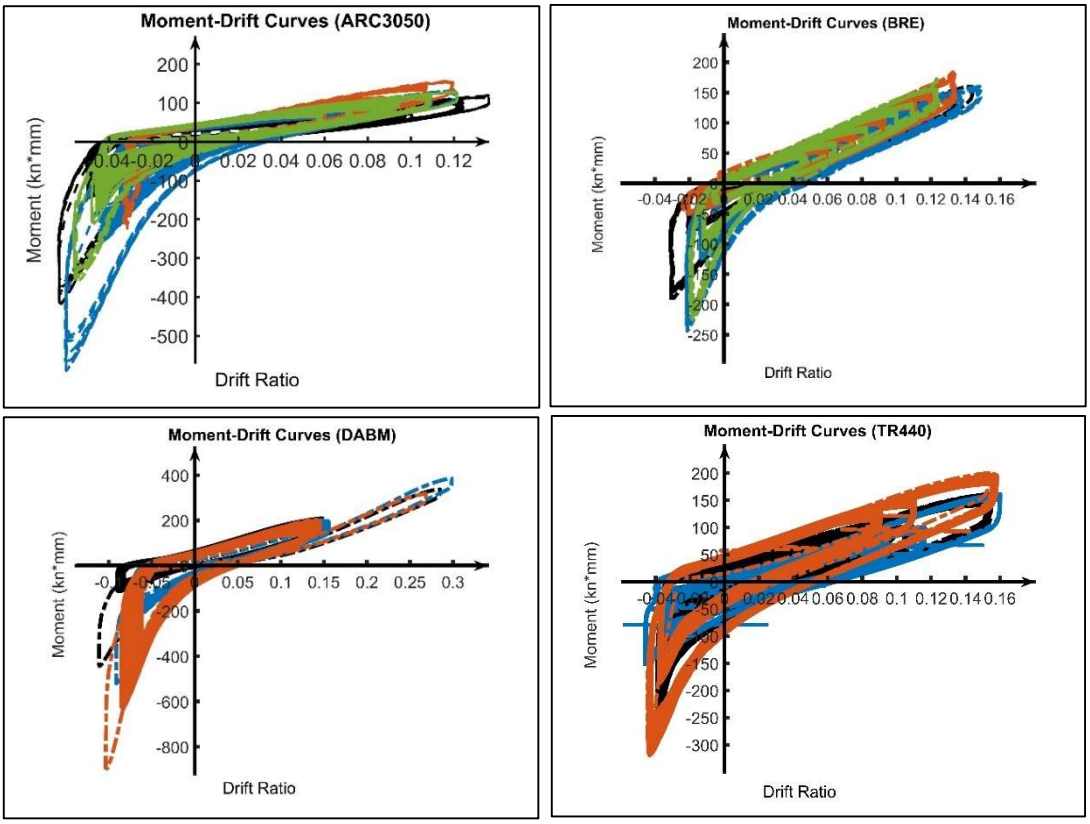

Figure 4-19:Cyclic moment-drift curves for all specimens (a) ARC3050 (b) BRE (c) DABM (d) TR440

Figure 4-20 shows the cyclic loading results for the BRE group, with the cyclic sequences indicated in different colours. The intensity impairment is then shown in Figure 4-21. The intensity decrease in the clockwise direction is smaller than in the counterclockwise direction. The graph shows a similar trend in strength loss in both directions, especially for specimens 1 and 2. It shows that although the main way of providing resistance differs in each direction, they interact with each other rather than working independently.

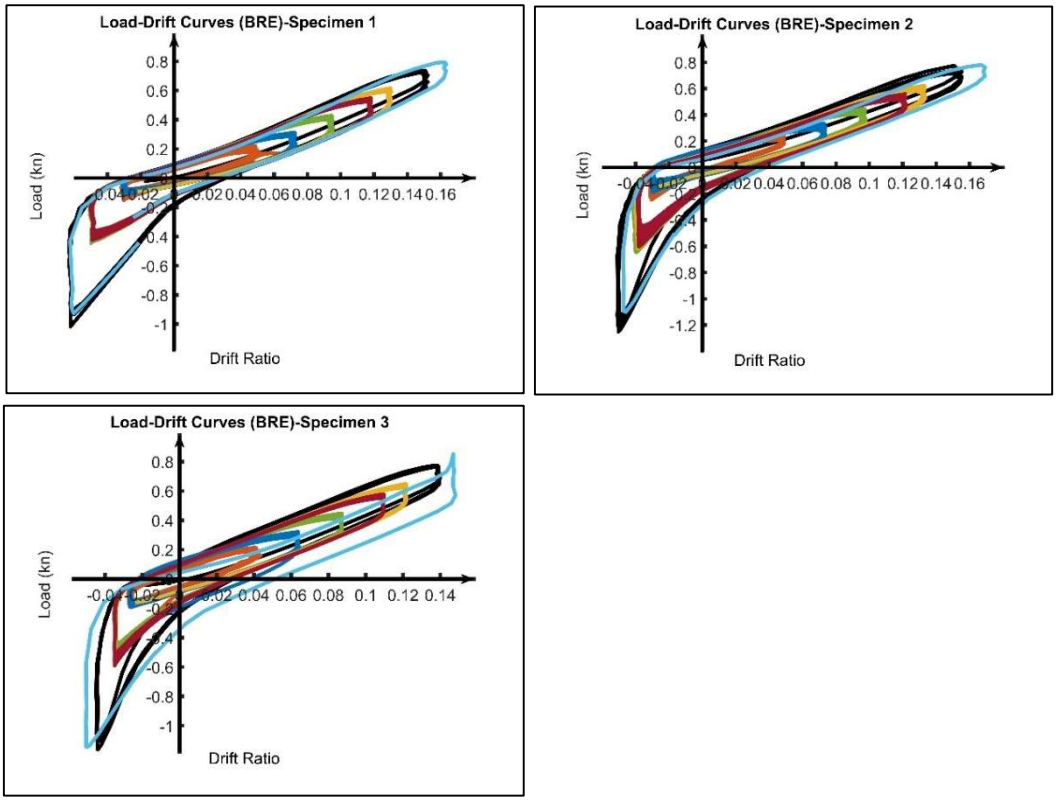

Figure 4-20:Load-drift curves for the BRE group

According to the loading protocol, the amplitude for sequence 4 is 2mm higher than sequence 2. However, the average strength decreased by 41% after the second cycle sequence, slightly higher than after the fourth sequence (36.9%). Similarly, the value for mean strength impairment after the third cycle sequence is 26.2%, which is more than after the first, fifth and sixth, meaning that the strength reduction increases with cycles in the counterclockwise direction when the loading amplitude differences remain low. The same trend can be observed in lines in the other direction, that the maximum impairment of strength values were15.6% and 11.1% after the second and fourth cycles, respectively.

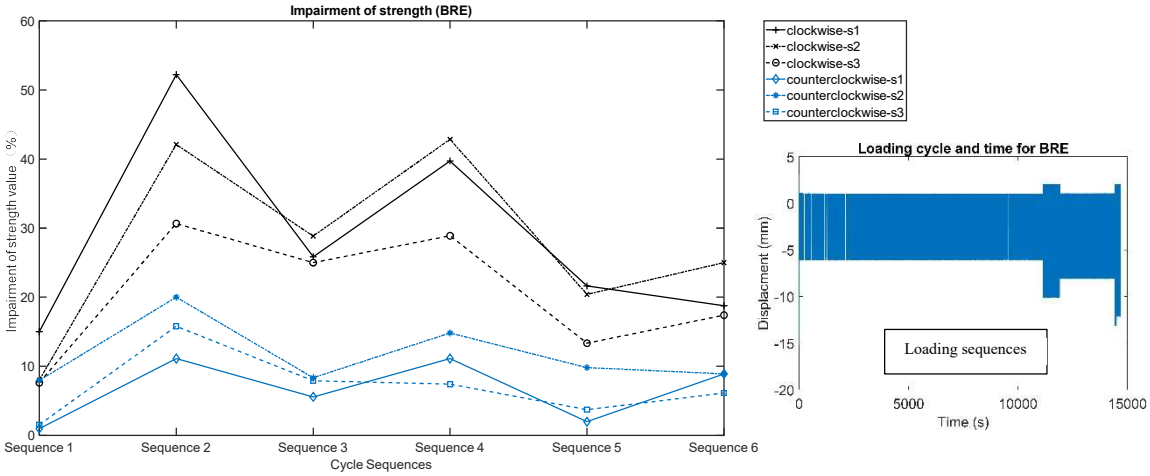

Figure 4-21:Impaired strength of BRE after all sequences

Figure 4-22 shows the relationship between loading displacement, dissipated energy and equivalent damping in the counterclockwise direction. Both dissipated energy and equivalent damping increased with the loading displacement. Thus the highest dissipated energy and equivalent damping value occur at 16cm with an average value of 0.027kn*mm and 8.95%, respectively. The average energy dissipation for this group is 0.013kn*mm, and the average damping ratio is 7.7%.

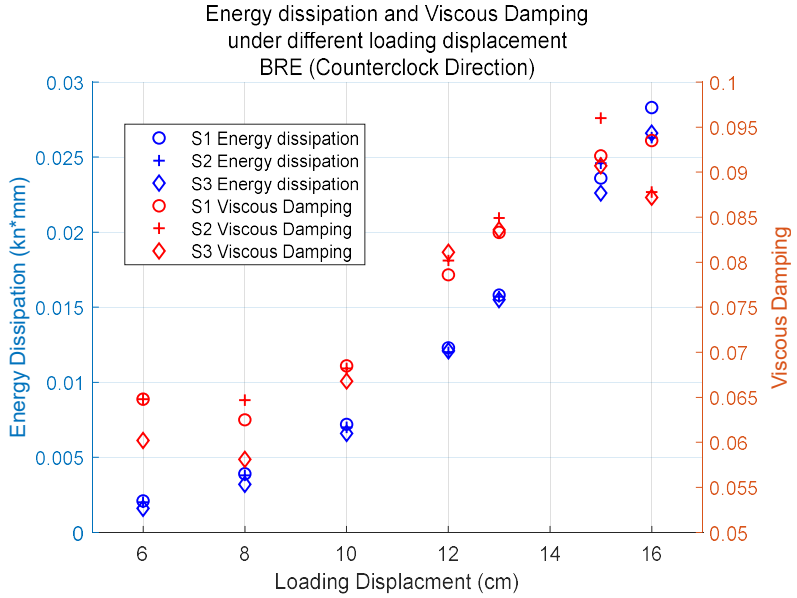

Figure 4-22: Relationship between loading displacement, energy dissipation and equivalent damping for BRE group

Figure 4-23 shows the relationship between loading displacement and energy dissipation in the clockwise direction, indicating that dissipated energy increased with the displacement value. The biggest value occurs when displacement reaches 3cm, and the

average value at this loading displacement is 0.02kn*mm. The average value in this direction is 1.0kn*mm.

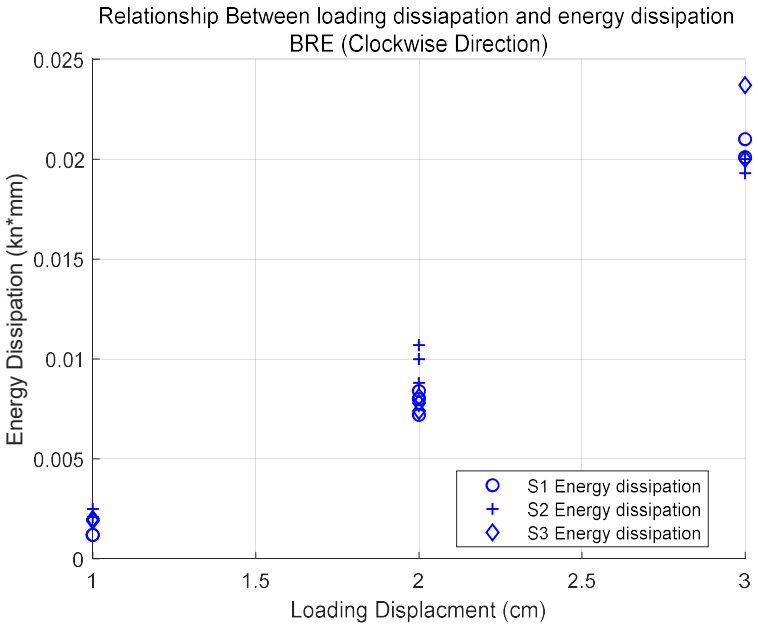

Figure 4-23: Relationship between loading displacement and energy dissipation BRE group in the clockwise direction

Figure 4-24 shows the relationship between loading displacement and equivalent damping in the clockwise direction for the BRE group. The damping ratio shows the same trend as the dissipated energy value in this direction, in which the damping ratio increased with the displacement. Although the loading displacement is significantly smaller than counterclockwise, the highest damping ratio in this direction is much higher than in the counterclockwise direction, with the most significant average of 94% occurring at 3mm loading displacement. The average damping at 1mm and 2mm loading displacement is 28.7% and 46.9%. Additionally, the line in this figure shows that the damping increased when loading displacement reached 3mm the second time for specimen 1, and this rule also applied to the other two samples. Considering that the dissipated energy did not change significantly in Figure 4-23, the results mean that the energy required to make the same displacement decreased after cyclic loading, proving the resistance strength was reduced.

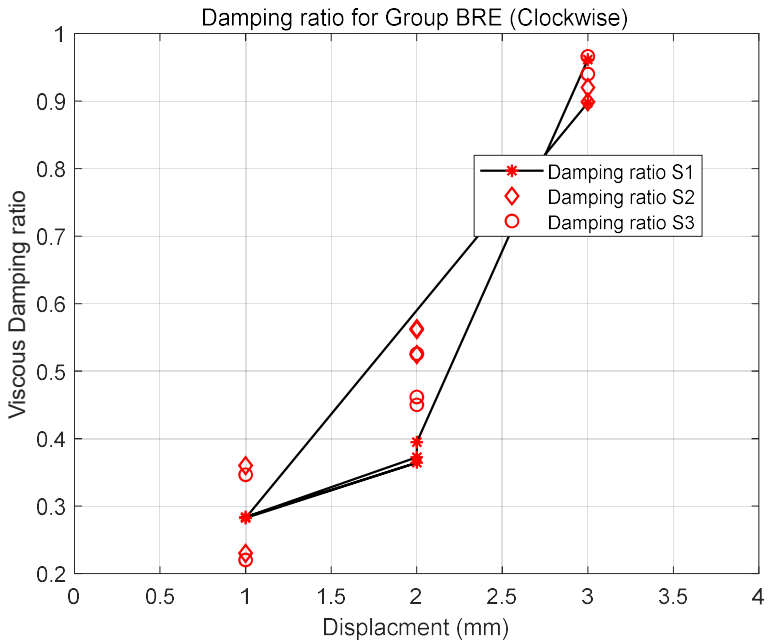

Figure 4-24: Relationship between loading displacement and equivalent damping BRE group in the clockwise direction

Figure 4-25 shows the damping ratio for the whole cycle under different loading amplitude. The damping ratio changed with loading amplitude, and a significant increase can be seen when the amplitude increased higher than 2mm. Most values lay between 0.1 and 0.16. The values at an amplitude of 7mm are lower than other amplitudes, with an average value of 4%. The average damping ratio for the BRE group during the cyclic load is 10.8%

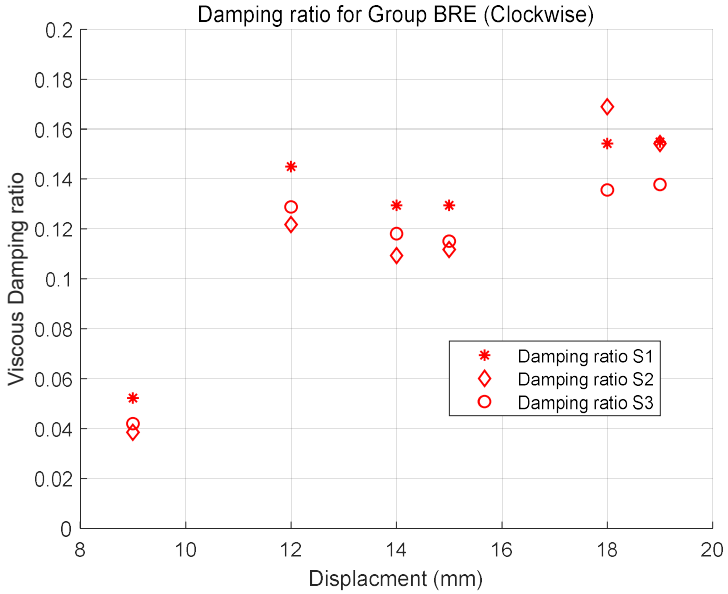

Figure 4-25: Relationship between damping ratio and loading amplitude

- **Group ARC3050**

Figure 4-26 plots the cyclic load and rotation ratio curves for the ARC3050 group, with the cyclic sequence, plotted in different colours. Then, Figure 4-27 shows the strength damage of each specimen after cyclic loading. The average energy reduction in the clockwise direction is approximately 0.13kn, while the other directions show a value of 0.05kn. The largest average reductions occur in clockwise and counterclockwise directions after the 2nd and 5th sequences. The clockwise loading amplitude for sequence 2 is 2 mm smaller than that of sequence 1, but the number of cycles is 75 times greater, resulting in a slightly higher average reduction (0.07kn) than that of sequence 1. Similar results can be observed in the clockwise direction. Although the loading amplitude of the 5th sequence is 1 mm smaller than that of the 7th sequence, the intensity reduction is 2.4 times that of the 7th sequence, which may also be a result of the increased number of cycles. However, this rule does not apply when there is no significant difference in the number of cycles between sequences, for example, the 4th and 6th sequences in Figure 4-27.

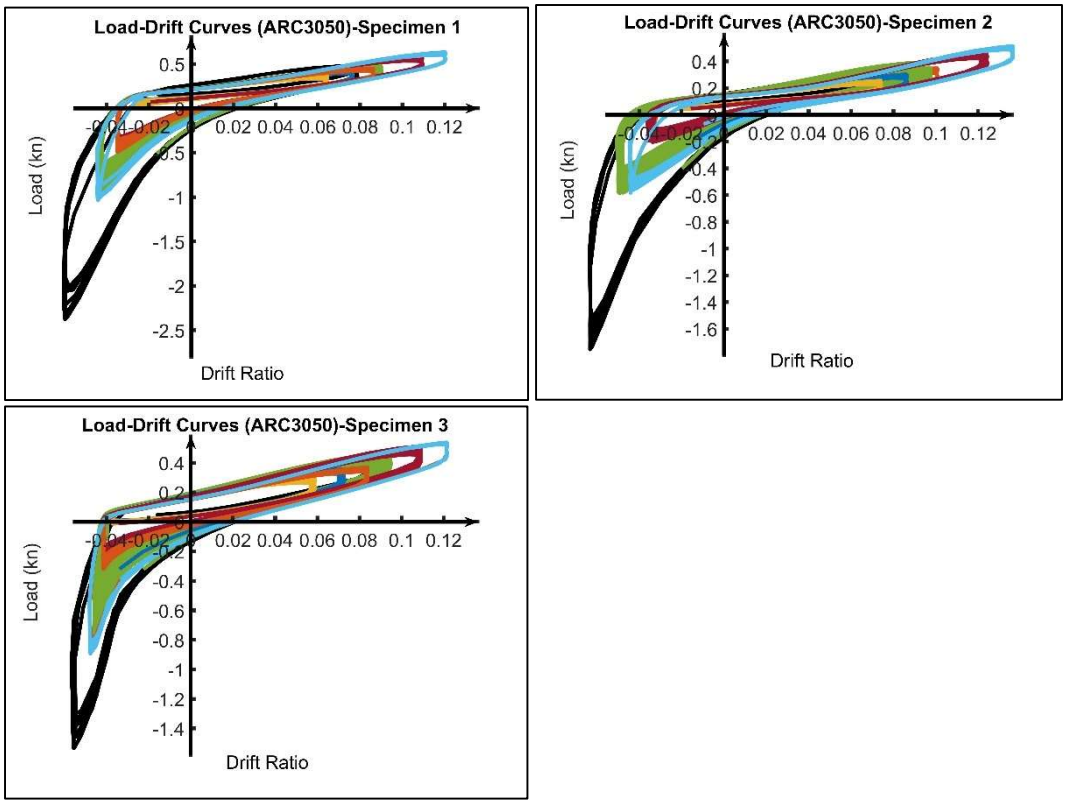

Figure 4-26: Load and Rotation ratio for all specimens of BRE group

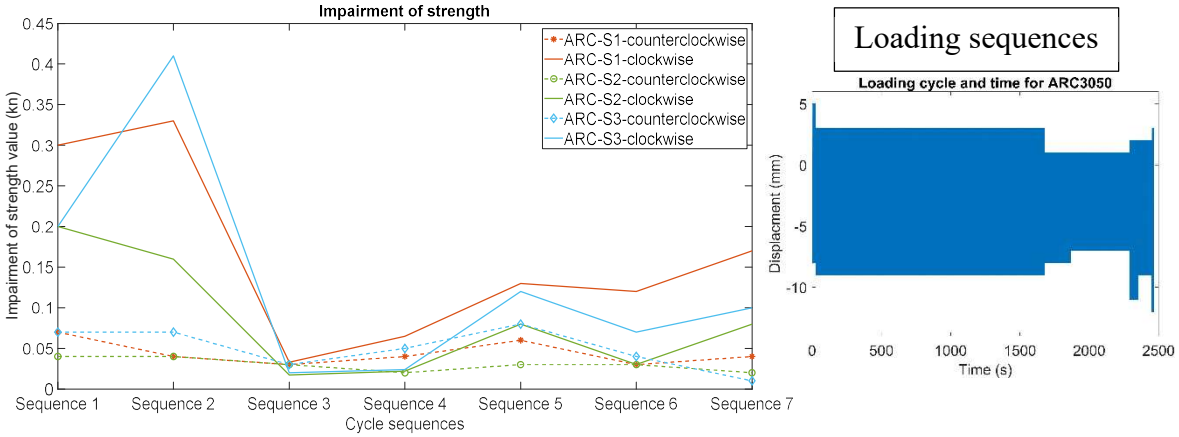

Figure 4-27: Impairment of strength for ARC3050 after all sequences

The dissipated energy value in the counterclockwise direction for specimens in group ARC3050 is shown in Figures 4-28. Although the differences between samples are significant, all samples' values increased with the loading displacement. The maximum value occurs at 12mm displacement, with an average of 0.008kn*mm for three specimens. Figure 4-29 shows the equivalent damping for this group in the counterclockwise direction. The damping ratio also increased with the displacement, with the highest average value of 7.51% at 12mm. The lowest value occurred at 7mm, with a value of 0.66%.

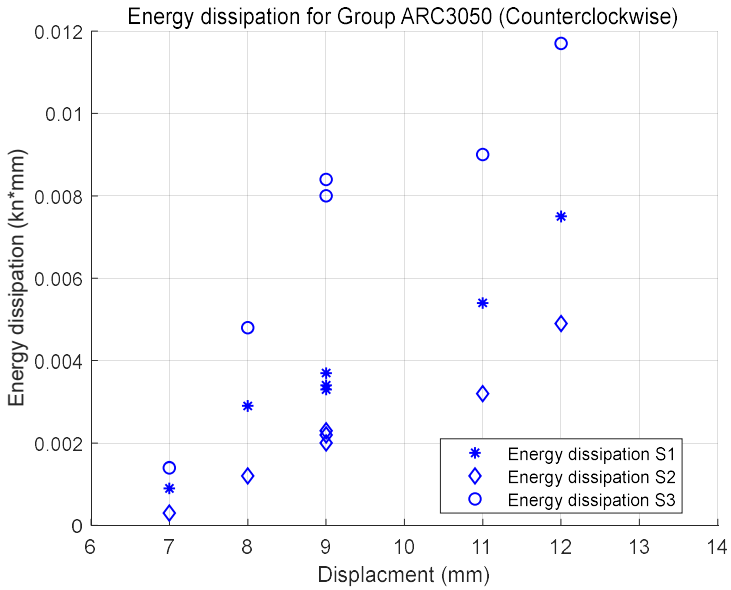

Figure 4-28:Energy dissipation of ARC3050 group

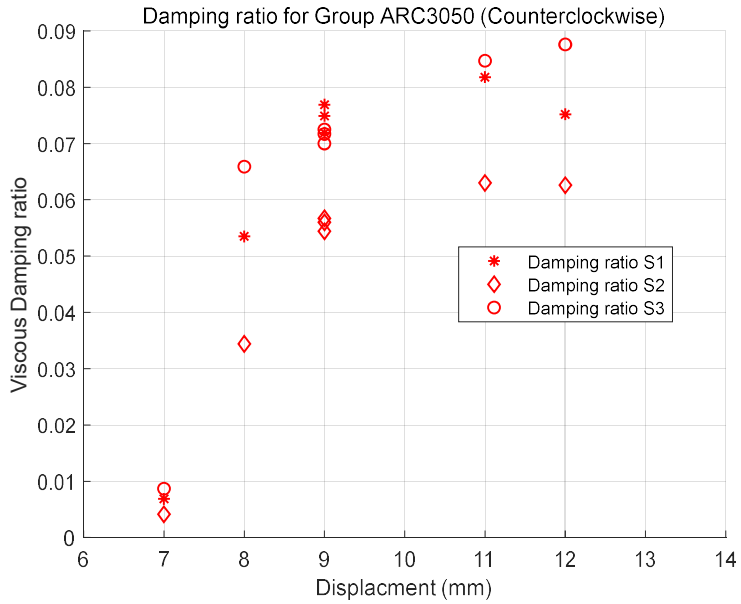

Figure 4-29:Equivalent equivalent damping for ARC3050 group (Counterclockwise)

Figures 4-30 and 4-31 show this group's dissipated energy and equivalent damping in the clockwise direction. Both energy dissipation and equivalent damping increased with the displacement. The maximum average dissipated in this direction is 0.032kn*mm at 5mm, and the maximum average damping is 62%.

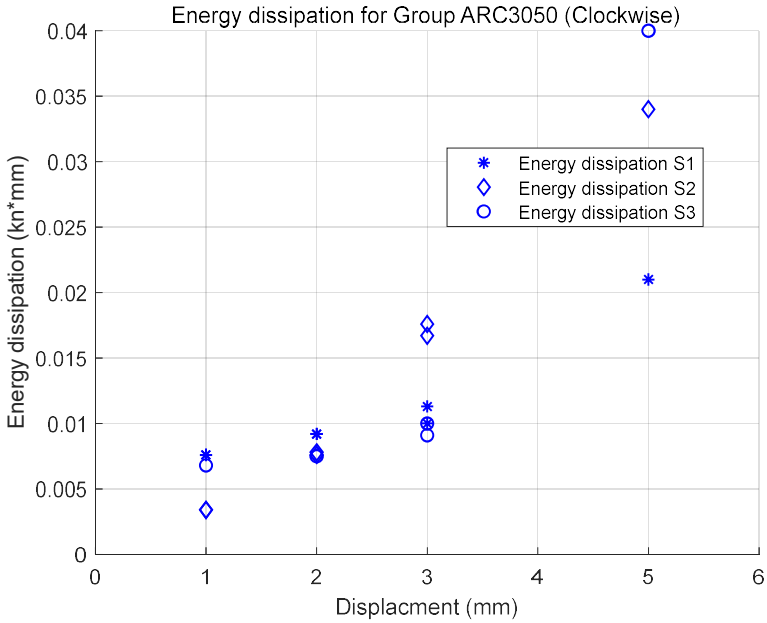

Figure 4-30:Disspated energy of ARC3050 group (Clockwise)

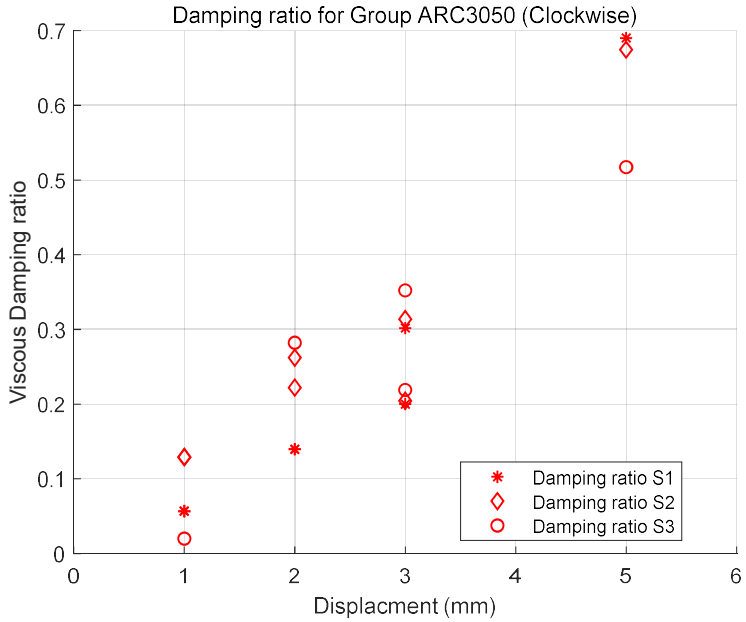

Figure 4-31:Equivalent damping of ARC3050 group (Clockwise)

Figure 4-32 shows the dampings for the whole cycle, and the values vary with amplitude but do not always increase with the loading amplitude. Most values in this group are within 12% and 8%, but the values at 15mm amplitude for all specimens are higher than others, with an average value of 12.7%. The smallest values are at 8mm amplitude, an average value of 6.2%.

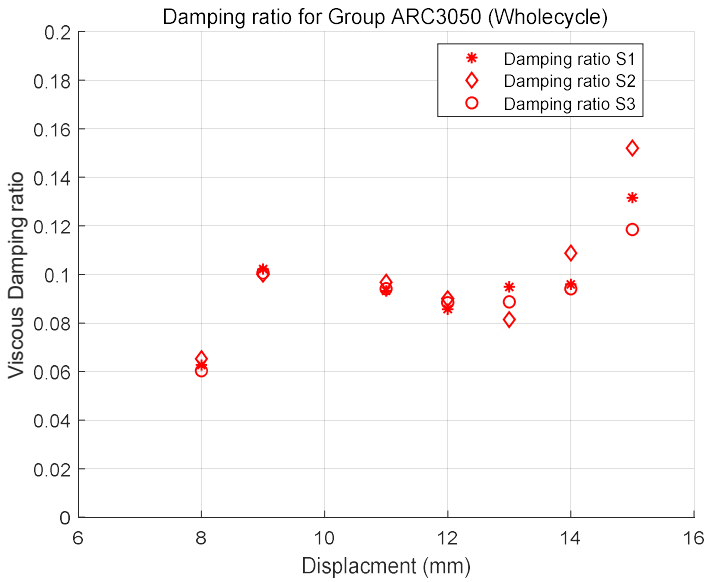

Figure 4-32:Equivalent damping of ARC3050 group (Wholecycle)

- **TR440 group and DABM group**

Figure 4-33 shows the different sequences of the latter group TR440 and DABM. Unlike the BRE group or the ARC3050 group, these two groups have fewer cyclic sequences but more cycles in each sequence. Figure 4-34 shows the strength impairment of TR440. The average intensity reduction in the clockwise direction is 0.14kn, approximately 2.8 times greater than in the other directions. Regarding the DABM group, the average intensity decrease is 0.57kn in the clockwise direction and 0.14kn in the counterclockwise direction.

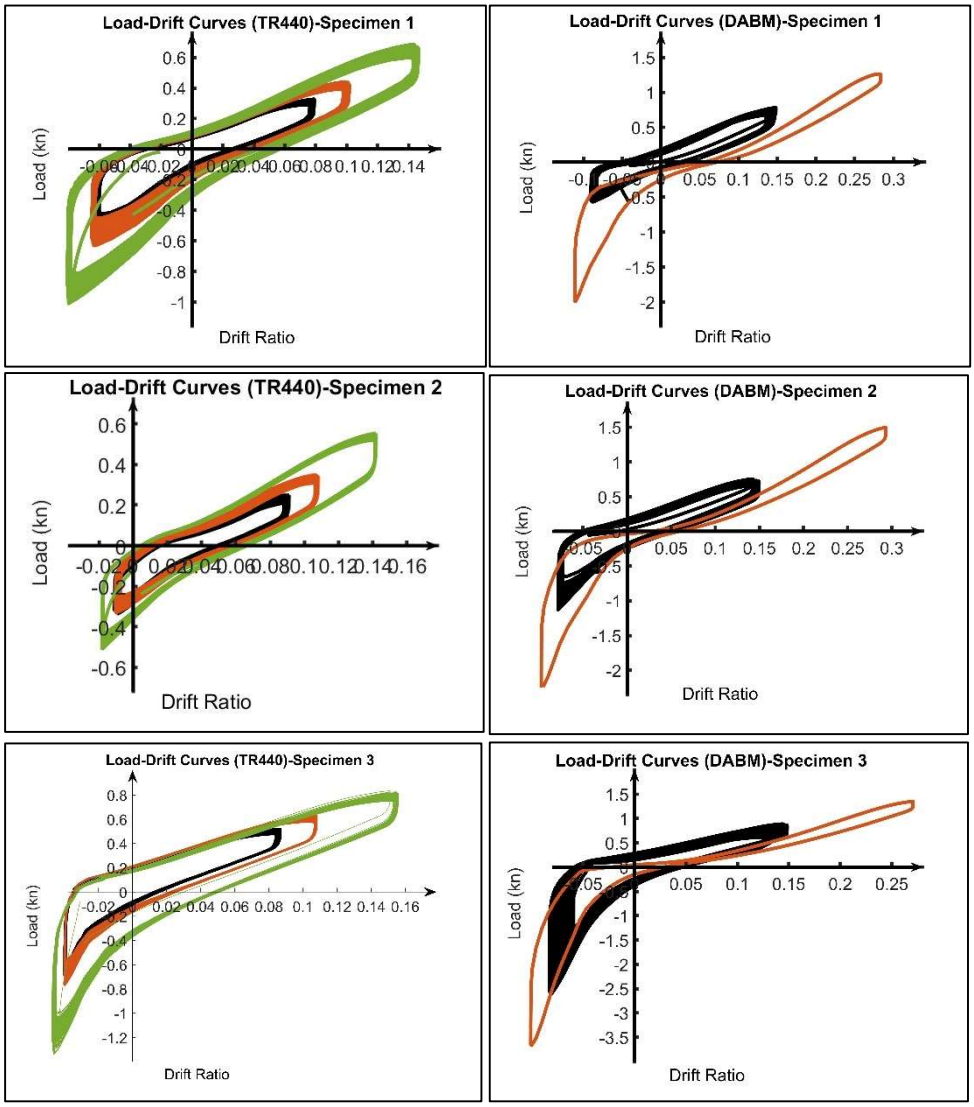

Figure 4-33:Load and drift curves for all specimens of TR440 and DABM

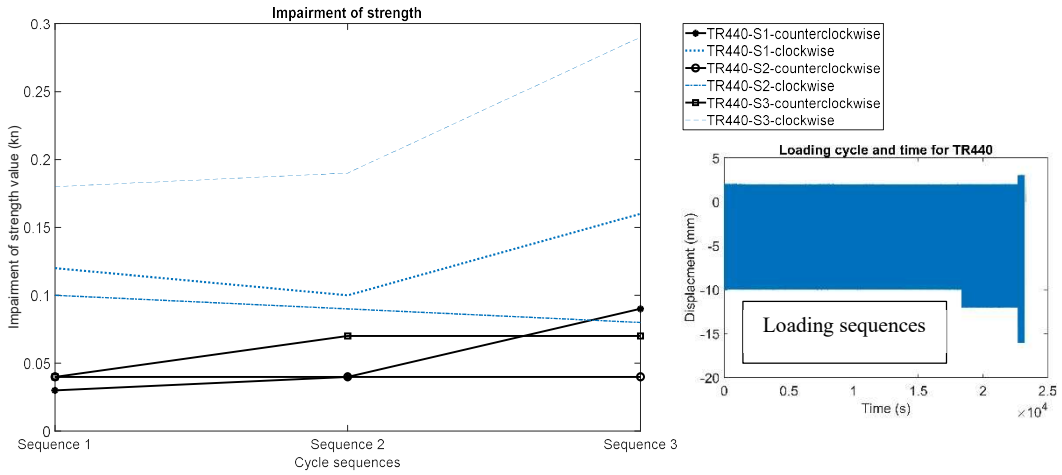

Figure 4-34: Impaired intensity of TR440 after all sequences

Figure 4-35 shows the dissipated energy and equivalent damping for TR440 in the counterclockwise direction. Those values increased with the loading displacement, and the maximum dissipated energy is 0.014kn*mm in 16mm displacement. The average dissipated energy at 10mm, and 12mm is 0.004 kn*mm and 0.007 kn*mm. In terms of damping ratio, the average value at 10mm, 12mm and 16mm are 4.5%, 5.3% and 6.7%, respectively.

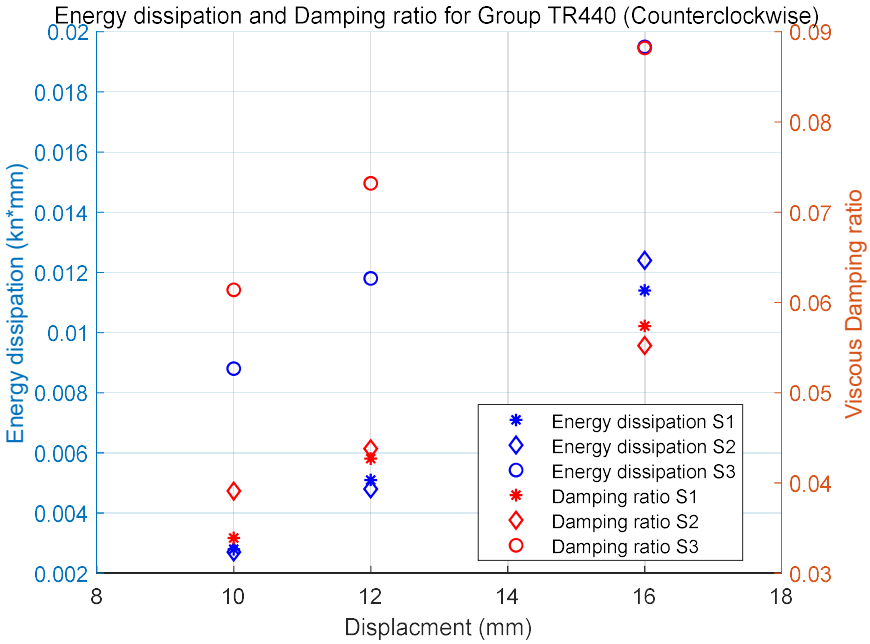

Figure 4-35: Energy dissipation and equivalent damping for group TR440 in the counterclockwise direction

Figures 4-36 and 4-37 show the energy dissipation and damping ratio for TR440 in a clockwise direction. The average energy dissipation for three specimens at 3mm is 0.024kn*mm. The dissipated energy and damping ratio at 3mm is higher than 2mm. Figure 4-37 shows that the damping ratio increases in the second 2mm loading sequence than in the first loading sequence. The average damping for 1st 2mm, 2nd 2mm, and 3mm is 37.6%,52.6% and 61.8%, respectively.

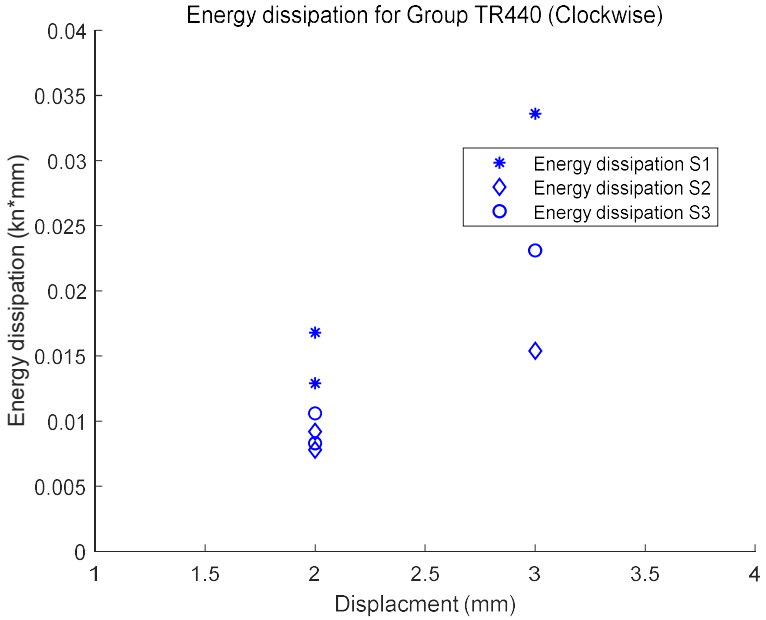

Figure 4-36: Energy dissipation for the TR440 group in the clockwise direction

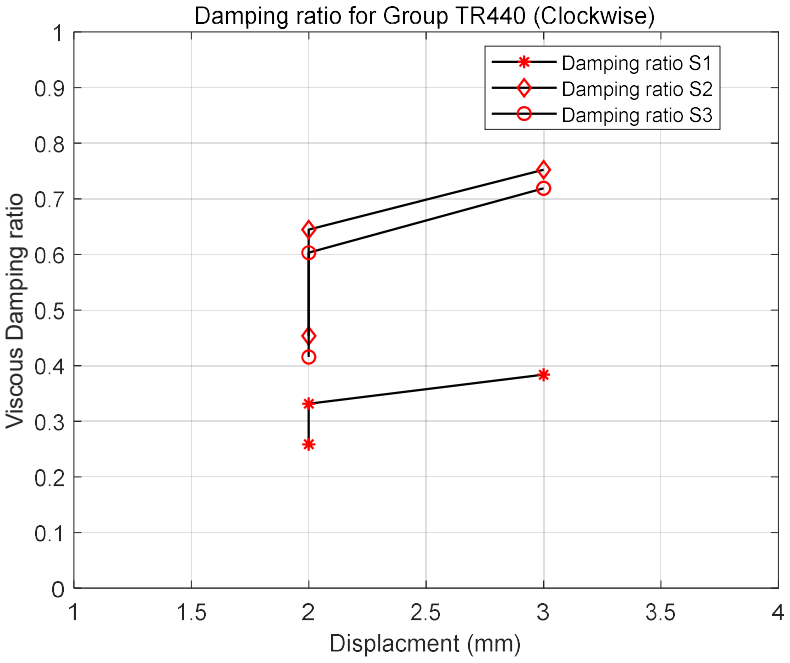

Figure 4-37: Equivalent damping for the TR440 group in the clockwise direction

Figures 4-38 and 4-39 show the dissipated energy and equivalent damping for group DABM in two directions. The average dissipated energy in 16mm, and 29mm is 0.015 and 0.049kn*mm, respectively, in the counterclockwise direction. The damping ratio in this direction is 5.3% and 7.5% at 16mm and 29mm. Clockwise dissipated energy values are 0.031 kn*mm and 0.045 kn*mm at 3mm and 5mm. Damping ratios in this direction are significantly higher than in the counterclockwise direction, with 27.4% and 36.4% values at 3mm and 5mm loading displacement.

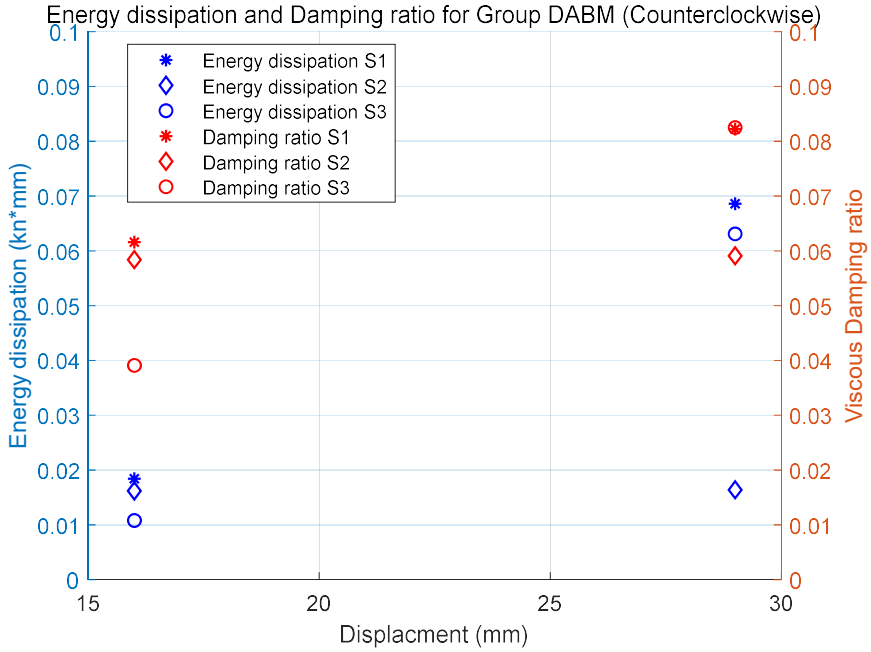

Figure 4-38: Dissipated energy and equivalent damping of the DABM group (Counterclockwise)

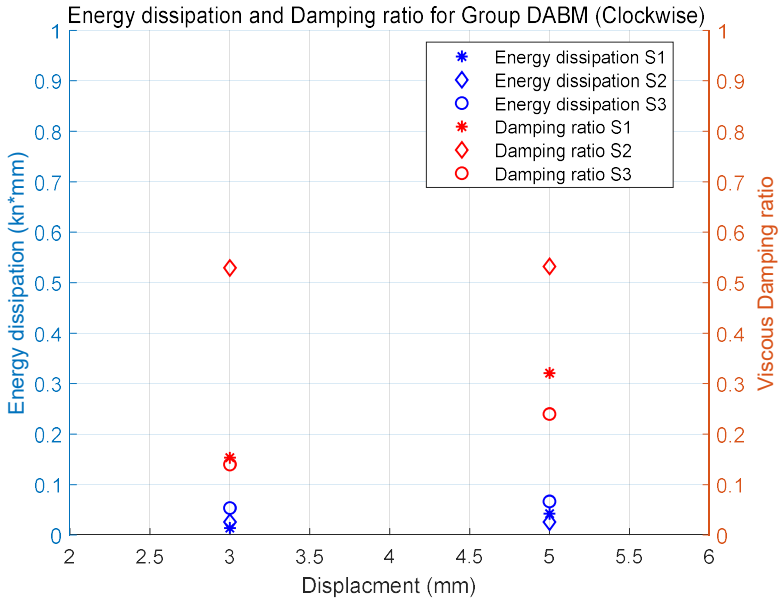

Figure 4-39: Dissipated energy and equivalent damping of the DABM group (Clockwise)

Figure 4-40 shows the Damping ratio for whole connections in group TR440 and DABM. The values are increased with loading amplitude for each group. The average values for TR440 in three different loading sequences are 12.3%, 13.1%, and 14.1%, and for group DABM, the average damping for 19mm and 31mm is 11.1% and 13%, respectively.

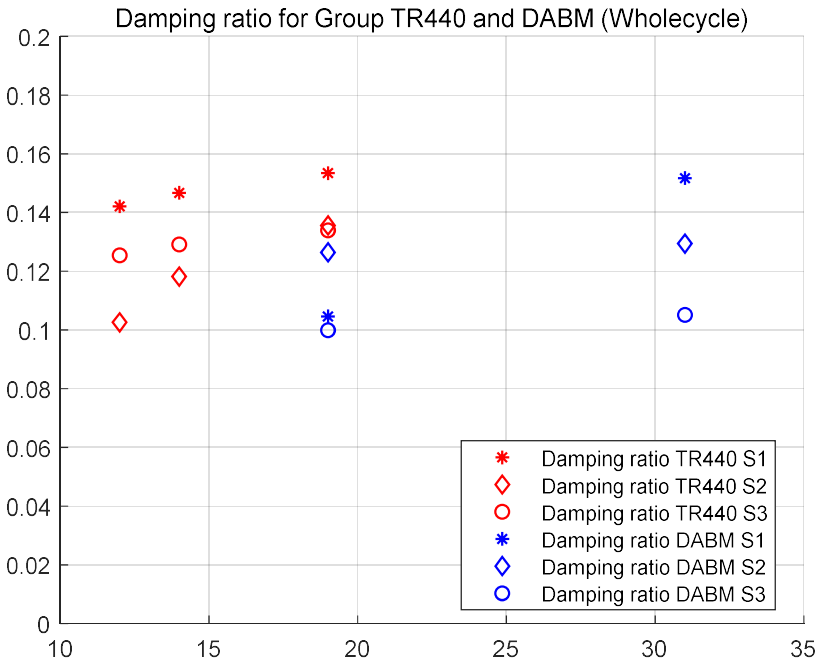

Figure 4-40: Equivalent damping for the TR440 and DABM groups (Whole).

- **Comparison**

Figure 4-41 shows the strength comparison damage for the four groups. The group with the most significant decrease in mean and maximum strength was DABM. in the clockwise direction, the mean strength decrease for the TR440 group was approximately 26% of DABM, followed by ARC3050 (21%) and BRE (13%). In the other direction, the strength reduction for DABM was about 22% of that for clockwise. For TR440, ARC3050, and BRE, the average strength reduction in the counterclockwise direction was about 36%, 29%, and 20% of the DABM.

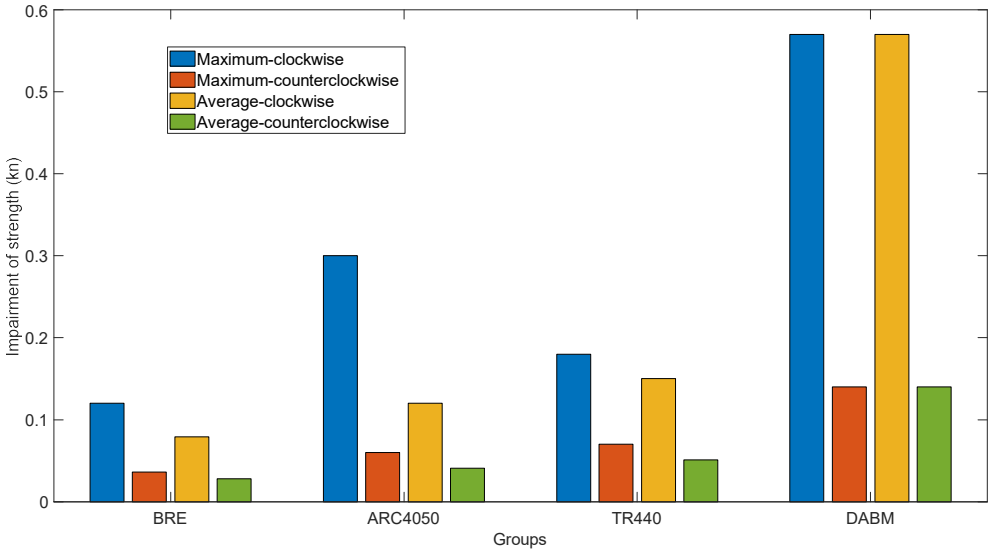

Figure 4-41: Impairment of strength of four groups

In the case of equivalent damping, the mean damping ratio for TR440 is 13.19% which is the highest among the groups, followed by the DABM (11.95%), and BRE(10.8%) and ARC3050 (9.4%). The maximum value for all those groups occurred at the maximum amplitude, and for group BRE, it is 14.9% which is 0.86% higher than that of TR440 (14.04%). DABM and ARC3050 have similar maximum values of 12.87% and 12.73%, respectively. In the counterclockwise direction, the differences between groups in maximum value are not significant as in the clockwise direction. The maximum values in the counterclockwise direction for BRE, TR440, DABM and ARC3050 are 8.95%, 6.69%, 7.46% and 7.51%. The clockwise damping is significantly higher than the counterclockwise direction and much more sensitive to the loading displacement. The maximum values for those groups vary from 36.4%(DABM) to 93.8% (BRE).

4.3.2 Residual of stiffness after cyclic test

This research's simplified angle bracket connections can be considered moment connections (Figure 4-17). Those connections significantly contribute to the rotation limits of the whole joint(Beg et al., 2004). Including these in design is often helpful in representing the moment-rotation curve analytically, as in Figures 4-42. The Eurocode 3 defended the rotation stiffness according to the moment-ration curve in Figure 4-43 (BSI, 2005), where S_j is the rotational stiffness at the rotation angle $Ø_{ed}$, and $S_{j,ini}$ is the initial rotation stiffness which indicates the elastic range of the design moment-rotation characteristics. $Ø_{Cd}$ is the rotation capacity of the Joint. Eurocode 3 also provided a calculation method for rotational stiffness and capacity, but Stoddart suggested(Stoddart, 2012)that experimental test data can get a more accurate moment-rotation curve for moment-rotation characteristics definition. Both Eurocode 3 and Eurocode 8 give the rotational limitation of joint, but they are particular for concrete or steel connections between column and beam rather than timber joints. Eurocode 8 provided the inelastic rotation limits for beams and columns under dimensionless axial load lower than 0.30, the brace in compression, tension, and reduced beam section (Table 15). Eurocode 3 gives the rotation capacity for welded beam-to-column connection, which should be not less than the value given by the following expression:

$$\emptyset_{Cd} = \frac{0.025 h_c}{h_b} \qquad 4.33$$

where: h_b is the depth of the beam; hc is the depth of the column.

Moreover, the rotation capacity is at least 0,015 radians for an unstiffened welded beam-to-column joint. Although those capacity regulations are not mainly designed for angle bracket timber connection, they can still be a reference for this research.

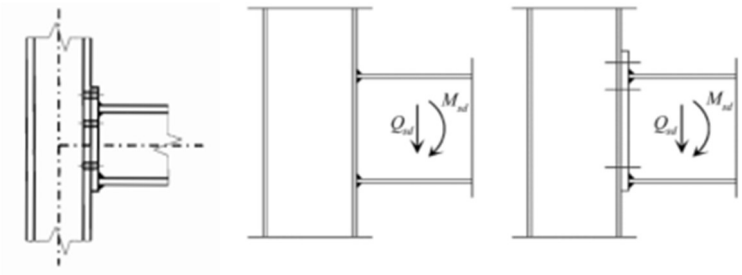

Figure 4-42: Moment connections and loading mechanisms

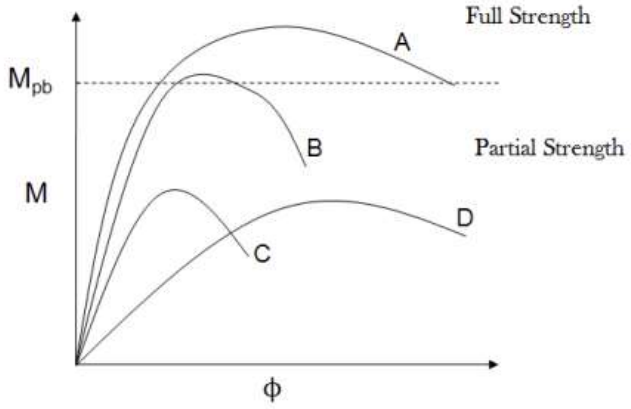

Figure 4-43: moment- rotation curves for different beam-column joints (Faella et al., 2000)

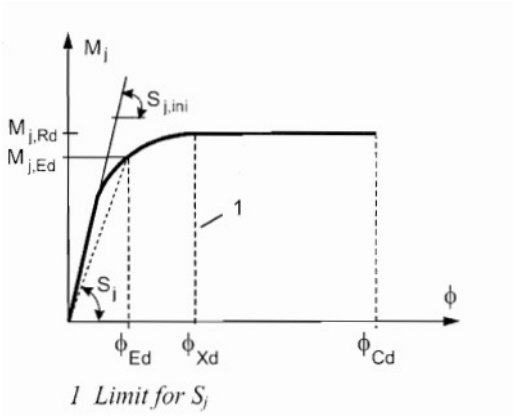

Figure 4-44: Rotation stiffness and rotation capacity definition from Eurocode 3.

Table 16: List of the rotational capacity from Eurocode 8

Plastic rotation capacity at the end of beams or columns with dimensionless axial load not greater than 0.30

Class of cross section	DL(Damage Limitation)	SD(Significant damage)	NC (Near collapse)
1	1.0 Θ_y	6.0 Θ_y	8 Θ_y
2	0.25 Θ_y	2 Θ_y	3 Θ_y
Θ_y: Chord rotation capacity			
Axial deformation capacity of braces in compression			
1	0,25 Dc	4,0 Dc	6,0 Dc
2	0,25 Dc	1,0 Dc	2,0 Dc
D_c: axial deformation of the brace at buckling load			
Required rotation capacity of reduced beam sections, RBSs (in radians)			
	0.01	0.025	0.04

1) Monotonic load in the counterclockwise direction

As the limitation of the testing equipment, the monotonic loading stops at 50mm displacement. Therefore the failure mode of the whole system is not observed. Figure 4-45 shows no significant cracks on timber specimens or buckling of steel angle bracket for group BRE, TR440, DAMB and ARC3050after the cyclic and monotonic process, but the nails near the conner were pulled out a bit. The upper part of the spacemen has a rotation, and a gap in the joint appears (Figure 4-46).

Figure 4-45:Observed deformation of the BRE group: the pegs are pulled out a little

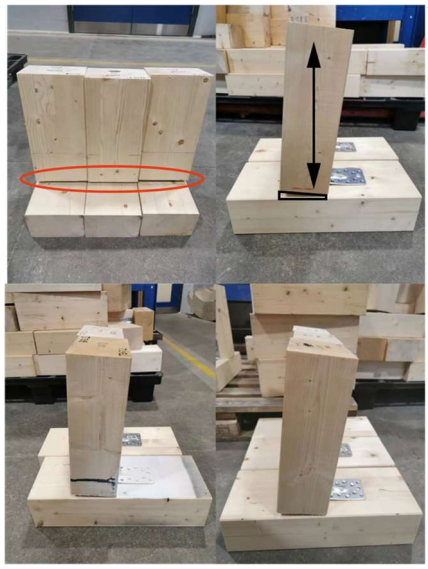

Figure 4-46:Observed deformations DAMB (top left), ARC3050 (top right), TR440 (bottom left), and BRE

Figure 4-47 shows load and rotation curves for different groups. Although after 50mm monotonic load, the samples in group Mop did not reach the yield point, and the rotation ratio is up to 0.2, which seems significantly higher than those regulations. Compared with other groups after cyclic tests, the stiffness decreased after cyclic load, and the rotation ratios were over 0.3. Figure 4-48 shows the percentage load required for the other four groups against the expected (MOP group) for different rotation ratios. After cyclic, the average required load decreased to 35.08%(DABM) and 47.01% (BRE). It shows that the required load for Group DABM is around 10% lower than other groups. For group TR440, the percentage remains 46.57% which is 2.59% higher than the Group ARC3050.

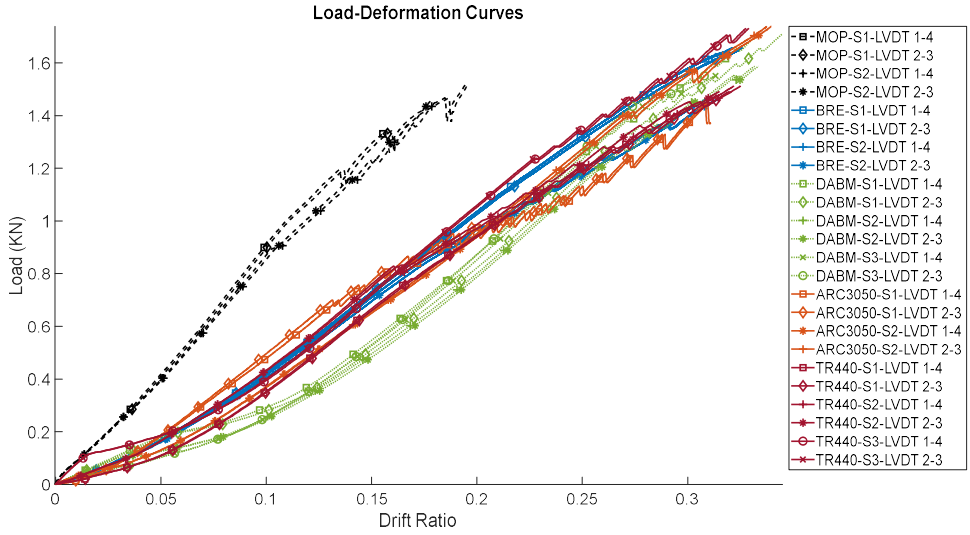

Figure 4-47: Load-Displacement Curves for different groups

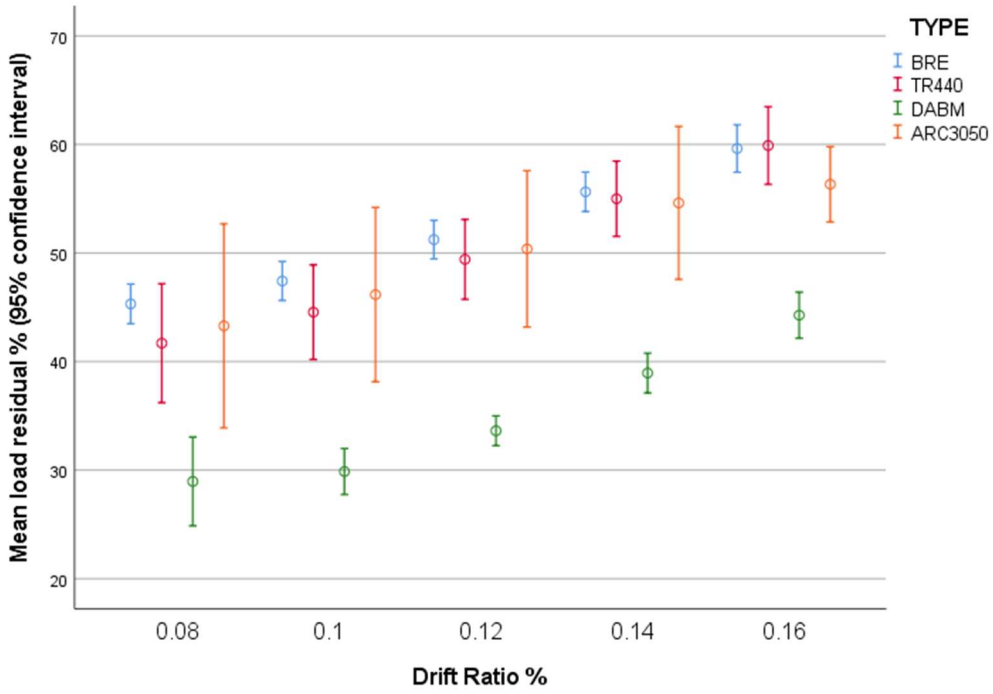

Figure 4-48: Residual of load for different group

By calculating rotation stiffness at rotation ratios from 0 to 0.05 and 0.05 to 0.1, the groups' stiffness is shown in Table 16. The stiffness grows with the rotation ratio for all groups, which may result from the cyclic load that has made the nail loosen, causing the stiffness reduction at an early stage, but when the loading displacement increase, the plate touches the nails again, leading to the stiffness increases.

Table 17:Stiffness at different rotation ratios

Rotation ratio Range	*0-0.05*	*0.05-0.1*
BRE	0.22 Mpa	0.3Mpa
DABM	0.29 Mpa	0.4Mpa
TR440	0.15Mpa	0.33Mpa
ARC440	0.24Mpa	0.36Mpa

2) Monotonic load clockwise direction

Group Mopu, as the control group, in which the specimens were pushed clockwise for 50 mm to compare with the groups after cyclic load: BREpu and ARC3050pu. Compared with samples loaded counterclockwise direction, more nails were pulled out, and the angle bracket was bent. The connector condition before and after unloading is shown in Figures 4-49.

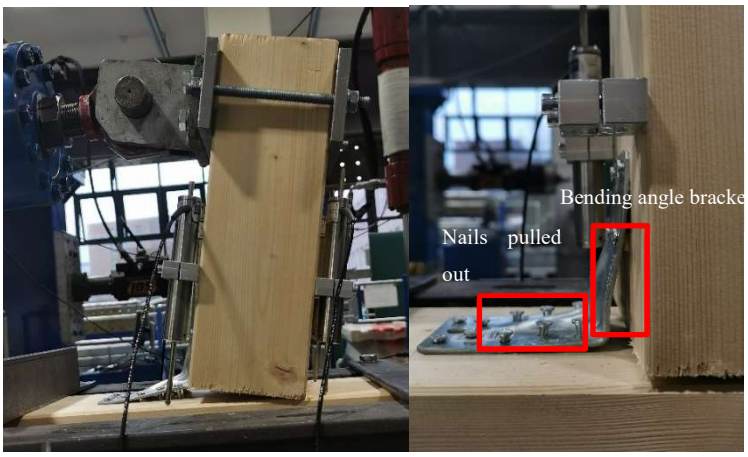

Figure 4-49: Photo of connection after positive direction loading

Figure 4-50 shows the relationship between clockwise directed loading and rotation ratio. When the rotation ratio is below 0.15, loadings required for group BREpu and ARC3050pu to make the same displacement are lower than group MOpu. This condition is more significant when the rotation ratio range is under 0.05, and the reason may be the same as mentioned earlier: the cyclic loading caused the loosening of nails. However, the rule does not exist when the rotation ratio is higher than 0.2, indicating that the influence of cyclic loading is not apparent after this, which is probably because the resistance capacity of the latter mainly depends on the angle bracket. The cyclic loading mainly influences fasteners rather than angle brackets. Moreover, there are no precise patterns between BREpu, and ARC3050pu, meaning that the influence of cyclic loading sequences on the resistance

capacity of the clockwise loading direction is not as significant as in the counterclockwise direction.

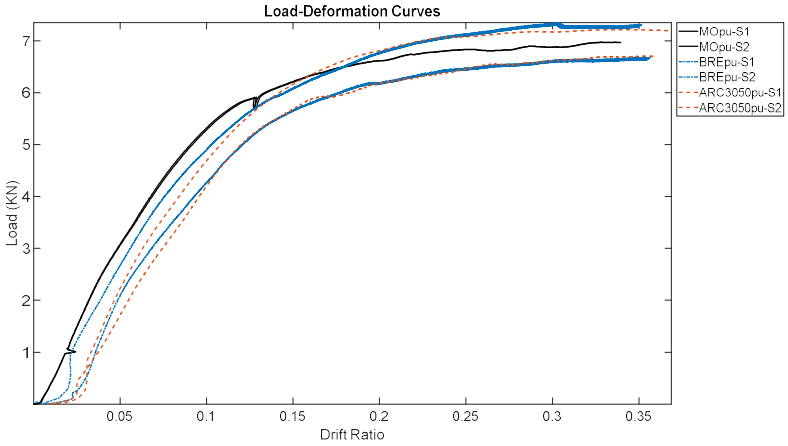

Figure 4-50:Loading-Drift curves for each group

4.4 Summary

This chapter begins with a description of the connection system for angle bracing of engineered timber structures and points out the advantages of this connection method. However, the review shows that most research has focused on cyclic performance under shear loading. Timber structures need to have some ductility to provide excellent seismic performance. Structures using timber infill walls must be somewhat elastic to provide excellent seismic performance and, therefore, may sacrifice stiffness, resulting in challenges when the structure is subjected to wind loads. Therefore, this chapter tests timber connections for angle bracing under wind loads.

Then, this chapter reviewed the cyclic testing method under wind load from different codes. There are more than eight testing sequences for wind fatigue analysis of building structures. Those testing guidances originated from research on roof fasteners in heavy wind regions. Compared with other fatigue testing methods such as ASTM E2126 and EN 12512(BSI, 2001), the advantage of these methods is that they can better represent the characteristics of cyclic wind pressure. However, some of those methods are complex and need hours of testing time. Thus, this research combines the CFD analysis results of Chapter 3 with the rain-flow counting method to develop a new test method for the timber-filled wall system.

After analyzing the results, the following points can be concluded from this study.

- The comparison of experimental results for different groups shows that similar degradation of joint stiffness to BRE and TR440 can be obtained with the new test method but with fewer cycles. Figure 4-51 indicates that the total testing time for DABM and TR440 is more than 6 hours, and even BRE testing requires around 4 hours per specimen. However, the testing time for the new method only needed less than one hour, significantly improving efficiency. Furthermore, the new test method is reproducible in different regions provided that sufficient wind data is available, indicating that applying the new design loading sequence is feasible to analyze the fatigue behaviour of wall connections under along-wind pressures.

- Moreover, testing results also show that during the 50-year return period, the stiffness reduction of connections could be up to 64.2% under the DABM method. In terms of the new method (ARC3050), the drop could be around 56.02%. Consequently, the strength of the connector is significantly affected by wind load, which may further influence the serviceability of in-fill wall systems.

- Furthermore, the equivalent damping ratio for different groups is also analysed, revealing that the values vary with loading amplitude. Meanwhile, the hysteresis results in clockwise and counterclockwise directions, suggesting that the mechanism of resisting load differs. Additionally, the strength reduction in the clockwise direction is higher than that in the counterclockwise.

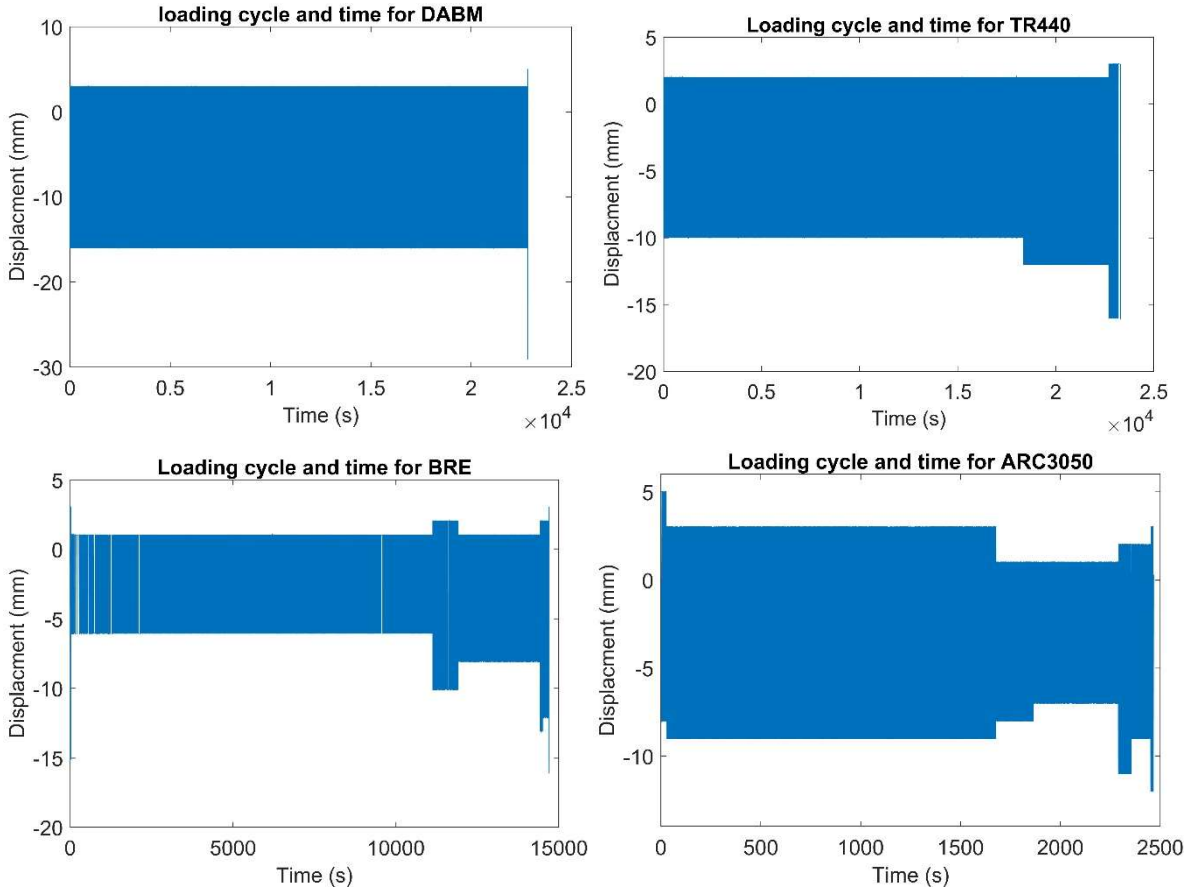

Figure 4-51: Loading cycle and testing time for different groups

Chapter 5. Effect of building height on wood joint fatigue

5.1 Introduction

Chapter 3 shows that the wind speed increase with the building height. This chapter aims to assess the fatigue behaviour of timber connection with angle brackets at different building heights under different levels of wind velocities with the newly developed testing scheme in Chapter 4. As the wind velocity change with height, the value at 10m, 30m and 60m are simulated based on the method introduced in Chapter 2. Table 17 shows the mean 40% to 100% extreme wind load at each building height, and Figure 5-1 illustrates the simulated dynamic wind load at these three heights. Then, Abaqus CFD has applied to analyse the wall panel vibration behaviour. The displacements for the test lab under 100% extreme wind load at different levels is shown in Figure 5-2. The loading sequences and schedule are shown in the next section, combined with the rain-flow counting method and equation 4.21.

Table 18:Mean extreme velocity for 50-year return period at different height

Percentage of extreme velocity	***40%***	***50%***	***60%***	***70%***	***80%***	***90%***	***100%***
Mean velocity at 10m (m/s)	9	12	14	16	19	21	23
Mean velocity at 30m (m/s)	14	18	22	25	29	32	36
Mean velocity at 60m (m/s)	18	23	28	33	38	42	47

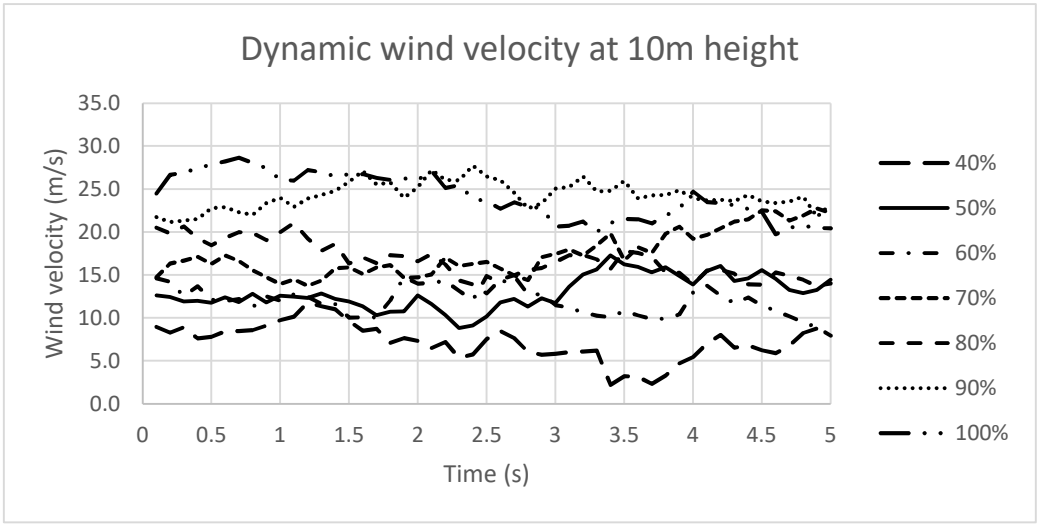

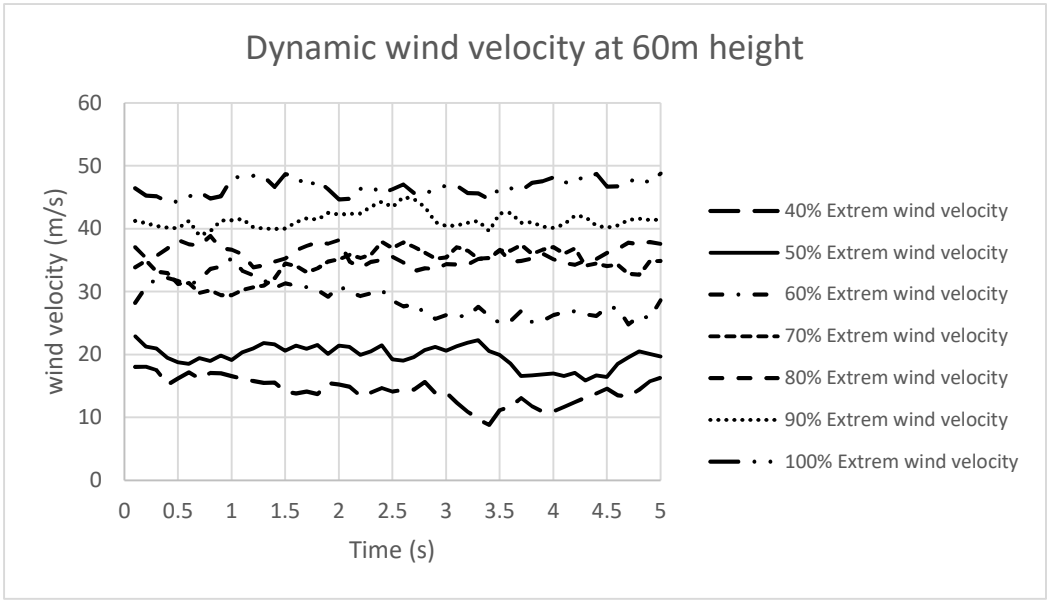

Figure 5-1:Wind velocity at 10m and 60m height

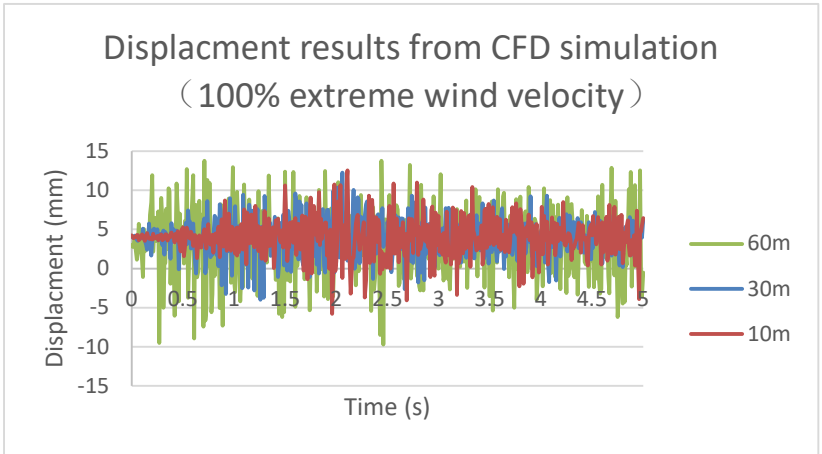

Figure 5-2: Displacement of specimens calculated from CFD simulation results for 100% extreme wind velocity at different height

5.2 Test Schedule

The example of displacement rain-flow count results under wind load at 30m is shown in Figure 4-2, and for 10m and 60m are shown in Figure 5-3. As introduced in Section 4.2.2, the largest amplitude and repeated times are extracted from each rain flow counting result. The loading protocol based on the newly developed ARC method for 30m height is shown in Table 12, and Table 18 shows the loading sequences for 10m and 60m height. Figure 5-4 shows these two groups' cyclic loading protocol curves.

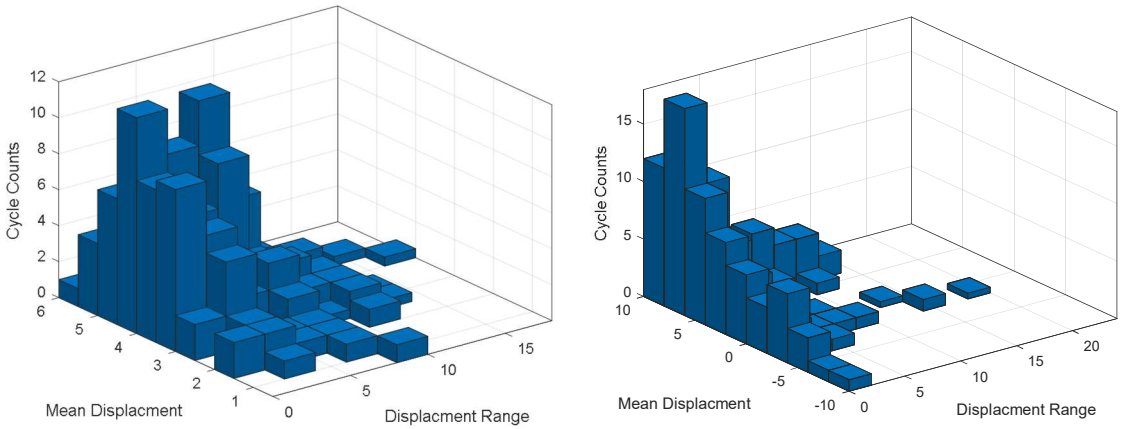

Figure 5-3 Rainfall statistics for 100% extreme velocity at 10 m (left) and 60 m (right) heights

Table 19: Loading protocol for groups ARC1050 and ARC6050

Test Group name	***Cycles Displacment***				***Number of Cycles***
ARC1050 (apply five times)	0 to -10	-10 to 0	0 to 1	1 to 0	2
	0 to -5	-5 to 0	0 to 3	3 to 0	150
	0 to -9	-9 to 0	0 to 4	4 to 0	20
	0 to -5	-5 to 0	0 to 1	1 to 0	50
	0 to -10	-10 to 0	0 to 1	1 to 0	4
	0 to -10	-10 to 0	0 to 3	3 to 0	9
	0 to -12	-12 to 0	0 to 3	3 to 0	1
ARC6050 (apply five times)	0 to -9	-9 to 0	0 to 9	9 to 0	2
	0 to -8	-8 to 0	0 to 4	4 to 0	150
	0 to -9	-9 to 0	0	0	20
	0 to -11	-11to 0	0 to 6	6 to 0	50
	0 to -12	-12 to 0	0 to 5	5 to 0	4
	0 to -12	-12to 0	0 to 1	1 to 0	9
	0 to -11	-11 to 0	0 to 7	7 to 0	1

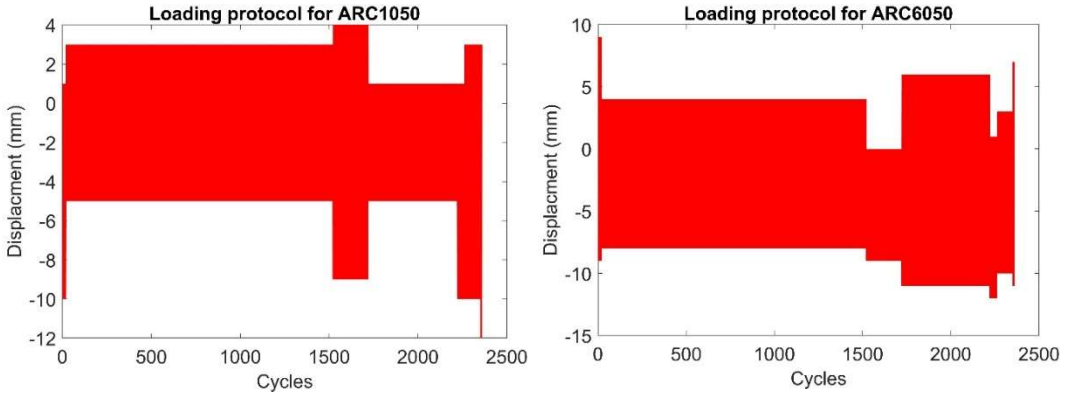

Figure 5-4: Cyclic loading protocol curves for groups ARC1050 and ARC6050

Table 19 lists every physical test carried out in this study. As the independent monotonic and cyclic tests for 30m height were finished in the former chapter, the testing results of this chapter are compared and discussed with them in the following sections.

Table 20: Test schedule

Group	Description	Number of specimens	Angle bracket type
ARC1050	Loading protocol from a newly designed scheme	3	ABR90 × 90 × 65 ×2.5mm
ARC6050	Loading protocol from the newly designed scheme	3	ABR90 × 90 × 65 ×2.5mm

5.3 Materials and methods

Again, this test was completed using an Eland 50kN 200mm stroke tensile and compressive digital servo-hydraulic actuator and cyclic testing at the Heavy Structures Laboratory at Sheffield. This test also used a 4-ply GLT and angle brackets ABR 90 x 90 x 65 x 2.5mm, with fasteners of 4 x 60mm CNA ring shank nails. The LVDT placement is shown in Figures 4-14. The test specimens were the same as in Chapter 3; details are shown in Figures 4-11. The test setup can be found in Figures 4-15. The displacement ratios for the cyclic tests ranged from 16-20 mm/sec.

This test also applied digital image correlation (DIC) to a detailed analysing of the cyclic behaviour of the angle bracket.

5.3.1 DIC principles

There are different techniques to measure surface deformation in mechanical testing. In addition to point strain measurements with LVDTs, several non-contact optical methods can be used, including interferometric and non-interferometric techniques (Pan et al., 2009).DIC is one of the non-contact optical non-interferometric evaluation techniques used to analyze strain or displacement. During laboratory testing, a series of digital images are taken of the specimen and compared to the initial state to analyze the change. A speckle pattern is drawn on the sample's surface as a reference. The deformation of the pattern is then analyzed by mathematical correlation using DIC software to find and generate the strain distribution for each image.

The digital image includes many pixels, and the greyscales of each pixel vary between 0 and 255 because the light reflected intensity from the object differs. The DIC software can analyse a specimen's deformation by comparing the greyscales of a located pixel in a distorted and original picture (Zhang et al., 2015). A collection of the greyscales of pixels around the located pixel is required because a pixel's greyscale can recur across the whole picture. The located pixel and its surroundings are known as a subset(Zhang et al., 2015). The DIC software calculated the total greyscales differences of a subset based on the correlation function to define its displacement and determine the specimens' strain.

Compared with other non-contact optical methods has many advantages. Firstly, the equipment for testing is simple. One fixed digital camera cooperated with a computer is required to take digital pictures. Secondly, the requirement of testing the lighting environment is not strict. Therefore, the testing can be done under white or natural light in laboratory or field conditions. Finally, using cameras of different resolutions and sensitivity, DIC can be used on various scales, even nanoscale.

The specimen preparation is relatively simple but requires creating a random and high-contrast speckle pattern on the surface. There is no preparation for a specimen whose surface has a natural random speckle pattern. Researchers recommended that one subset contain at least three speckles(Lionello and Cristofolini, 2014). For others, paint guns, spray cans, stencils, or laser printers can create speckle patterns. Additionally, using a paint

gun can create a suitable pattern. However, the quality can be influenced by the airflow and spray distance(Lionello and Cristofolini, 2014).

5.3.2 DIC preparation

The application of DIC in this section is intended to observe the displacement of the angle brackets. Matte white paint was sprayed on the surface as a background to reduce glare from the metal plate. The stencil method was used for the preparation of the speckle pattern. The stencil was generated by a python program from the Laboratory of Machine and Structural Dynamics of the University of Ljubljana (https://github.com/ladisk/speckle_pattern.git) (Figure 5-5). Then, the speckle pattern was printed on the cardboard with a laser cutter (Figure 5-6). The size and distance of the spots were adjusted to a suitable level, as spots too small or too dense were challenging to draw on the surface. Because the angular support has a rib in the middle, making the surface rugged and challenging to apply the spot pattern with a spray gun or paint sprayer. Therefore, a black marker is used to draw the pattern. The target area is the angle bracket, so the pattern covers the plate of the angle bracket and the surrounding wood (Figure 5-7). A Sony ILCE-7M2 interchangeable lens digital camera was used to take the photographs, and a PC was used to control the camera and allow the camera to take four images per minute. The settings for the DIC measurements are shown in Figure 5-8.

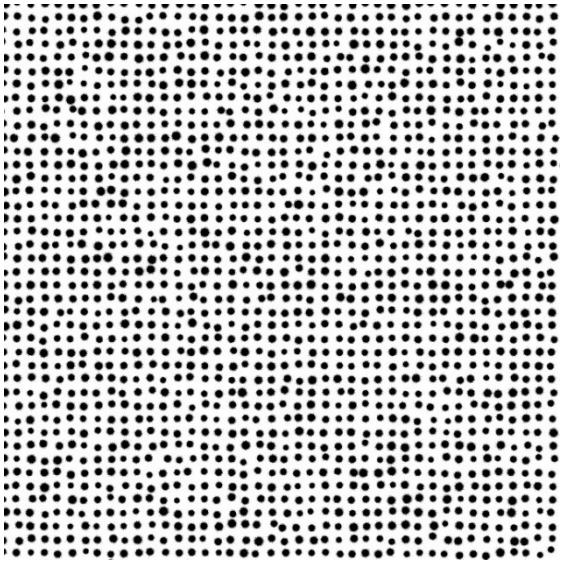

Figure 5-5: Stencil generated by a programme

Figure 5-6: prepare the stencil by laser cutting

Figure 5-7: speckle pattern on a specimen

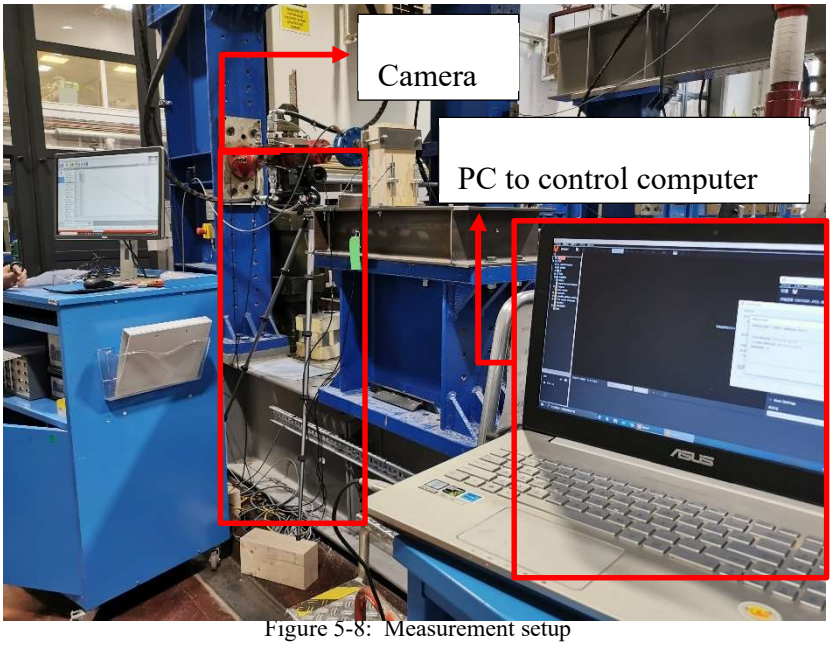

Figure 5-8: Measurement setup

5.4 Results and discussion

5.4.1 Cyclic loading and fatigue behaviour

The detailed performance of ARC3050 has been analyzed in Chapter 4. Figures 5-9 show the bending moment and rotation ratio curves for all three sets of specimens. It is clear that bending moments up to 200 kpa.m3 in the counterclockwise direction need to cause a rotation ratio of 0.1 in all three sets of specimens. However, a rotation ratio of 0.04 in the clockwise direction needs to exceed 400 kpa.m3 for some specimens, indicating that some specimens need a higher resistance in the clockwise direction than in the counterclockwise direction. The following sections will analyze the ARC1050 and ARC6050.

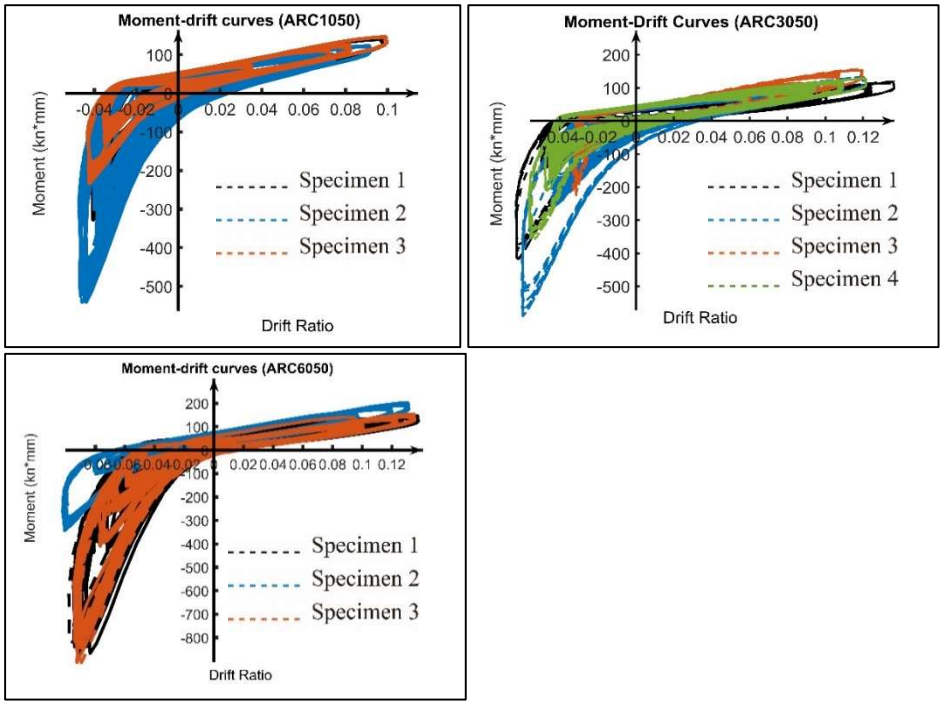

Figure 5-9: Moment-Rotation ratio Curves for Group ARC1050, ARC3050 and ARC105

- **Group ARC1050**

The detailed load and rotation ratio curves for group ARC1050 is in figure 5-10, and each loading sequence is illustrated in different colours. The impairment of strength after each loading sequence is shown in Figure 5-11. The average strength reduction clockwise is 0.12kn four times counterclockwise (0.03kn). The average clockwise values for different sequences fluctuate from 0.008kn to 0.27kn with a standard deviation of 0.028kn. The counterclockwise fluctuation is relatively small, and the standard deviation is 0.01kn. According to the figure, in sequences 2,3,6 and 7, the clockwise strength is significantly higher than that of counterclockwise. The clockwise displacement of these four loading sequences is between 3 and 4 cm, while the other displacement is 1mm. The loading displacement varies between -5 and -12mm in the counterclockwise direction. It indicates that the influence of loading displacement in the clockwise direction is more significant than that in the counterclockwise direction.

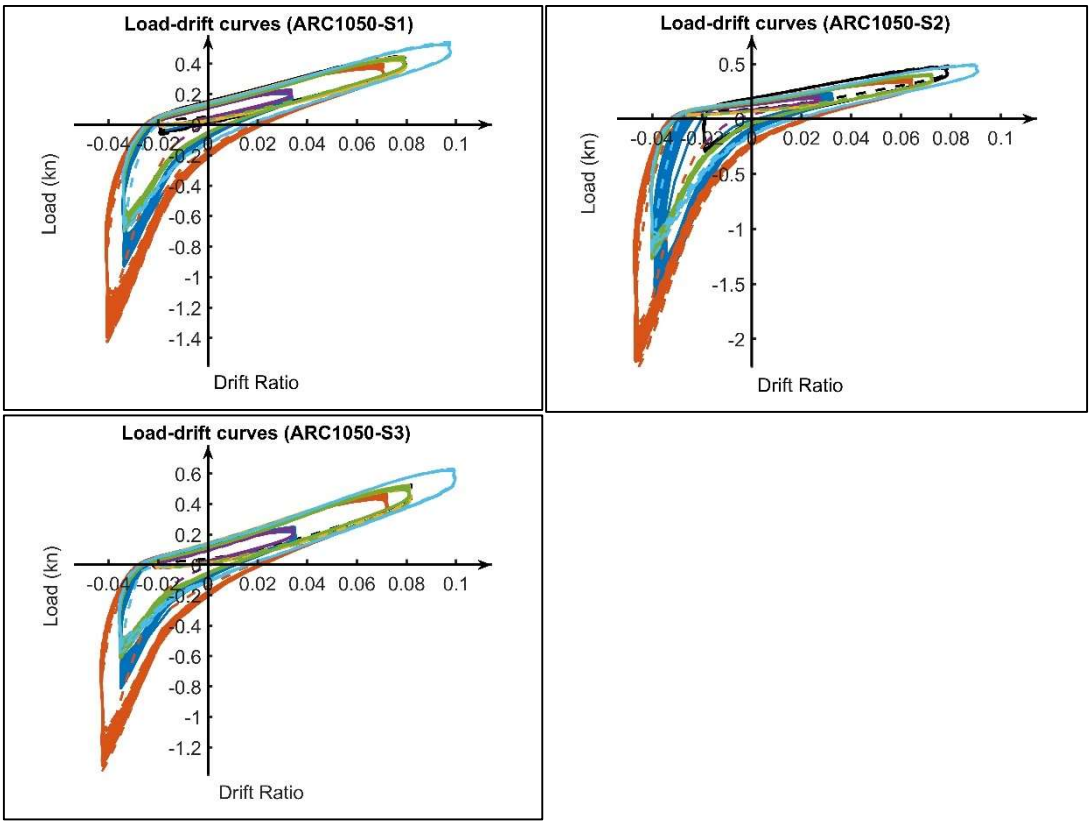

Figure 5-10:Loading-drift curves for ARC1050 group

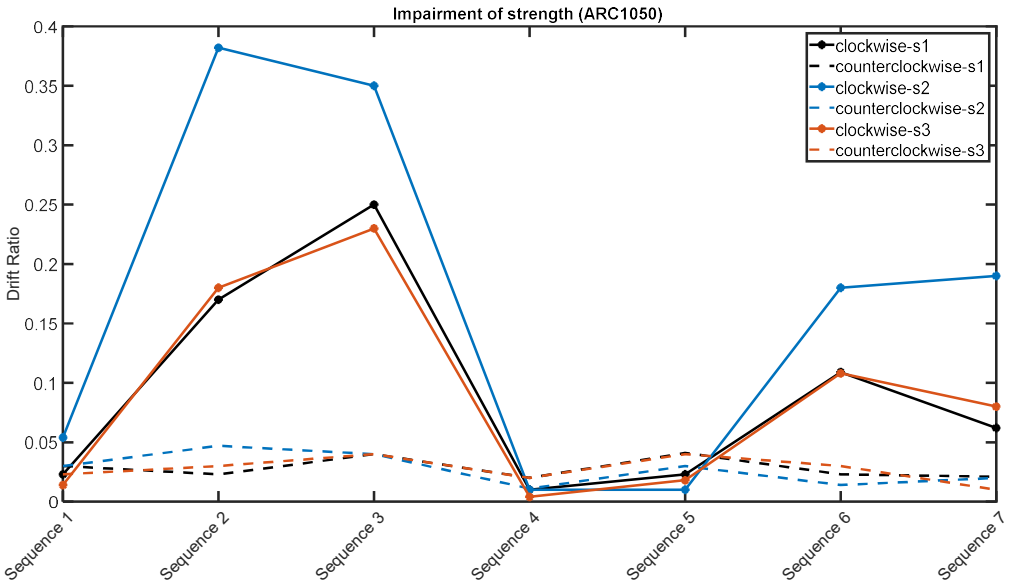

Figure 5-11:Strength impairment of ARC1050

Figure 5-12 shows the dissipated energy for group ARC1050 in the counterclockwise direction. The maximum value can be observed in 12mm loading displacement with an average value of 0.008kn*mm, and the values increased with the displacement. Similarly, Figure 5-13 shows that the equivalent damping increased with the loading displacement in this direction. The average values at 5mm, 9mm,10mm and 12mm are 4.5%,5.1%,5.5% and 6.4% respectively.

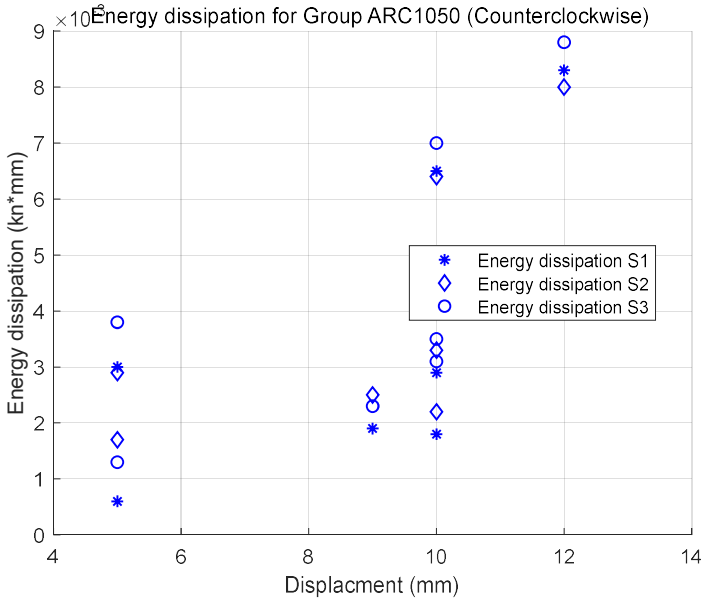

Figure 5-12: Energy dissipation of ARC1050

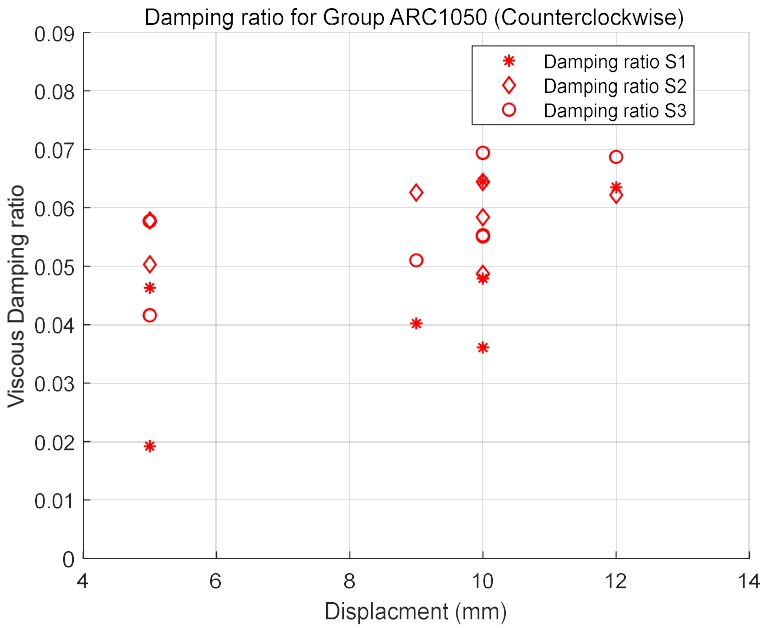

Figure 5-13: Equivalent damping ratio for ARC1050 group

Figures 5-14 and 5-15 presented this group's dissipated energy and equivalent damping in the clockwise direction, and they also grew with the loading displacement. The energy dissipation values increased from 0.007kn*mm to 0.045kn*mm, and for damping ratios, the average values vary from 26% at 1mm to 47% at 4mm. By comparing the two directions, the maximum equivalent damping value in the clockwise direction is almost seven times that in the counterclockwise direction.

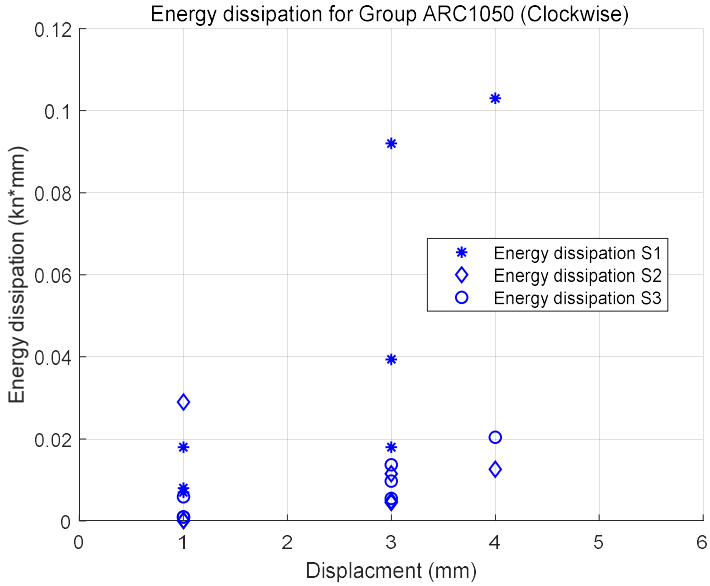

Figure 5-14: Energy dissipation in the clockwise direction for the ARC1050 group

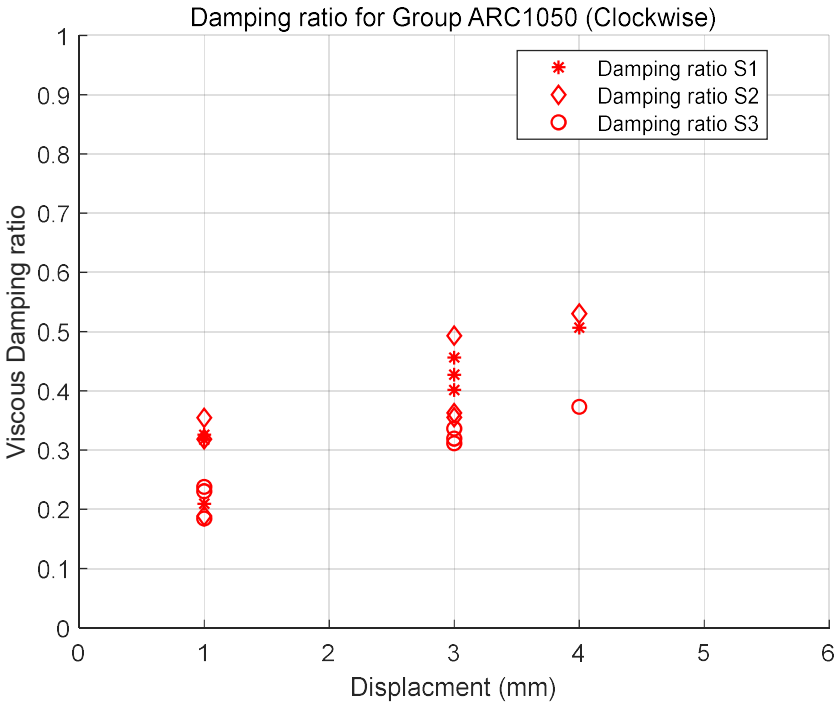

Figure 5-15:Equivalent damping in the clockwise direction for the ARC1050 group

- **Group ARC6050**

The detailed loading and rotation ratio curves are shown in Figure 5-16. there is a graphical difference between the second specimen and specimens 1,3. The numerical analysis of the strength loss is shown in Figure 5-17. The average strength reduction for clockwise and counterclockwise is 0.136kn and 0.045kn. There is a close relationship between strength reduction and loading displacement in the clockwise direction, i.e., the strength reduction value increases with increasing displacement. In addition, specimen 2 showed lower strength reduction values in the clockwise direction than the other two specimens, but with the same trend. In terms of counterclockwise, the strength reduction values for specimen 2 were not numerically significantly different from the other specimens, except for the first sequence. This may indicate that the graphical differences between the specimens on the loading and rotation ratio curves are caused by the variation in the mass of the angle brackets rather than by manual installation.

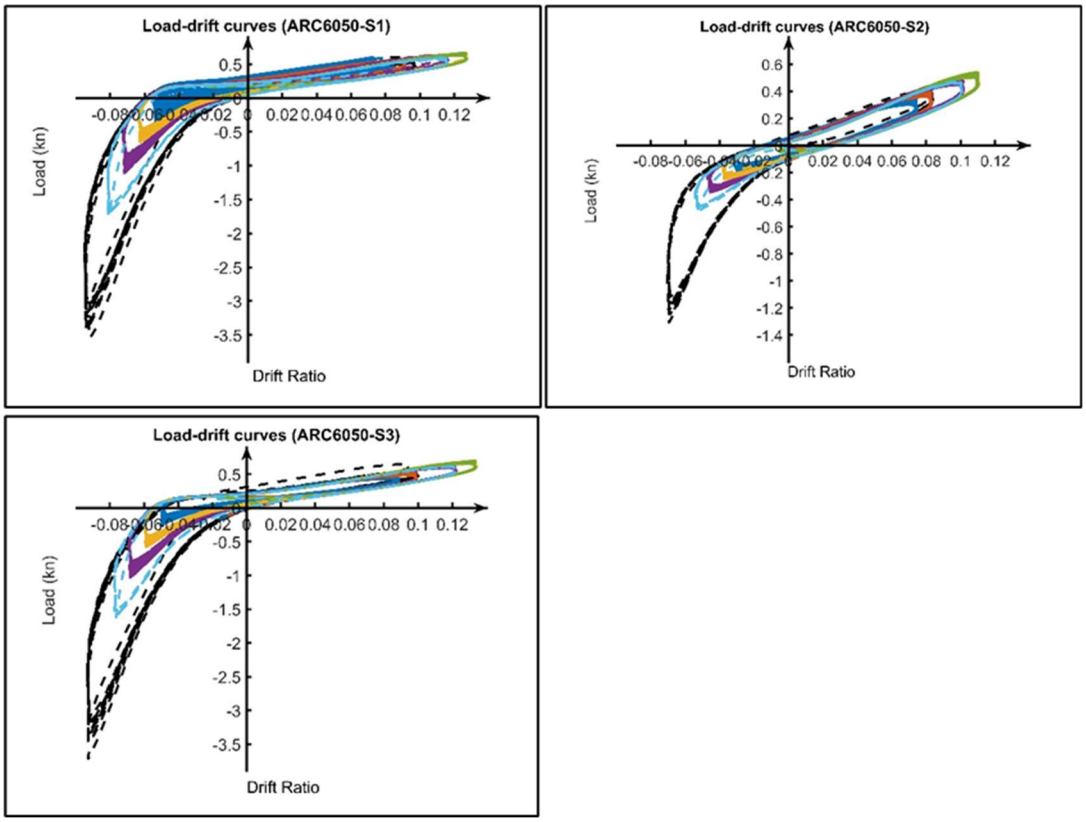

Figure 5-16:Loading and rotation ratio curves for all ARC6050 specimens

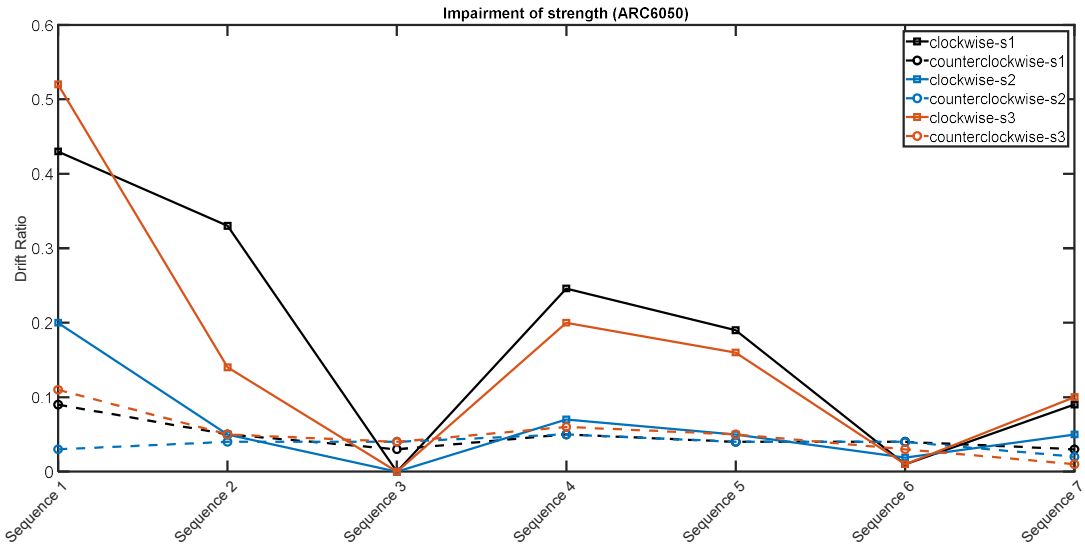

Figure 5-17:Strength Impairment of ARC 6050

Figure 5-18 shows the energy dissipation values for group ARC6050 in the counterclockwise direction, with the average values of 0.003kn*mm,0.004 kn*mm,0.007 kn*mm and 0.009kn*mm at 8mm, 9mm,11mm, and 12mm. The damping ratios are shown in Figure 5-19, and the average values increased with the loading displacement and varied from 5% to 6%. Additionally, the damping increased when the loading reached 9mm the second time, and a similar trend can be seen at 11mm and 12mm, which indicates the energy required to make the same distance decreased and the resistance strength in this direction was reduced after a long term cyclic load.

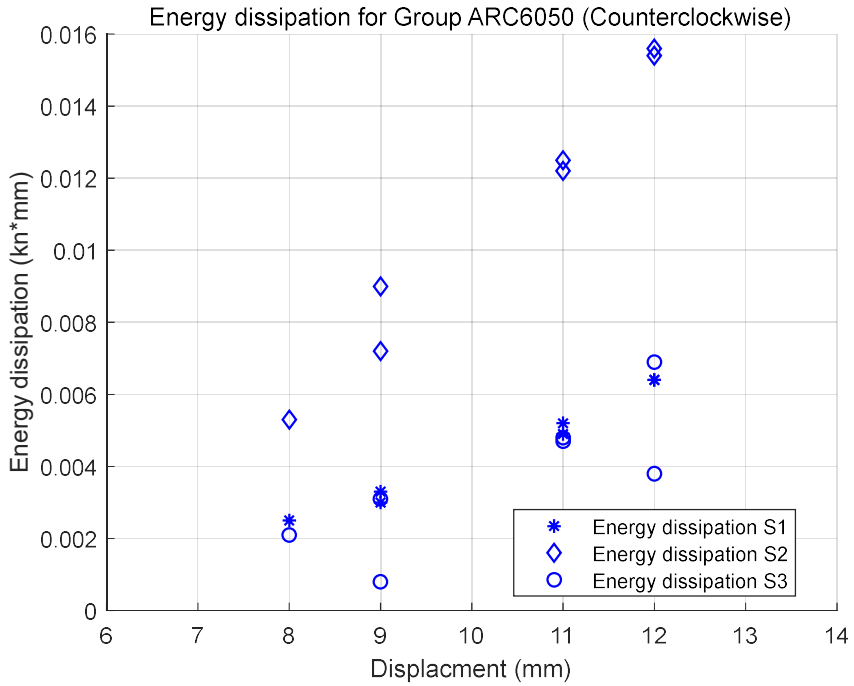

Figure 5-18: Energy dissipation of ARC6050

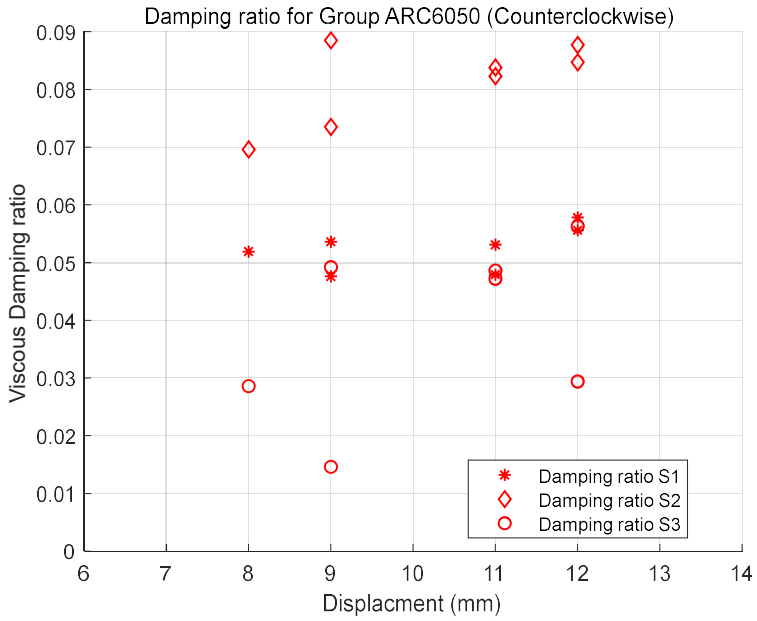

Figure 5-19: Equivalent damping ratio of ARC6050

Figures 5-20 and 5-21 show this group's dissipated energy and damping ratio in the clockwise direction, indicating the value increase with loading displacement. The maximum average value at 9mm is 0.05kn*mm, and except for the value at 0mm, the minimum average value is 0.0015kn*mm at 1mm displacement. Regarding the damping ratio, the maximum average value is 25% at 9mm and 10.4% at 1mm. The maximum average damping in this direction is around four times that in the counterclockwise direction.

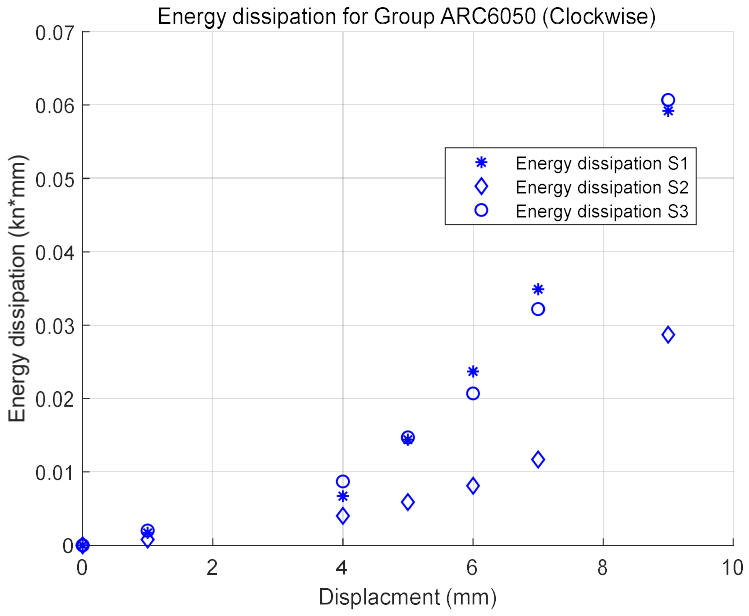

Figure 5-20: Energy dissipation in the ARC6050 group in the clockwise direction.

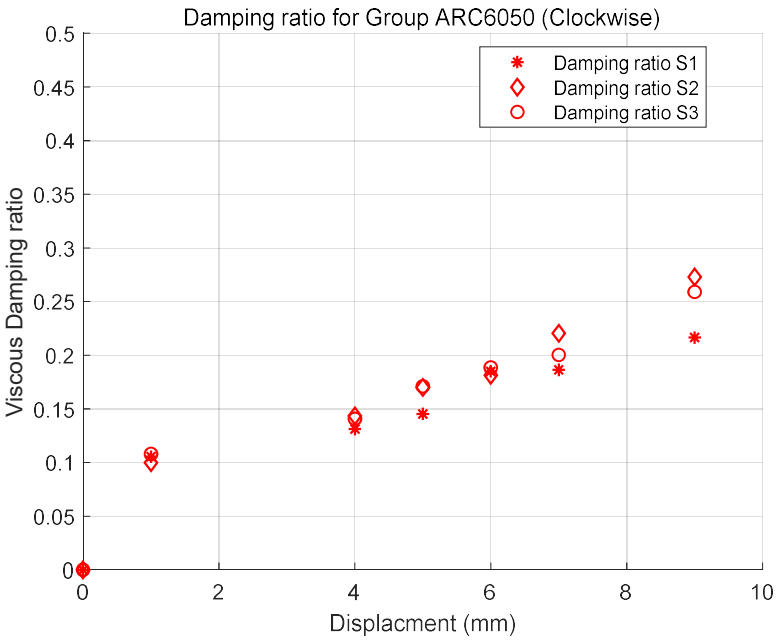

Figure 5-21: Damping ratio in the clockwise direction for group ARC6050.

- **Comparison**

Figure 5-22 compares the impairment of strength between different groups. It is clear that in both directions, the reduction value grows with the wind velocity. Additionally, the reduction in clockwise is higher than counterclockwise. The reduction value for ARC6050 clockwise is 13.3% higher than ARC3050 and around 20% higher than ARC1050. For counterclockwise, the strength reduction of ARC6050 is 8% and 38% higher than that of ARC3050 and ARC1050, respectively.

Figure 5-23 shows the full-cycle equivalent damping ratios for the three groups, and the values increased with the loading amplitudes in each group. The minimum and maximum values for ARC1050 are 5.8% and 15.5%, respectively; for ARC3050, those are 6.3% and 12.7%. The average value at 9mm amplitude and 18mm amplitude for group ARC6050 are 4.5% and 11.1%, respectively. According to Figure 5-23, the damping ratio for ARC groups decreased with the building height, in which the average damping for connection at 60m height is 8.8%, and 0.6% lower than 30m, 2.7% lower than 10m. This indicated that the connections' energy dissipation ratio decreased with the building's height.

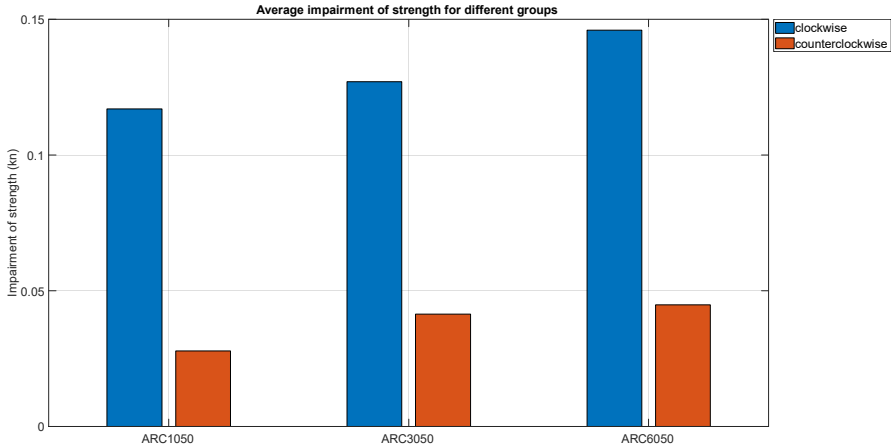

Figure 5-22: Average strength impairment of groups

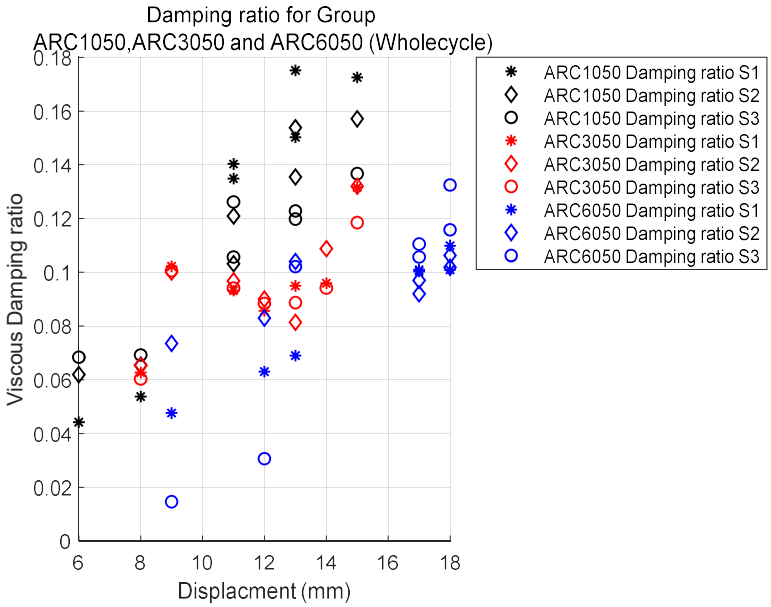

Figure 5-23: Equivalent damping of connected systems under different wind speed

5.4.2 Residual of stiffness after cyclic test

1) Monotonic load in the counterclockwise direction

Figures 5-24 show the test specimens for the ARC1050 and ARC6050 groups. Details are shown in Figure 5-25, where the compressed timber members were lifted, and the nails were pulled out. The experiments did not cause significant structural damage to the timber members or the angle brackets.


Figure 5-24: Tested specimens for groups ARC1050 and ARC6050

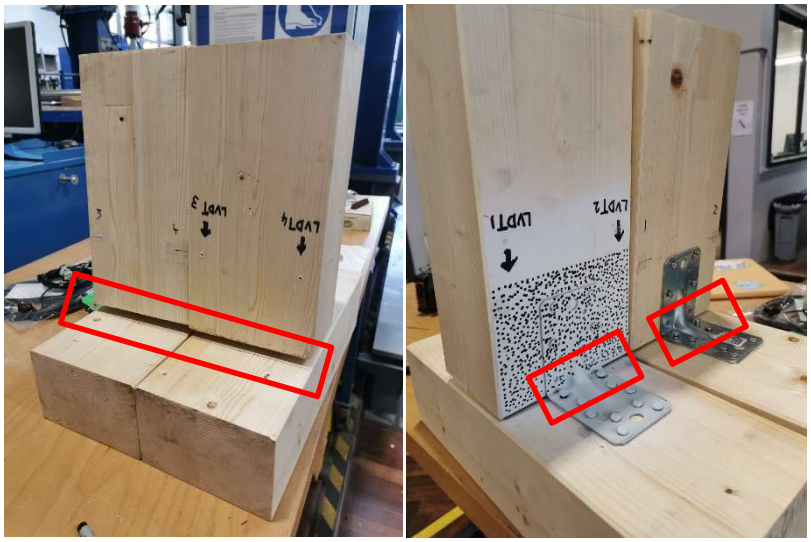
Figure 5-25: Tested specimens for groups ARC1050 and ARC6050

The loading and deformation curves for each group are shown in Figure 5-26, which indicates that the load required to bring the rotation ratio to 0.2 decreases for the ARC group compared to the MOP. After cycling, the average required loads for ARC1050 and ARC6050 decreased to 53.5% and 41.9%. The comparison of stiffness reduction for ARC1050, ARC3050 and ARC6050 groups at different rotation ratios is shown in Figure 5-27. The required loads for ARC1050 were more significant than those for ARC3050. Regarding the loading cycle characteristics shown in Table 20, the mean and median of the loading displacements are higher for ARC1050 than for ARC3050 and are closer to 0. This situation is similar to the conclusion reached in the previous chapter that the smaller the mean and median, the more significant the required load reduction. In addition, the cyclic range of ARC3050 is broader than that of ARC1050. Also, the ARC3050 has a maximum to minimum displacement ratio of -0.41, closer to -1, compared to the ARC1050. These load characteristics may have resulted in a minor reduction in stiffness for the ARC1050 group.

The average load required for ARC6050 is 41.9% of the MOP, which is 2.2% less than that for ARC3050. Considering the loading characters, the median for ARC6050 is less than ARC3050. However, the mean value for ARC6050 is higher, indicating that the mean value of a loading sequence does not alone contribute to the magnitude of the stiffness reduction. The cyclic range for ARC6050 is higher than ARC3050 and ARC1050. Additionally, the maximum to minimum displacement ratio (R-ratio) for ARC6050 is -0.75, closer to -1 than the other two groups. Researchers pointed out that for timber material, under cyclic load

with a negative R-ratio, the residual value decreased when the R-ratio was closer to -1 (Smith, 2003). This condition is also applied to the fatigue behaviour of timber joints with the angle bracket system.

The required load for ARC6050 is higher than ARC3050 at rotation ratios of 0.2 and 0.4 when comparing the TR440 and DABM groups with ARC3050. With and rotation ratio of 0.6, the required load for these three groups becomes lower than ARC30. This may result in the resistance caused by the nails' ring when pulling the nail out.

The average Stiffness for the three groups with different rotation ratio ranges is shown in Table 21. The stiffness of ARC6050 decreased the most, followed by ARC3050 and ARC1050. In addition, the stiffness of all groups increased with increasing rotation ratios, indicating that the cyclic tests had loosened the nails as the rotation ratio increased, and the performance of the angle bracket adjusted because the nails were not pulled out completely when they touched the flange the stiffness increased.

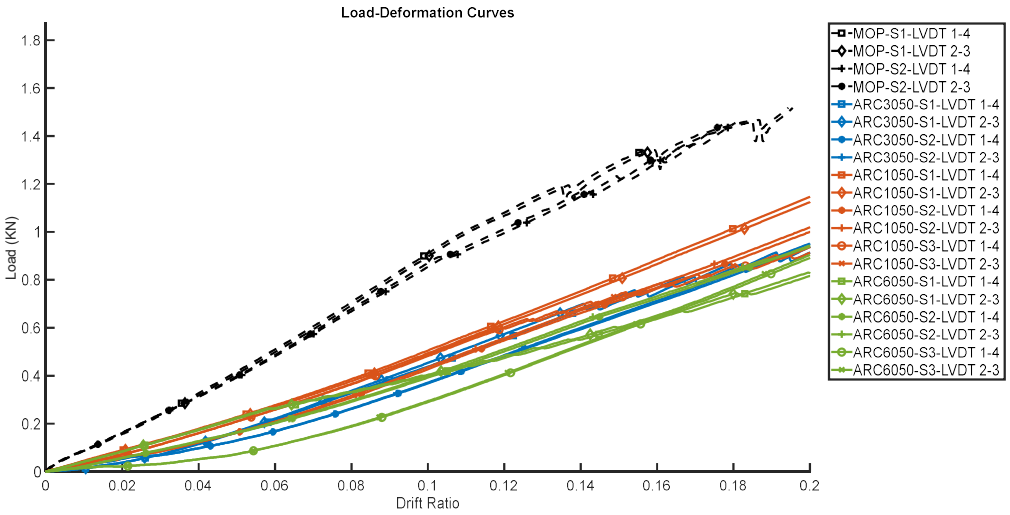

Figure 5-26: Loading and Rotation ratio curve for different ARC groups

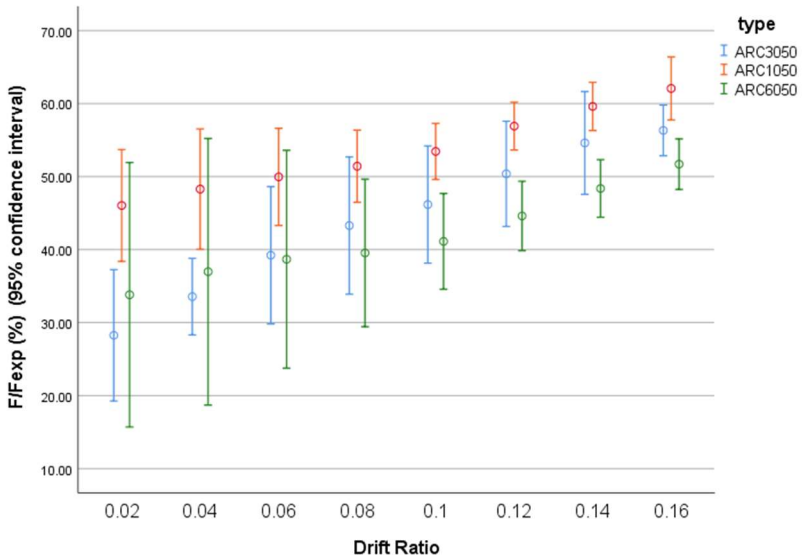

Figure 5-27: Stiffness reduction of ARC groups

Table 21: Loading caracters of different loading sequences

TYPE	*Mean (mm)*	*Total cycle*	*SD(mm)*	*Median(mm)*	*Minimum(mm)*	*Maximum(mm)*	*Range (mm)*
ARC1050	*-1.7*	*1360*	*4.5*	*-2*	*-12.00*	*4.00*	*16*
ARC3050	*-3.3*	*1360*	*5.7*	*-3.0*	*-12.00*	*5.00*	*17*
ARC6050	*-2.6*	*1360*	*6.8*	*-4.0*	*-12.00*	*9.00*	*21*

Table 22: Stiffness at different rotation ratio

Rotation ratio Range	*0-0.05*	*0.05-0.1*	*0.1-0.15*
ARC1050	0.26 Mpa	0.62Mpa	1.00Mpa
ARC3050	0.24Mpa	0.54Mpa	0.91 Mpa
ARC6050	0.20Mpa	0.50Mpa	0.83Mpa

5.4.3 DIC results

This research used the free software GOM Correlate system to study the DIC images. To further analyse the relative movement between timber components and angle brackets during cyclic load, this research selected Eighteen pictures from the beginning of the first loading sequence and picked them every 15 seconds. Due to the limitations of the test setup, this section only analyzes the deformation and displacement conditions of the stressed wood members and the panels on them. Figure 5-28 shows the initial condition of an ARC3050 sample. Figure 5-29 shows that three points were selected to analyze the deformation condition in the cyclic test. Eighteen pictures were used to analyze the cyclic phase, six shown in Figures 5-30. The higher values were near the boundary between the sheet metal and the wood, according to the pictures. Figure 5-31 shows the deformation rates for the selected three points. For point 1, the value is as high as 1.7%, which is significantly higher than the other two points. At the same time, the other two points have values below 0.3%. Because there is no deformation of the wood components, the high values around the boundaries and points may be caused by the relative motion between the angle brackets and the lumber, indicating that the cyclic experiment causes the loosening of the fasteners.

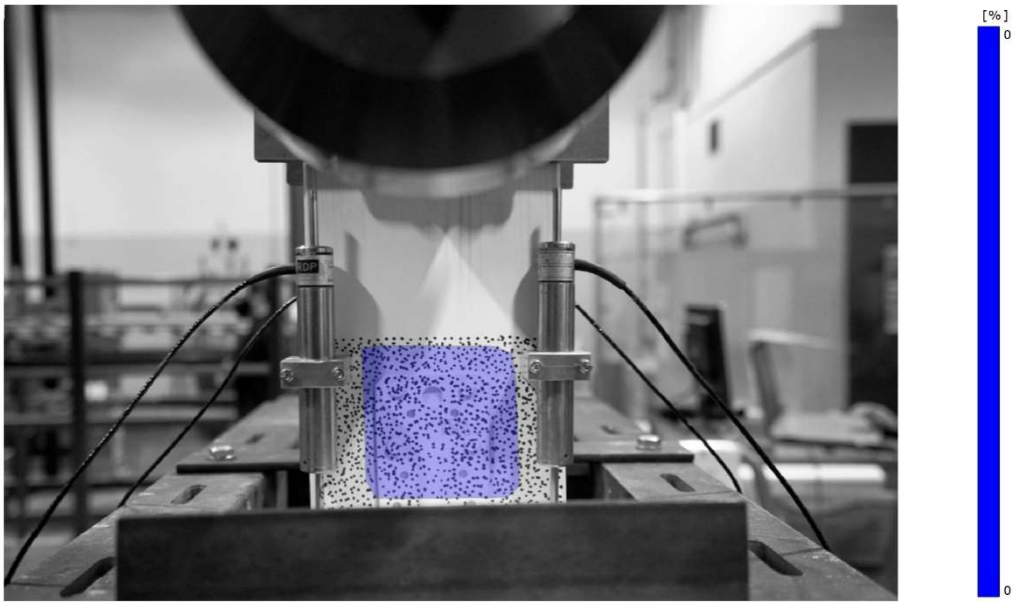

Figure 5-28:DIC images of the initial phase of the ARC3050 group

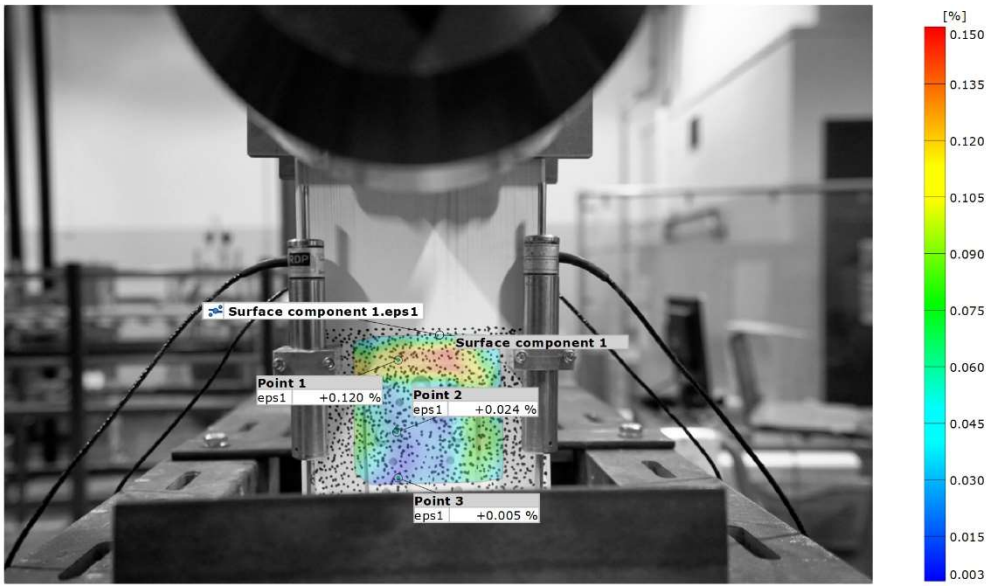

Figure 5-29:Points selected for analysis of deformation rates

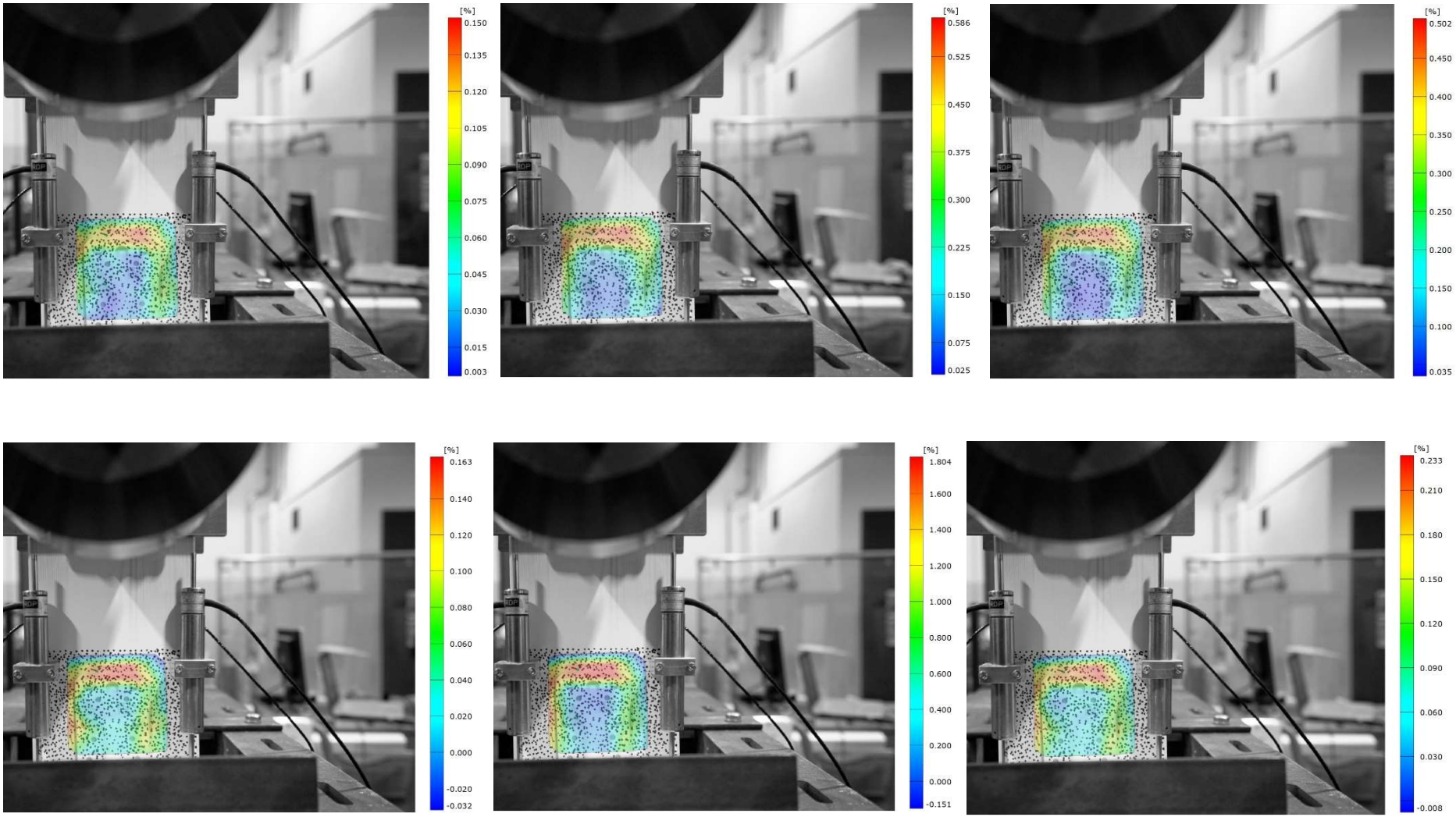

Figure 5-30: Pictures from DIC deformation analysis

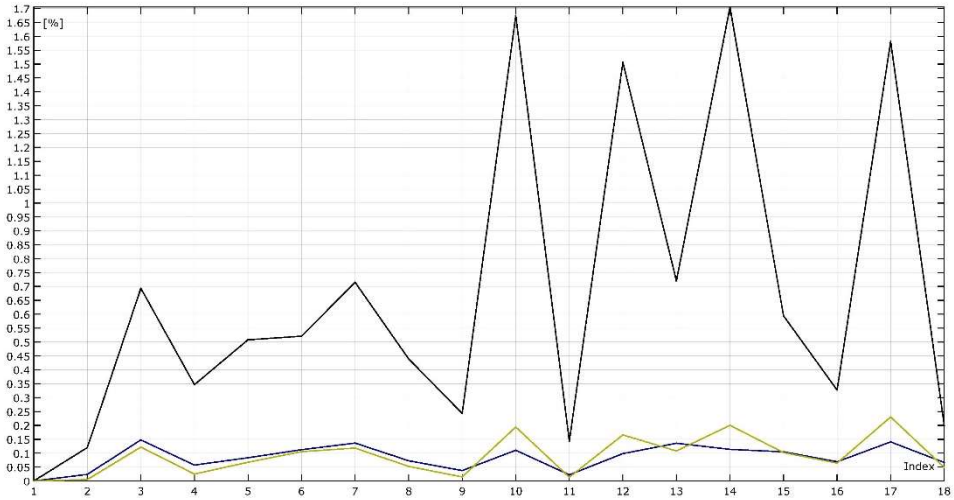

Figure 5-31: Deformation ratio of the selected point

For the monotonic test, this research selected the last picture and the other four pictures before, which were all taken during the monotonic test. Figure 5-32 shows the three points chosen to analyse the deformation and displacement of the sample during the counterclockwise monotonic test. Five pictures, including the initial stage shown in Figure 5-33, are taken for this stag. The strain ratio is concentrated at the junction between the upper edge of a metal plate and timber panel, and the value on plate or timber is relatively low. Figure 5-34 shows the strain ratio increase with the loading displacement for three selected points, and the values for point 3 are lower than the other two points. Combined with Figure 5-35, the displacement along the y axis of these three points shows that the value and changing rate of point 3 are lower than the other two. It can be concluded that the strain at point 2 is mainly caused by the relative moment of metal plate and timber, which can cause the bending of fasteners.

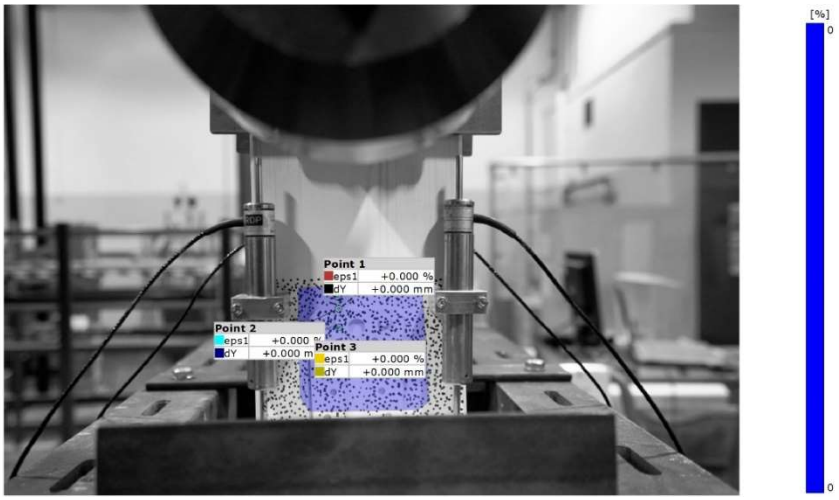

Figure 5-32:Points selected for DIC numerical analysis

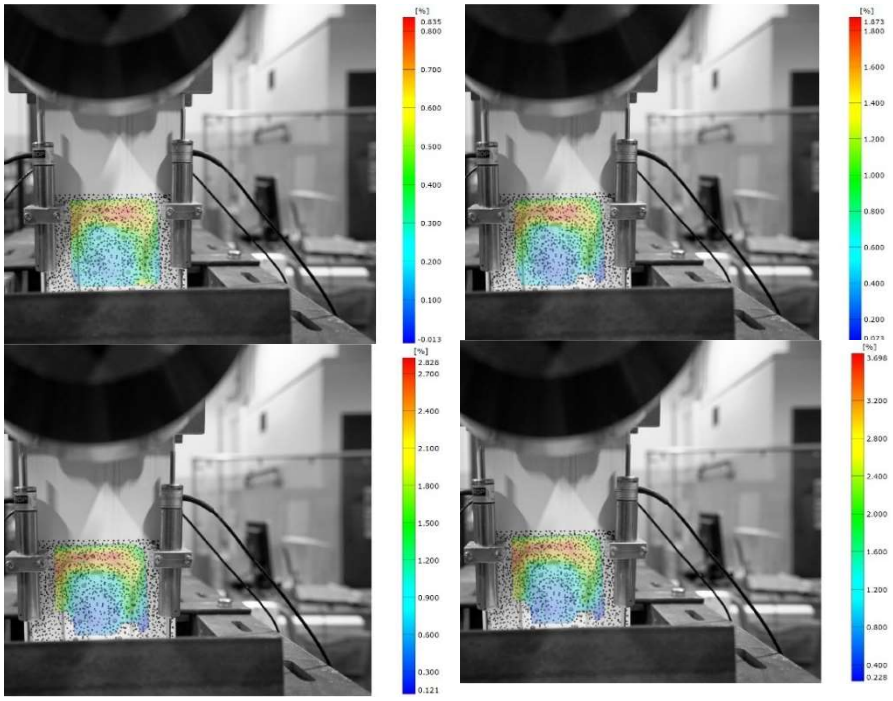

Figure 5-33: Pictures with DIC strain ratio analyse results

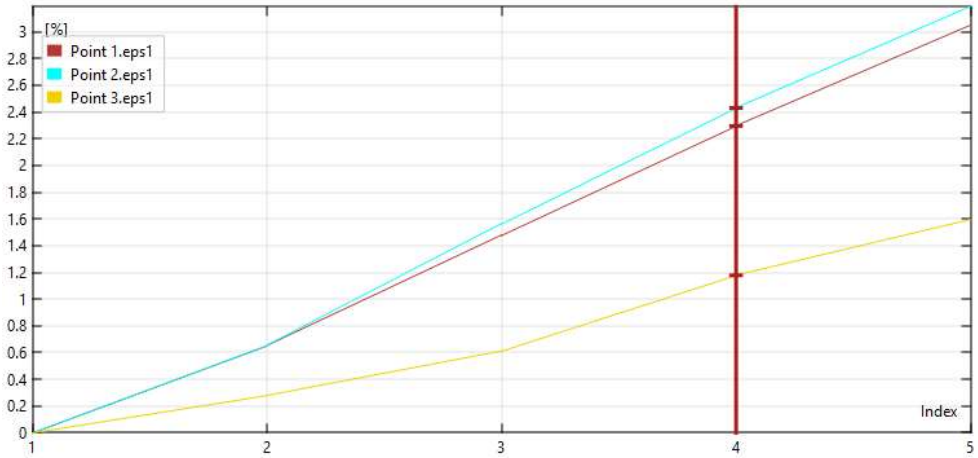

Figure 5-34: DIC strain ratio for three selected points

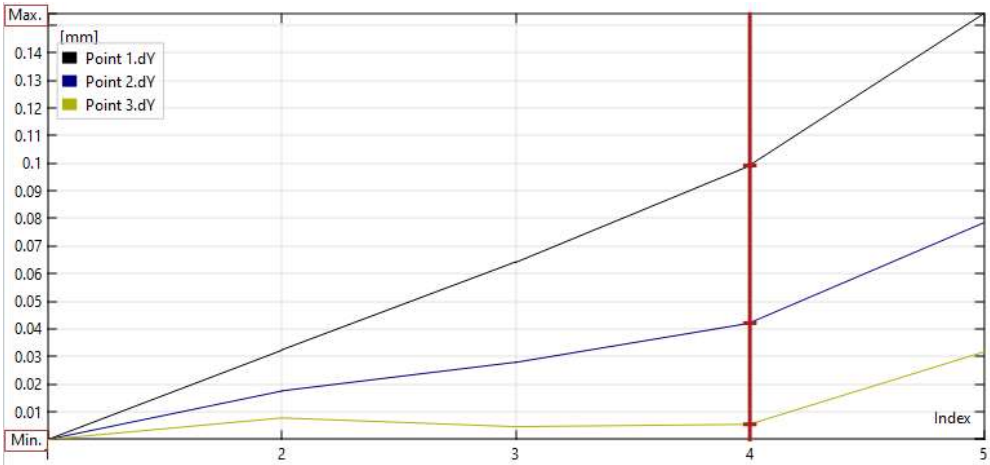

Figure 5-35: DIC displacement for three selected points

5.5 Summary

This chapter used the new loading sequences design method introduced in Chapters 3 and 4 to study the effect of wind velocity on the connections between timber panels. Firstly, the dynamic velocity at 10m, 30m and 60m simulated in Chapter 3 was used in this chapter. Moreover, the loading sequences were built based on the CFD simulation with these wind velocity input values. The cyclic and monotonic results were analysed, and the DIC method was introduced in this chapter and applied to analyse the deformation and displacement of metal plates, and timber members stressed.

The main findings are.

- First, different wind speed patterns lead to different loading sequences, and in this study, this difference is mainly reflected in the range of loading displacements and the minimum to maximum displacement ratio. According to the stiffness analysis of the different groups, the reduction values increase with building height or, in other words, with wind speed. In addition, the results of the cyclic performance analysis show that the average strength reduction value increases with increasing velocity.

- Secondly, the DIC analyses results show that the deformation of metal plate and timber panel is small, but relative movement between two members occurred during cyclic and monotonic tests, which means that the cyclic test mainly affects the performance of fasteners rather than the angle bracket.

The limitations of this study are mainly manifested in the setup of the DIC test. Firstly, this method could not detect the performance of metal plates on the fixed timber component due to test space limitations. Additionally, when there is the rotation of testing samples, 3D DIC would be better to define the strain of this study than the 2D method.

Chapter 6. Effect of boundary conditions on fatigue of wood joints

6.1 Introduction

As mentioned in Chapter 2, the angle bracket connection system has become a choice to connect timber panels with a frame made of different materials. However, the selection of angle bracket and nail pattern can influence the performance of this connection system under cyclic load. Additionally, some researchers have tested the performance of this connection system timber to steel or timber to timber under shear load, but few tested the connection timber to concrete. Therefore, this part aims to analyse the fatigue behaviour of this connection system with different boundary conditions under the same loading sequences.

6.2 Materials and methods

6.2.1 Materials and set-up

As in the previous tests, the same 4-ply GLT was used to make the specimens. One set of specimens (ARC3050-AB2) used the same angle brackets and fasteners as in the previous tests but with a different nail pattern. Compared to the previous test, the ARC3050-AB2 assembly had four other nails for securing the panels to the stressed wood members, and the nail patterns for flanges A and B are shown in Figure 6-1. In addition to the second set of samples (ARC3050-AB3) used, another angle bracket ABR90 × 90 × 65 × 2.5 mm was used. The dimensions and nail pattern of the angel bracket ABR105×105×65×3.0mm are shown in Figure 6-2, and these samples were also secured with 4×60mm CNA ring shank nails. The third set of samples (ARC3050-TC) was attached with angel brackets ABR 90 x 90 x 65 x 2.5mm. However, this group used concrete and timber as the base and stressed components to analyse the joint performance between timber and concrete. Concrete of

C20 grade was used for this experiment. The concrete elements were prepared 28 days before the test, and through-bolt anchors (M8 × 66 mm) were pre-placed in the concrete as fasteners. In addition, the fasteners between the sheet metal and the timber were the same as in Group 1. The assembly of Group ARC3050-TC is shown in Figure 6-3. The machine used for this testing is the same as Chapter 4 and Chapter 5, and the testing setups are shown in Figures 4-15. DIC technique is also used in this test.

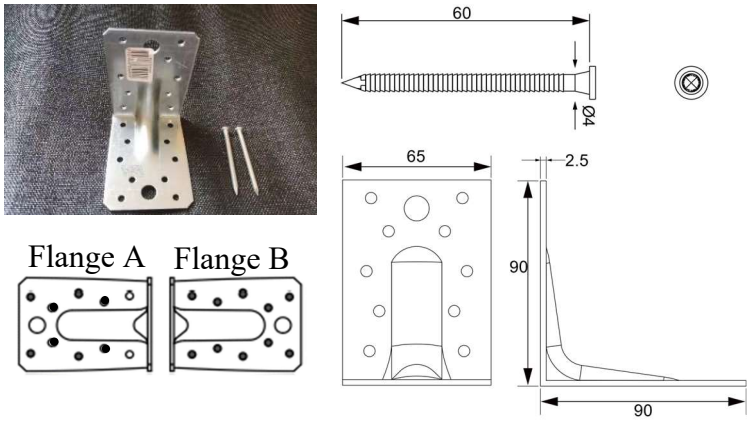

Figure 6-1: Nail pattern for Group ARC3050-AB2

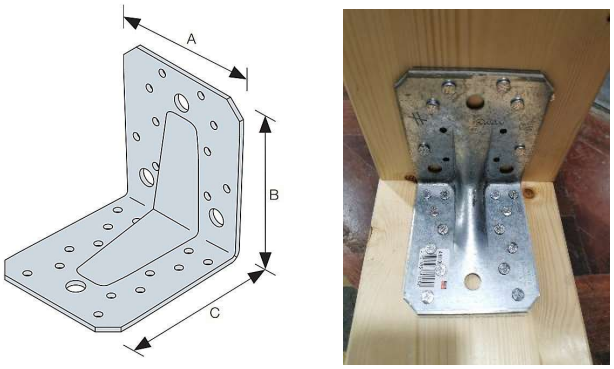

Figure 6-2: Nail pattern for ARC3050-AB3

Figure 6-3: Assemble of ARC3050-TC

6.2.2 Test schedule

The newly designed 30 m height loading sequence was applied to this test shown in Figure 6-4 and then completed with a monotonic load of -50 mm. Moreover, Table 22 lists the number of tests performed in this section.

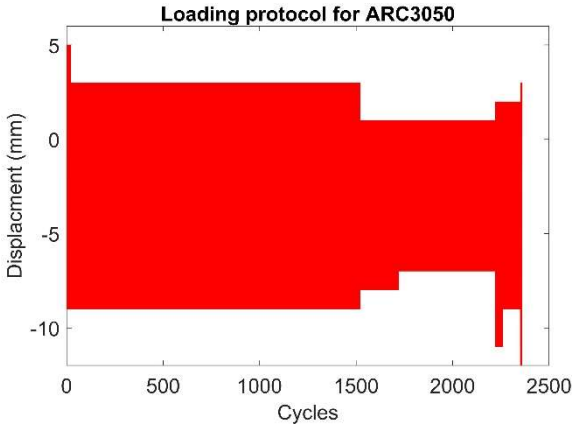

Figure 6-4: Loading sequences for the tests in this chapter

Table 23: Test schedule

Group	Description	Number of specimens	Angle bracket type
ARC3050-AB2	Loading protocol from the newly designed scheme	2	ABR90 × 90 × 65 ×2.5mm
ARC3050-AB3	Loading protocol from the newly designed scheme	3	ABR90 × 90 × 65 ×2.5mm
ARC3050-TC	Loading protocol from the newly designed scheme	3	ABR90 × 90 × 65 ×2.5mm
ARC3050-AB2pu	Loading protocol from the newly designed scheme (Push positive direction 50mm)	2	ABR90 × 90 × 65 ×2.5mm

6.3 Results and discussion

6.3.1 Cyclic loading and fatigue behaviour

Figure 6-5 shows the moment and rotation ratio curves for three groups and ARC3050. Comparing the graphic of these four groups, the stiffness of ARC3050-TC seems lower than the other three groups counterclockwise during cyclic load. For the clockwise direction,

there is a variation between different specimens in the same group. However, the group TC is relatively significant, and the reason will be analysed in the following part.

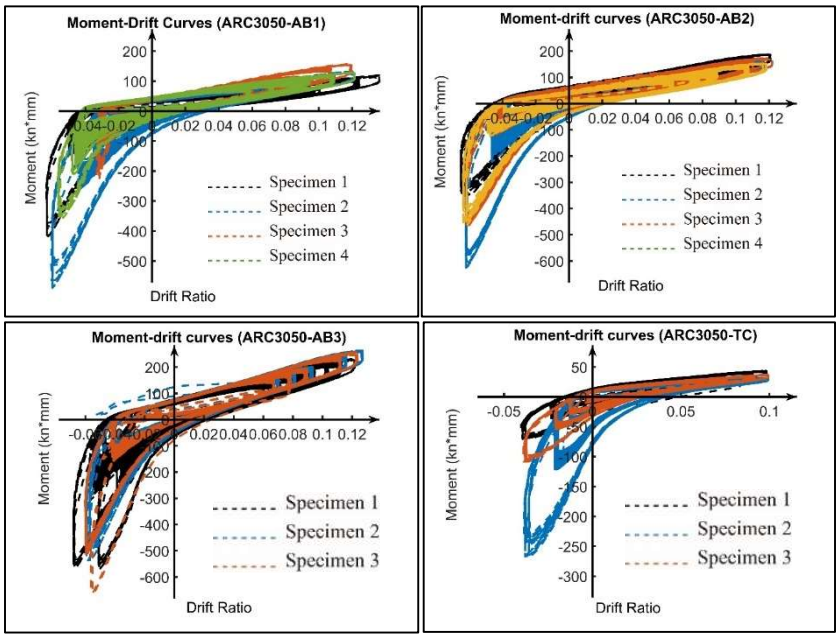

Figure 6-5:Periodic moment-drift curves for each group

- **ARC3050-AB2**

The detailed load and rotation ratio curves for different loading sequences are plotted in Figure 6-6. The dissipated energy and damping ratio for this group in a counterclockwise direction is shown in Figures 6-7 and 6-8. The energy dissipation value grew from 0.004kn*mm to 0.013kn*mm between 7mm and 12mm loading displacement. Regarding the equivalent damping, the minimum average value is 6.1% which occurred at 7mm, and the maximum average occurred at 12mm, with a value of 8.2%.

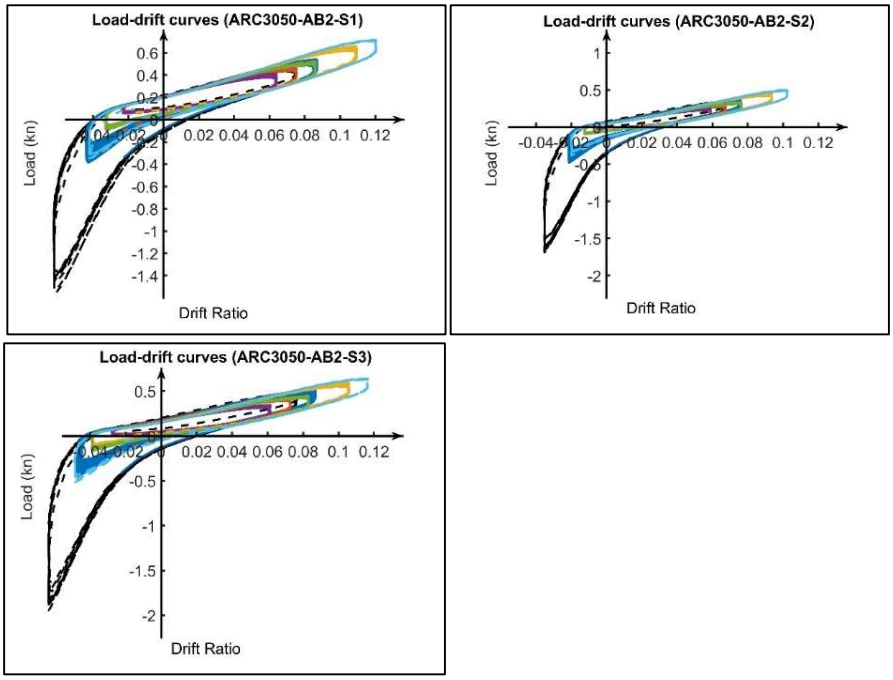

Figure 6-6: Cyclic Moment-Drift curves for each specimen

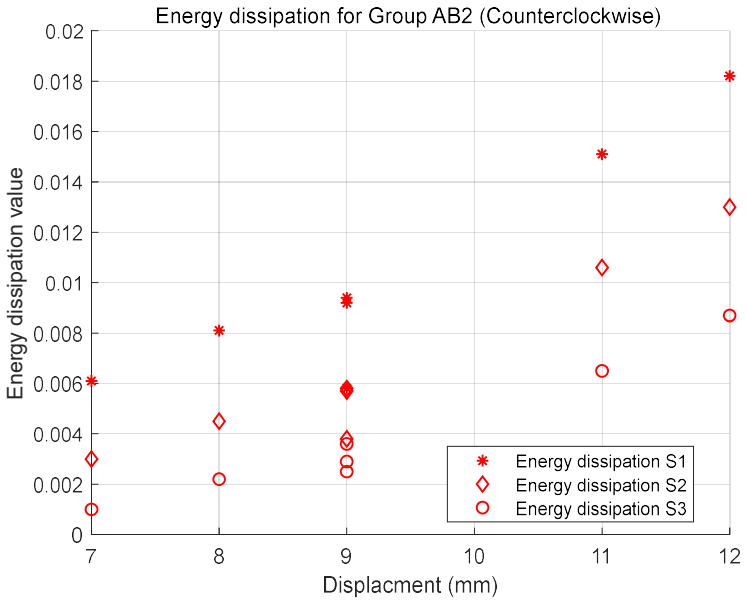

Figure 6-7:Energy dissipation of ARC3050-AB2

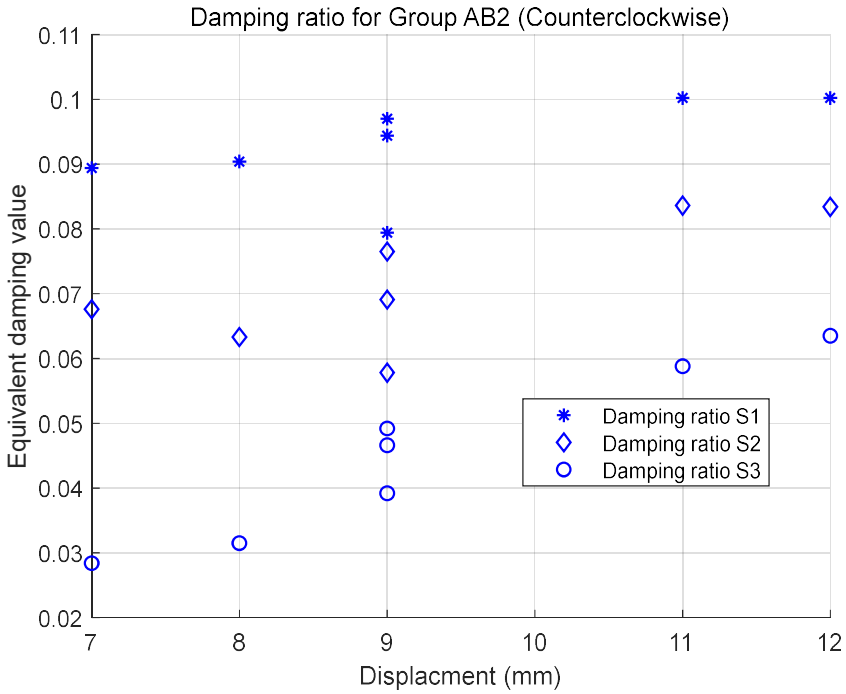

Figure 6-8:Equivalent equivalent damping ratio of ARC3050-AB2

Figure 6-9 shows the dissipated energy in the clockwise direction, and the average values at 1mm,2mm,3mm and 5mm loading displacement are 0.0009kn*mm,0.002 kn*mm,0.006 kn*mm and 0.03kn*mm. The average damping for three specimens varied between 22.9% and 53.2% at different loading displacements (Figure 6-10). The maximum damping ratio in this direction is around six times that in the counterclockwise direction.

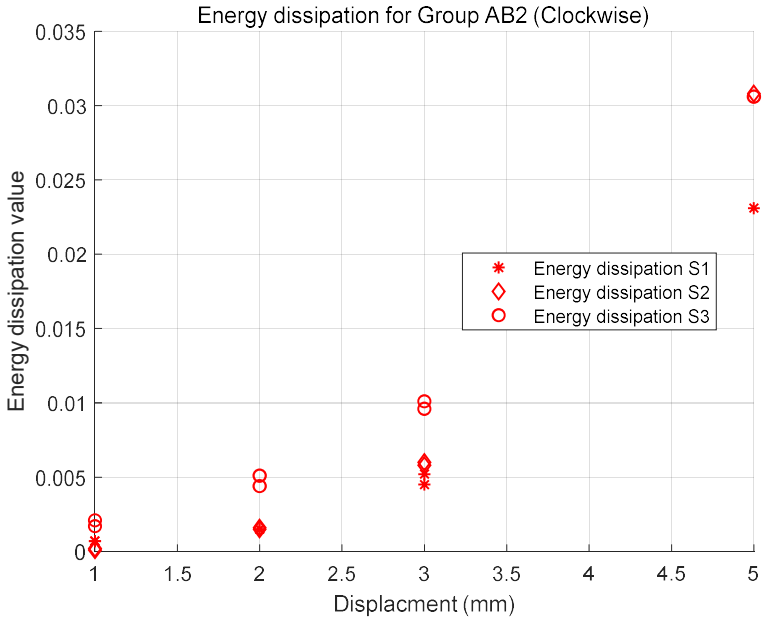

Figure 6-9:Energy dissipation of ARC3050-AB2 in the clockwise direction

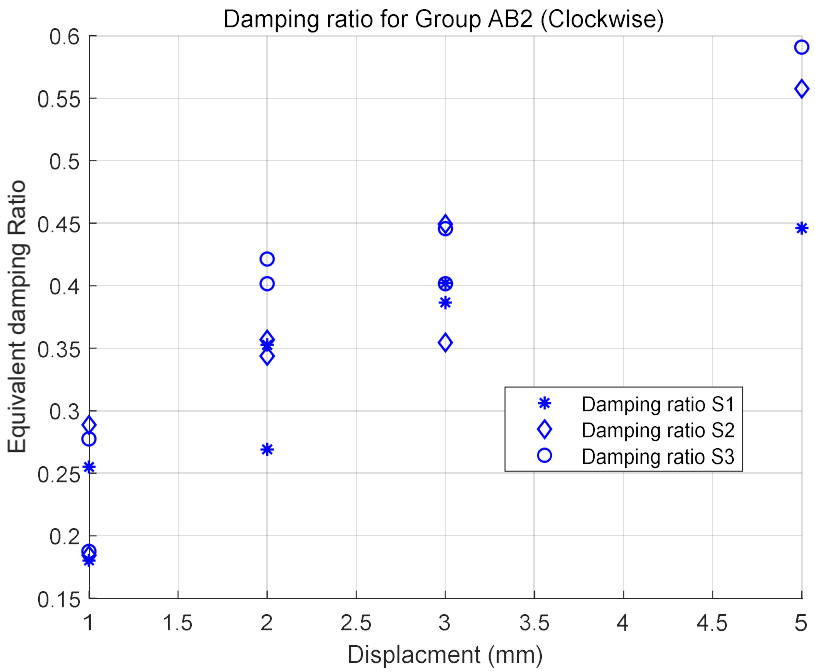

Figure 6-10: Damping ratio of ARC3050-AB2 in the clockwise direction

- **ARC3050-AB3**

Figure 6-11 shows the cyclic load and rotation ratio curves for each loading sequence, and Figure 6-12 shows the energy dissipation in the counterclockwise direction in this group. The maximum value occurred at 12mm displacement with a value of 0.022kn*mm. Similarly, the maximum damping happens at 12mm displacement with a value of 8.97% (Figure 6-13). Both energy dissipation and equivalent damping increased with the loading displacement. For the other direction, the results are shown in Figures 6-14 and 6-15. They have a similar trend with the counterclockwise direction which values increased with the loading displacement. The maximum dissipated energy and damping are at the 5mm displacement with the average value of 0.038kn*mm and 64%.

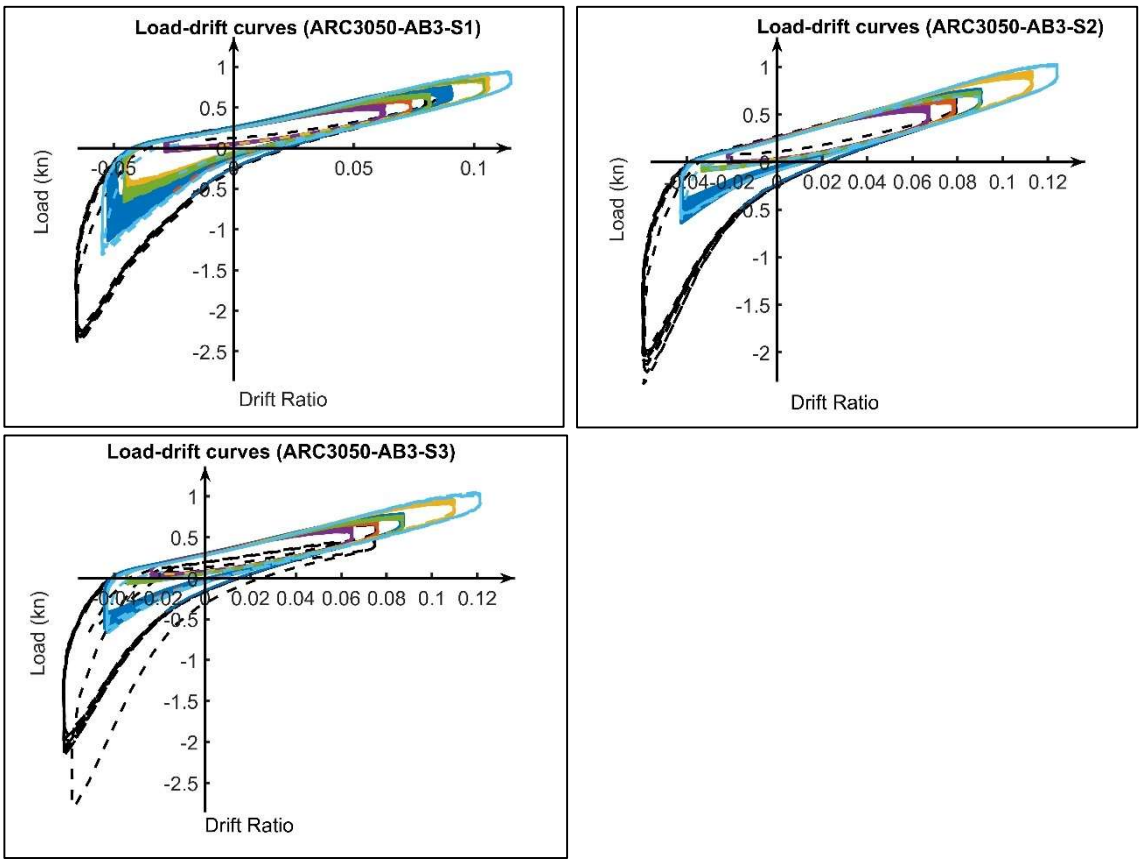

Figure 6-11: Cyclic Moment-Drift curves for ARC3050-AB3

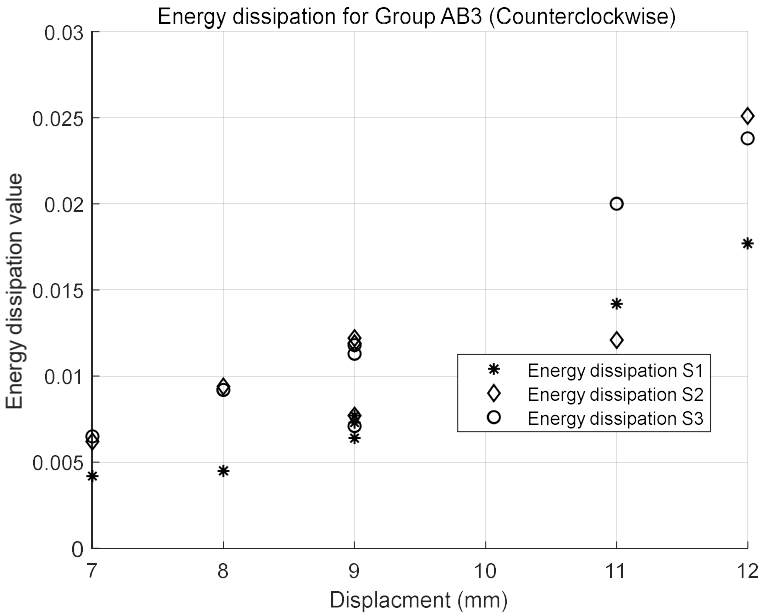

Figure 6-12:Energy dissipation of ARC3050-AB3 Counterclockwise direction

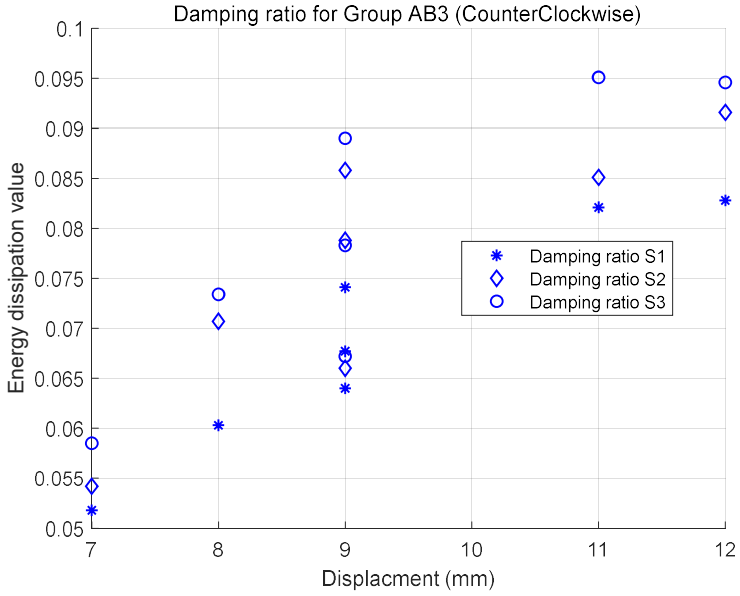

Figure 6-13:Equivalent damping of ARC3050-AB3 Counterclockwise direction

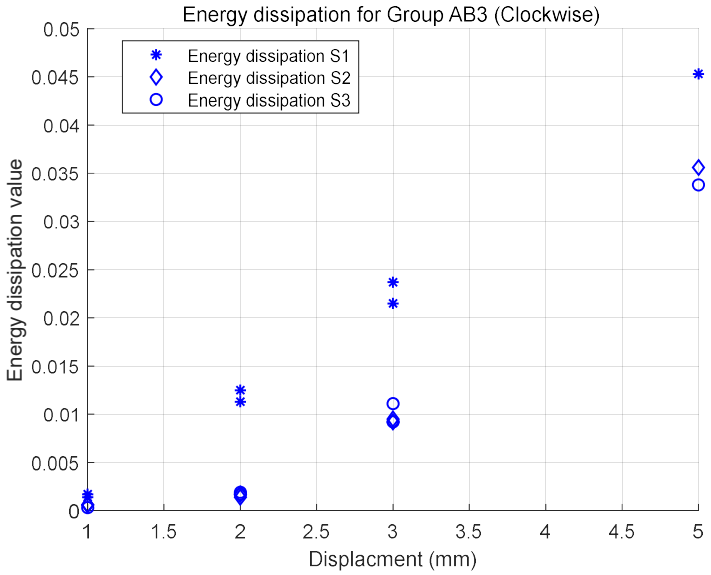

Figure 6-14: Energy dissipation of ARC3050-AB3 in the clockwise direction

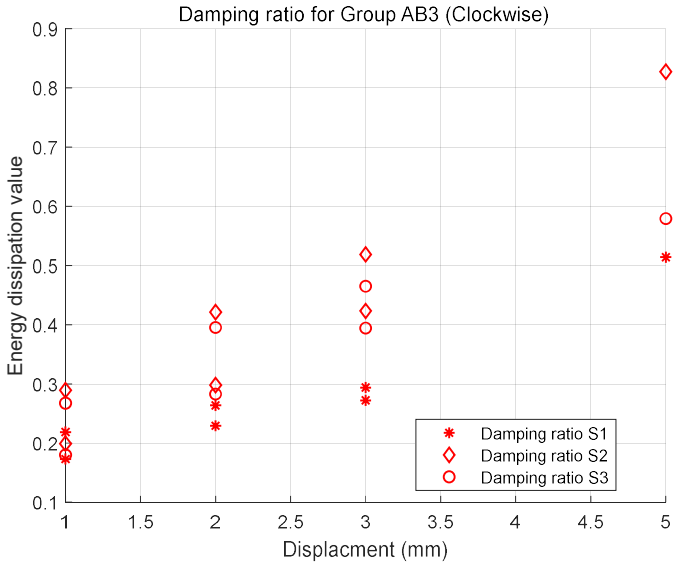

Figure 6-15: Equivalent damping of ARC3050-AB3 in the clockwise direction

- **ARC3050-TC**

Figure 6-16 shows the cyclic load and rotation ratio curves for ARC3050-TC. The damping and energy dissipation values in counterclockwise directions are shown in figures 6-17 and 6-18. The average energy dissipation values in 7mm, 8mm, 9mm,11mm, and 12mm are 0.0021kn*mm,0.0024kn*mm,0.0028kn*mm,0.0044kn*mm, and 0.0049kn*mm. The maximum damping in this direction is 10.89% at 12mm displacement. Figures 6-19 and 20 show the results for the other direction, and the dissipated energy values at 1mm, 2mm, 3mm and 5mm loading displacement are 0.00023 kn*mm,0.0017 kn*mm,0.0053 kn*mm and 0.014 kn*mm. The average damping values at the loading displacement mentioned above are 21.7%,32.2%, 37.7% and 50%, respectively.

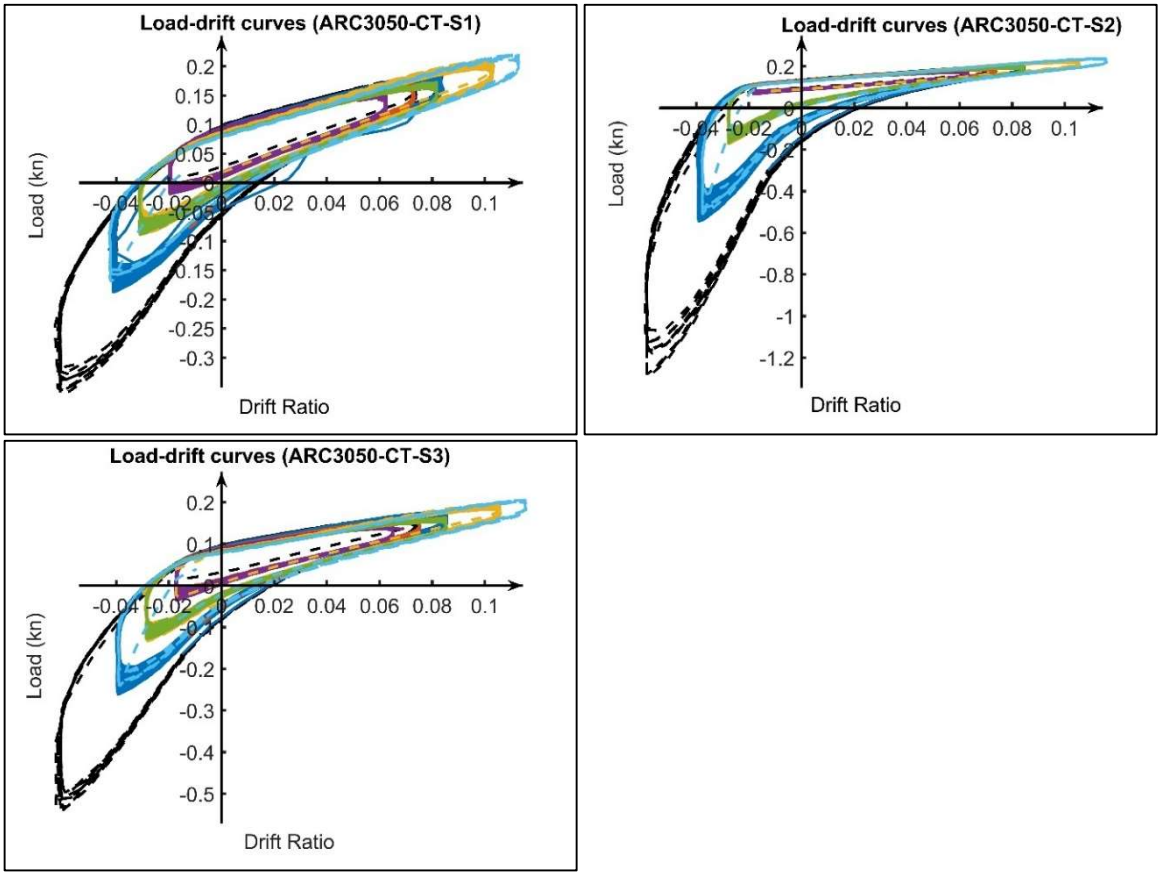

Figure 6-16: Load-rotation ratio curves for group ARC3050-CT

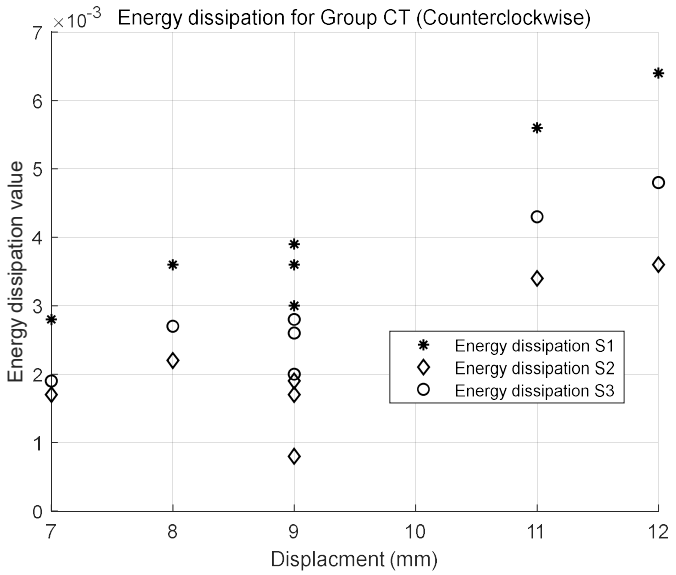

Figure 6-17: Energy dissipation of ARC3050-CT group in the counterclockwise direction

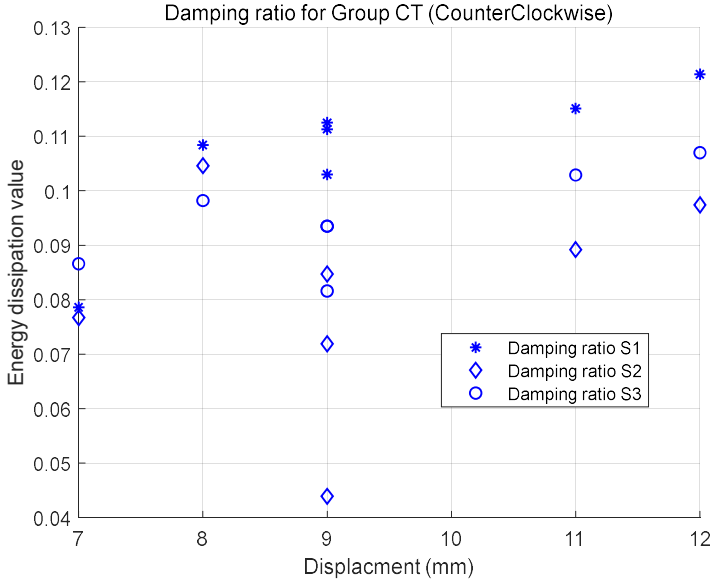

Figure 6-18: Equivalent damping of ARC3050-CT in the counterclockwise direction

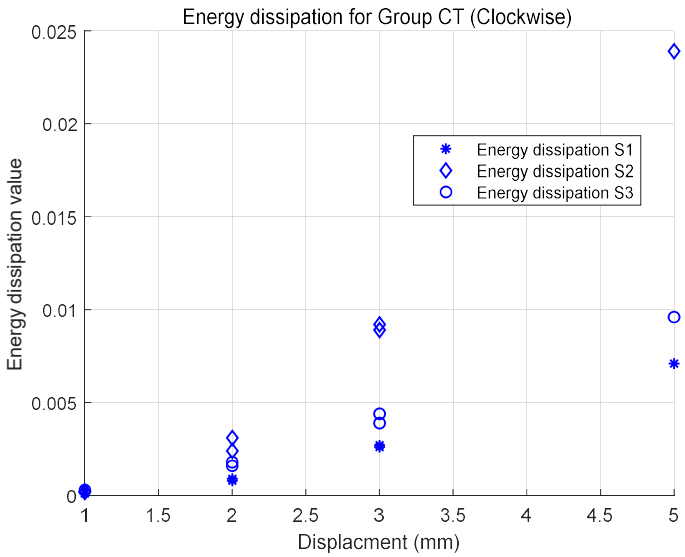

Figure 6-19: Energy dissipation of ARC3050-CT group in the clockwise direction

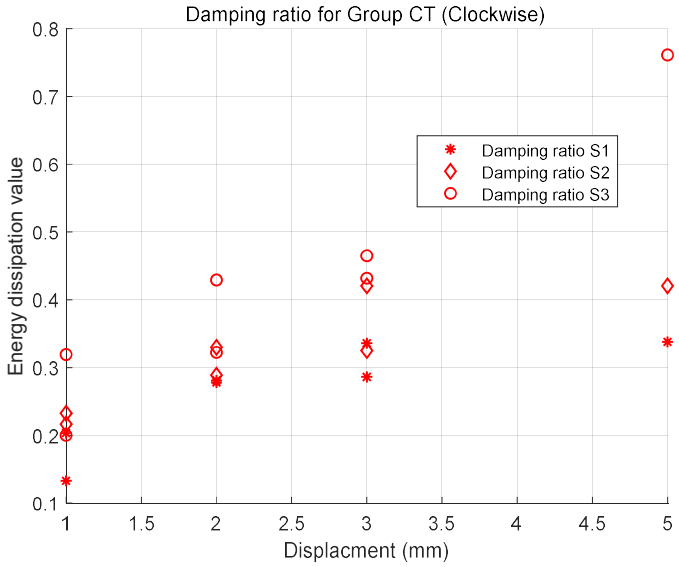

Figure 6-20: Equivalent damping of ARC3050-CT group in the clockwise direction

- **Comparison**

Figure 6-21 shows the strength reduction calculated from each specimen's load and rotation ratio curves. For all specimens, the largest value of strength reduction occurs in the clockwise direction at sequence 2nd. Then the clockwise strength reduction value at the first sequence was the second largest. In this cyclic test scheme, both sequences have the most significant number of cycles and displacements in the clockwise direction. Also, according to Figure 6-21, the loading displacement in the clockwise direction has a more significant effect on strength than in the counterclockwise direction. The average strength reduction of the four groups is shown in Figure 6-22. The figure shows that the strength reduction values for ARC3050-TC are less than the other three groups in both directions, which indicates that the cyclic test has less effect on the strength of the angle bracket than the fasteners. Comparing the values between groups AB1 and AB2 shows that adding plates that change the nailing pattern to the stressed wood members increases the load-carrying capacity clockwise but has no significant effect on the other directions. In the case close to those of group AB2.

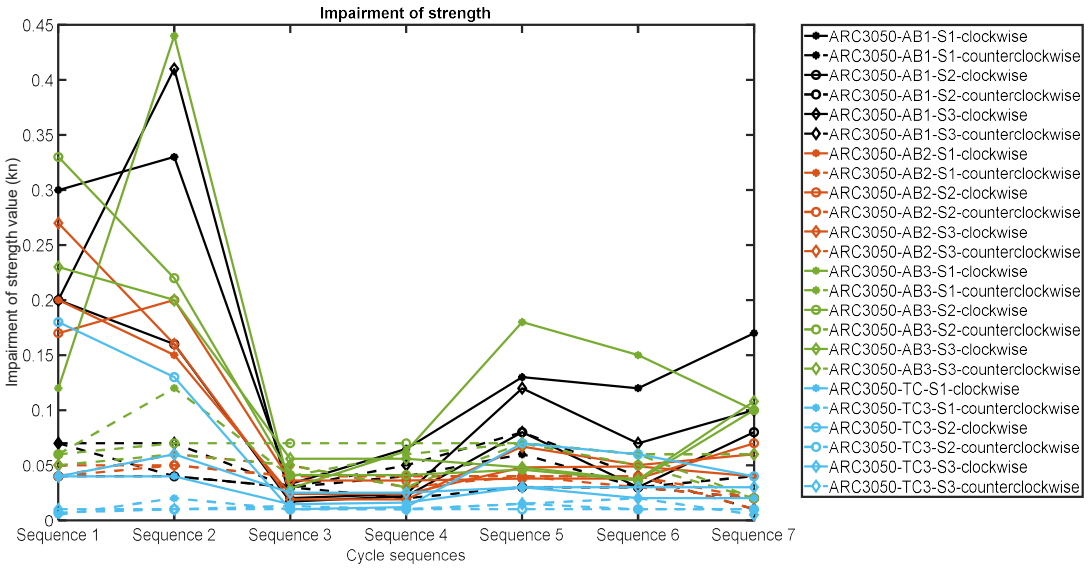

Figure 6-21:Average intensity reduction for all specimens in each sequence.

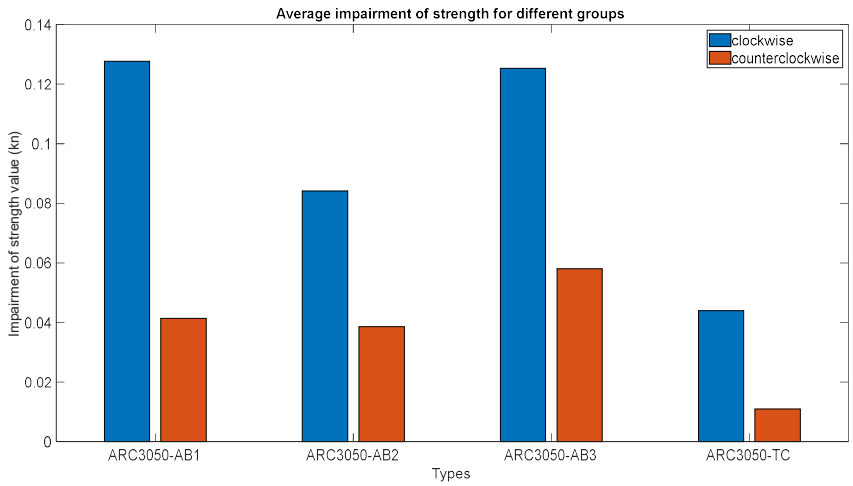

Figure 6-22: Comparison of mean strength decreases for the four groups

Figure 6-23 shows the four groups' whole connection system damping ratio. The damping ratio for groups AB2, AB3 and TC increased compared with the group ARC3050-AB1. The average damping ratios for AB1, AB2, AB3 and TC are 9.4%,10.3%, 11.1% and 14.3%, respectively. Figures 6-24 and 25 show that the damping ratio for groups AB2 and AB1 in the counterclockwise direction is close. However, in the clockwise direction, the value for AB1 is smaller than AB2 at 1mm, 2mm and 3mm displacement, indicating that adding nails to the stressed flange can increase the damping of the angle bracket connection system.

Furthermore, comparing AB1 and AB3 shows that choosing the higher strength angle bracket can also increase the system damping. Although the strength of TC groups is lower than other groups, the damping ratios are significantly higher than those of the other three groups. Figures 6-26 and 27 compare the damping ratio in two directions between the group TC and AB2. The results show that the two groups' damping ratio is similar in the clockwise direction, but in the other direction, the values of the TC group are higher than AB2 at the same loading displacement. This indicates the complexity of the angle bracket system that the damping cannot simply be judged by the number of nails or the strength of the angle bracket.

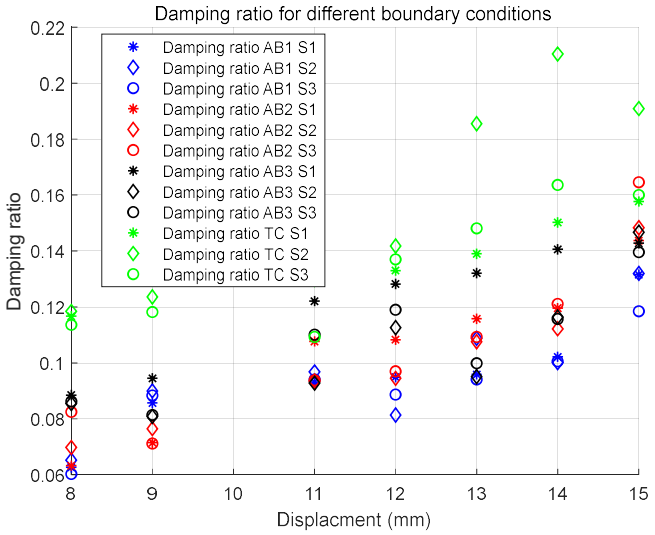

Figure 6-23: Comparison of equivalent damping for four groups

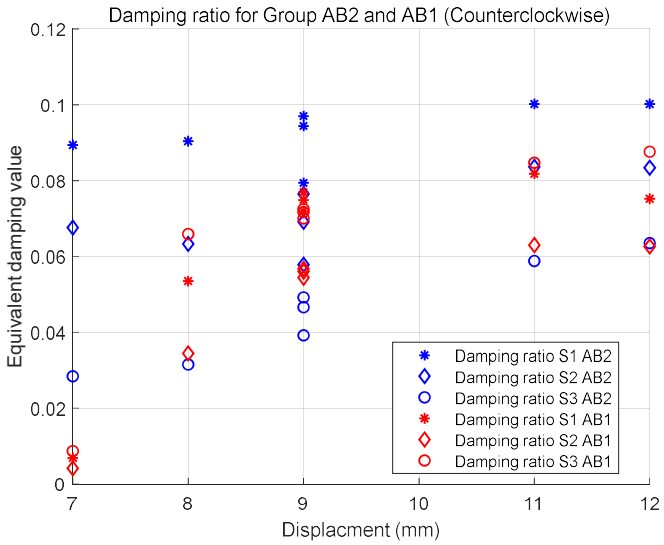

Figure 6-24: Comparison of equivalent damping in the counterclockwise direction for AB1 and AB2

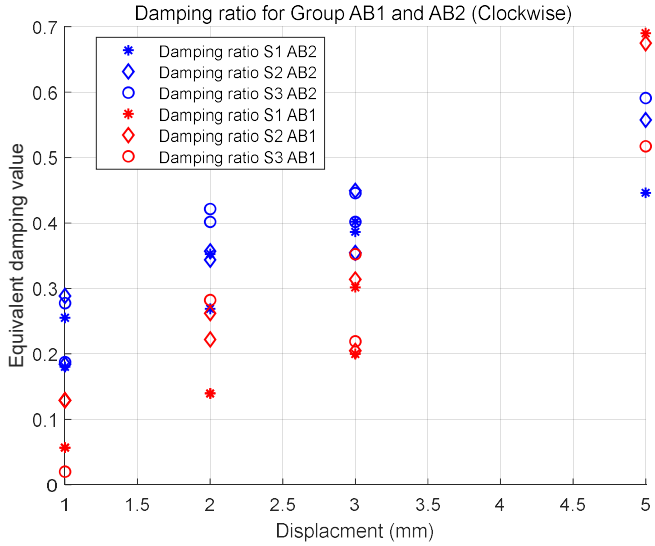

Figure 6-25: Comparison of equivalent damping in the clockwise direction for AB1 and AB2

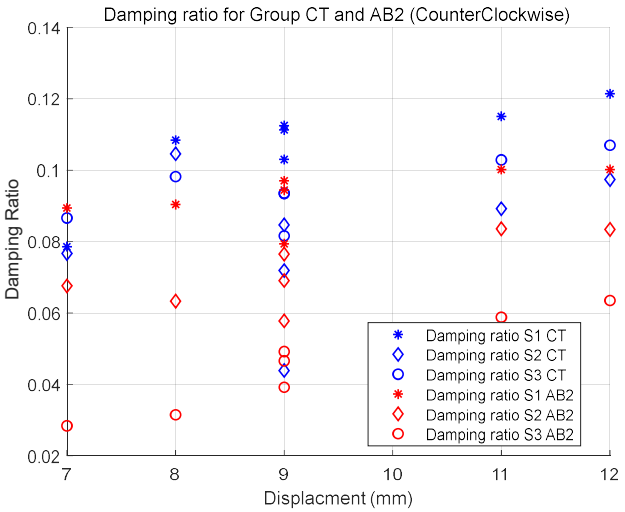

Figure 6-26: Comparison of equivalent damping in the counterclockwise direction for CT and AB2

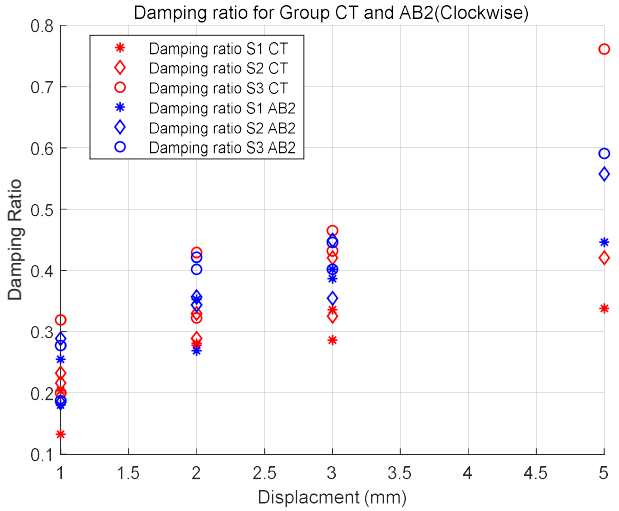

Figure 6-27: Comparison of equivalent damping in the clockwise direction for CT and AB2

6.3.2 Residual of stiffness after cyclic test

1) Monotonic load in the counterclockwise direction

From the side view (Figure 6-28), all three groups of specimens twisted after a -50mm monotonic load. The front view of the specimens (Figure 6-29) shows that the gap between the stresses caused by the forces and the fixed components is more pronounced in the third set of specimens than in the other two sets. Figure 6-30 shows the details of the connection. Unlike ARC3050-AB2, the fasteners in the other two groups were not pulled out. However, there was significant sheet metal deformation near the bolts in ARC3050-TC. In addition, there was no visible damage to the wood or concrete blocks.

Figure 6-28: Side view of the specimen ARC3050-AB2(left), ARC3050-AB3(middle) and ARC3050-TC (right) after cyclic and monotonic load

Figure 6-29: front view of the specimen ARC3050-AB2(left), ARC3050-AB3(middle) and ARC3050-TC (right) after cyclic and monotonic load

Figure 6-30: Connection details of the specimen ARC3050-AB2(left), ARC3050-AB3(middle) and ARC3050-TC (right) after cyclic and monotonic load

Figure 6-31 shows that the percentage of groups AB1, 2 and 3 increases with increasing rotation ratios, indicating a stiffness recovery. For these three groups, the load-carrying capacity depends on the nails, and the cyclic tests caused loosening of the nails or resulted in pull-out or cumulative fatigue damage. However, the cyclic tests did not cause complete failure of the joints or nails. As the drift rate increased, the portion of the nail embedded in the base continued to provide resistance after contact between the sheet metal and the nail, resulting in a stiffness recovery. For the TC group, the percentage decreased as the drift rate increased, and no stiffness recovery was observed. This indicates that the stiffness and strength of the joints with angle brackets are closely related to the corner fasteners in the early stages. Furthermore, according to Figures 6-32, the percentages for the three groups decreased and remained stable between 0.02 and 0.08, which implies that ARC3050-AB1 showed a greater decrease in resistance between 0.02 and 0.08 drift rates than the other groups.

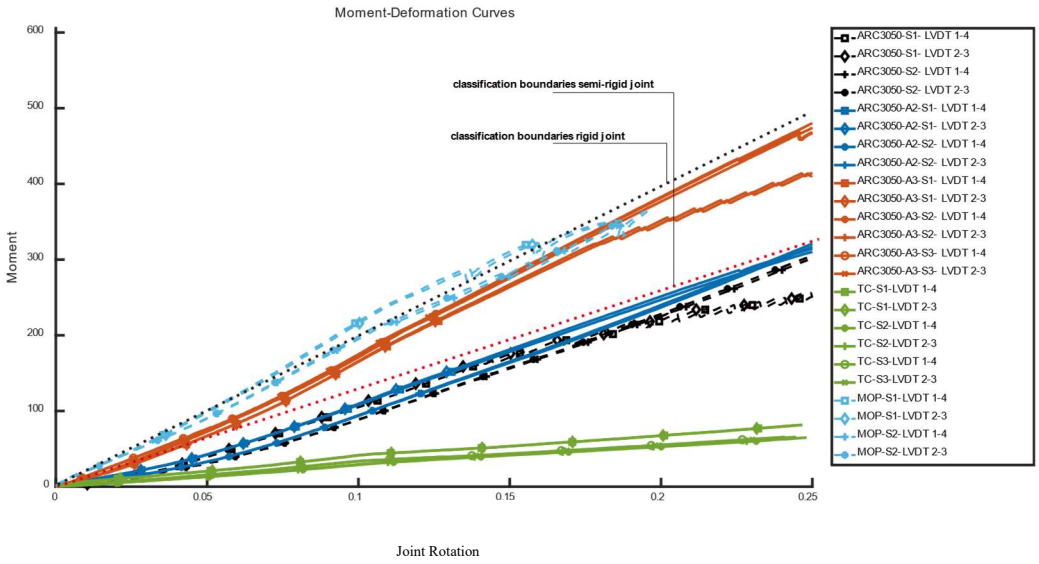

Figure 6-31: Moment-rotation ratio curves for each group

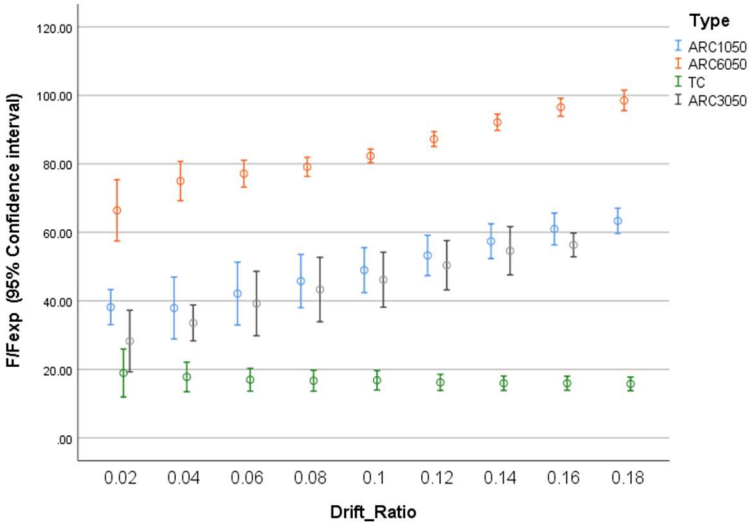

Figure 6-32: percentage of load for the cyclic groups to MOP

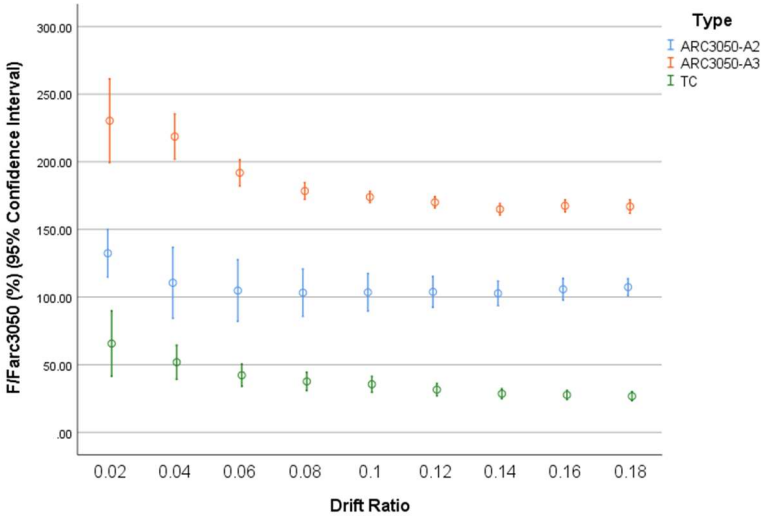

Figure 6-33: Percentage of load for the cyclic groups to ARC3050

1) Monotonic load in the clockwise direction

Figure 6-34 shows detailed connection pictures for ARC3050-AB1 and ARC3050-AB2 after lateral monotonic load clockwise. For boundary condition AB1, it is clear that the plate on the stressed timber member bent significantly, and the nails on the base timber component were pulled out. Differently, for connection AB2, visually, the bending of the plate on the stressed member is smaller than that former but more significant on the fixed member

Figure 6-34: connection details after the monotonic test

The numerical information is shown in Figure 6-35. The stress and rotation ratio curves show that in the elastic phase, AB2 has a higher stiffness in the clockwise direction than AB3.AB2 reaches the yield point at a ratio of 0.1 and has a yield strength of 0.375 Mpa. For AB3, the yield point is at a ratio of 0.15 and has a yield strength of about 0.385 Mpa. The results show that adding nails at the corners of the plate on the stress number increases the stiffness but reduces the ductility of the joint.

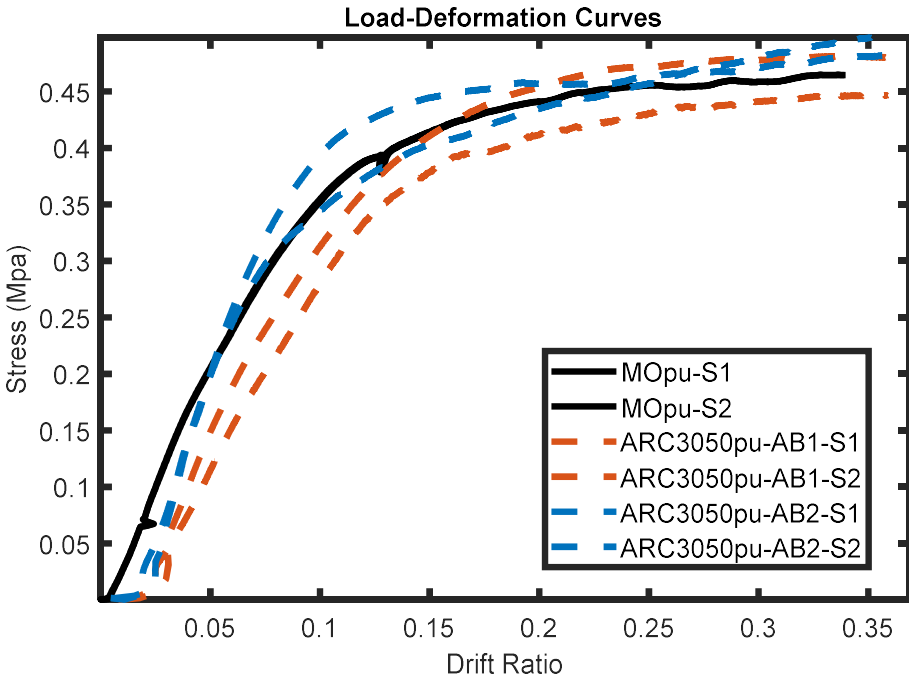

Figure 6-35: Loading-Drift curves for each group

6.3.2 DIC results

The DIC method was used to analyse the deformation of the samples further. This research used the free software GOM Correlate system to study the DIC images. First, pictures of the ARC3050-AB2 and AB3 groups in the same loading sequence were analyzed for comparison. Figure 6-36 shows the selected points of the DIC software's cyclic strain ratio curves, and Figures 6-37 and 6-38 show the strain ratio curves for the different groups. The two groups are the same, with the strain concentrated on the boundary between the sheet metal and the wood, where point 1 is higher than the other two. The peak in these two groups is around 0.9%, which is lower than the ARC3050-AB1 group (in Chapter 5), indicating that the relative motion between the metal plate and the wood is lower than AB1.

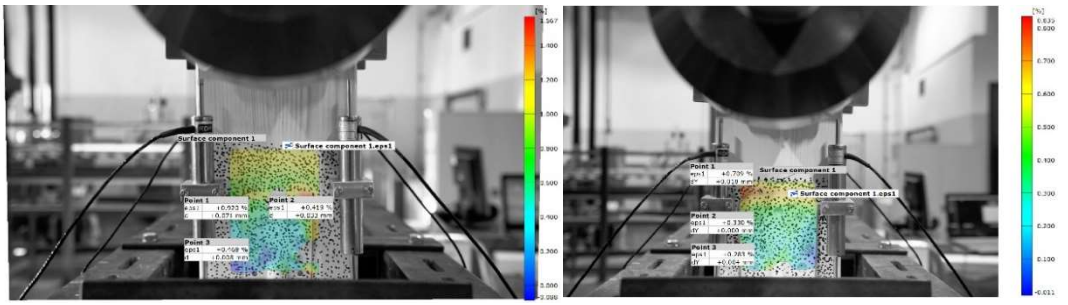

Figure 6-36: Points selected in DIC analyses for groups ARC3050-AB2(left) and ARC3050-AB3 (right)

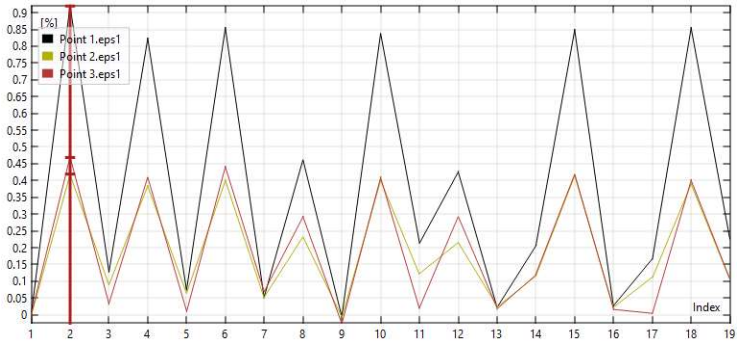

Figure 6-37:Cyclic strain rate for ARC3050-AB2 group

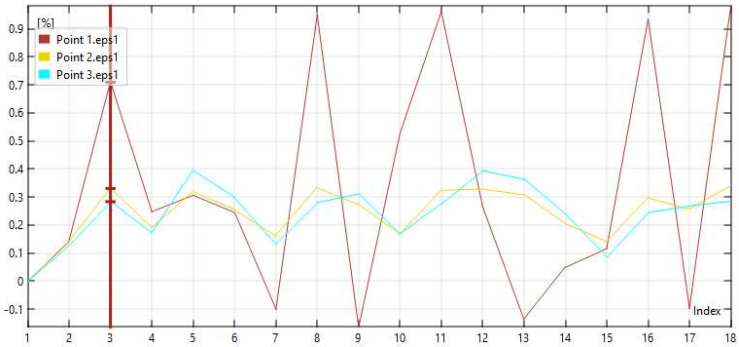

Figure 6-38: Cyclic strain ratio for group ARC3050-AB3

Then, Figure 6-39 shows the selected points on samples ARC3050-AB1 and ARC3050-AB2 for strain and displacement analysis during the clockwise monotonic loading. According to Figure 6-40, the displacement difference between three points in the group ARC3050-AB2 is smaller than that in the other group and has a slightly lower changing rate, and this may be the main reason that, in Figure 6-41, the strain ratio difference between two groups is significant. It means that adding fasteners can increase the vertical loading capacity.

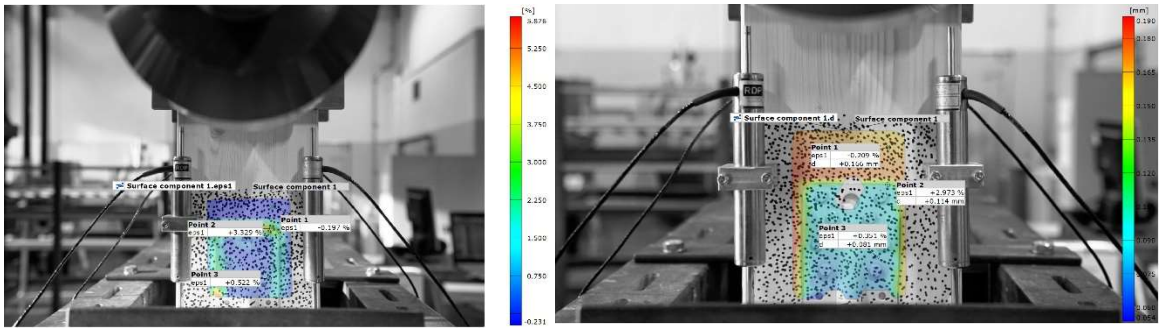

Figure 6-39:Point selection for two samples (ARC3050-AB1: left, ARC3050-AB2: right)

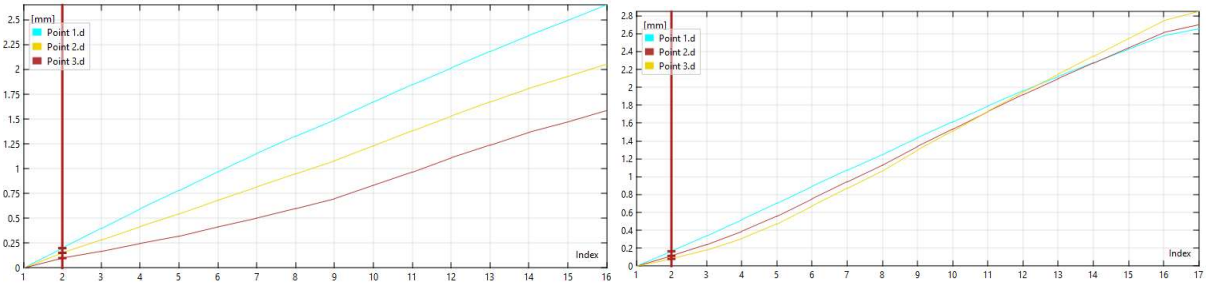

Figure 6-40:Displacement of selected points (ARC3050-AB1:left, ARC3050-AB2:right)

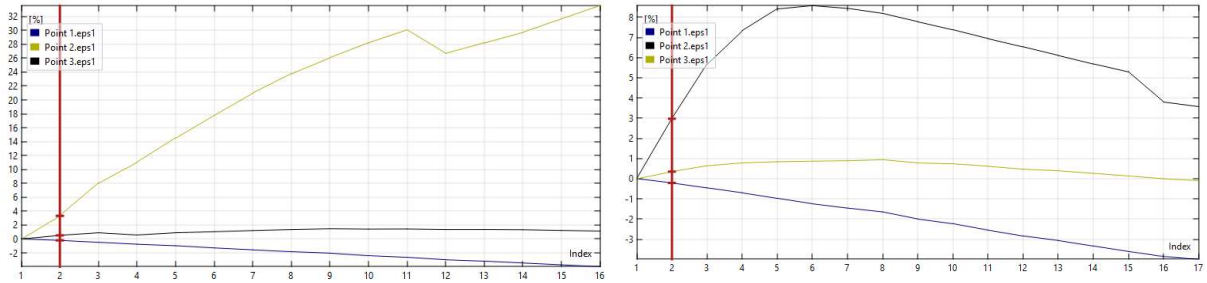

Figure 6-41:Rotation ratio of selected points (ARC3050-AB1:left, ARC3050-AB2:right)

6.4 Summary

In summary, this part of the study analyzed the performance of different joint boundaries under cyclic testing using a new 30 m height wind loading sequence. Three conditions, including varying the nailing pattern, angle bracket type and fixing material, were investigated and compared with the control ARC3050-AB1. The DIC method was again applied in this section. The results showed that the stiffness of the joint after cyclic testing was related to the design strength. The fasteners around the corners provide resistance to rotation, so the nailing pattern can greatly affect the stiffness and strength of this type of joint system. Angle brackets with a bolt hole away from the corner do not appear suitable for rotation-resistant joints, so choosing angle bracket type is important when joining timber to steel or concrete. In addition, the timber connections of the angle brackets used in this test can be seen as semi-rigid connections, and the increased flexibility of these connections after cyclic loading may need to be considered in the long-term performance structural design. In terms of system viscous damping, the value increased when adding more nails to the stressed flange by comparing AB1 and AB2. And increasing the strength of the angle bracket can also increase the damping of the connection system.

Chapter 7. Application: Life-cycle assessment considering the connectors service time

7.1 Introduction

In recent years, due to the transformation of the construction sector into one of the biggest energy consumers, timber has been widely accepted as one type of sustainable building material replacement that can reduce energy consumption and adverse environmental impact. The literature review in Chapter 2 shows that engineered timber buildings can provide a better thermal environment. Additionally, the energy for timber production is less than RC and steel buildings. To provide further evidence, some research's life cycle assessment methods indicate that engineered timber buildings can save energy and reduce CO_2 impact in both material production and operation stages. Nevertheless, most research ignored the repair and replacement stage of CLT buildings. Results from previous Chapters evince that the fatigue caused by along-wind pressure can influence the connection stiffness of high timber buildings. Structural life or service performance will be further affected by the reduction of the indices of stiffness and strength, leaving the maintenance or replacement with a lifecycle over 50 years.

This chapter aims to use the life-cycle assessment method to analyse the energy consumption and environmental impact of a CLT building with the repair and replacement of the angle bracket connection system. Comparison among different repair scenarios can demonstrate the importance of the repair stage in a life cycle assessment in CLT building analyses. The comparison between the energy consumption and CO_2 emissions of CLT and RC buildings and the indication of the energy efficiency potential of the CLT building is also included in this chapter.

7.2 Concept of life cycle assessment

The Life Cycle Assessment (LCA) is a standard method to analyse a product's or service's environmental impact from raw material to the end of life. The standards of LCA develops in the following steps: the first official LCA standard was published in 1994 called Z-760 Environmental Life-cycle Assessment(Ali et al., 2014); then, the ISO 14040, published by International Standards Organization, was widely accepted in recent years, which introduced the basic framework including four phrases of goal and scope definition, inventory analysis (LCI), impact assessment (LCIA) and interpretation analyses(Scheuer et al., 2003).

Goal and scope definition is the first step of LCA to clarify the boundaries and features of a study(Penadés-Plà et al., 2017). A product or service boundary typically includes four parts: raw material production, manufacturing, operation or usage, and end-of-life. Due to the disparities in research goals, not all aspects are involved in a study, which means that the LCA can be divided into three types 'cradle-to-grave', 'cradle-to-gate' and 'Gate-to-Gate'(Sahoo et al., 2019). The phrase includes product recycling can be defined as the 'cradle-to-cradle' type(Ali et al., 2014). Figure 7-1 exhibits the boundaries for standard LCA. The functional unit, period, impact indicator considered, and data quality required will be specified in this stage(Tupenaite et al., 2021). In addition, the functional unit and time depend on the product or service characteristic concerned in the study(Corporation and Curran, 2006).

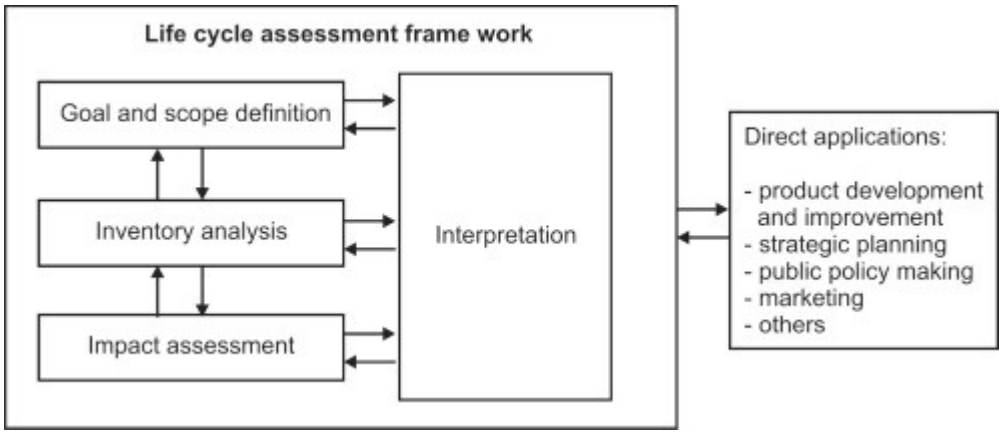

Figure 7-1: LCA framework from ISO 14040

LCI is the second step in LCA, aiming to collect input data for all relevant boundaries defined in the previous step, of which data type depends on the impact that can be quantified

energy, emissions, solid wastes, or capital of a product in specified life-span. There are mainly three approaches to the LCI, including input-output (IO) analysis, process-based analysis, and Hybrid process-based analysis, all of which will be detailed and introduced in subsequent content.

LCIA includes two phases, which are the midpoints and endpoints methods. The midpoints method is utilized to figure out the results of environmental impact factors from one industry or product, of which endpoint is the damage-oriented method aiming to point to the final influence of the environment, people's health or resources (Bare et al., 2000). After the step of LCI, the environment or economic impact is calculated with the input data from different LCI based on other assessment models and results from assessment in LCIA and interpretation stage. The impact assessment requires tools such as OpenLCA, GaBi, and SimaPro, a program or assessment table built with Matlab, Python or Excel can also be applied (Stadler, 2021).

7.2.1 Different Life-Cycle inventory methods (LCI)

- Economic I-O method

The I-O method is a top-down approach to collecting data required for LCA following the economic transactions of a targeted sector. Leontief (Leontief, 1936)built the model for the I-O method in 1936 for economic system assessment, in which the function for the economic output (x) of the selected product sector (y) is as follows:

$$x = [I - A]^{-1}y \tag{7.1}$$

Where: I is the identity matrix, and A is the technical matrix of all correlated sectors.

Then, Hendrickson applied this model to the environmental impact assessment(Hendrickson et al., 1998) and accordingly developed the following equation:

$$f = Ex = E[I - A]^{-1}y \tag{7.2}$$

Where: f is the final footprints of the selected sector, and E is the environmental indicator output matrix(Chang et al., 2016).

In practice, the I-O tables are applied to calculate the material, energy and capital used during the economic transactions of the targeted sector (Bullard and Herendeen, 1975). The tables can be divided into 400-500 categories and vary from region to region (Bawden and Williams, 2015). Furthermore, the selection of the I-O table also depends on the boundaries defined in the former step. Because the services in the related sectors are involved in the input data, the results of this method are higher than those of other methods. With time-saving as one of the method's benefits, related data for all sectors are aggregated in the database, and the only information users need to extract is the cared data. However, these aggregated sectoral data can solely represent the average state of an industry and can not apply to individual products.

- **Process-based method**

The process-based method focuses on the impact of representative products and is the down-to-top approach from the physical perspective (Bawden and Williams, 2015). The basic processes of this method consist of quantitive determination of the material and energy needed for the selected products and the analysis of the emission or waste caused during the manufacturing or operation stages. What is shown in Figure 7-2 is the typical boundaries for the process-based method. Compared with the I-O method, this approach is more complex and time-consuming to a great extent, with weak accuracy in economic efficiency analyses. Despite all of those factors, it is still widely applied in research, especially for comparing products within one industry (Castellani et al., 2019).

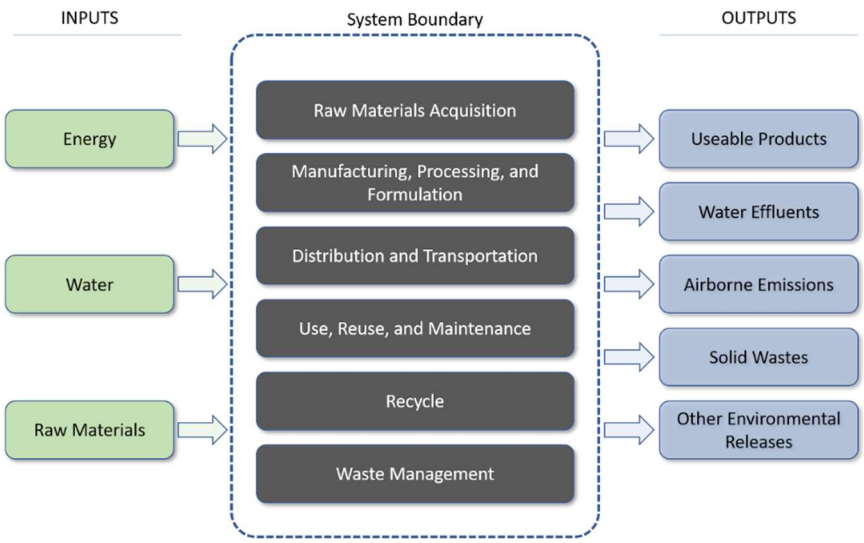

Figure 7-2: process-based inventory analysis

- **Hybrid process-based method**

The hybrid process-based method combines O-I and process-based methods to elaborate the advantages of each method and reduce errors (Bullard et al., 1978). The combination of two methods in a different stage of an LCA elastically depends on the access of the database, following the following equation (Bawden and Williams, 2015):

$$Etotal = E_{material} + E_{\text{manufacturing}} + \text{E}_{\text{operation}} + \text{E}_{\text{end}} \quad 7.3$$

Although this method does not mean more accuracy when compared with the other two methods (Yang et al., 2017), it provides flexibility for a different industry. Yang (Yang, 2017) pointed out that this method is suitable for pivot sectors that do not primarily rely on human or natural resources and capital with a relatively rigid production process.

In conclusion, the choice of LCI methods is based more on the characteristics of the target industrial structure and the research goals. The hybrid and O-I methods are suitable for environmental impact research coherent to the economic effects, and the process-based approach is better for single products or studies coherent to energy effects. The selection of methods can further influence the application of the database provided by EXIOBASE 3, which can give the I-O table for around 200 products in 163 industries of different regions and is typically used for economic Multi-Regional Input-Output research (Stadler et al., 2018). In the production level research, data in Ecoinvent can be utilized as a supplement to the scientific literature (Weidema et al., 2013, Castellani et al., 2019). Some regional or sectoral databases are also available for free usages, such as the US LCID, BEES, and Product Environmental Footprints (PEF) (Abd Rashid et al., 2015). By the diversity of boundary conditions in research, no database can be regarded as complete. Therefore, in practice, combining data from various databases can occur (Ortiz et al., 2009, Khasreen et al., 2009b).

7.2.2 LCA in the construction sector

With the growth of attention paid to the construction sector's environmental impact, research with the LCA method has increased since it was applied in 1990 (Khasreen et al., 2009a). The method in the building industry includes the following procedures: evaluation of energy, emission, and economic impacts. Based on the principle of LCA, the application has been modified due to the complexity of the building sector (Abd Rashid et al., 2015). There are different scales of LCA in the building industry, which can be divided into building material, whole building process and building industry assessment (Ortiz et al., 2009). The assessment boundaries for this sector, following the EN15978, can be classified into five main stages: production, construction, operation, end-of-life and supplementary benefits. The detailed system boundary classification is shown in Figure 7-3. In terms of functional units, researchers prefer per square meter ($1m^2$) of floor area, the concerned part of which can be the total, occupied or heated in different research (Abd Rashid et al., 2015, Ortiz-Rodríguez et al., 2010, Blengini and Di Carlo, 2010). In addition, the definition of a lifetime for buildings can also eminently influence the results. Typically, a period of 50 years is suitable for residential or commercial buildings.

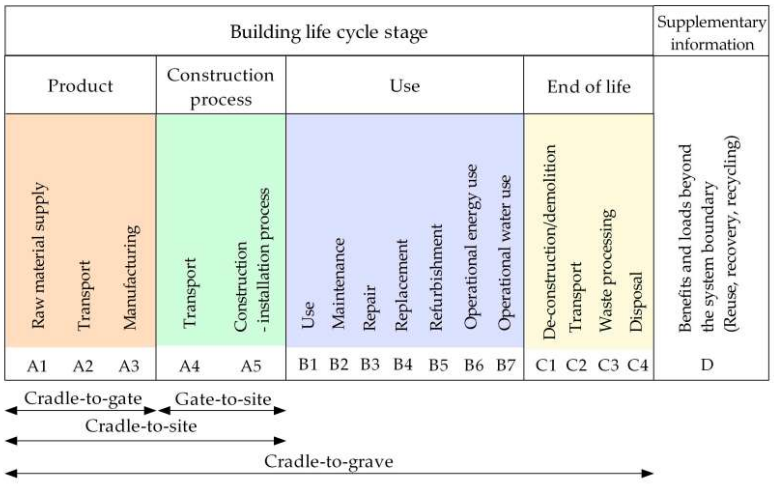

Figure 7-3: LCA boundary for the building sector (Song, 2020)

Both I-O and process-based inventory assessment methods are valid. For the process-based method, in the production stage, the first step is to acquire the material data from the quantity calculation of the drawing of a building or bill of materials (Iyer-Raniga and Wong, 2012, Blengini and Di Carlo, 2010). A literature review on the related sector for the materials cost model is a primary way for the I-O method(Bawden and Williams, 2015). In

terms of transportation and construction, most of the data are based on the literature review(Santero et al., 2011). Because these two factors account for a small proportion of the total impact, they are constantly omitted in some studies(Rossi et al., 2012). In terms of the operation stage, building energy simulation methods are widely accepted, for which available software includes IES VE(Liang et al., 2021b), energy plus(Santero et al., 2011), ECOTECT(Utama and Gheewala, 2008). As for the rest stages, which include maintenance, end-of-life and material recycling, reasonable assumptions can be acceptable when scarce data is available (Blengini and Di Carlo, 2010, Santero et al., 2011).

There are mainly two perspectives to evaluate the environmental impact on the construction sector: energy and economics, and these two methods have different effects determined by the purpose of the study. Energy-based LCA could cause research problems of energy-saving in architecture design, material selection or HAVC system management. The economic-based method can influence the decision-makers in deciding the project or policy(Ozbay et al., 2004).

- Energy-coupled building LCA

The energy of buildings can be divided into embodied and operation. Research pointed out that the operation stage contributed to the largest energy consumption during the whole life span, ranging between 80% and 90% (Adalberth et al., 2001, Adalberth and environment, 1997). Because of the improvement of sustainable building design technology, the operation energy for passive houses or self-sufficient houses can be reduced to zero (Zimmermann et al., 2005). Whereas, it is indicated in the research that adding insulation material or a high-efficiency HVAC system can lead to higher life-cycle energy consumption of sustainable buildings than traditional ones (Sartori and Hestnes, 2007). Moreover, for conventional structures, the material accounts for 5% to 20% of the total life-cycle energy consumption, and the value can increase to 77% in low-energy buildings (Bawden and Williams, 2015). The results implied the significance of research on the embodied energy and environmental impact when LCA in buildings is related.

- Economic-coupled building LCA

There are also studies involved in the life-cycle cost analyses (LCCA) and the environmental LCA to evaluate the impact of buildings. The analysis method of economic-

coupled building LCA can be applied on different scales: building industry, single buildings or equipment in buildings providing various stakeholders with the information on the cost of building in a lifetime and may also support the decision-making process from the economic perspective(Fuller and Petersen, 1996, Fuller, 2010). Ochoa et al. (2002) used the O-I method to assess the economic activity of the residential building sector in the U.S. They noted that although the energy consumption in the construction stage occupies 5% of total energy consumption, the economic input accounted for 46% of the total. Oregi et al.(2017) have analysed the life cycle economic impact of building refurbishment, which illustrates that the raw material, construction and maintenance stage contributes to most of the economic activities. Furthermore, researchers indicated that to achieve energy savings in the building operation stage, the cost of the building may be accumulated(Tiwari, 2001, Mahdavi and Doppelbauer, 2010). Muga et al. (2008) studies on green roofs have shown a diversity where the maintenance cost for a green roof is relatively low than build-up roofs. Moreover, Bhatia et al. (2009)deemed that the cost of investment in energy efficiency technology would pay off over time, while the payback time merely depends on the policy(Blanchard and Reppe, 1998)

In conclusion, life cycle energy assessment (LCEA) and LCCA reflect the impact of the building industry on the environment in two different sides: on the one hand, reducing energy consumption can reduce the carbon emissions of the construction industry; on the other hand, the new technology may lead to a burden of expenses. Therefore, the results of different methods of analysis may effects decision-makers differently.

- Dynamic life cycle assessment (DLCA) in the building sector

DLCA method has been applied in buildings since 2013 by Collinge et al. (2013), in which the dynamic alterations caused by the environment and time during the life cycle of the building are taken into account. Many DLCA research in different sectors has focused on the effect of a policy or industrial structure adjustment, which can be regarded as the changes in economic-social progress(Pehnt, 2006, Filleti et al., 2014). Additionally, the time-dominated environmental impact changes are also relevant, i.e. global warming impact, and these can be summed up as dynamic characterization factors (CFs)(Levasseur et al., 2010). Researchers in the building sector applied DLCA to analyse the building environmental impact and indoor air quality, emphasizing the importance of considering

dynamic alterations in this field (Collinge et al., 2013, Fouquet et al., 2015, Collinge et al., 2014). However, by the complexity of this industry, plenty of dynamic influencing factors in different stages have led to difficulties in DLAC adoption comparing with some other single-product industries (Su et al., 2017). What has been suggested by Su et al. (Su et al., 2017) is the framework for DLCA in buildings, in which the dynamic factors, including technological progress, variation in occupancy behaviour, environmental factor, and policy changes. The assessment steps in this framework include the process for the static LCA method and the impact factor analyses at the end.

7.2.3 Life-cycle assessment of timber buildings

The development of energy-efficiency buildings emphasised the embodied carbon in the building industry and promoted the related LCA research of sustainable materials, including timber. Studies on the comparison of timber and other frame buildings show that because of the thermal properties of wood, the energy and carbon impact of timber buildings are less than concrete or steel frame buildings in operation stages(Cole et al., 1996, Gong et al., 2012, Liu et al., 2016). Guo et al. (Guo et al., 2017) pointed out that the energy-saving potential of timber building in house cooling and heating during the operation stage varies between 10% and 40% in different climate regions in China when compared with the concrete frame building. Additionally, in terms of embodied carbon, the researchers compared the impact of timber-based material with concrete and pointed out that the energy-saving in the manufacturing stage can be up to 80% (Gustavsson et al., 2006a, Gustavsson et al., 2006b, Ximenes and Grant, 2013, Asif et al., 2007).

Developing engineered timber made more researchers focus on the life cycle environmental impact of CLT buildings. Table 23 shows the summary of some LCA of CLT buildings. Robertson et al. (2012) compared the embodied energy and environmental performance of a reference 5-story office building and pointed out that the energy consumption of CLT is 80% higher than concrete in the raw material manufacturing stage. Durlinger et al. (2013) made the environmental assessment of the Forté building based on the process-based inventory analysis method. They compared it with a reference building, indicating lower energy, water consumption and global warming potential from CLT buildings. However, the energy consumption caused by labour and building maintenance stages is not included

in this research. Dodoo et al.(2014)used the LCA method to compare the energy consumption and CO_2 emission of different timber building systems and concluded that CLT building has the lowest embodied carbon among these three timber frame buildings. Skullestad (2016) supported the conclusion that concrete building has lower embodied energy than CLT by applying a 60-years lifecycle assessment to CLT buildings with different stories. Teh et al.(2017) discussed and analysed the possibility of replacing conventional building materials with CLT in new buildings from the perspective of the economy and construction industry. They suggested that the best phrase reduces 26 Mt CO_2 if all new residential buildings are built with timber in Australia. Jayalath et al.(2020) applied both LCEA and LCCA to compare an 8-story timber building with a reference RC building. The results show that CLT building seems more efficient in energy consumption during the lifespan but costs more money to maintain during operation. Lechón et al.(2021) designed a passiv-haus with CLT, analysed its environmental performance, and provided the design improvement for buildings in Spain. Balasbaneh (2021) compared the energy and cost efficiency of CLT and GLT buildings and concluded that CLT has less environmental impact than GLT but is more expensive.

With the application of the LCA in CLT buildings, confronting challenges are as follows: first, most LCA results confirmed that CLT buildings are more environmental-efficient than RC or steel buildings in a 'cradle to grave' phrase, but the embodied part is still in controversy; second, some research ignored the energy and cost consumed during the maintenance and repair stage, causing the environmental impact during the operation phase being underestimated; last but not least, the results from the LCCA assessment indicate that the cost-benefit of CLT seems less competitive than RC or GLT building. However, the focus on the energy-based lifecycle of CLT is more than cost-based.

Table 24: Review of LCA on CLT buildings

Number	*Researcher*	*RB*	*RB Typee*	*RB story*	*Boundary*	*LCI method*	*Coupled LCA*

1	Robertson et al,, 2012	Redesigned	Office building	5-story	Manufacturing	Process-based	LCEA and environmental LCA
2	Durlinger et al,, 2013	Forté	Residential	10-story	Cradle to grave	Process-based	LCEA and environmental LCA
3	Dodoo et al,, 2014	Redesigned	Residential	4-story	Production to end-of-life	Process-based	LCEA and environmental LCA
4	Skullestad et al,, 2016	Redesigned	Residential	3,7,12,21-story	Manufacturing	Process-based	environmental LCA
5	Teh et al,, 2017	Building industry	Residential and non-residential	-	Manufacturing	O-I based hybrid method	environmental LCA
6	Jayalath et al,, 2020	Redesigned	Residential	7-story	Production to end-of-life	Process-based	LCCA and environmental LCA
7	Lechón et al,, 2021	New designed	Residential	2-story	Production to end-of-life	Procrss-based	LCCA, LCEA and environmental LCA
8	Balasbaneh et al,, 2021	Resesigned	Residential	Single - story	Manufacturing, maintance and end-of-life	Procrss-based	LCCA, LCEA and environmental LCA

7.3 Methodology

7.3.2 Case study building

- **RC building**

The archetype building in the case study is an existing 10-story RC residential building in Shandong, China. Figure 7-4 illustrates the layout of the reference building, where the total floor area and height for this building are 4001.2 m^2 and 29m, respectively. Apart from the 1st floor, three additional apartments exist on each level. The quantity and cost for the RC building are from the bill of the buildings, in which only primary materials, including cement, pre-mixed concrete, steel, stone, brick and timber, are considered relevant with energy and environmental impact (Table 24). The RC building is constructed with an RC frame, RC floor slab and brick walls. The detail for the energy efficiency design of the building systems based on the Design Standard for Energy Efficiency of Residential Buildings in Severe Cold and Cold Zones in China (JGJ26－2010) is shown in Table 25 and will be applied for further energy consumption simulation in the operation stage.

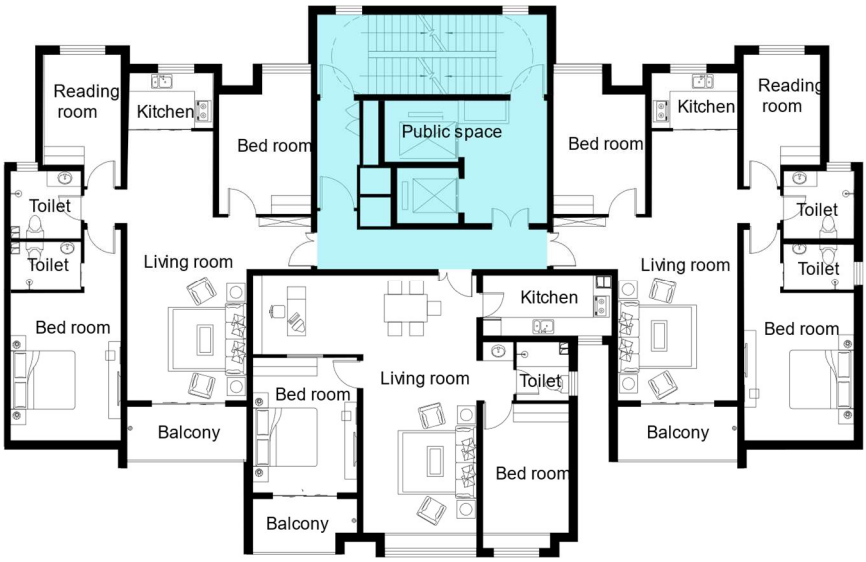

Figure 7-4: Floor layout for archetype building

Table 25: Primary material quantity and cost for reference RC building

Material list	*Quantity*	*Unit*	*Cost (Yuan)*
Cement	818.18	Ton	256538.64
Steel	631.44	Ton	1760695.11
Pre-mixed concrete	3369	m3	1295075.69
Stone	165	Ton	13227.52
Brick	218.17	10^3 pieces	142227.5
Timber	61.30	m3	110358.46

Table 26:Details for reference RC building

Description	***Details***		***U-value***
Roof	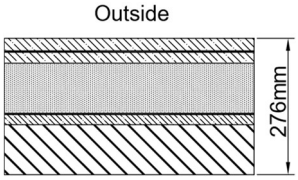	25mm Cement rendering 3mm Waterproof asphalt 20 mm Cement rendering 100 mm EXP (insulation) 3mm Waterproof asphalt 20 mm Cement rendering 100mm RC slab	0.31 W/m2k
External wall	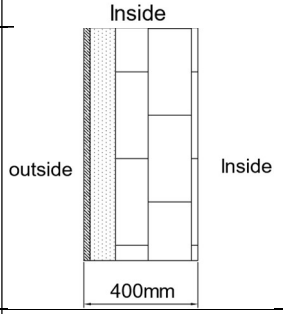	Outside to inside 20mm Cement rendering 90 mm EXP (insulation) 100mm Brickwork	0.32 W/m2k
Internal wall	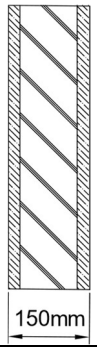	Outside to inside 25mm Cement rendering 100 mm RC wall 25mm Cement rendering	1.9W/m2k
Floor (Between 1st floor and basement)	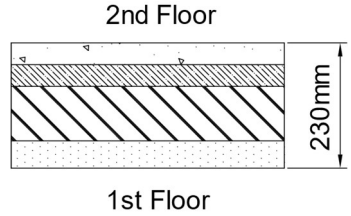	40 mm Concrete finishing 40 mm Cement rendering 100 mm RC slab 50 mm EXP (insulation)	0.53W/m2k
Floor (Other floors)	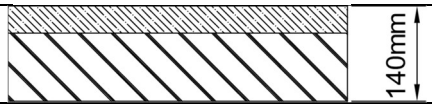	40 mm Cement rendering 100 mm RC slab	2.31W/m2k

- **Redesigned timber building**

The Timber building design is under the guidance of 50 years residential category in GB50009-2012(China, 2012)in China, with the floor plan slightly changed from the original RC building, 402m^2 each story (Figure 7-5). The structure system for this newly designed building is a heavy timber platform structure, in which the floor act as a platform for walls on the next level with a concrete basement(Mohammad et al., 2013). It is recommended by TRADA (TRADA, 2009) design Handbook that when the timber wall is parallel to the span of the floor, the wall is supposed to be regarded as non-load-bearing. The live, snow and dead load are 2.0kn/m2, 0.77kn/m2 and 2.1kn/m2, respectively, and the self-weight for C24 timber is 4.1 kN/m3. The floor panels are 5-ply CLT with each 35mm layer, and the wall panels for the stair core and load-bearing walls are 7-ply CLT. For non-load bearing walls (Mpidi Bita and Tannert, 2019, Liang et al., 2021a), the CLT panels are 3-ply (TRADA, 2009).

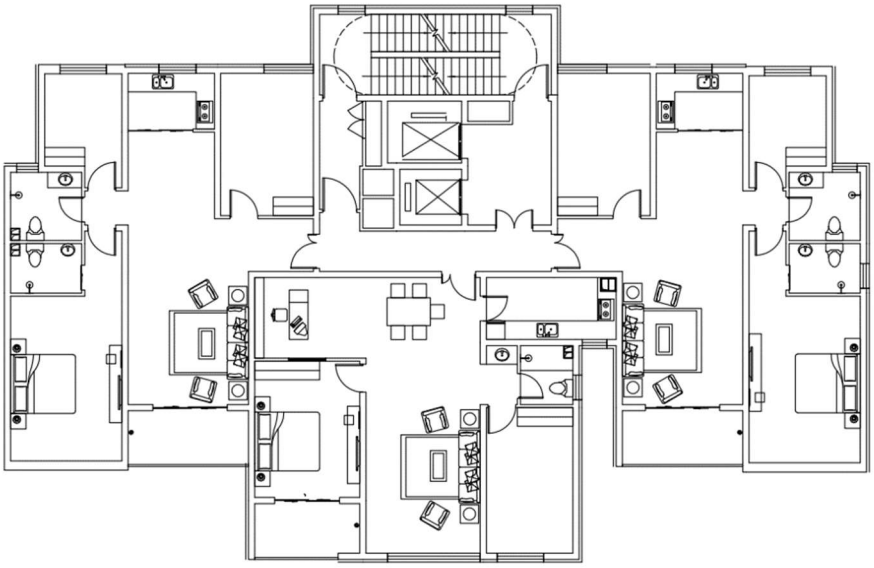

Figure 7-5: Plan for CLT building

The connection system between the wall and floor in this timber building is angle brack fastened with nails. The angle bracket type is ABR90 × 90 × 65 ×2.5mm (ETA., 2021), while fasteners are 4×60mm CNA annular ring-shank nails, of which the nail pattern is shown in Figure 4-4. The distance between angle brackets is around 650mm, following the recommendation from Popovski (Popovski and Karacabeyli, 2012b). Thus, the total number required for this redesigned timber building is 7340. Table 26 shows the envelope

design based on the energy efficiency standard in the cold region in China. The design recommendations are from Dodoo (Dodoo et al., 2014). The insulation material and thickness are the same as the original RC building, with no decoration being considered for the interior walls and floors except between the first and second floors.

Table 27: Details for reference timber building

Description	***Details***		***U-value***
Roof	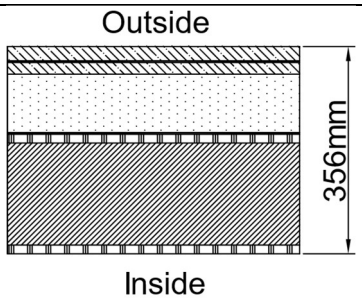	· 25mm Cement rendering · 3mm Waterproof asphalt · 20 mm Cement rendering · 100 mm EXP (insulation) · 3mm Waterproof asphalt · 15 mm plasterboard · 175 mm CLT Panel · 15 mm plasterboard	0.211 W/m2k
External wall	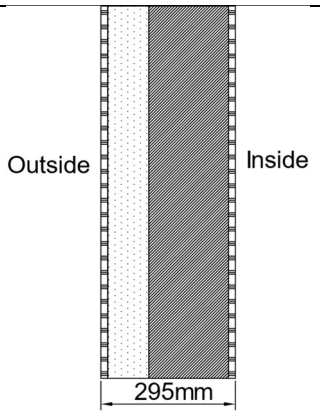	· 15mm plasterboard · 90 mm EXP (insulation) · 175 mm CLT Panel · 15 mm plasterboard	0.25 W/m2k
Floor (Between 1st and 2nd floor)	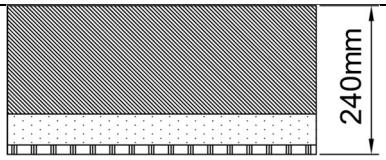	· 175mm CLT panel · 50 mm EXP (insulation) · 15 mm plasterboard	0.314 W/m2k

For the maintenance stage, Table 27 shows the material required and frequency for normal maintenance or repair, and assumptions are according to the recommendation from the previous research literature (Gu and Bergman, 2018). However, considering the previous chapter's research result, the timber building at this height can encounter the problem caused by wind pressure, and the stiffness of the joint between the external wall and floor may decrease up to 60% in a 50-year life span. Thus, in the next part, what will be analyzed are the environmental impact and energy consumption caused by different design and repair scenarios:

Baseline: Design with the original number of connectors in Table 27, without considering the maintenance of timber components joints.

Scenario 1: Double the number of connections between the external walls and floor, no further reinforcement is required after 50 years, and repair under the normal assumption condition in Table 28;

Scenario 2: Design with the initial number of connections, and the maintenance strategy after 50-year is to add one angle bracket on each side of the original connector for reinforcement with replacement of plasterboard, and the frequency of repairing plasterboard and connectors increases to every ten years;

Table 28:Material list for CLT building

Material list	Quantity	Unit	Cost (Yuan)/Unit	Total Cost (Yuan)
Cement	15.9	Ton	**-**	6678.7
Steel	440.79	Ton	**-**	867282
Pre-mixed concrete	2193.3	m3	**-**	847803
Brick	129.29	10^3 pieces	**-**	55578.6
Timber (not CLT)	24.13	m3	**-**	43429.5
CLT	2258.4	m3	**9600***	21680640
Angle bracket	12912	each	**25.92***	334679.04
Nails	1084.61	kg	**45.56***	49414.83
Plasterboard	25	m^3	**716.33**	17908.25

*** USD to Chinese yuan rate: 6.4**

Table 29:Material for building maintenance

Material	*Frequency (year)*	*Percentage of material usage*
Cement mortar	1	1.5
Plasterboard	20	2
Conctete slab	15	2
Steel	15	2
Wood	20	2
Connector	20	2

7.3.1 Goal and scopes

With the basis of the review in the previous section, the following case study aims to:

1) Evaluate the environmental impact of a CLT building with different repair scenarios

2) Compare the life cycle environmental emissions of CLT and RC buildings;

The LCA is based on the approach described in ISO 14040 (Arvanitoyannis, 2008). The scopes for LCA of the two building systems include production to operation during a 50-year life span. But the factors of equal input, such as HVAC system, windows and doors, are not considered. The functional unit for this assessment is per m^2 floor area.

7.3.3 Inventory

- Manufacturers and construction

With the factors of material quantity and cost for two building systems explained in the previous section, this study takes the hybrid assessment method into the application in the material production stage. Inventory data for different materials come from I-O and process-based inventory databases based on -availability. Table 29 shows the database used for various materials.

Table 30:Inventory assessment for different material

Material/ Resources	***Database***	***Inventory assessment method***
Cement	EXIOBASE	I-O method
Steel	EXIOBASE	I-O method
Pre-mixed concrete	EXIOBASE	I-O method
Brick	EXIOBASE	I-O method
Stone	EXIOBASE	I-O method
Timber (not CLT)	EXIOBASE	I-O method
CLT	AGRIBALYSE	Process-based method
Angle bracket	EXIOBASE	I-O method
Nails	EXIOBASE	I-O method
Plasterboard	EXIOBASE	I-O method
Electricity	AGRIBALYSE	Process-based method
Coal	AGRIBALYSE	Process-based method
Diesel	AGRIBALYSE	Process-based method

The inventory assessment for the transportation and construction stage is based on the energy consumed in these two stages. The transportation method is assumed to be the lorry, and in China, the energy consumed is around 2.3MJ/t per kilometre (Zhang, 2014), and the energy source is diesel. The material transport distance assumption is under the guidance of the previous study by Canada Wood in China (CABR, 2014) and is shown in Table 30. The energy conversion coefficient in China is listed in Table 31(NSPRC, 2008).

Table 31:Average transportation distance of building materials in China

Material	Average distance (km)	Material	Average distance (km)
Sand/Stone	200	Glass	100
Cement	100	Coating	80
Steel	60	Ceramic	50
Bricks	60	Non-metallic mineral	50

Table 32:Energy conversion coefficient

Name of energy resources	Convert coefficient	Name of Energy resources	Convert coefficient
Hard Coal (MJ/kg)	20.9	**Brown coal (MJ/kg)**	12.6
Gasoline (MJ/kg)	41.9	**Diesel (MJ/kg)**	42.7
Gas (MJ/m^3)	39.0	**Electricity (MJ/kg)**	3.6
Propane (MJ/kg)	50.2	**Wood biomass (MJ/kg)**	16.7

The RC construction progress can be divided into steelwork and concrete two steps. The detailed energy consumption in these two stages in China is shown in Table 32, based on literature reviews (Li, 2001; Chen, 2014; Sun, 2015), and is assumed to be supplied by electricity power. In terms of timber building, researchers suggest that the energy consumption in this stage should be around 2% of the embodied energy, minus the transportation energy(Cole et al., 1996, Cole and Environment, 1998). This study assumed the transportation distance of the CLT panel is 600km and delivered with a diesel lorry.

Table 33:Construction energy consumption for RC building

Process			Energy (MJ/t)
		Product Size	
Steelwork	**Reinforcement straightening**	<Φ10	10.30
		Φ12~ Φ14	13.54
	Reinforcement cutting	Φ10>	0.40
		<Φ10	0.32
	stirrup	Φ10>	12.24
		<Φ10	8.64
	Conjunction	Φ10>	162.72
		<Φ10	40.32
Concrete work	**Concrete mixing**		158.4
	Concrete prefabricating		90
Lifting			39.75(MJ/m2)

- Operation and maintenance

The energy consumption during the operation stage comes from the building environmental simulation with the assistance of software IES VE. The floor plan in the simulation is shown in Figures 7-7 under the direction of the original RC building plan. Input data for simulation include enveloping thermal characters, HAVC system setting, human activity definition and location selection. Shandong province is the simulation location defined as a cold climate zone in China following Residential Building Code (MOHURD, 2003). In this simulation, energy consumed by cooling and heating is the sole index to be considered. To provide a comfortable thermal environment, the maxi and minimum temperature set point is 18^{oC} and 26^{oC}(Chen et al., 2012). Also, ventilation rate and internal heat gain can influence the energy consumption to maintain the indoor thermal environment. This research chooses the recommendation from ISO 7730 for these two parameters, which are 30 m^2/h and 75w/person. Each apartment has three residents, and the assumption of natural ventilation time and internal heat gain is demonstrated in Table 33. The enveloping design for this simulation is according to Table 25 and Table 26. The inventory assessment in this stage is based on the energy consumption in a 50-year life span. In this simulation, the energy source for heating is coal, and cooling is electricity.

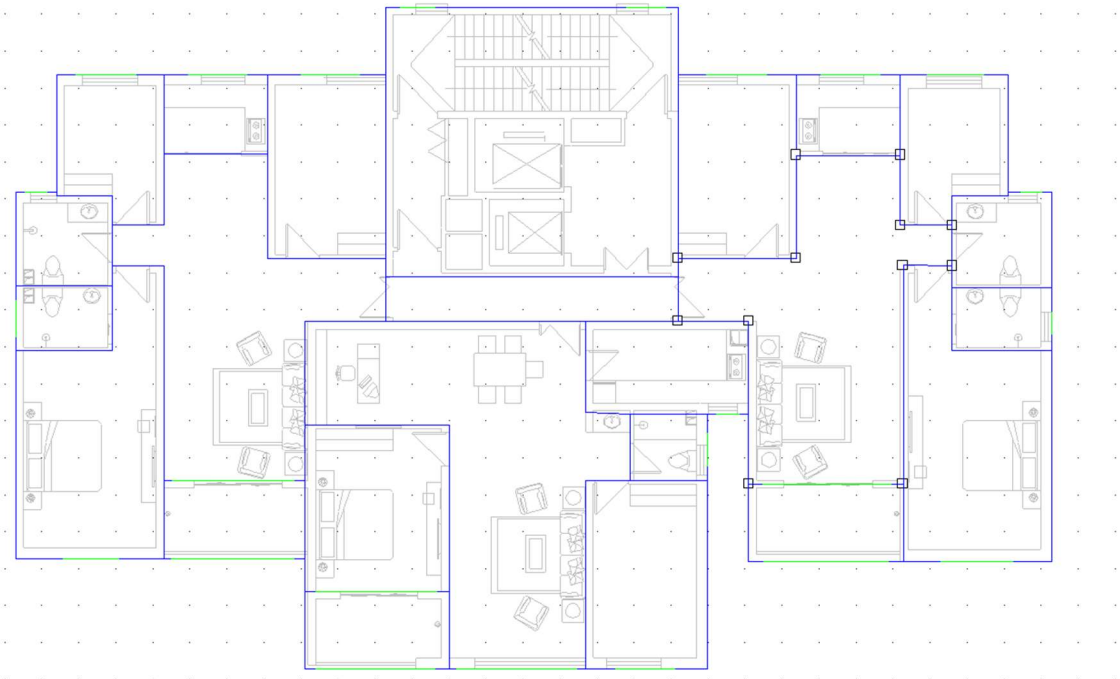

Figure 7-7: Floor plane for IES simulation

Table 34:Ventilation and internal gain settings for simulation

Room	*Natural Ventilation Time*	*Number of Occupants (Internal gain)*
Bedroom 1	24:00 -8:00	2
Bedroom 2	24:00 -8:00	1
Living room	8:00-24:00	3
Kitchen	/	0
Toilet	/	0
Balcony	0:00-24:00	0
Reading room	/	0

Energy consumed by materials used for the maintenance stage is also accrued. Material required for two types of buildings and frequency in the maintenance stage is shown in the previous chapter in Table 28. The façade maintenance material for the RC building, containing cement mortar and concrete, is involved in the inventory assessment. For CLT building, the repair scenario described in section 7.3.2 comprises plasterboard replacement, and joint reinforcement. The cement mortar for roof maintenance should be considered in a timber building.

7.3.4 Impact assessment

The midpoint impact assessment method can provide quantitative results of greenhouse gas emissions and water and material consumption without explaining the consequence caused by these factors. Compared with midpoint assessment, the endpoint method clearly illustrates the influence of human health, ecosystem, and resources without detailed data. Penadés-Plà (Penadés-Plà et al.) stated that the midpoint method is more reliable than the endpoint method. After comparing the environmental impact between two building systems numerically, thus applying the midpoint method. Different LCA assessment software exerted a significant impact on assessment indexes. OpenLca, an open-source LCA software, was used in the study for analysis with the impact assessment method of the CML 2001 category due to the universality of this method among different databases.

7.5 Results and discussion

7.5.1 Envriomental impact of CLT building

- **Manufacture and construction**

CLM 2001 baseline method analyses the environmental impact potential of products from the following factors: acidification, eutrophication, freshwater aquatic ecotoxicity, global warming (GWP100), human toxicity, photochemical oxidation and Terrestrial ecotoxicity. The measurement of acidification and eutrophication, global warming, and photochemical oxidation effects is relatively following the SO_2, PO_4, CO_2, and C_2H_4 equivalent. The rest factors are assessed according to the 1,4-dichlorobenzene equivalent.

This section first shows the environmental impact from the material production stage of the CLT building, given the baseline scenario. What is shown in the Figures 7-8 is the environmental impact caused by materials production, where the most significant influence of CLT building is on global warming. In addition, the influence of freshwater aquatic ecotoxicity and human toxicity is also evident. According to Figure 7-9, the total CO_2 emission is 571.5 kg/m^2, and the production of steel, concrete, CLT panel and connections contribute 95% of the total. Steel and concrete production for basement construction emitted CO_2, 204.86 kg/m^2 and 143.1 kg/m^2, and together accounted for 61% of the total emission. Figure 7-10 exhibit that the 1,4-DB equivalent emission related to human toxicity is 134.4kg/m^2, and around 40% comes from CLT panel production. Furthermore, Figure 7-

11 shows that CLT panel production caused the most freshwater aquatic ecotoxicity, followed by concrete, with a total value of 50kg/m^2.

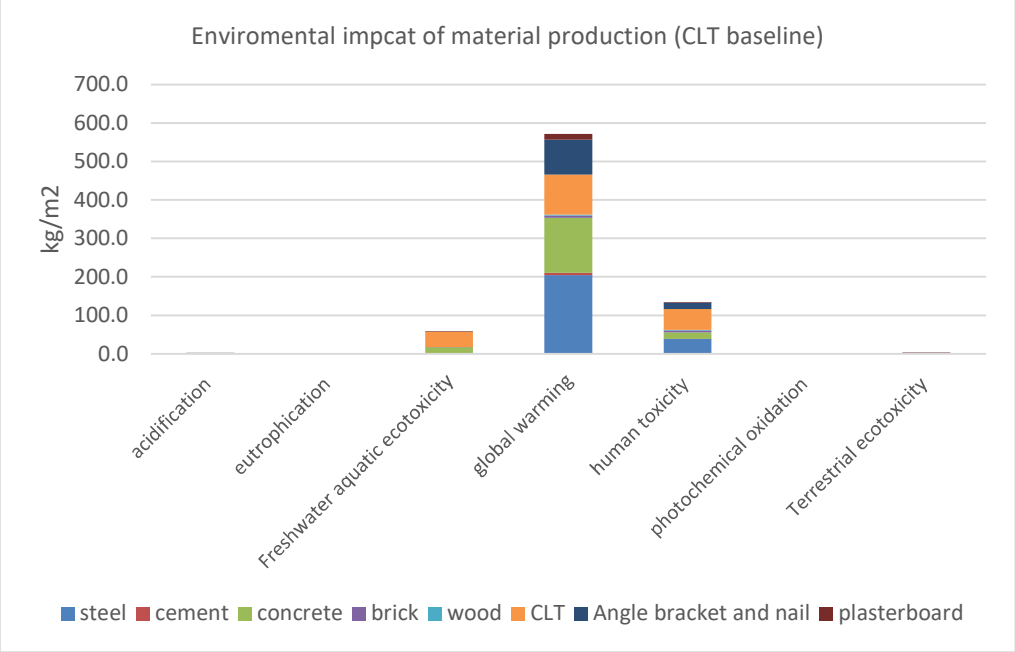

Figure 7-8: Environmental impact of material production of CLT building (Baseline)

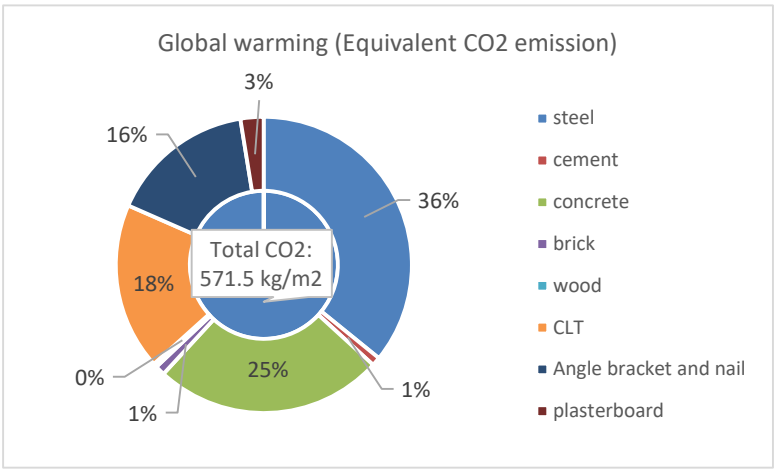

Figure 7-9:Global warming impact from different building materials

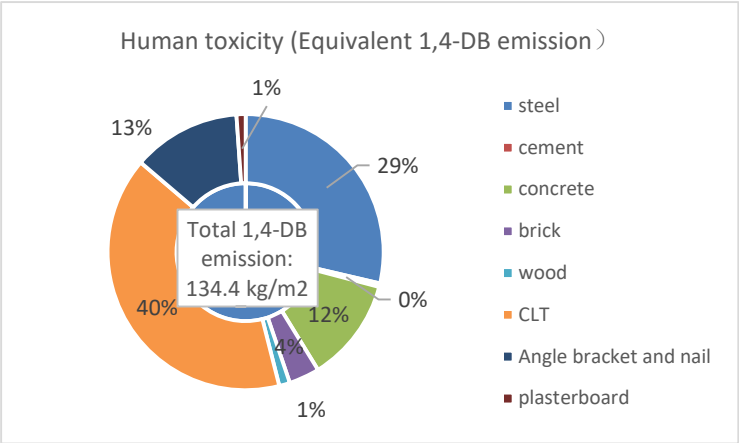

Figure 7-10:Human toxicity of timber building

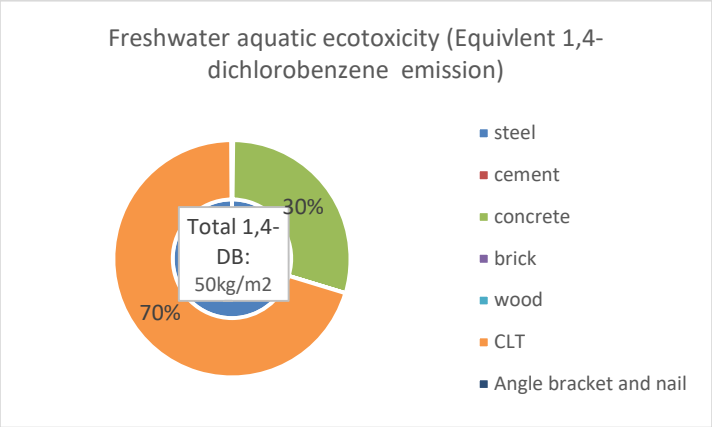

Figure 7-11: Freshwater aquatic ecotoxicity of timber building

Figures 7-12 and 7-13 indicate that the total energy consumption for the CLT building material production stage equals 2.47 GJ/m^2. CLT panel production consumed 46% of the total energy, followed by the steel for basement construction with 19%. The third-largest consumer is concrete, with a ratio of 12

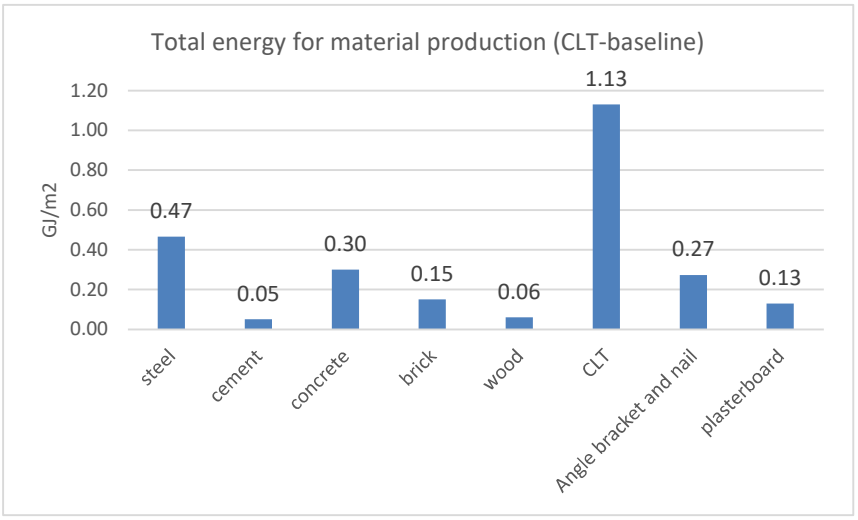

Figure 7-12: Energy for CLT building's material production

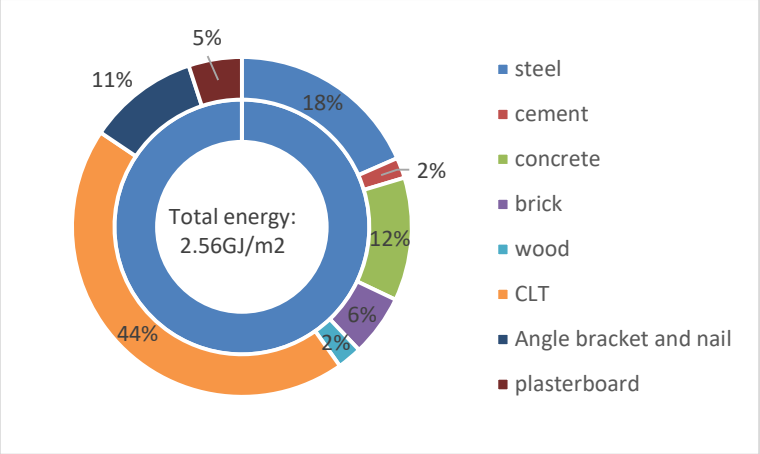

Figure 7-13: Percentage of energy consumption from different materials

In scenario 1 (CLT-S1), around 4610 more angle bracket is required at the construction stage to fix the external wall. As a result, the total angle bracket and nails for scenario 1 increased to 3504.4kg and 1434.05kg, and the total price increased accordingly to 507841.56 yuan for connection. Figures 7-14 and 7-15 display the quantity and percentage of CO_2 emission from the CLT-S1 materials. The CO_2 emission from connector production increased from 90.7kg/m^2 to 120kg/m^2, and the total CO_2 increased to 600kg/m^2. Additionally, the percentage of CO_2 emission from angle bracket and nails become 20% and exceed CLT panels. Regarding human toxicity, the total value increased to 139.9kg/m^2, and connection production accounted for 20%, which increased by 4% compared to the baseline (Figure 7-16). And the energy consumption for CLT-S1 increased to 2.56GJ/m^2.

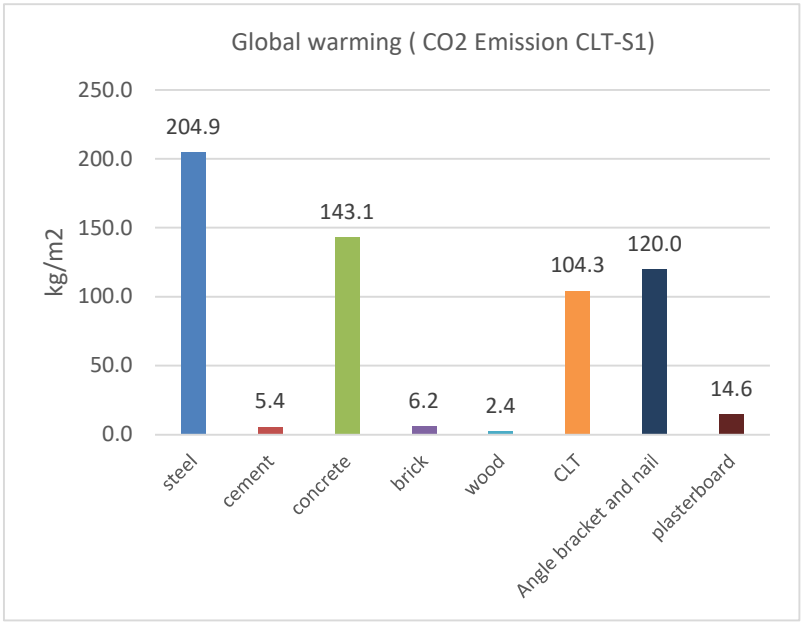

Figure 7-14:CO_2 emission from CLT buildings' material

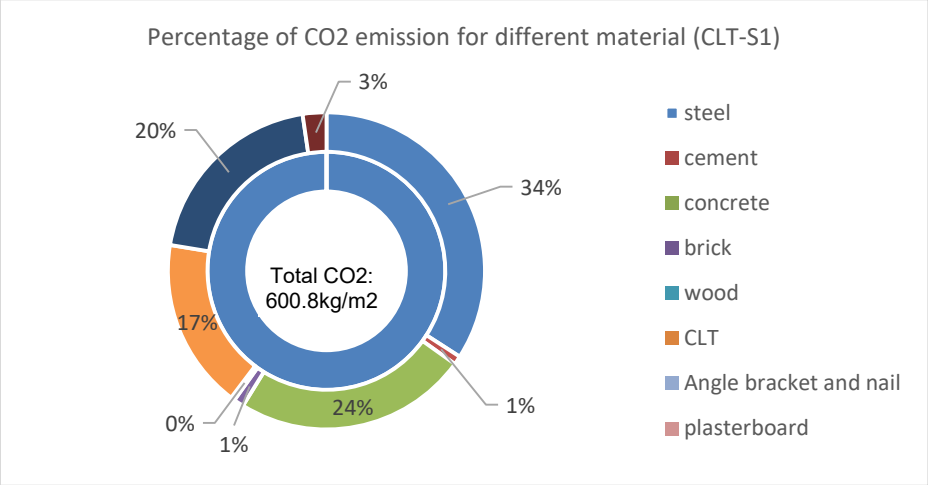

Figure 7-15:Percentage of CO2 emission from different materials

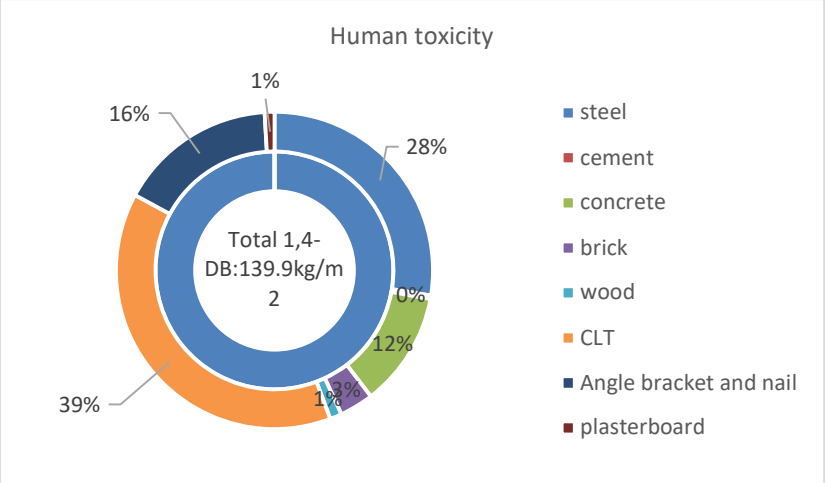

Figure 7-16: Human toxicity emission from different material

Energy consumption for CLT baseline building construction and material transportation is 0.04 GJ/m^{2}and 0.44GJ/m^2, respectively. These two stages' environmental impact is shown in Figures 7-17 and 7-18. The construction stage lays a graver impact on freshwater aquatic ecotoxicity and human toxicity than global warming, and the material transportation stage principally affects global warming. The total CO_2 emission from these two stages is 73.96kg/m^2. Furthermore, the increase of angle bracket numbers has no significant influence in this stage.

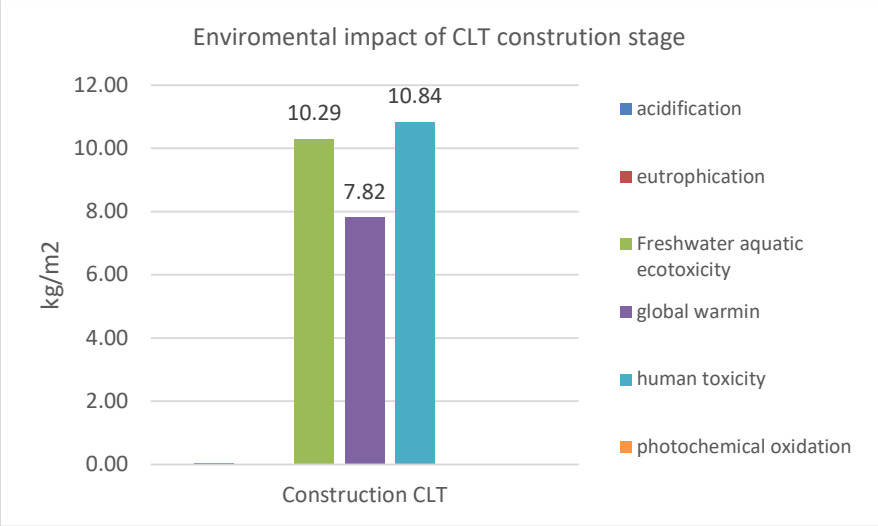

Figure 7-17: Environmental impact of CLT building construction stage

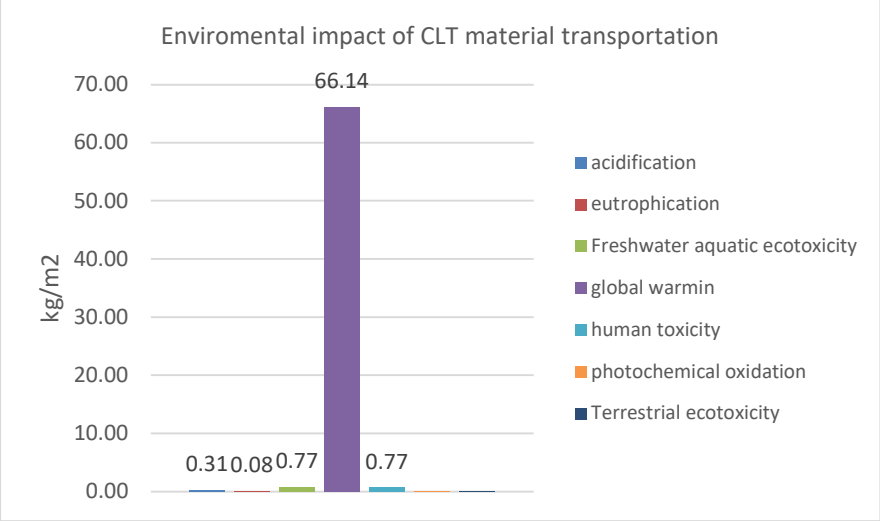

Figure 7-18: Environmental impact of CLT building transportation stage

- **Operation and maintenance**

The cooling season of buildings is from June to September, and the heating season is from November to March. The annual and monthly energy consumption for heating and cooling in the CLT building is shown in Figure 7-19. It is demonstrated in Figure 7-21 that the total energy for cooling and heating of CLT building is 7.4GJ/m^2 in a 50-year life span. Heating energy consumption (5.3GJ/m^2) is around two times higher than cooling (2.1GJ/m^2). Figure 7-20 shows that in the operation stage, the issue of human toxicity is more significant than global warming potential. In addition, the third most environmental severe impact factor appears to be freshwater aquatic ecotoxicity in this stage, and cooling produced more water ecotoxicity than heating but impacted the aspects of global warming and human toxicity less (Figure 7-22). The total CO_2 emission is around 883.7kg/m^2 for timber buildings.

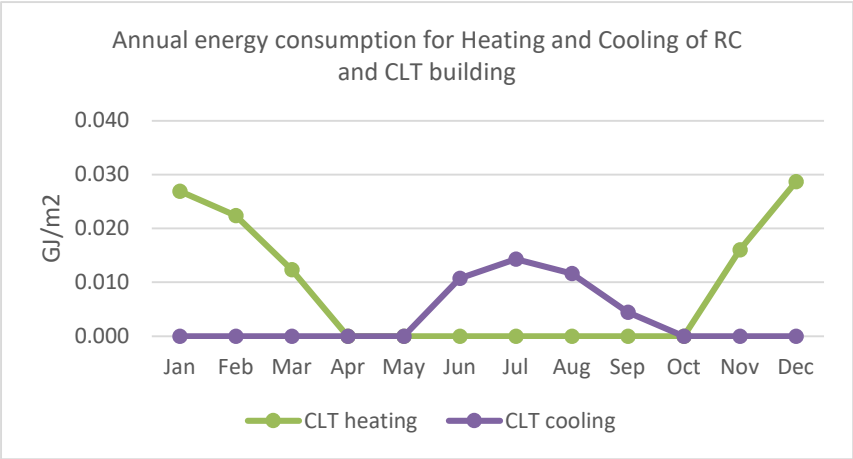

Figure 7-19:Monthly CLT building cooling and heating energy from simulation results

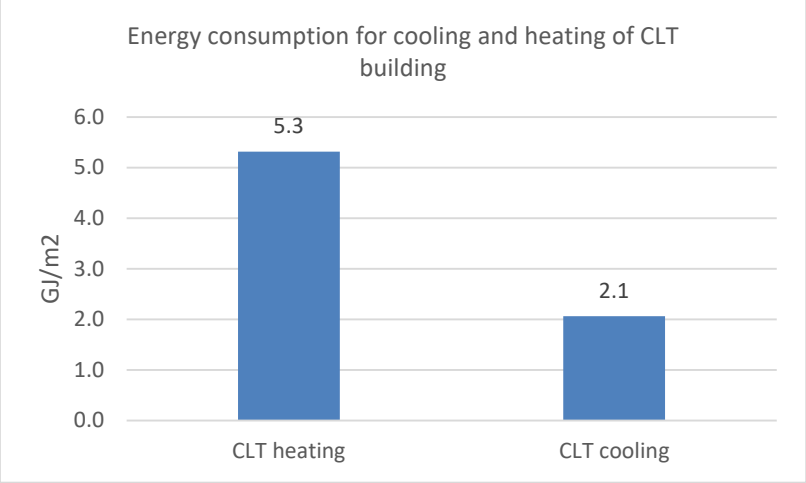

Figure 20: 50-year energy consumption for CLT building cooling and heating

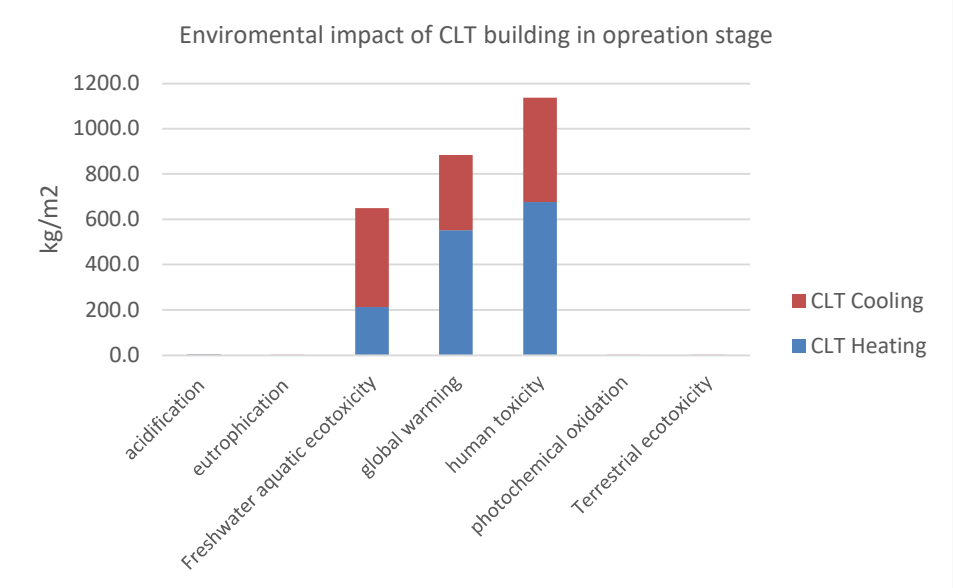

Figure 7-21: Environmental impact from operation stage of CLT building

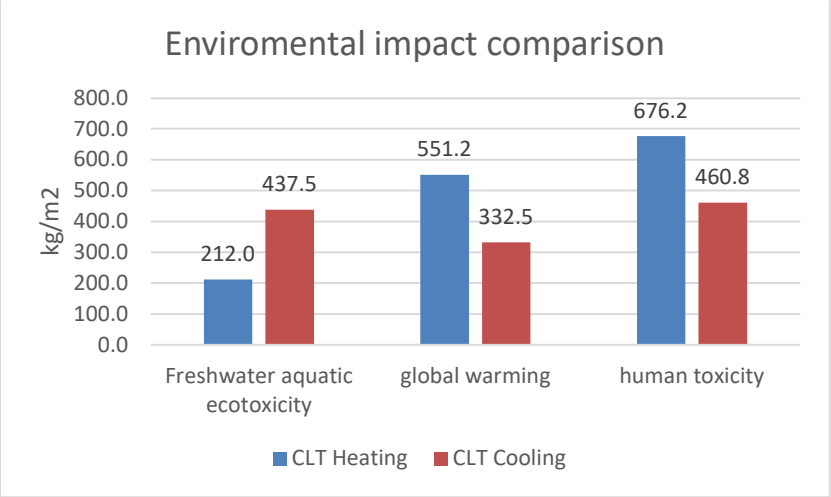

Figure 7-22: Three most significant environmental impact comparisons (CLT building)

The repair material for the CLT building under different scenarios is shown in Table 34. Figure 7-23 indicates that the repair stage significantly influences global warming and produces human toxicity. The total CO_2 emission from the baseline situation is 35.59kg/$m^{2,}$ and human toxicity related 1,4 DB emission is 5.6kg/m^2. It is displayed in Figures 7-24 that the most pollution is derived from steel production for basement repair, of which the connector and concrete follow the priority. For scenario 1, the total CO_2 and human toxicity 1,4-DB emission decreased to 30.9kg/m^2 and 4.8kg/m^2, respectively (Figure 7-25). It is indicated in Figures 7-26 that in scenario one, the percentage of pollution from connectors has declined slightly. As for scenario 2, when considering the reinforcement of angle bracket connectors, the emission of pollutants is significantly increased, especially the CO_2 emission (Figure 7-27). The total CO_2 and 1,4-DB emissions are 119.88kg/m^2 and 20.10kg/m^2 from this stage under scenario 2. It is shown in Figure 7-28 that the CO_2 and 1,4-DB emissions from angle bracket connections increased to 66% and 74%, exceeding the basement's steel and concrete. Additionally, the CO_2 emission from plasterboard increased to 14.5kg/m2, around ten times the baseline. Figure 7-29 shows that the energy consumption for each scenario is 0.38GJ/m^2, 0.37GJ/m^2 and 0.66GJ/m^2.

Table 35:Material for CLT building repair and replacement

	Material	Quantity	Unit	Cost (yuan/year)	Frequency
Baseline	Cement *	0.24	Ton/year	100.18	Every year
	Steel*	8.82	Ton/year	17345.64	Every 15 year
	Concrete*	43.87	m3/year	16956.06	Every 15 year
	Wood *	0.48	m3/year	868.59	Every 20 year
	Angle bracket	289	each/year	6693.58	Every 10 year
	Nail	21.69	kg/year	998.29	Every 10 year
	Plasterboard	0.5	m3/year	358.15	Every 10 year
Scenario 1	Angle bracket	382	each/year	9901.44	Every 20 year
	Nail	28.68	kg/year	1306.66	Every 20 year
	Plasterboard	0.5	m3/year	358.15	Every 20 year
Scenario 2 Repair	Angle bracket	289	each/year	6693.58	Every 10 year
	Nail	21.69	kg/year	998.29	Every 10 year
	Plasterboard	0.5	m3/year	358.15	Every 10 year
Reinforcment	Angle bracket	9920	each	257126.4	Every 50 year
	Nail	833.28	kg	37964.23	Every 50 year
	Plasterboard	25	m3	17908.25	Every 50 year
	* The same for each scenario				

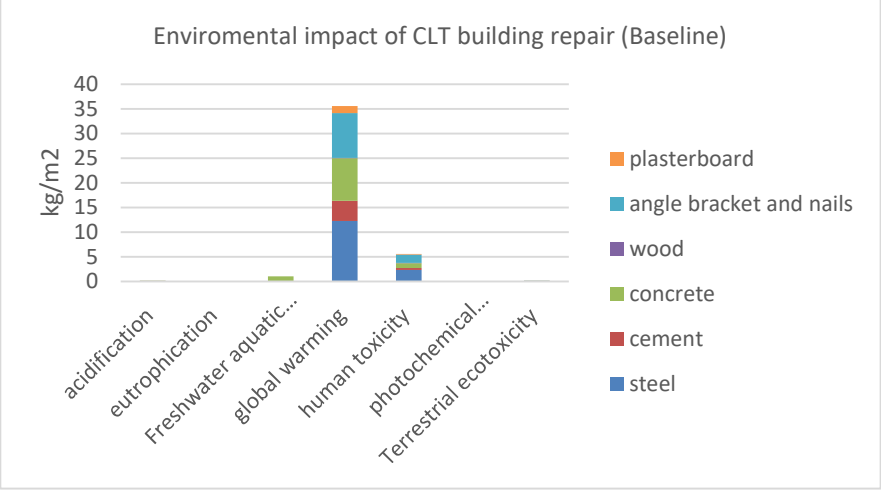

Figure 7-23: Environmental impact of CLT baseline building repair

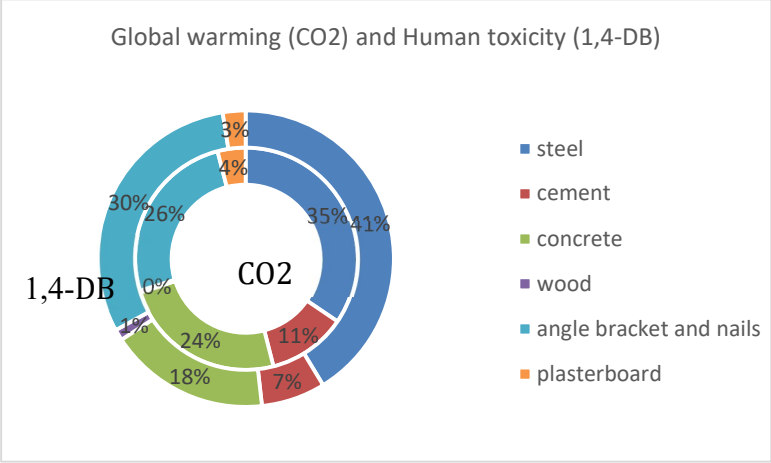

Figure 7-24: Percentage of CO2 emission and 1,4-DB emission from materials for CLT baseline building repair

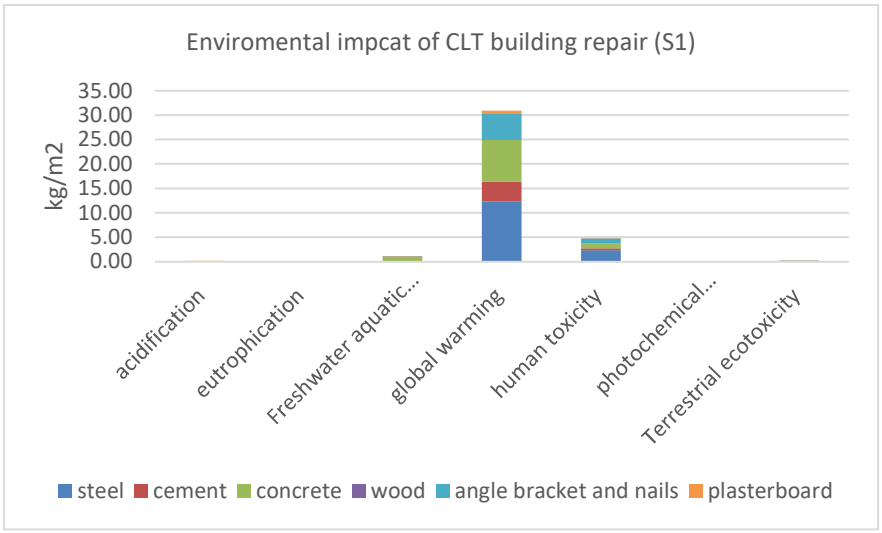

Figure 7-25: Environmental impact of CLT building repair under scenario 1

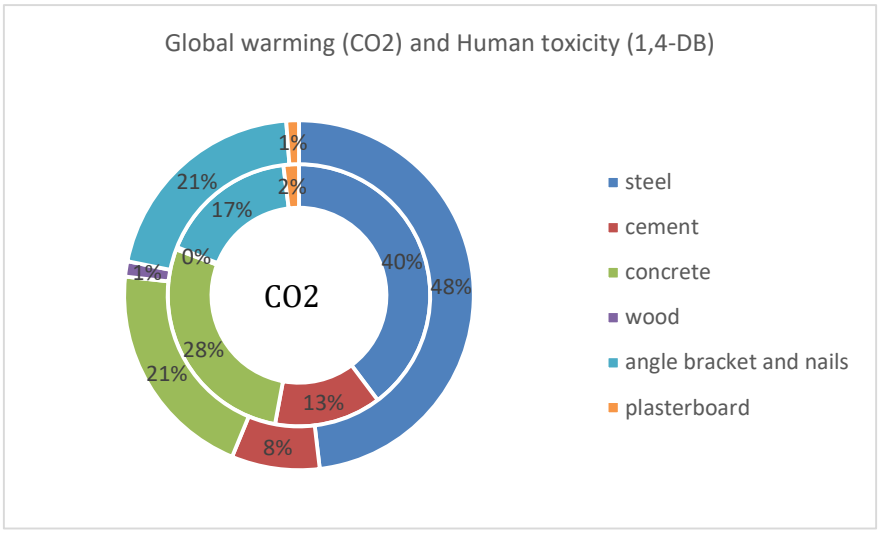

Figure 7-26: Percentage of CO2 emission and 1,4-DB emission from materials for CLT building repair (S1)

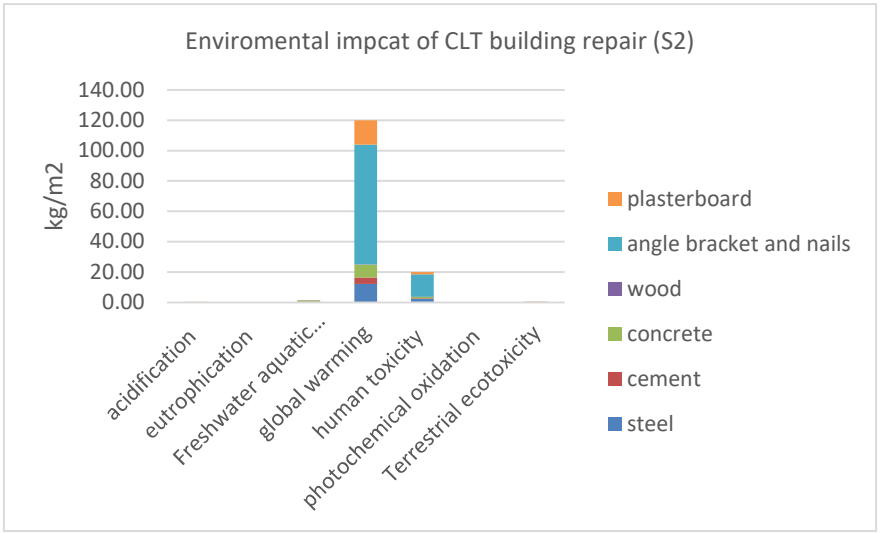

Figure 7-7: Environmental impact of CLT building repair under scenario 2

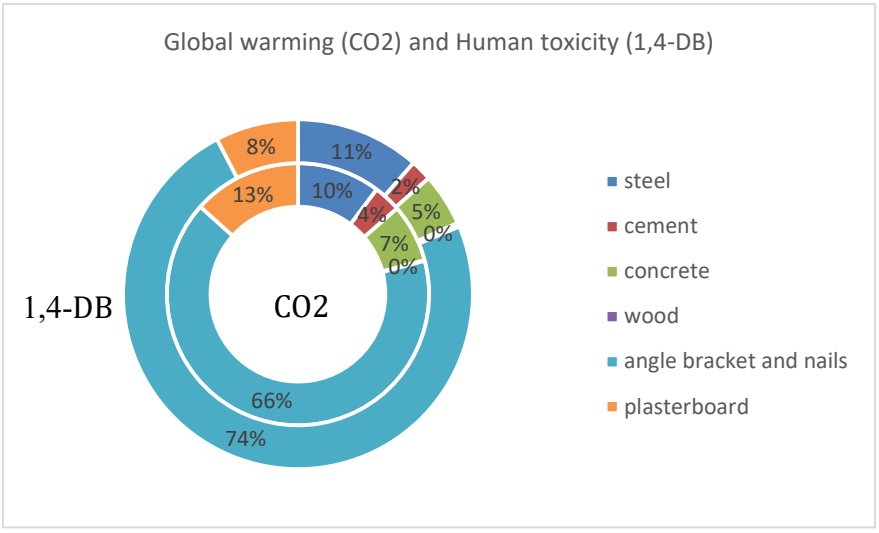

Figure 7-28: Percentage of CO2 emission and 1,4-DB emission from materials for CLT building repair (S2)

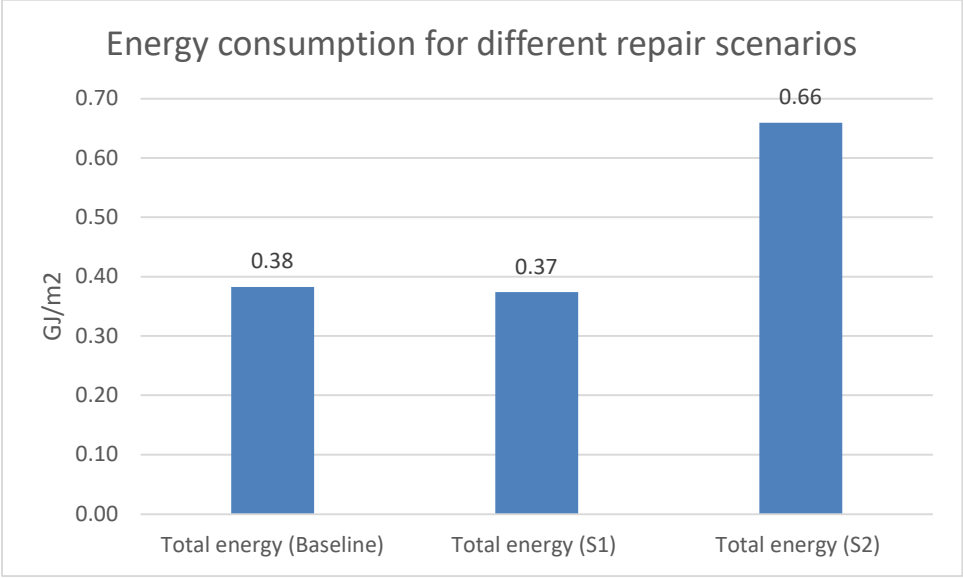

Figure 7-29: Energy consumption for different repair scenarios

7.5.2 Envriomental impact of RC building

- **Manufacture and construction**

The stacked bar charts (Figure 7-30 and 7-31) display each material's quantitive and percentage effect on different factors. Whereas it can be inferred from Figure 7-28 that materials in RC buildings have a greater influence on global warming than other factors, of which the total CO_2 emission in this stage is 865kg/m^2. Steel production accounted for 48.1% of that, followed by concrete (25.2%) and cement (24.1%). It should be noted that human toxicity is vital, meaning the emission of health-related pollutants is second to carbon dioxide emissions. Figure 7-32 shows the energy consumption of each material and their percentage of the total energy consumed in the material production stage, with a total value of 3.76GJ/m^2. Steel contributes to the most energy consumption, which is 45% of the total.

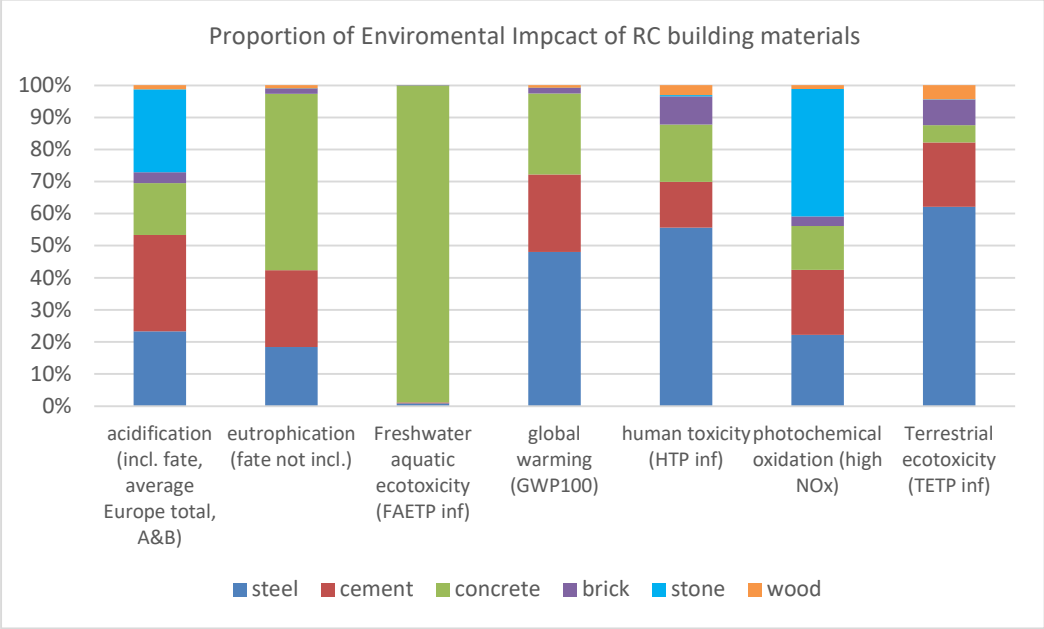

Figure 7-30: Environmental impact of RC building material

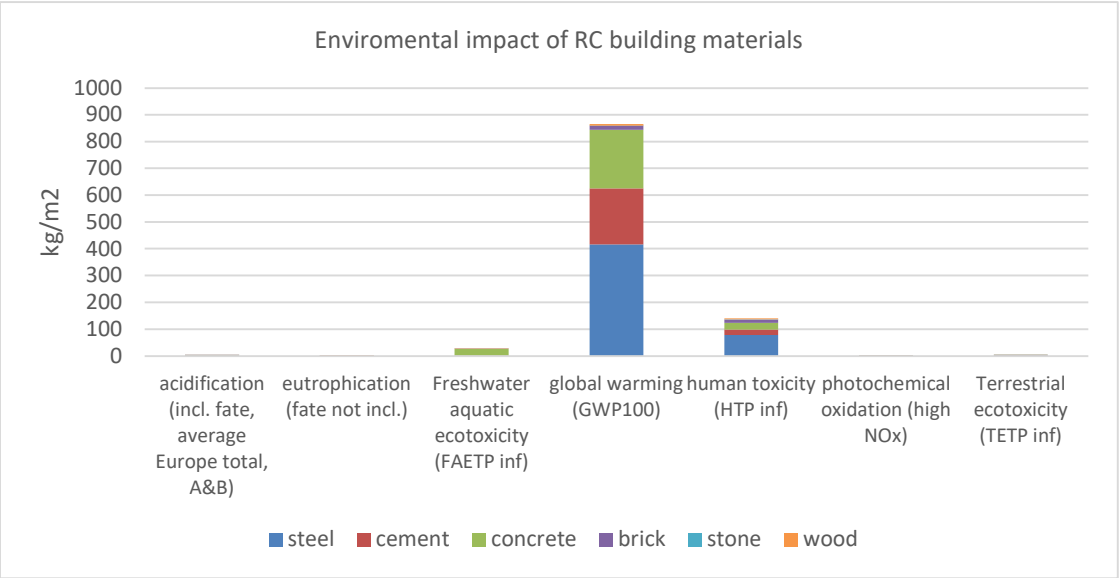

Figure 7-31:Percentage of Environmental Impact of RC building materials

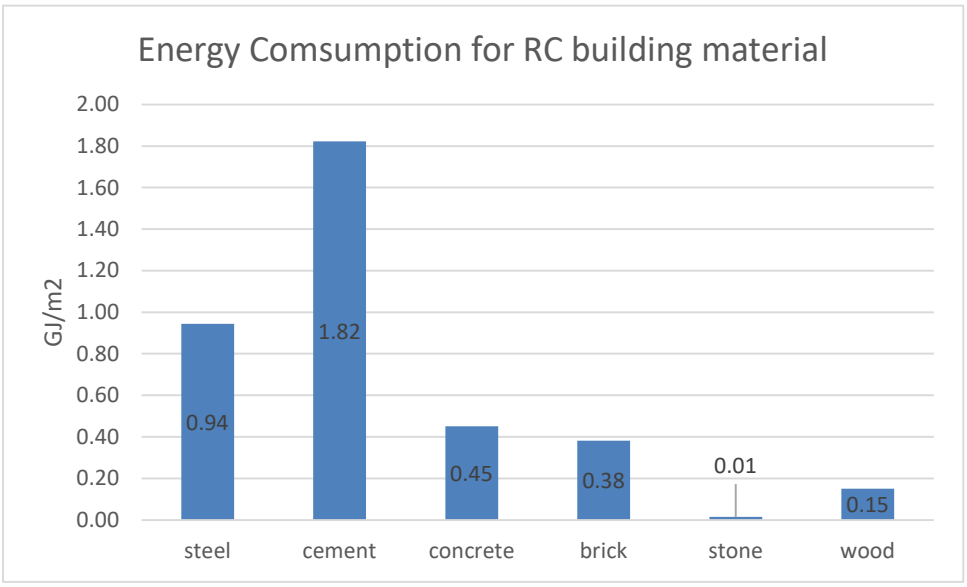

Figure 7-32: Energy consumption in the material production stage for RC building

Figure 7-33 show the environmental impact of RC in the construction and transportation stage. These two stages have a more hazardous effect on freshwater aquatic ecotoxicity and human toxicity than global warming. The total CO_2 emission for the RC building is 131.44kg/m^2, and the emission in the construction stage is greater than in the transportation stage. Figure 7-34 shows that the total energy consumed in these two stages for RC equals 0.69GJ/m^2.

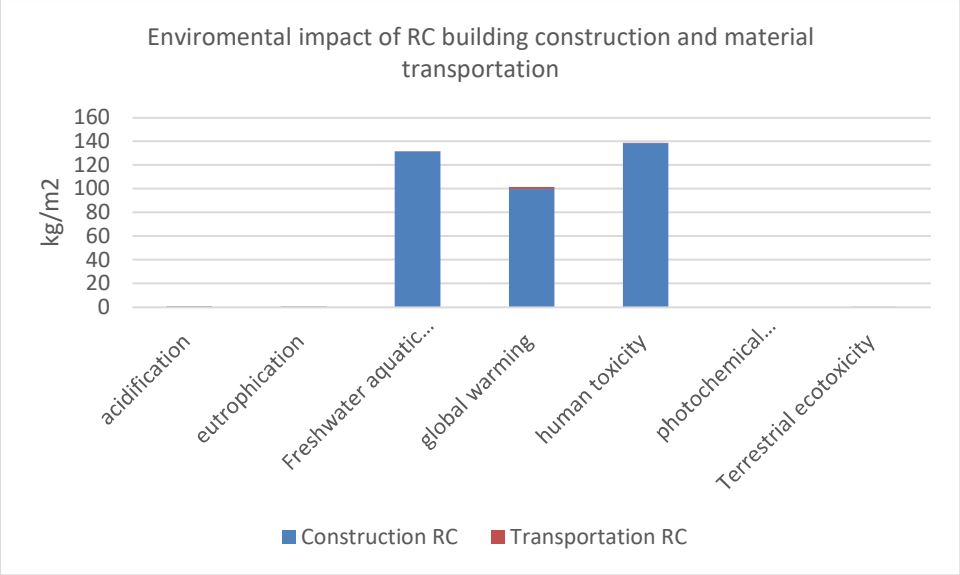

Figure 7-33: Environmental impact of construction and material transportation (RC building)

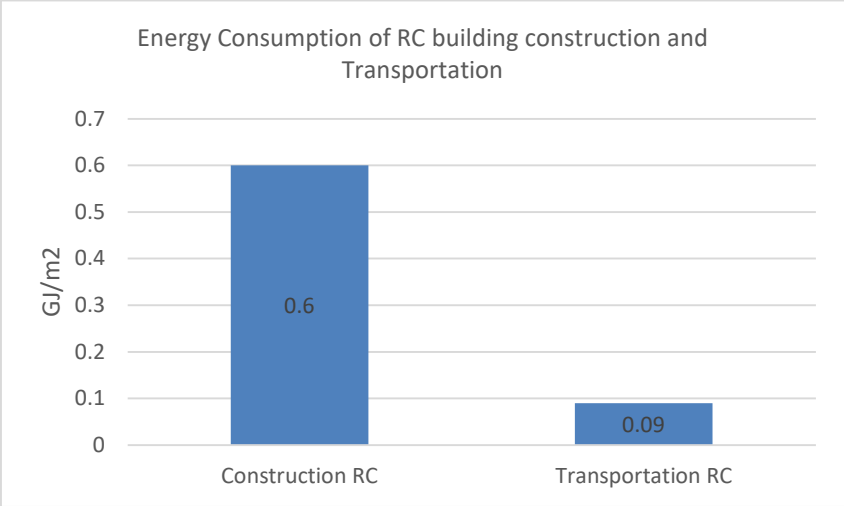

Figure 7-34:Energy consumption of construction and transportation (RC building)

- **Operation and maintenance**

Figure 7-35 shows simulation results, including the RC buildings' annual, monthly energy consumption for heating and cooling. The energy consumption for cooling and heating in the total RC buildings is 10GJ/m^2 and 2.2GJ/m^2 in a 50-year life span, respectively (Figure 7-36). According to Figure 7-37, the impact of RC buildings is evidently on water ecotoxicity, global warming and human toxicity, among which the most severe issue dwells in human toxicity. The detailed emission values for these three impact factor is shown in Figure 7-38. Cooling effects global warming and human toxicity less than heating, but the negative influence on water ecotoxicity is more grave. The total CO2 emission in the operation stage during the 50-year life span is 1388.3kg/m^2

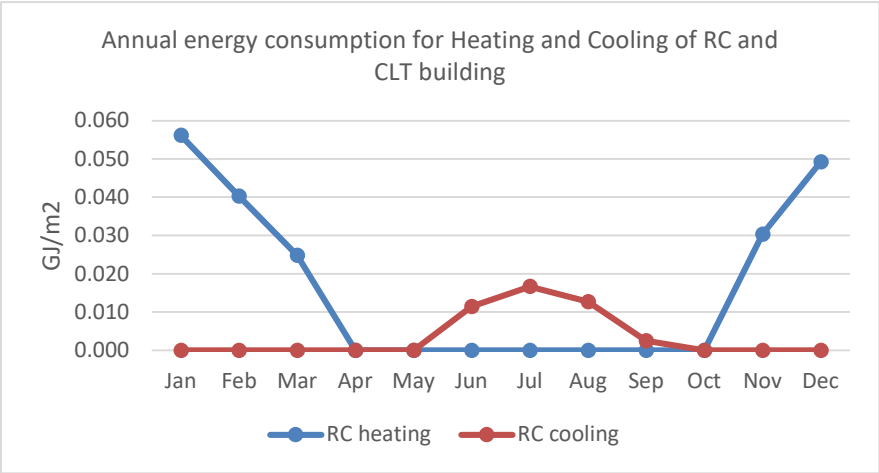

Figure 7-35: Monthly cooling and heating energy consumption for two buildings

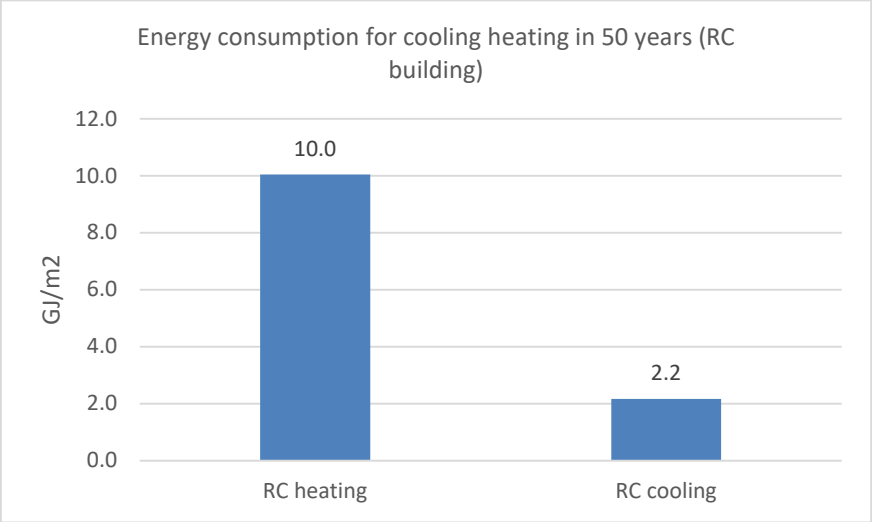

Figure 7-36: Energy consumption for operation stage in a 50-year life span

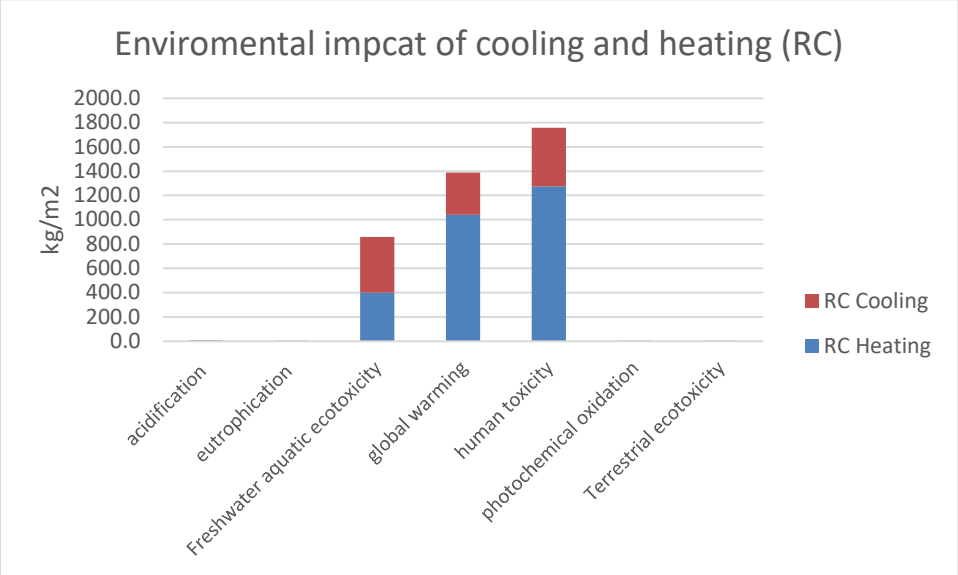

Figure 7-37: Environmental impact caused by cooling and heating

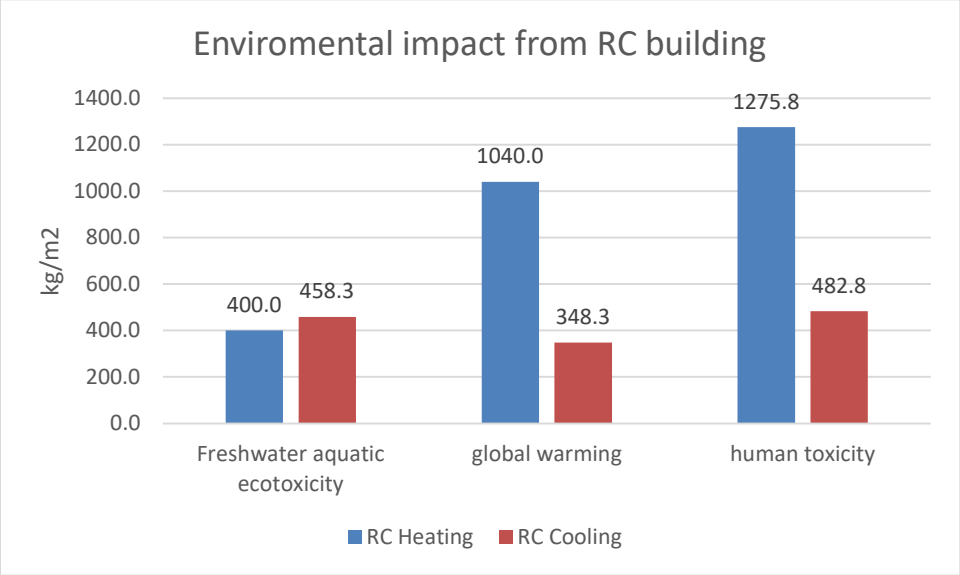

Figure 7-38:CO_2 emissions from cooling and heating in a 50-year lifetime

According to the assumption from Table 35, the total material required for RC building maintenance in a 50-year life span is calculated (Table 35). The environmental impact of the repair stage of the RC building is shown in Figure 7-39. This stage has a substantial influence on global warming and a light influence on human toxicity. Figure 7-40 shows that the most impact is initiated from the cement mortar, which accounts for 80% of the total value. The total CO_2 emission in this stage is 195kg/m^2. The total energy consumed in this stage is around 1.49GJ/m^2 for material production in a 50-year lifetime.

Table 36:Material for RC building repair

Material	*Quantity*	*Unit*	*Cost (yuan/year)*	*Frequency*
Cement	12.27	Ton/year	3848.08	Every year
Steel	12.63	Ton/year	35213.9	Every 15 year
Concrete	67.38	m3/year	25901.5	Every 15 year
Stone	2.20	m3/year	264.55	Every year
Wood	1.23	m3/year	220.7	Every 20 year

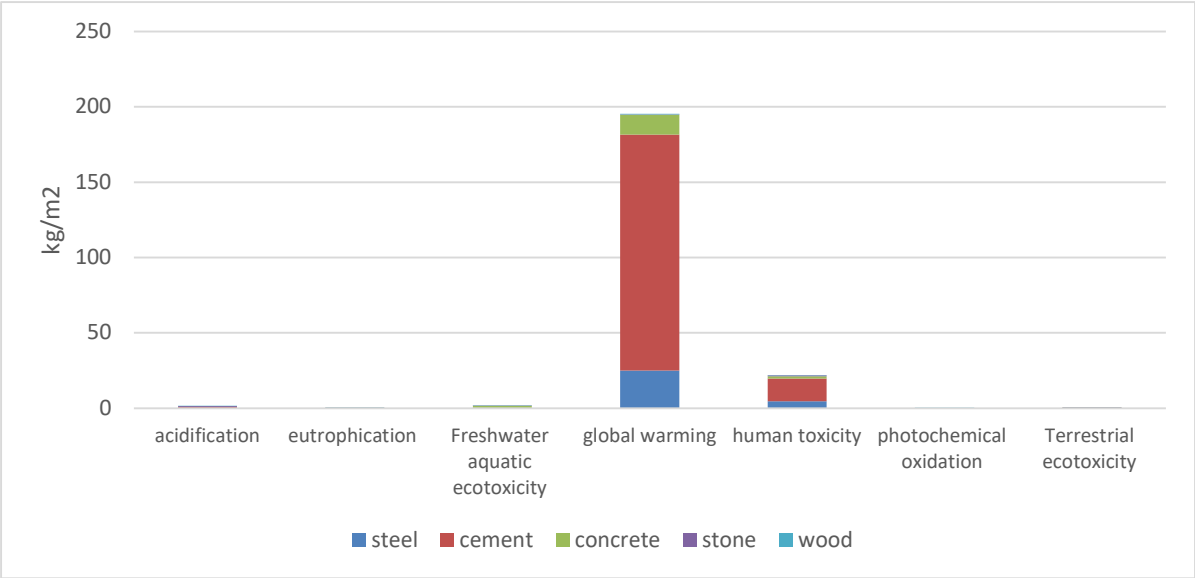

Figure 7-39: Environmental impact of RC building for repairment

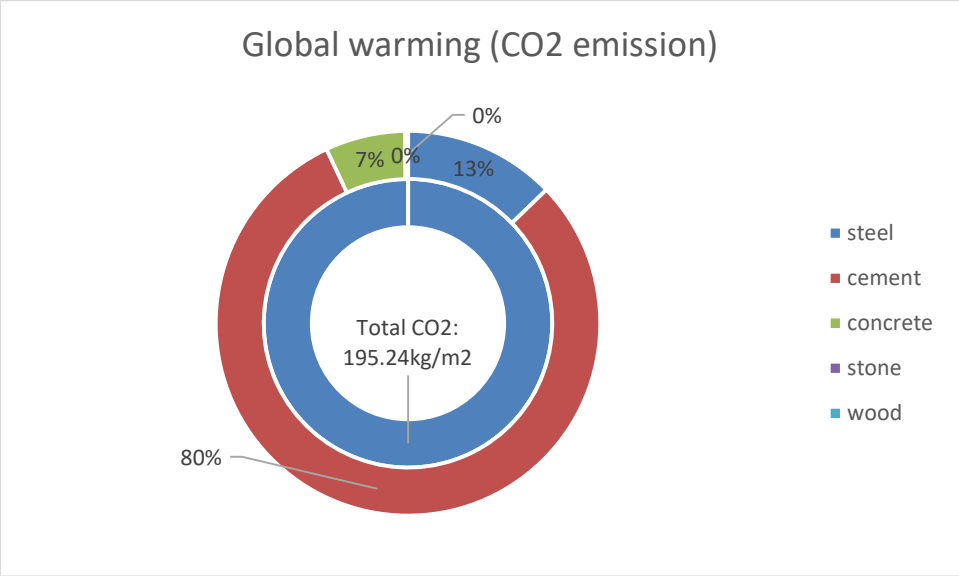

Figure 7-40: percentage of CO2 emission from RC building repairment

7.5.3 Comparision

Figure 7-41 exhibits the CO_2 emission of CLT buildings in material production and repair stages. Compared with the baseline, CO2 emission increased 21% in these two stages for scenario 2, while scenario 1 is around 4% higher than the baseline. Regarding energy consumption, scenario 1 is 0.1GJ/m2 higher than the baseline. However, scenario 2 is 20% (0.66GJ/m^2) higher, implying that the embodied energy consumption and environmental impact could be underestimated without considering the repair stage (Figure 7-42).

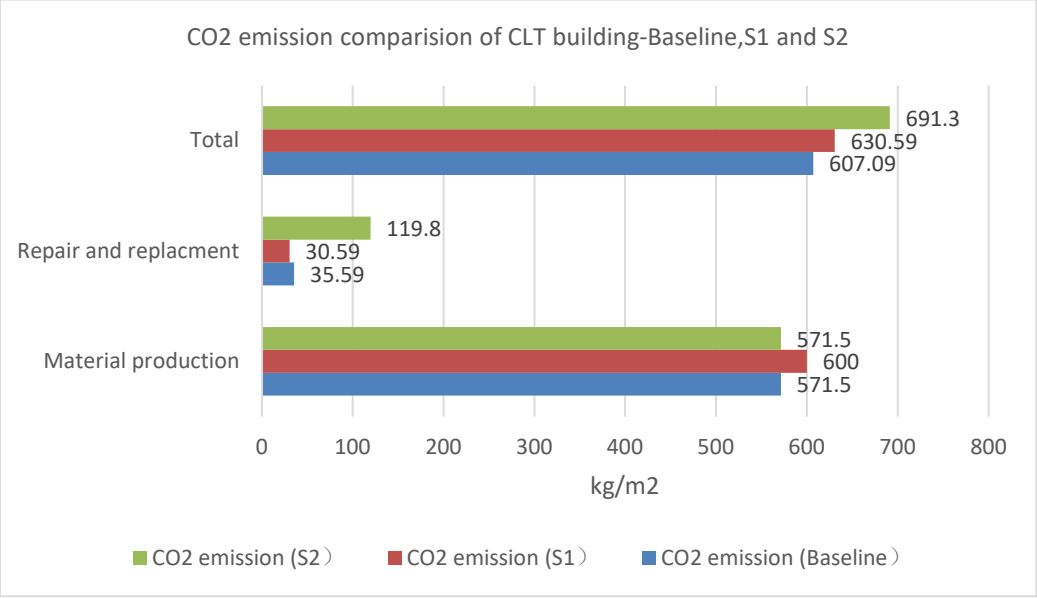

Figure 7-41: Embodied CO2 emission from CLT buildings under different repair scenarios

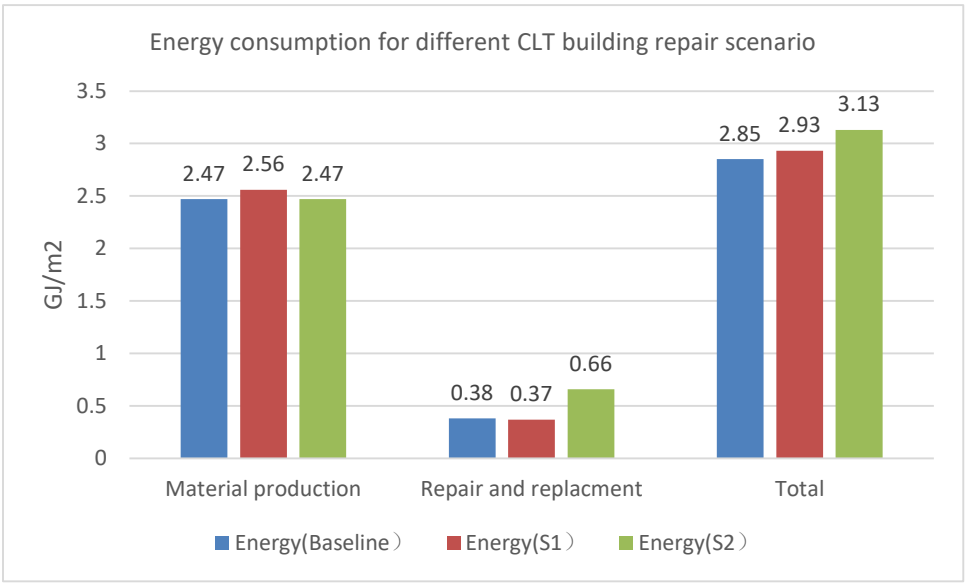

Figure 7-42: Embodied energy of CLT buildings under different repair scenarios

What was compared in Figure 7-43 is the energy consumption of the RC building and CLT-S2 under different stages. The operation stage consumes the greatest energy, accounting for around 67% of both building systems. The material stage of RC building accounts for 20% of the total energy consumption, and the percentage for CLT-S2 is slightly increased, with a value of 22.4%. The total energy consumption for the RC building in the 50-year life span is 18.14GJ/m^2, and for the CLT building is 11.11GJ/m^2, which is 39.3% less than the RC building (Figure 7-44). Regarding CO_2 emission, the RC building and CLT operation stage account for 54%. The CO_2 emission from the RC building's material production stage accounts for 34% of the total emission, and for the CLT building, the percentage is around 35%. The total CO_2 emission for the RC and CLT building is 2559.74kg/m^2 and 1648.96kg/m^2, respectively. Compared with the RC building, the global warming potential of CLT can be reduced by around 35.6%.

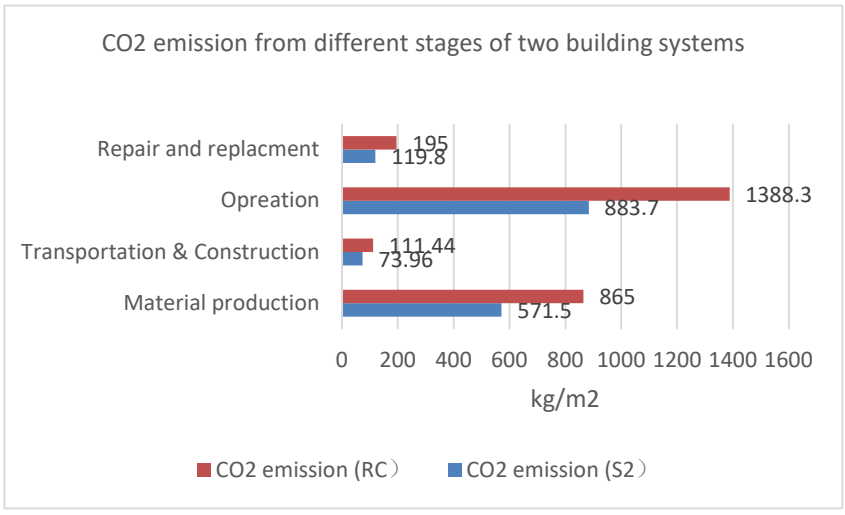

Figure 7-43: CO2 emission from different stages of two building systems

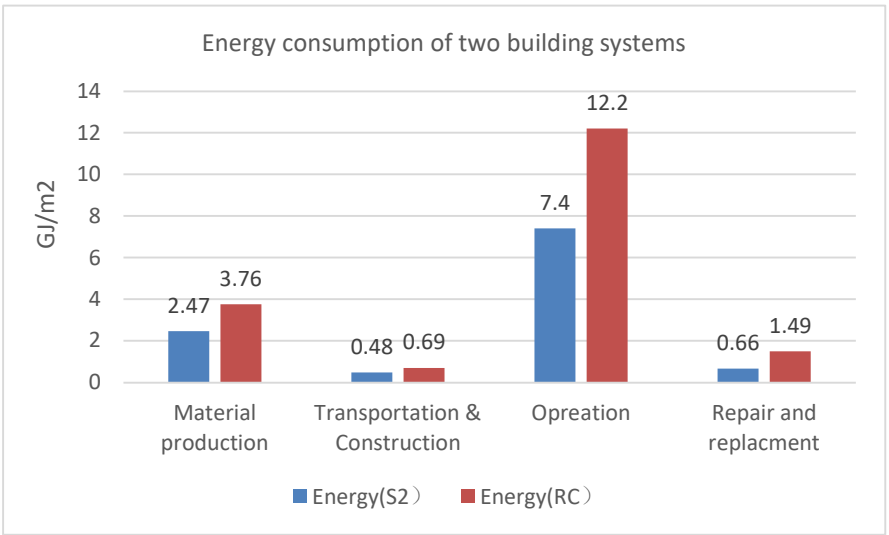

Figure 7-44: Energy consumption of different stages of two building systems

7.6 Conclusion

This chapter reviewed the application in the construction sector, followed by introducing the LCA method. The LCA method applied to construction sectors covers energy coupled environmental LCA, economic associated LCA, and dynamic LCA. For CLT buildings, most research used the energy coupled LCA, which is focused on the energy and environmental impact of this building system.

The energy couple LCA method to analyse the energy consumption and environmental impact of CLT buildings was utilized in the research. The results have indicated that the operation stage accounts for more than 50% of the total energy consumption and environmental impact. In comparison, the repair stage only accounts for 6%. Nevertheless, without considering the repair stage of CLT building, embodied energy consumption and carbon dioxide emissions will be reduced by 20%.

Apart from global warming, these two buildings can significantly impact freshwater ecotoxicity and human toxicity. Comparing the two building systems shows that replacing the RC building with the CLT building can reduce more than 30% of the total energy and CO2 emissions. But, the production of CLT panels may aggravate pollution issues on freshwater than RC building materials.

The inventory assessment method for this study includes O-I and a process-based hybrid method based on the availability of databases. When the unit price for different building materials is calculated, the CLT panels' price is higher than other building materials, leading to a higher embodied cost and a lower operation cost. Further research may continue with the economic coupled LCA to analyse the cost-benefit of CLT buildings compared to RC buildings to help the decision-maker understand the barrier.

Chapter 8. Conclusion

8.1 Summary

8.1.1 Wind load cyclic testing process design

To investigate the performance of wood connections under long-time wind pressure, this thesis started with designing the loading protocol through laboratory experiments. The first step for loading sequence design is collecting wind load data from a target city or area. Although most building regulations constrain wind pressure values for building wind load design, the author adopted the method of collecting annual hourly wind velocity data from open databases. The reasons are as follows: first, the up-to-date data can provide a more realistic reflection of the actual situation in the chosen area; second, it will be convenient to predict the extreme wind velocity for different return periods with enough data collected from the database; last but not least, some databases can provide both hourly maximum mean velocity, maximum gust velocity and wind direction, suitable for wind pressure research of different conservative degrees. This study collected both mean and gust velocity data for further research.

The second step is to predict the extreme wind load. The extreme value analysis theory and Gumbel and Weibull methods have been selected to estimate the extreme wind velocity in 50 year return period. The result from the Gumbel method is higher than the Weibull method. Therefore, the Gumbel method appears to be much more suitable within the temperate area. Thus, the study selected the values from the Gumbel method for the third step.

The third step is to obtain the dynamic velocity by adding a random wind velocity sequence of time on the static extrema wind velocity. The 5-order AR model combined with the Davenport spectrum has been utilized in this study to generate the time history of fluctuating wind speed. The results indicate that the power spectrum of dynamic-wind velocity fits the target spectrum curve well. Furthermore, the standard deviation of the

secondly dynamic wind load is similar to the hourly gust wind load, indicating that this model can provide reliable results.

The fourth step is to apply the dynamic wind velocity to the targeted structure to analyse the wind pressure and structural behaviour. The Structure and CFD co-simulation procedures have been selected in this study to finish this step, which is economical and convenient. Under the guidance of building regulations from different countries, the simulation results are compared to the numerical calculation results, which shows that it is feasible to use the finite element method to analyse the structure vibration behaviour under wind load. The last step is to build the loading protocol by combining the recorded displacement data from step 4 with the Rain flow count method. In this research, only the cycle with the largest amplitude is extracted, reducing the total cycle number for the cyclic load test and reflecting the most significant vibration of each wind speed group.

8.1.2 Feasibility of newly designed loading sequences

The behaviour during four cyclic sequences shows no significant plastic damage. In this research, the newly designed loading sequences have been applied to test the joint timber samples, which have been compared with samples tested under three other existing loading sequences from different countries afterwards (DABM, BRE, TR440). In this study, the mechanical response of joints is divided into clockwise and counterclockwise, and the strength impairment, viscous damping, and energy dissipation in each direction are analyzed. The strength impairment in the clockwise direction is higher than counterclockwise. Loading protocol DABM caused the most strength impairment, followed by the TR440 and ARC3050, and the BRE loading protocol made the smallest strength reduction. In terms of damping ratio, the mean values for those four groups are around 10%, and there are slight differences between the groups. The damping differences between counterclockwise directions are insignificant as clockwise that vary between 36.4% and 93.8% for those four groups. Furthermore, the mean damping in the clockwise direction for BRE, TR440, DABM and ARC3050 is 54.8%, 50%,31.9% and 24.8%, respectively. Those are significantly higher than the counterclockwise direction, indicating that the two directions' resistance mechanisms are different. The counterclockwise direction depends

much more on the fasteners, but the clockwise direction relies on the flange of the angle bracket.

Additionally, monotonic tests are applied to the specimens after the cyclic test to analyse the residual required load, which implies stiffness reduction. The stiffness values are calculated, showing that the value increased with the rotation ratio rather than consistent, indicating that the stiffness reduced compared with the original condition. The results show that the value in the counterclockwise direction after cyclic loading according to the DABM can be reduced to 55%. For ARC3050, the reduction value is around 45%, slightly higher than TR440 and BRE. The stiffness adjustment indicates that the nails loosened after cyclic load but are not entirely pulled out.

Lab test results imply that long-term wind load can significantly reduce the stiffness of timber joints, and the wind load can influence the strength factor. The residual stiffness results obtained by the ARC3050 method are similar to those obtained by BRE and TR440, but more than 5 hours compared with TR440 and DABM method have been saved, and 3 hours with BRE in testing time. The comparison between different loading scenarios manifests that the DABM method is relatively conservative than the other three methods. Furthermore, a reasonably straightforward logic theory behind the newly designed test method can be repeated for different wind load conditions analyses.

8.1.3 Influence factor on fatigue behaviour of timber joints

In chapters 5 and 6, this study modifies the impact factors, including building height and connection details, and then tests the performance of timber joints after cyclic testing. The result suggests that wind velocity is possibly related to building height. Based on the new procedure to analyse building height's impact, this research will design the loading sequences under different wind loads. Additionally, this research applied the DIC method to observe the angle bracket behaviour.

Lab test results revealed that the energy dissipation value increased with loading displacement in counterclockwise and clockwise directions. The average damping ratio for joints at 60m height is lower than at the other two heights, with a value of 8.8%, 0.6% lower than 30m, and 2.7% lower than 10m. This indicated that the connections' energy dissipation

ratio decreased with the building's height. In contrast, the strength impairment value is higher than others. Regarding residual stiffness, the value for joint at 60m height is around 51% at the 0.16% rotation ratio, for 30m is around 55% and 61% for 10m. Those results indicate that with the building height increase, the fatigue damage of joints caused by long-term wind load will become more severe. The DIC analysis results proved that there is relative movement between the angle bracket and timber component; Thus, the effect of the cyclic tests on the timber connection system used in this study was mainly induced by the loosening of nails than the damage of angle bracket.

By comparing the performance between different connection boundaries, the mean value for AB1, AB2, AB3 and TC is 9.4%,10.3%, 11.1% and 14.3%, respectively. It is found in the study that adding nails on the nails to stressed parts has no significant influence on the damping counterclockwise direction but can improve the damping clockwise from 24.82% to 35.97%. Additionally, the research has also revealed that this kind of modification makes the AB2 reach the yield point in a clockwise direction early than AB1, which indicates that a change in nail pattern can further influence the ductility of the whole joint.

In terms of the connection between timber and concrete test, the connection type used in this study can only be classified as a nominally pinned joint. As the stiffness of the angle bracket connection system is highly dependent on the fastener, especially the ones near the corner, the study recommended connecting the timber to concrete with an angle bracket that has the bolt hold near the corner rather than the far end.

8.1.4 Environmental impact of timber building

This study provided one example for research on the connection wind-load fatigue behaviour and proved that long-term wind load could reduce structural bearing capacity, meaning demand for repair or replacement of connectors, while most life cycle assessment research ignored the repairing stage. Therefore, the embodied energy or environmental impact may be underestimated without considering the repair stage. The results from chapter 7 display that given the maintenance of the connectors CLT building, the embodied energy and global warming potential can increase by 20%. In this LCA study, the angle bracket distance for the reference building is assumed to be 65cm, which is normally used in practice. However, in designing the fatigue test loading protocol, the distance between

the angle bracket in the CFD simulation is 20cm. If the fatigue test is performed under a 65cm distance condition, the residual loading capacity of the timber joint may be lower, which can lead to a more frequent repair. Thus combining the LCA method with the structural performance of timber buildings seems important in estimating more accurate environmental impact.

Despite the disadvantages in the repair stage, CLT building is still more energy and environmentally efficient than RC building. The study also noted that these two building systems significantly impact water ecotoxicity and human toxicity apart from global warming. In material production, CLT building also made more freshwater ecotoxicity than RC.

8.3 Research limitation and Potential future work

Firstly, the sample edges of the foundation part were extended to fix the sample on the testing machine, which can prevent the whole sample rotation. However, this may lead to a difference from the actual practice, which is one limitation of the sample design. Additionally, this test applied a two-dimensional DIC to test three-dimensional motion, resulting in a cosine error. Figure 8-1 shows that at a rotation angle of 2, the error is as high as 0.06%; therefore, to get more accurate deformation results, a 3d measurement may be required. Furthermore, this research introduced a new method to develop a loading sequence to represent the wind load improvement in the process of loading protocol designs that is still required. Such as, when estimating the extreme wind velocity, the influence of wind load direction is ignored in this study. Therefore, the following CFD simulation considers only the wind from 90 degrees to the wall panel. Although this method can

provide a short testing time, the loading sequence design procedure is complex and highly dependent on data collection and CFD simulation results.

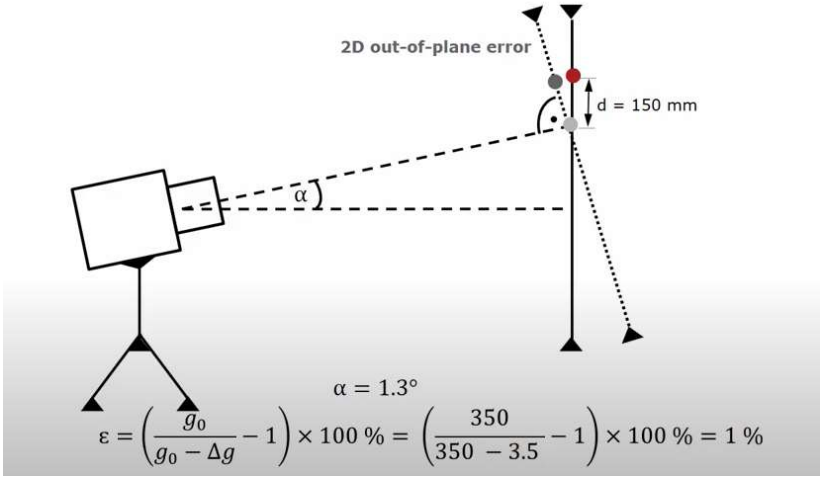

Figure 8-1: Out-of-plane error for DIC method (GOM Metrology, 2017)

This thesis has identified some areas for future study. Firstly, adding the influence of wind direction to the loading protocol can complicate the research of wind load effect on connections. Therefore, simulations or experiments are needed to analyse the sensitivity of timber wall vibration to wind direction. Furthermore, it is also helpful to make experimental results closer to reality by involving the influence of cross-wind pressure on the wall vibration.

This research tested the fatigue behaviour under 50 years of extreme wind load. Further research can be conducted based on the new loading protocol designed to test the fatigue behaviour under different return periods and then find the relationship between fatigue damage, return period and fatigue life by combining the N-S curve of the joint and stress-strain results. In addition, due to the limitation of experimental equipment, only residual stiffness was analysed in this research. Further work can continue studying this connection system's failure mode, and residual strength under lateral load rotates the specimen.

Moreover, this research considered the cyclic behaviour of joints under long-term wind load and showed the stiffness reduction. This consequence may further affect the vertical bearing capacity of the walls, shear resistance and the whole building structure. As a result, the future coupled shear, and vertical load test can comprehensively make the researchers understand the mechanical performance of such a connecting system.

Appendix A. Wind field validation

Pope (2000)explained that the hydrodynamically fully developed velocity profile collapses to a universal velocity profile when normalized with appropriated viscous units. To validate the wind field, the concept of that 'law of wall' is used in this research. The area in the wind field can be divided into three parts: the inner layer, the outer layer and the buffer layer. The inner and outer profiles are described below. The non-dimensional velocity $U^+$and wall-normal distance $y^+$is defined as

$$U^+ = \begin{cases} y^+ & \text{if } y^+ < 11 \\ \frac{1}{\kappa}\ln(y^+) + B & \text{if } y^+ \geq 11, \end{cases}$$

where

$$U^+ = \frac{U}{u_\tau},$$

$$y^+ = \frac{y u_\tau}{\nu},$$

$$u_\tau = \sqrt{\frac{\tau_w}{\rho}},$$

$$\tau_w = \mu \left.\frac{\partial u}{\partial y}\right|_{y=w}.$$

Where U is the streamwise velocity, y is the wall-normal direction, ν is the kinematic viscosity, μ is the dynamic viscosity, ρ is the fluid density, τ_w is the shear stress at the wall and u_τ is the friction velocity or characteristic velocity of the shear stress at the wall. $\kappa = 0.41$ and $B = 5.2$ are constants.

The turbulent flow in a plane channel is characterized by a Reynolds number that uses the friction velocity and half-width channel (H/2). The Reynolds number based on friction velocity is

$$Re_\tau = \frac{u_\tau H}{2\nu}.$$

This study uses a channel flow with Ret=395 for this test as it is sufficiently high for a fully turbulent flow with less mesh requirement. The model is the same as the previous wind field model used in this research but reduces the inlet area, which is 50 in height, 50 in length and 5 in wide Figure A-1.

The inlet and outlet wall are the same as in Figure 3-8. The inlet flow is defined by pressure (P). The top and bottom surfaces are defined as no-slip/no-penetration boundary conditions. For the turbulence model, the Spalart-Allmaras turbulent viscosity / is set to zero, and the wall-normal distance is also set to zero. At the outflow, surface pressure is defined to be zero. The normal gradients of velocities and Spalart-Allmaras viscosity, $\widetilde{\nu}$, are automatically set to zero for this boundary. These conditions correspond to the well-known natural or "do-nothing" boundary condition.The initial velocity, V, is set to zero everywhere in the flow domain. The Spalart-Allmaras turbulent viscosity is initialized to five times the kinematic viscosity $\widetilde{\nu} = 5\nu$.

The flow parameters are ρ =1 kg/m3, p_{in} = 0.4783 × 10–1, and μ =0.6190 × 10–4. The total execution time was set to t = 1000 s to reach a steady-state in all meshes. The solver options are set to the defaults except for the pressure Poisson equation (PPE) and momentum solver tolerance, which is set to 10^{-8}.

Following ASME V&V 20-2009, the error in the numerical solution can be computed as

$$E_h = u_\tau(h) - u_\tau^{exact} = Ch^p + H.O.T.,$$

Where H.O.T. are the Higher-Order Terms and h denotes the characteristic mesh metric size.

Following ASME V&V 20-2009, the observed convergence between the two calculations can be approximated as

$$p = \frac{ln\left(\left|\frac{E_{h2}}{E_{h1}}\right|\right)}{ln\left(r_{21}\right)},$$

Where $E_{h2} = E_h(h_i)$ and $r_{12} = h_2/h_1$, with $h_1 < h_2$.

Figure A-1 shows the relationship between simulation results and the targeted line. The results show steady good agreement with the well-known law of the wall solution. Furthermore, Figure A-2 shows that the estimated convergence rate to be in close agreement with the theoretical second-order spatial accuracy of the code.

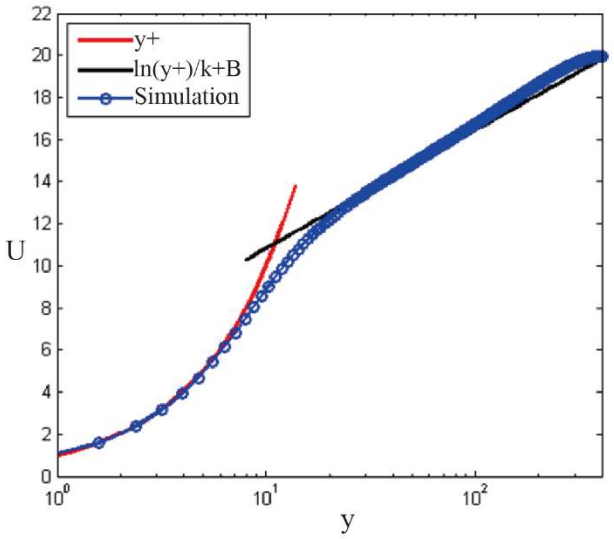

Figure A-1: Simulation results for velocity and point location

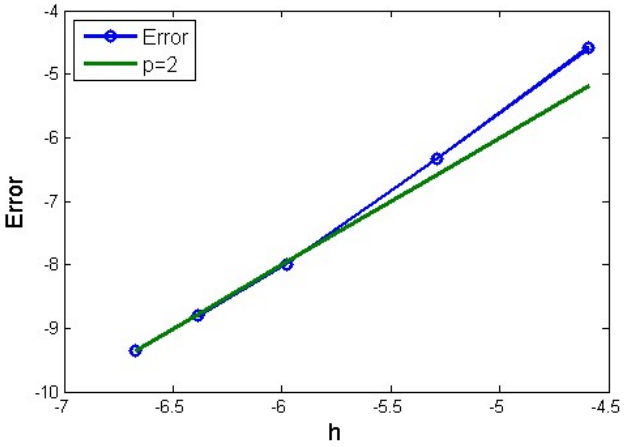

Figure A-2: Convergence of the friction velocity

BibliographyUncategorized References

2020. CWB observation Data inquiry system (CODis). Central Weather Bureau.

ABD RASHID, A. F., YUSOFF, S. J. R. & REVIEWS, S. E. 2015. A review of life cycle assessment method for building industry. 45**,** 244-248.

ABEYSEKERA, I. & MALAGA CHUQUITAYPE, C. 2015. Dynamic response of tall timber buildings.

ABILD, J., ANDERSEN, E. Y. & ROSBJERG, D. 1992a. The climate of extreme winds at the great belt, Denmark. *Journal of Wind Engineering and Industrial Aerodynamics,* 41**,** 521-532.

ABILD, J., MORTENSEN, N. G. & LANDBERG, L. 1992b. Application of the wind atlas method to extreme wind speed data. *Journal of Wind Engineering and Industrial Aerodynamics,* 41**,** 473-484.

ABRAHAMSEN, R. Mjøstårnet-Construction of an 81 m tall timber building. Internationales Holzbau-Forum IHF, 2017. 1-12.

ABRAHAMSEN, R., BJERTNAES, M. A., BOUILLOT, J., BRANK, B., CABATON, L., CROCETTI, R., FLAMAND, O., GARAINS, F., GAVRIC, I. & GERMAIN, O. Dynamic Response of Tall Timber Buildings Under Service Load: The DynaTTB Research Program. EURODYN 2020, XI International Conference on Structural Dynamics, Athens, Greece, 22–24 June 2020, 2020. National Technical University of Athens, 4900-4910.

ABRAHAMSEN, R. B. & MALO, K. A. Structural design and assembly of" Treet"–A 14-storey timber residential building in Norway. World conference on timber engineering, 2014.

ADALBERTH, K., ALMGREN, A., PETERSEN, E. H. J. I. J. O. L. E. & BUILDINGS, S. 2001. Life cycle assessment of four multi-family buildings. 2.

ADALBERTH, K. J. B. & ENVIRONMENT 1997. Energy use during the life cycle of single-unit dwellings: examples. 32**,** 321-329.

AHMADI, B. & SAKA, M. J. J. O. S. E. 1993. Behavior of composite timber-concrete floors. 119**,** 3111-3130.

ALI, D. A., NEGM, A. & BADY, M. 2014. *Estimating Carbon Emissions from Industrial Process by using Life Cycle Assessment Tool*.

ALINEJAD, H. & KANG, T. H.-K. J. J. O. S. E. 2020. Engineering Review of ASCE 7-16 Wind-Load Provisions and Wind Effect on Tall Concrete-Frame Buildings. 146**,** 04020100.

AMZALLAG, C., GEREY, J. P., ROBERT, J. L. & BAHUAUD, J. 1994. Standardization of the rainflow counting method for fatigue analysis. *International Journal of Fatigue,* 16**,** 287-293.

AN, K., FUNG, J. C. H. & YIM, S. H. L. 2013. Sensitivity of inflow boundary conditions on downstream wind and turbulence profiles through building obstacles using a CFD approach. *Journal of Wind Engineering and Industrial Aerodynamics,* 115**,** 137-149.

ARGYROPOULOS, C. D. & MARKATOS, N. C. 2015. Recent advances on the numerical modelling of turbulent flows. *Applied Mathematical Modelling,* 39**,** 693-732.

ARıDURU, S. 2004. *Fatigue life calculation by rainflow cycle counting method.* Middle East technical university.

ARVANITOYANNIS, I. S. J. W. M. F. T. F. I. 2008. ISO 14040: life cycle assessment (LCA)–principles and guidelines. 97-132.

ASCE 2017. Minimum Design Loads and Associated Criteria for Buildings and Other Structures. Reston, Virginia: American Society of Civil Engineers.

ASIF, M., MUNEER, T., KELLEY, R. J. B. & ENVIRONMENT 2007. Life cycle assessment: A case study of a dwelling home in Scotland. 42**,** 1391-1394.

ASIZ, A. & SMITH, I. 2011. Connection System of Massive Timber Elements Used in Horizontal Slabs of Hybrid Tall Buildings. 137**,** 1390-1393.

ASTM 2019. ASTM E2126 Standard test methods for cyclic (reversed) load test for shear resistance of vertical elements of the lateral force resisting systems for buildings.

BACH, L. 1966. *Nonlinear mechanical behavior of wood in longitudinal tension*, State University of New York College of Environmental Science and Forestry.

BAETKE, F., WERNER, H. & WENGLE, H. 1990. Numerical simulation of turbulent flow over surface-mounted obstacles with sharp edges and corners. *Journal of Wind Engineering and Industrial Aerodynamics,* 35**,** 129-147.

BAINES, W. D. Effects of velocity distribution on wind loads and flow patterns on buildings. Proceedings of Conference "Wind effects on buildings and structures", 26-28 June 1963 Teddington UK. National Physical Laboratory 198-225.

BAKER, W., HOROS, D., JOHNSON, B. & SCHULTZ, J. Timber tower research: Concrete jointed timber frame. Structures Congress 2014, 2014. 1255-1266.

BALASBANEH, A. T., SHER, W. J. B. & ENVIRONMENT 2021. Comparative sustainability evaluation of two engineered wood-based construction materials: Life cycle analysis of CLT versus GLT. 204**,** 108112.

BASKARAN, A. & CHEN, Y. 1998. Wind load cycle development for evaluating mechanically attached single-ply roofs. *Journal of Wind Engineering and Industrial Aerodynamics,* 77-78**,** 83-96.

BASKARAN, A. & LEI, W. A new facility for dynamic wind performance evaluation of roofing systems. Proceedings of the fourth international symposium on roofing technology, 1997. 168-179.

BASKARAN, A. J. J. O. A. E. 2002. Dynamic wind uplift performance of thermoplastic roofing system with new seaming technology. 8**,** 97-107.

BAWDEN, K. & WILLIAMS, E. J. C. 2015. Hybrid life cycle assessment of low, mid and high-rise multi-family dwellings. 6**,** 98-116.

BECK, V. & STEVENS, L. 1979. Wind loading failures of corrugated roof cladding. *In: Diamond Jubilee Conference 1979. Perth, W.A.: Institution of Engineers, Australia, 1979: [163]-[174].*

BEG, D., ZUPANČIČ, E. & VAYAS, I. 2004. On the rotation capacity of moment connections. *Journal of Constructional Steel Research,* 60**,** 601-620.

BELLAMY, L. & MACKENZIE, D. Thermal performance of concrete versus timber framed walls in side-by-side test buildings: results from base-case and ventilation trials. Proceedings of the 37th Annual Conference of ANZSES, 1999 Geelong.

BEZABEH, M., TESFAMARIAM, S. & STIEMER, S. J. J. O. S. E. 2016. Equivalent viscous damping for steel moment-resisting frames with cross-laminated timber infill walls. 142**,** 04015080.

BEZABEH, M. A., BITSUAMLAK, G. T., POPOVSKI, M. & TESFAMARIAM, S. 2018a. Probabilistic serviceability-performance assessment of tall mass-timber buildings subjected to stochastic wind

loads: Part I - structural design and wind tunnel testing. *Journal of Wind Engineering and Industrial Aerodynamics,* 181**,** 85-103.

BEZABEH, M. A., BITSUAMLAK, G. T., POPOVSKI, M. & TESFAMARIAM, S. 2018b. Probabilistic serviceability-performance assessment of tall mass-timber buildings subjected to stochastic wind loads: Part II - structural reliability analysis. *Journal of Wind Engineering and Industrial Aerodynamics,* 181**,** 112-125.

BEZABEH, M. A., BITSUAMLAK, G. T., POPOVSKI, M. & TESFAMARIAM, S. 2020. Dynamic Response of Tall Mass-Timber Buildings to Wind Excitation. *Journal of Structural Engineering,* 146**,** 04020199.

BHATIA, A., GARG, V. & MATHUR, J. 2009. Determination of energy saving with cool roof concept using calibrated simulation: Case of a learning centre in composite Indian climate. TR/2009/177. Centre for Agriculture and Rural Development International ….

BISPING, J. R., PETERWERTH, B., BLEICHER, C., WAGENER, R. & MELZ, T. 2014. Fatigue life assessment for large components based on rainflow counted local strains using the damage domain. *International Journal of Fatigue,* 68**,** 150-158.

BJERTNæS, M. A. & MALO, K. A. J. W. Q. 2014. Wind-induced motions of "Treet"-A 14-storey timber residential building in Norway.

BLANCHARD, S. & REPPE, P. 1998. Life cycle analysis of a residential home in Michigan.

BLENGINI, G. A. & DI CARLO, T. 2010. The changing role of life cycle phases, subsystems and materials in the LCA of low energy buildings. *Energy and Buildings,* 42**,** 869-880.

BOCHICCHIO, G., CECCOTTI, A., FRANGI, A. & LAURIOLA, M. Natural full-scale fire test on a 3 storey XLam timber building. Proceedings of 10th World Conference on Timber Engineering (WCTE), Miyazaki, Japan, 2008.

BODIG, J. & JAYNE, B. A. 1993. *Mechanics of wood and wood composities.* , Malabar, Fla.: Krieger Publishing.

BONFIELD, P. & ANSELL, M. P. J. J. O. M. S. 1991. Fatigue properties of wood in tension, compression and shear. 26**,** 4765-4773.

BöRJESSON, P. & GUSTAVSSON, L. J. E. P. 2000. Greenhouse gas balances in building construction: wood versus concrete from life-cycle and forest land-use perspectives. 28**,** 575-588.

BRANDNER, R., FLATSCHER, G., RINGHOFER, A., SCHICKHOFER, G., THIEL, A. J. E. J. O. W. & PRODUCTS, W. 2016. Cross laminated timber (CLT): overview and development. 74**,** 331-351.

BRE 1989. *The assessment of wind loads. Part 7: wind speeds for serviceability and fatigue assessments (DG 346-7)*, BREPress.

BSI 2005. BS EN 1993-1-8:2005：Eurocode 3: Design of steel structures - Part 1-8: Design of joints.

BSI 2009. Timber structures. Test methods. Load bearing nails, screws, dowels and bolts. Brussels, Belgium.

BSI 2011. Mechanical vibration and shock — Evaluation of human exposure to whole-body vibration Part 1: General Requirements.

BULLARD, C. W. & HERENDEEN, R. A. 1975. The energy cost of goods and services. *Energy Policy,* 3**,** 268-278.

BULLARD, C. W., PENNER, P. S. & PILATI, D. A. 1978. Net energy analysis: Handbook for combining process and input-output analysis. *Resources and Energy,* 1**,** 267-313.

BURGERS, J. J. F. R. O. V. & PLASTICITY 1935. Mechanical considerations-model systems-phenomenological theories of relaxation and of viscosity. 1.

CASTELLANI, V., BEYLOT, A. & SALA, S. J. J. O. C. P. 2019. Environmental impacts of household consumption in Europe: Comparing process-based LCA and environmentally extended input-output analysis. 240**,** 117966.

CEBON, D. 1993. Interaction Between Heavy Vehicles and Roads. SAE International.

CECCOTTI, A., LAURIOLA, M., FOLLESA, M. & SANDHAAS, C. SOFIE Project - Test results on the lateral resistance of cross-laminated wooden panels. 2006.

CECCOTTI, A. J. T. E. S. 1995. Timber-concrete composite structures. 2**,** E13.

CHAKER, A. A. & CHERIFATI, A. 1999. Influence of masonry infill panels on the vibration and stiffness characteristics of R/C frame buildings. 28**,** 1061-1065.

CHANG, F.-K. J. J. O. T. S. D. 1973. Human response to motions in tall buildings. 99**,** 1259-1272.

CHANG, Y., HUANG, Z., RIES, R. J. & MASANET, E. 2016. The embodied air pollutant emissions and water footprints of buildings in China: a quantification using disaggregated input–output life cycle inventory model. *Journal of Cleaner Production,* 113**,** 274-284.

CHAPMAN, J., REYNOLDS, T. & HARRIS, R. A 30 level cross laminated timber building system and analysis of the eurocode dynamic wind loads. World Conference on Timber Engineering 2012: The Future of Timber Engineering, WCTE 2012, 2012. 49-56.

CHE, A., HE, Y., GE, X., IWATATE, T. & ODA, Y. 2006. Study on the dynamic structural characteristics of an ancient timber—Yingxian Wooden Pagoda. *Soil and Rock Behavior and Modeling.*

CHEN, J., TIAN, B. & CHEN, W. 2012. JGJ26—2010《 严寒和寒冷地区居住建筑节能设计标准》 探析. 60-62.

CHEN, X. & KAREEM, A. J. J. O. S. E. 2005. Coupled dynamic analysis and equivalent static wind loads on buildings with three-dimensional modes. 131**,** 1071-1082.

CHENG, H., ZHONG, H., ZHOU, L. & WANG, L. 2016. Numerical Simulation of Fluctuating Wind Velocity Time Series. *Journal of Ordnance Equipment Engineering,* 4**,** 143-148.

CHENG, Y.-W. & BROZ, J. J. 1986. Cycle-counting methods for fatigue analysis with random load histories: A FORTRAN user's guide.

CHINA, N. S. O. T. P. S. R. O. 2012. Load code for the design of building structures. Beijing, China: China Architecture & Building Press.

CHOWDHURY, A. G., CANINO, I., MIRMIRAN, A., SUKSAWANG, N. & BAHERU, T. 2013. Wind-Loading Effects on Roof-to-Wall Connections of Timber Residential Buildings. 139**,** 386-395.

COCHRAN, L. & DERICKSON, R. 2011. A physical modeler's view of Computational Wind Engineering. *Journal of Wind Engineering and Industrial Aerodynamics,* 99**,** 139-153.

COLE, R. J., KERNAN, P. C. J. B. & ENVIRONMENT 1996. Life-cycle energy use in office buildings. 31**,** 307-317.

COLE, R. J. J. B. & ENVIRONMENT 1998. Energy and greenhouse gas emissions associated with the construction of alternative structural systems. 34**,** 335-348.

COLLINGE, W. O., LANDIS, A. E., JONES, A. K., SCHAEFER, L. A. & BILEC, M. M. 2013. Dynamic life cycle assessment: framework and application to an institutional building. *The International Journal of Life Cycle Assessment,* 18**,** 538-552.

COLLINGE, W. O., LANDIS, A. E., JONES, A. K., SCHAEFER, L. A. & BILEC, M. M. 2014. Productivity metrics in dynamic LCA for whole buildings: Using a post-occupancy evaluation of energy and indoor environmental quality tradeoffs. *Building and Environment,* 82**,** 339-348.

CONRADSEN, K., NIELSEN, L. B. & PRAHM, L. P. 1984. Review of Weibull Statistics for Estimation of Wind Speed Distributions. *Journal of Applied Meteorology and Climatology,* 23**,** 1173-1183.

COOK, N. J., KEEVIL, A. P. & STOBART, R. K. 1988. Brerwulf - the big bad wolf: I'll huff and I'll puff and I'll blow your house down! *Journal of Wind Engineering and Industrial Aerodynamics,* 29**,** 99-107.

CORPORATION, S. A. I. & CURRAN, M. A. 2006. Life-cycle assessment: principles and practice. National Risk Management Research Laboratory, Office of Research and ….

CRESPELL, P. & GAGNON, S. J. F. S. P. 2010. Cross laminated timber: a primer. 52.

CUMMINGS, R. M., MASON, W. H., MORTON, S. A. & MCDANIEL, D. R. 2015. *Applied computational aerodynamics: A modern engineering approach*, Cambridge University Press.

D'ARENZO, G., CASAGRANDE, D., POLASTRI, A., FOSSETTI, M., FRAGIACOMO, M. & SEIM, W. J. J. O. S. E. 2021. CLT Shear Walls Anchored with Shear-Tension Angle Brackets: Experimental Tests and Finite-Element Modeling. 147**,** 04021089.

DANZIG, I. Tall Wood in Canada: Feasibility Study, Technical Guide, and Wood Innovation and Design Centre. Internationales Holzbau-Forum (IHF 2013) Aus der Praxis–Für die Praxis, 2011.

DAO THANG, N. & VAN DE LINDT JOHN, W. 2012. Loss Analysis for Wood Frame Buildings during Hurricanes. I: Structure and Hazard Modeling. *Journal of Performance of Constructed Facilities,* 26**,** 729-738.

DAVENPORT, A. G. 1961. The spectrum of horizontal gustiness near the ground in high winds. 87**,** 194-211.

DAVENPORT, A. G. J. J. O. T. S. D. 1967. Gust loading factors. 93**,** 11-34.

DAVIDS, W. G., WILLEY, N., LOPEZ-ANIDO, R., SHALER, S., GARDNER, D., EDGAR, R. & TAJVIDI, M. 2017. Structural performance of hybrid SPFs-LSL cross-laminated timber panels. *Construction and Building Materials,* 149**,** 156-163.

DAVISON, A. C. & SMITH, R. L. 1990. Models for Exceedances over High Thresholds. *Journal of the Royal Statistical Society. Series B (Methodological),* 52**,** 393-442.

DE LUCA, V., MARANO, C. J. C. & MATERIALS, B. 2012. Prestressed glulam timbers reinforced with steel bars. 30**,** 206-217.

DIAS, A., SKINNER, J., CREWS, K., TANNERT, T. J. E. J. O. W. & PRODUCTS, W. 2016. Timber-concrete-composites increasing the use of timber in construction. 74**,** 443-451.

DICKOF, C. 2013. *CLT infill panels in steel moment resisting frames as a hybrid seismic force resisting system.* University of British Columbia.

DICKOF, C., STIEMER, S., BEZABEH, M. & TESFAMARIAM, S. J. J. O. P. O. C. F. 2014. CLT–steel hybrid system: Ductility and overstrength values based on static pushover analysis. 28**,** A4014012.

DIETSCH, P. & BRANDNER, R. 2015. Self-tapping screws and threaded rods as reinforcement for structural timber elements – A state-of-the-art report. *Construction and Building Materials,* 97**,** 78-89.

DODOO, A., GUSTAVSSON, L., SATHRE, R. J. E. & BUILDINGS 2014. Lifecycle primary energy analysis of low-energy timber building systems for multi-storey residential buildings. 81**,** 84-97.

DOREY, A. B. & CHENG, J. R. 1996. *Glass fiber reinforced glued laminated wood beams*, Citeseer.

DOWELL, E. H. & HALL, K. C. J. A. R. O. F. M. 2001. Modeling of fluid-structure interaction. 33**,** 445-490.

DOWLING, N. E. 1971. Fatigue failure predictions for complicated stress-strain histories. Illinois Univ At Urbana Dept Of Theoretical And Applied Mechanics.

DUJIC, B., AICHER, S. & ZARNIC, R. Testing of wooden wall panels applying realistic boundary conditions. Proceedings of the 9th World Conference on Timber Engineering, Portland, Oregon, USA, 2006.

DUJIC, B., KLOBCAR, S. & ZARNIC, R. Shear capacity of cross-laminated wooden walls. Proceedings of the 10th World Conference on Timber Engineering, Miyazaki, Japan, 2008.

DURLINGER, B., CROSSIN, E. & WONG, J. P. C. 2013. Life cycle assessment of a cross laminated timber building. RMIT University.

ECHAVARRIA, C., JIMENEZ, L. & OCHOA, J. C. J. D. 2012. Bamboo-reinforced glulam beams: an alternative to fiberglass-reinforced glulam beams. 79**,** 24-30.

EDSKäR, I. & LIDELöW, H. 2019. Dynamic properties of cross-laminated timber and timber truss building systems. *Engineering Structures,* 186**,** 525-535.

ENGINEERS, A. S. O. C. 2017. Minimum design loads and associated criteria for buildings and other structures. Reston, VA, USA: ASCE.

ETA. 2019. European Technical Approval: Nails and screws for use in nailing plates in timber structures. Brussels, Belgium: European Organisation for Technical Approcals

ETA. 2021. European Technical Approval: Three-dimensional nailing plate (timber-to-timber/timber-toconcrete angle bracket). Brussels, Belgium: European Organisation for Technical Approcals

ETAG015 2012. GUIDELINE FOR EUROPEAN TECHNICAL APPROVAL of THREE-DIMENSIONAL NAILING PLATES.

FADL, M. & KARADELIS, J. 2013. CFD Simulation for Wind Comfort and Safety in Urban Area: A Case Study of Coventry University Central Campus. *International Journal of Architecture, Engineering and Construction,* 2**,** 131-143.

FAIRHURST, M., ZHANG, X. & TANNERT, T. Nonlinear dynamic analysis of a novel timber–steel hybrid system. Proceedings of the World Conference on Timber Engineering, 2014.

FALK, M. & MAROHN, F. 1993. Von Mises Conditions Revisited. *The Annals of Probability,* 21**,** 1310-1328.

FANG, D., IWASAKI, S., YU, M., SHEN, Q., MIYAMOTO, Y. & HIKOSAKA, H. J. J. O. S. E. 2001. Ancient Chinese timber architecture. I: Experimental study. 127**,** 1348-1357.

FELDMANN, A., HUANG, H., CHANG, W.-S., HARRIS, R., DIETSCH, P., GRäFE, M. & HEIN, C. 2016. *Dynamic properties of tall Timber Structures under wind-induced Vibration*.

FELICITA, M. 2021. Timber High-Rise Buildings: Parametric study of the influence of preliminary design parameters on the wind-induced dynamic response of timber high-rise buildings.

FERDOUS, W., BAI, Y., NGO, T. D., MANALO, A. & MENDIS, P. J. E. S. 2019. New advancements, challenges and opportunities of multi-storey modular buildings–A state-of-the-art review. 183**,** 883-893.

FILLETI, R. A., SILVA, D. A., SILVA, E. J. & OMETTO, A. R. J. P. C. 2014. Dynamic system for life cycle inventory and impact assessment of manufacturing processes. 15**,** 531-536.

FISHER, R. A. & TIPPETT, L. H. C. 1928. Limiting forms of the frequency distribution of the largest or smallest member of a sample. *Mathematical Proceedings of the Cambridge Philosophical Society,* 24**,** 180-190.

FLATSCHER, G., BRATULIC, K. & SCHICKHOFER, G. Experimental tests on cross-laminated timber joints and walls. 2015.

FOSTER, R. M., RAMAGE, M. H. & REYNOLDS, T. J. C. J. 2017. Rethinking CTBUH height criteria in the context of tall timber. 28-33.

FOSTER, R. M. & RAMAGE, M. H. J. P. O. T. I. O. C. E.-C. M. 2017. Briefing: Super tall timber–Oakwood Tower. 170**,** 118-122.

FOSTER, R. M., REYNOLDS, T. P. & RAMAGE, M. H. J. J. O. S. E. 2016. Proposal for defining a tall timber building. 142**,** 02516001.

FOTHERGILL, C., ROBERTS, P., PACKWOOD, A. J. W. & STRUCTURES 2002. Flow and dispersion around storage tanks-A comparison between numerical and wind tunnel simulations. 5**,** 89-100.

FOUQUET, M., LEVASSEUR, A., MARGNI, M., LEBERT, A., LASVAUX, S., SOUYRI, B., BUHé, C. & WOLOSZYN, M. 2015. Methodological challenges and developments in LCA of low energy buildings: Application to biogenic carbon and global warming assessment. *Building and Environment,* 90**,** 51-59.

FRAGIACOMO, M., DUJIC, B. & SUSTERSIC, I. 2011. Elastic and ductile design of multi-storey crosslam massive wooden buildings under seismic actions. *Engineering Structures,* 33**,** 3043-3053.

FRANGI, A. & FONTANA, M. J. F. S. S. 2005. Fire performance of timber structures under natural fire conditions. 8**,** 279-290.

FRANKE, J., HIRSCH, C., JENSEN, A., KRüS, H., SCHATZMANN, M., WESTBURY, P., MILES, S., WISSE, J. & WRIGHT, N. 2004. Recommendations on the use of CFD in wind engineering. *Proceedings of the International Conference on Urban Wind Engineering and Building Aerodynamics*.

FULLER, S. & PETERSEN, S. 1996. Life-cycle costing manual for the federal energy management program, NIST Handbook 135.

FULLER, S. J. N. I. O. B. S., AN AUTHORITATIVE SOURCE OF INNOVATIVE SOLUTIONS FOR THE BUILT ENVIRONMENT 2010. Life-cycle cost analysis (LCCA). 1090.

FUREBY, C. & GRINSTEIN, F. F. 2002. Large Eddy Simulation of High-Reynolds-Number Free and Wall-Bounded Flows. *Journal of Computational Physics,* 181**,** 68-97.

GAGNON, S., BILEK, E. T., PODESTO, L., CRESPELL, P. J. I. C. H. C.-L. T. E. B. E. K., BRAD DOUGLAS.--US ED. & 1-45., P. 2013. CLT Introduction to cross-laminated timber. 1-57.

GAGNON, S. & PIRVU, C. 2011. *CLT handbook: Cross-laminated timber*, FPInnovations.

GAVRIC, I., FRAGIACOMO, M. & CECCOTTI, A. 2015a. Cyclic Behavior of CLT Wall Systems: Experimental Tests and Analytical Prediction Models. 141**,** 04015034.

GAVRIC, I., FRAGIACOMO, M. & CECCOTTI, A. 2015b. Cyclic behaviour of typical metal connectors for cross-laminated (CLT) structures. *Materials and Structures,* 48**,** 1841-1857.

GAVRIC, I., FRAGIACOMO, M., POPOVSKI, M. & CECCOTTI, A. 2014. Behaviour of cross-laminated timber panels under cyclic loads. *Materials and Joints in Timber Structures.* Springer.

GEORGE, P. 2015. Wood Innovation and Design Centre：A TECHNICAL CASE STUDY.

GEREKE, T., GUSTAFSSON, P. J., PERSSON, K. & NIEMZ, P. 2010. The hygroscopic warping of cross-laminated timber. *Delamination in Wood, Wood Products and Wood-Based Composites.* Springer.

GERHARDT, H., KRAMER, C. J. J. O. W. E. & AERODYNAMICS, I. 1986. Wind induced loading cycle and fatigue testing of lightweight roofing fixations. 23**,** 237-247.

GHOSAL, S. & MOIN, P. J. J. O. C. P. 1995. The basic equations for the large eddy simulation of turbulent flows in complex geometry. 118**,** 24-37.

GILBERT, C. F. & EROCHKO, J. J. E. S. 2019. Development and testing of hybrid timber-steel braced frames. 198**,** 109495.

GONG, M. & SMITH, I. 2005. Effect of stress levels on compressive low-cycle fatigue behaviour of softwood.

GONG, M. & SMITH, I. J. W. S. U. A. H. T. C. W. E. R. P.-.-P. 2000. Failure mechanism of softwood under low-cycle fatigue load in compression parallel to grain.

GONG, X., NIE, Z., WANG, Z., CUI, S., GAO, F. & ZUO, T. J. J. O. I. E. 2012. Life cycle energy consumption and carbon dioxide emission of residential building designs in Beijing: a comparative study. 16**,** 576-587.

GRASSER, K. K. 2015. Development of cross laminated timber in the United States of America.

GREEN, M. & D KARSH, J. E. 2012. Tall wood—The case for tall wood buildings. Wood Enterprise Coalition.

GRINGORTEN, I. I. 1963. A plotting rule for extreme probability paper. *Journal of Geophysical Research (1896-1977),* 68**,** 813-814.

GU, H. & BERGMAN, R. J. G. T. R. F.-G.-M., WI: US DEPARTMENT OF AGRICULTURE, FOREST SERVICE, FOREST PRODUCTS LABORATORY. 1-73. 2018. Life cycle assessment and environmental building declaration for the design building at the University of Massachusetts. 255**,** 1-73.

GU, M., XU, Y. L., CHEN, L., XIANG, H. J. J. O. W. E. & AERODYNAMICS, I. 1999. Fatigue life estimation of steel girder of Yangpu cable-stayed bridge due to buffeting. 80**,** 383-400.

GUAN, Z., RODD, P., POPE, D. J. C. & STRUCTURES 2005. Study of glulam beams pre-stressed with pultruded GRP. 83**,** 2476-2487.

GUHA, T. K. & KOPP, G. A. 2014. Storm duration effects on roof-to-wall-connection failures of a residential, wood-frame, gable roof. *Journal of Wind Engineering and Industrial Aerodynamics,* 133**,** 101-109.

GULVANESSIAN, H. A. C., J.-A.%A HOLICKý, M.%A GULVANESSIAN, HAIG *Designers' Guide to Eurocode: Basis of Structural Design*.

GUO, H., LIU, Y., CHANG, W.-S., SHAO, Y. & SUN, C. 2017. Energy Saving and Carbon Reduction in the Operation Stage of Cross Laminated Timber Residential Buildings in China. 9.

GUSTAFSSON, A. 2019. *The CLT Handbook*, Skogsindustrierna.

GUSTAVSSON, L., PINGOUD, K., SATHRE, R. J. M. & CHANGE, A. S. F. G. 2006a. Carbon dioxide balance of wood substitution: comparing concrete-and wood-framed buildings. 11**,** 667-691.

GUSTAVSSON, L., SATHRE, R. J. B. & ENVIRONMENT 2006b. Variability in energy and carbon dioxide balances of wood and concrete building materials. 41**,** 940-951.

HAN, Y., CHUN, Q. & JIN, H. J. J. O. W. S. 2021. Wind-induced vibration performance of early Chinese hall-style timber buildings. 67**,** 1-18.

HANJALIC, K. J. L. N. A. V. K. I. 2004. Closure models for incompressible turbulent flows. 75.

HANULIAK, P. & HARTMAN, P. J. M. V. 2021. MODERN WOODEN BUILDINGS IN SLOVAKIA AND ABROAD. ASPECT OF SUSTAINABLE ARCHITECTURE & ACTUAL LEGISLATION. 9**,** 74-85.

HAROON, A. 2019. *Evaluation of Remaining Fatigue Life of a Non-Cantilever Highway Truss With Tubular Joints*, The University of Toledo.

HARRIS, R. 2015. Cross laminated timber. *In:* ANSELL, M. P. (ed.) *Wood composites.* Woodhead Publishing.

HARRIS, R. I. 1982. An improved method for the prediction of extreme values of wind effects on simple buildings and structures. *Journal of Wind Engineering and Industrial Aerodynamics,* 9**,** 343-379.

HARRIS, R. J. P. O. T. I. O. C. E.-S. & BUILDINGS 2011. Design of timber gridded shell structures. 164**,** 105-116.

HARRIS, R. J. T. S. E. 2004. 21st Century Timber Engineering-the age of enlightenment for timber design. Part 1: An Introduction to Timber. 82**,** 52-57.

HARRIS, R. J. T. S. E. 2005. 21st Century Timber-the age of enlightenment for timber design Part 2: Environmental Credentials. 83**,** 23-28.

HARTE, A. M. J. J. O. S. I. & MAINTENANCE 2017. Mass timber–the emergence of a modern construction material. 2**,** 121-132.

HASSANIEH, A., VALIPOUR, H. & BRADFORD, M. J. E. S. 2017. Experimental and numerical investigation of short-term behaviour of CLT-steel composite beams. 144**,** 43-57.

HASSANIEH, A., VALIPOUR, H. & BRADFORD, M. J. J. O. C. S. R. 2016. Experimental and numerical study of steel-timber composite (STC) beams. 122**,** 367-378.

HE, D. 2006. *风工程与工业空气动力学 (in chinese)*, 国防工业出版社.

HEIDUSCHKE, A., KASAL, B. & HALLER, P. 2008. Performance and Drift Levels of Tall Timber Frame Buildings under Seismic and Wind Loads. *Structural Engineering International,* 18**,** 186-191.

HENDERSON, D., GINGER, J. & KOPP, G. 2010. Wind Induced Fatigue of Metal Roof Cladding during Severe Tropical Cyclones. *Structures Congress 2010*.

HENDERSON, D. J., MORRISON, M. J. & KOPP, G. A. 2013. Response of toe-nailed, roof-to-wall connections to extreme wind loads in a full-scale, timber-framed, hip roof. *Engineering Structures,* 56**,** 1474-1483.

HENDRICKSON, C., HORVATH, A., JOSHI, S., LAVE, L. J. E. S. & TECHNOLOGY 1998. Peer reviewed: economic input–output models for environmental life-cycle assessment. 32**,** 184A-191A.

HOLMES, J. D. 2015a. Wind Loading of Structures. CRC Press.

HOLMES, J. D. 2015b. Wind Loading of Structures. CRC Press.

HOLMES, J. D. & MORIARTY, W. W. 1999. Application of the generalized Pareto distribution to extreme value analysis in wind engineering. *Journal of Wind Engineering and Industrial Aerodynamics,* 83**,** 1-10.

HOSKING, J. R. M. 1984. Testing Whether the Shape Parameter is Zero in the Generalized Extreme- Value Distribution. *Biometrika,* 71**,** 367-374.

HOVEN, I. V. D. J. J. O. M. 1957. POWER SPECTRUM OF HORIZONTAL WIND SPEED IN THE FREQUENCY RANGE FROM 0.0007 TO 900 CYCLES PER HOUR. 14**,** 160-164.

HUANG, S., LI, Q. S. & XU, S. 2007. Numerical evaluation of wind effects on a tall steel building by CFD. *Journal of Constructional Steel Research,* 63**,** 612-627.

INSTITUTION, B. S. 2005. Eurocode 1 :Actions on Building Structures. *parts 1-4: General Actions- Wind actions.* London UK: BSI.

IRWIN, P., DENOON, R. & DAVID, S. 2013. *Wind Tunnel Testing of High-Rise Buildings: An output of the CTBUH wind Engineering Working Group,* Chicago, Council on Tall buildings and Urban Habitat.

ISSA, C. A., KMEID, Z. J. C. & MATERIALS, B. 2005. Advanced wood engineering: glulam beams. 19**,** 99-106.

ISYUMOV, N. 2012. Alan G. Davenport's mark on wind engineering. *Journal of Wind Engineering and Industrial Aerodynamics,* 104-106**,** 12-24.

IYER-RANIGA, U. & WONG, J. P. C. 2012. Evaluation of whole life cycle assessment for heritage buildings in Australia. *Building and Environment,* 47**,** 138-149.

IZZI, M., CASAGRANDE, D., BEZZI, S., PASCA, D., FOLLESA, M. & TOMASI, R. 2018a. Seismic behaviour of Cross-Laminated Timber structures: A state-of-the-art review. *Engineering Structures,* 170**,** 42-52.

IZZI, M., POLASTRI, A. & FRAGIACOMO, M. 2018b. Modelling the mechanical behaviour of typical wall-to-floor connection systems for cross-laminated timber structures. *Engineering Structures,* 162**,** 270-282.

JAPAN, A. I. O. 2015. Recommendations for Loads on Buildings *Chapter 6 Wind Load* Tokyo, Japan: Architectural Institute of Japan.

JAYALATH, A., NAVARATNAM, S., NGO, T., MENDIS, P., HEWSON, N., AYE, L. J. E. & BUILDINGS 2020. Life cycle performance of Cross Laminated Timber mid-rise residential buildings in Australia. 223**,** 110091.

JOHANSSON, M., LINDERHOLT, A., JARNERö, K. & LANDEL, P. J. P. O. T. W. 2016. Tall timber buildings-a preliminary study of wind-induced vibrations of a 22-storey building.

KARACABEYLI, E. & DOUGLAS, B. 2013. *CLT: handbook cross-laminated timber*, FPInnovations.

KAREEM, A., ZHOU, Y. J. J. O. W. E. & AERODYNAMICS, I. 2003. Gust loading factor—past, present and future. 91**,** 1301-1328.

KASPERSKI, M., NIEMANN, H.-J. J. J. O. W. E. & AERODYNAMICS, I. 1992. The LRC (load-response-correlation)-method a general method of estimating unfavourable wind load distributions for linear and non-linear structural behaviour. 43**,** 1753-1763.

KASPERSKI, M. J. E. S. 1992. Extreme wind load distributions for linear and nonlinear design. 14**,** 27-34.

KATHEKEYAN, M. & MAHENDRAN, M. Low-high-low cyclic tests of steel roof batten systems. Proceedings of the 2018 Australasian Structural Engineering Conference, 2018. Engineers Australia, 337-345.

KHASREEN, M. M., BANFILL, P. F. & MENZIES, G. F. J. S. 2009a. Life-cycle assessment and the environmental impact of buildings: a review. 1**,** 674-701.

KHASREEN, M. M., BANFILL, P. F. G. & MENZIES, G. F. 2009b. Life-Cycle Assessment and the Environmental Impact of Buildings: A Review. 1**,** 674-701.

KHOSROVANEH, A. K. & DOWLING, N. E. 1990. Fatigue loading history reconstruction based on the rainflow technique. *International Journal of Fatigue,* 12**,** 99-106.

KIM, J., MOIN, P. & MOSER, R. 1987. The Turbulence Statistics in Fully Developed Channel Flow at Low Reynolds Number. *Journal of Fluid Mechanics,* 177.

KIM, Y., KANDA, J. J. T. S. D. O. T. & BUILDINGS, S. 2008. Wind response characteristics for habitability of tall buildings in Japan. 17**,** 683-718.

KOHARA, M. & OKUYAMA, T. 1992. Mechanical responses of wood to repeated loading V. Effect of duration time and number of repetitions on the time to failure in bending. *Journal of the Japan Wood Research Society* 38**,** 753-758.

KöHLER, J. & FABER, M. H. A probabilistic creep and fatigue model for timber materials. Proceedings to the 9th International Conference on Applications of Statistics and Probability in Civil Engineering ICASP9, 2003. 1141-1148.

KOTWICA, E. & KRZOSEK, S. J. W. U. O. L. S. 2018. Glulam, LVL and X-lam–engineering wood products in the buildings of the future. 256.

KUZMAN, M. K. & SANDBERG, D. A new era for multi-storey timber buildings in Europe. Forest Products Society International Convention: 26/06/2016-29/06/2016, 2016. Forest Products Society.

LALANNE, C. 2014. Concepts of Material Fatigue. *Fatigue Damage.*

LAM, F., HE, M. & YAO, C. J. S. E. I. 2008. Example of traditional tall timber buildings in China–the Yingxian pagoda. 18**,** 126-129.

LANGENBACH, R. J. S. E. I. 2008. Building tall with timber: A paean to wood construction. 18**,** 130-132.

LARASATIE, P., ALBEE, R., MUSZYŃSKI, L., GUERRERO, J. E. M. & HANSEN, E. GLOBAL CLT INDUSTRY SURVEY: THE 2020 UPDATES.

LAURIOLA, M. & SANDHAAS, C. Quasi-static and pseudo-dynamic tests on X-lam walls and buildings. 2006.

LAWRENCE, G. J. E. J. O. A. I. O. S. C. 2003. Serviceability limit states under wind load.

LAWSON, M., OGDEN, R. & GOODIER, C. I. 2014. *Design in modular construction*, CRC Press Boca Raton, FL.

LAZZARINI, E., FRISON, G., TRUTALLI, D., MARCHI, L., SCOTTA, R. J. T. S. D. O. T. & BUILDINGS, S. 2021. Comfort assessment of high ‐ rise timber buildings exposed to wind ‐ induced vibrations. 30**,** e1882.

LECHNER, J. A., LEIGH, S. D. & SIMIU, E. 1992. Recent approaches to extreme value estimation with application to wind speeds. Part I: the pickands method. *Journal of Wind Engineering and Industrial Aerodynamics,* 41**,** 509-519.

LECHóN, Y., DE LA RúA, C. & LECHóN, J. J. J. O. B. E. 2021. Environmental footprint and life cycle costing of a family house built on CLT structure. Analysis of hotspots and improvement measures. 39**,** 102239.

LEE, Y.-L. & TJHUNG, T. 2012. Chapter 3 - Rainflow Cycle Counting Techniques. *In:* LEE, Y.-L., BARKEY, M. E. & KANG, H.-T. (eds.) *Metal Fatigue Analysis Handbook.* Boston: Butterworth-Heinemann.

LEHMANN, S., HAMILTON, C. J. Z. W. S. R. C. F. S. D. & BEHAVIOUR: UNIVERSITY OF SOUTH AUSTRALIA, A., AUSTRALIA 2011. Sustainable Infill Development using Low Carbon CLT Prefabrication: Adaptation for the South Australian Context.

LEHMANN, S. J. S. 2012. Sustainable construction for urban infill development using engineered massive wood panel systems. 4**,** 2707-2742.

LEHRINGER, C., GABRIEL, J. J. M. & STRUCTURES, J. I. T. 2014. Review of recent research activities on one-component PUR-adhesives for engineered wood products. 405-420.

LEONTIEF, W. W. 1936. Quantitative Input and Output Relations in the Economic Systems of the United States. *The Review of Economics and Statistics,* 18**,** 105-125.

LEVASSEUR, A., LESAGE, P., MARGNI, M., DESCHêNES, L. & SAMSON, R. 2010. Considering Time in LCA: Dynamic LCA and Its Application to Global Warming Impact Assessments. *Environmental Science & Technology,* 44**,** 3169-3174.

LI, H., WANG, B. J., WEI, P., WANG, L. J. J. O. B. & BIOPRODUCTS 2019a. Cross-laminated timber (CLT) in China: a state-of-the-art. 4**,** 22-31.

LI, J., RISMANCHI, B., NGO, T. J. B. & ENVIRONMENT 2019b. Feasibility study to estimate the environmental benefits of utilising timber to construct high-rise buildings in Australia. 147**,** 108-120.

LI, T. & QIN, H. J. E. M. 2005. Structural analysis and repair of Yingxian Wooden Tower. 22**,** 199-212.

LI, Z., WANG, X., HE, M. & DONG, H. J. J. O. S. E. 2019c. Seismic performance of timber–steel hybrid structures. II: Calibration of performance objectives and design method. 145**,** 04019114.

LI, Z., WANG, X., HE, M., DONG, W. & DONG, H. J. J. O. S. E. 2019d. Seismic performance of timber–steel hybrid structures. I: Subassembly testing and numerical modeling. 145**,** 04019113.

LI, Z., ZHENG, X., NI, C., TAO, D. & HE, M. J. S. S. 2020. Reliability-based investigation into the duration of load effect for the design of timber structures based on Chinese standard. 87**,** 102001.

LI;, J. W. L. 2005. Digital simulation of turbulent wind field *Journal of Zhejiang University of Science and Technology,* 14 (1)**,** 34-37.

LIANG, S., GU, H. & BERGMAN, R. 2021a. Environmental Life-Cycle Assessment and Life-Cycle Cost Analysis of a High-Rise Mass Timber Building: A Case Study in Pacific Northwestern United States. 13**,** 7831.

LIANG, S., GU, H., BERGMAN, R., KELLEY, S. S. J. W. & 217-229., F. S. 2020. Comparative life-cycle assessment of a mass timber building and concrete alternative. 52**,** 217-229.

LIANG, S., GU, H. & BERGMAN, R. J. S. 2021b. Environmental Life-Cycle Assessment and Life-Cycle Cost Analysis of a High-Rise Mass Timber Building: A Case Study in Pacific Northwestern United States. 13**,** 7831.

LIONELLO, G. & CRISTOFOLINI, L. 2014. A practical approach to optimizing the preparation of speckle patterns for digital-image correlation. *Measurement Science and Technology,* 25**,** 107001.

LIU, J. & LAM, F. 2018. Experimental test of coupling effect on CLT angle bracket connections. *Engineering Structures,* 171**,** 862-873.

LIU, Y., GUO, H., SUN, C. & CHANG, W.-S. 2016. Assessing Cross Laminated Timber (CLT) as an Alternative Material for Mid-Rise Residential Buildings in Cold Regions in China—A Life-Cycle Assessment Approach. 8**,** 1047.

LORENZON, A., ANTONELLO, M. & BERTO, F. J. P. S. I. 2017. Megastructures: use of CFD turbulence models for the evaluation of wind-induced fatigue loads. 3**,** 370-379.

LOSS, C. & FRANGI, A. J. E. S. 2017. Experimental investigation on in-plane stiffness and strength of innovative steel-timber hybrid floor diaphragms. 138**,** 229-244.

LOSS, C., PIAZZA, M., ZANDONINI, R. J. C. & MATERIALS, B. 2016a. Connections for steel–timber hybrid prefabricated buildings. Part I: Experimental tests. 122**,** 781-795.

LOSS, C., PIAZZA, M., ZANDONINI, R. J. C. & MATERIALS, B. 2016b. Connections for steel–timber hybrid prefabricated buildings. Part II: Innovative modular structures. 122**,** 796-808.

LOSS, C., ROSSI, S. & TANNERT, T. J. J. O. S. E. 2018. In-Plane stiffness of hybrid steel–cross-laminated timber floor diaphragms. 144**,** 04018128.

LU, Y. J. J. O. S. E. 2002. Comparative study of seismic behavior of multistory reinforced concrete framed structures. 128**,** 169-178.

LUNDTANG PETERSEN, E. T., IB; FRANDSEN, STEN TRONæS; HEDEGAARD, K. 1981. *Danish Windatlas : A Rational Method of Wind Energy Siting.,* Denmark., Forskningscenter Risoe. Risoe-R.

MAHDAVI, A. & DOPPELBAUER, E.-M. 2010. A performance comparison of passive and low-energy buildings. *Energy and Buildings,* 42**,** 1314-1319.

MAHENDRAN, M. & STATION, J. C. U. O. N. Q. C. T. 1993. *Fatigue behaviour of light gauge steel roof claddings under simulated cyclonic wind forces,* Townsville, Qld, James Cook Cyclone Structural Testing Station.

MAI, K. Q., PARK, A., NGUYEN, K. T., LEE, K. J. C. & MATERIALS, B. 2018. Full-scale static and dynamic experiments of hybrid CLT–concrete composite floor. 170**,** 55-65.

MALO, K. A., ABRAHAMSEN, R. B. & BJERTNæS, M. A. 2016. Some structural design issues of the 14-storey timber framed building "Treet" in Norway. *European Journal of Wood and Wood Products,* 74**,** 407-424.

MANDARA, A., RUSSO, E., FAGGIANO, B. & MAZZOLANI, F. M. J. P. E. 2016. Analysis of fluid-structure interaction for a submerged floating tunnel. 166**,** 397-404.

MARTIN, Z. A., STITH, J. K. & TINGLEY, D. A. Commercialisation of FRP reinforced glulam beam technology. Proceedings of the 6th world conference on timber engineering WCTE, Whistler, Canada, 2000. Citeseer.

MAYENCOURT, P. & MUELLER, C. 2019. Structural Optimization of Cross-laminated Timber Panels in One-way Bending. *Structures,* 18**,** 48-59.

MICELLI, F., SCIALPI, V. & LA TEGOLA, A. J. J. O. C. F. C. 2005. Flexural reinforcement of glulam timber beams and joints with carbon fiber-reinforced polymer rods. 9**,** 337-347.

MIKITARENKO, M., PERELMUTER, A. J. J. O. W. E. & AERODYNAMICS, I. 1998. Safe fatigue life of steel towers under the action of wind vibrations. 74**,** 1091-1100.

MILLER, S., WOODS, J. E., EROCHKO, J., LAU, D. T. & GILBERT, C. F. 2021. Experimental and analytical fragility assessment of a combined heavy timber–steel-braced frame through hybrid simulation. 50**,** 270-289.

MINER, M. A. 1945. Cumulative damage in fatigue.

MOCHIDA, A., TOMINAGA, Y., MURAKAMI, S., YOSHIE, R. J. W. & STRUCTURES 2002. Comparison of various k-ε models and DSM applied to flow around a high-rise building. 5**,** 227-244.

MOHAMMAD, M., DOUGLAS, B., RAMMER, D. & PRYOR, S. 2013. Chapter 5: Connection in Cross-Laminated Timber Buildings.

MOODY, R. C., LIU, J. Y. J. W. H. W. A. A. E. M. M., WI: USDA FOREST SERVICE, FOREST PRODUCTS LABORATORY, . GENERAL TECHNICAL REPORT FPL & 11.1-11.24, G.-P. 1999. Glued structural members. 113.

MORGAN, J. & BECK, V. Failure of Sheet-metal Roofing Under Repeated Wind Loading. 1976.

MORLIER, P. 1994. *Creep in timber structures*, CRC Press.

MORRISON, M. J. & KOPP, G. A. 2011. Performance of toe-nail connections under realistic wind loading. *Engineering Structures,* 33**,** 69-76.

MOUDGIL, M. 2017. *Feasibility study of using cross-laminated timber core for the UBC Tall Wood building.* University of British Columbia.

MPIDI BITA, H. & TANNERT, T. 2019. Disproportionate collapse prevention analysis for a mid-rise flat-plate cross-laminated timber building. *Engineering Structures,* 178**,** 460-471.

MUGA, H., MUKHERJEE, A. & MIHELCIC, J. 2008. An Integrated Assessment of the Sustainability of Green and Built-up Roofs. *Journal of Green Building,* 3**,** 106-127.

MUSZYNSKI, L., GUERRERO, P. L. J. E. M. & HANSEN, R. A. E. N. Global CLT industry in 2020: Growth beyond the Alpine Region. Proceedings of the 63rd International Convention of Society of Wood Science and Technology, 2020. 0-8.

NEUENSCHWANDER, J., SANABRIA, S. J., SCHUETZ, P., WIDMANN, R. & VOGEL, M. J. H. 2013. Delamination detection in a 90-year-old glulam block with scanning dry point-contact ultrasound. 67**,** 949-957.

NSPRC 2008. General principles for calculation of the comprehensive energy consumption.

OCHOA, L., HENDRICKSON, C. & MATTHEWS, H. S. 2002. Economic Input-output Life-cycle Assessment of U.S. Residential Buildings. 8**,** 132-138.

OKUYAMA, T., ITOH, A. & MARSOEM, S. N. 1984. Mechanical responses of wood to repeated loading. I. Tensile and compressive fatigue fractures. *Journal of the Japan Wood Research Society* 30**,** 791-798.

ONG, C. B. 2015. Glue-laminated timber (Glulam). *In:* ANSELL, M. P. (ed.) *Wood composites.* Woodhead Publishing.

OREGI, X., HERNANDEZ, P. & HERNANDEZ, R. 2017. Analysis of life-cycle boundaries for environmental and economic assessment of building energy refurbishment projects. *Energy and Buildings,* 136**,** 12-25.

ORTIZ-RODRíGUEZ, O., CASTELLS, F. & SONNEMANN, G. 2010. Life cycle assessment of two dwellings: One in Spain, a developed country, and one in Colombia, a country under development. *Science of The Total Environment,* 408**,** 2435-2443.

ORTIZ, O., CASTELLS, F. & SONNEMANN, G. 2009. Sustainability in the construction industry: A review of recent developments based on LCA. *Construction and Building Materials,* 23**,** 28-39.

PALUTIKOF, J. P., BRABSON, B. B., LISTER, D. H. & ADCOCK, S. T. 1999. A review of methods to calculate extreme wind speeds. 6**,** 119-132.

PAN, B., QIAN, K., XIE, H. & ASUNDI, A. 2009. Two-dimensional digital image correlation for in-plane displacement and strain measurement: a review. *Measurement Science and Technology,* 20**,** 062001.

PEHNT, M. J. R. E. 2006. Dynamic life cycle assessment (LCA) of renewable energy technologies. 31**,** 55-71.

PEI, S., LINDT, J. W. V. D. & POPOVSKI, M. 2013. Approximate R-Factor for Cross-Laminated Timber Walls in Multistory Buildings. 19**,** 245-255.

PENADéS-PLà, V., MARTí, J. V., GARCíA-SEGURA, T. & YEPES, V. J. S. 2017. Life-cycle assessment: A comparison between two optimal post-tensioned concrete box-girder road bridges. 9**,** 1864.

PERRIN, O., ROOTZéN, H. & TAESLER, R. 2006. A discussion of statistical methods used to estimate extreme wind speeds. *Theoretical and Applied Climatology,* 85**,** 203-215.

PETROV, A. A. J. J. O. W. E. & AERODYNAMICS, I. 1998. Dynamic response and life prediction of steel structures under wind loading. 74**,** 1057-1065.

POLASTRI, A., GIONGO, I. & PIAZZA, M. 2017. An Innovative Connection System for Cross-Laminated Timber Structures. *Structural Engineering International,* 27**,** 502-511.

POPE, S. B. 2000. *Turbulent Flows,* Cambridge, Cambridge University Press.

POPOVSKI, M. & KARACABEYLI, E. 2012a. *Seismic behavior of cross-laminated timber structures*.

POPOVSKI, M. & KARACABEYLI, E. Seismic behaviour of cross-laminated timber structures. Proceedings of the World Conference on Timber Engineering, 2012b.

POPOVSKI, M., SCHNEIDER, J. & SCHWEINSTEIGER, M. Lateral load resistance of cross-laminated wood panels. World Conference on Timber Engineering, 2010. 20-24.

PORTEOUS, J. & KEMANI, A. 2013. *Structueal Timber Design to Eurocide 5,* United Kindom, Blcakwell Publishing

PORTEOUS, J. & KERMANI, A. 2013. *Structural timber design to Eurocode 5*, John Wiley & Sons.

POTTER, J. M. & WATANABE, R. T. 1989. *Development of fatigue loading spectra*, ASTM International.

REPETTO, M. P. & SOLARI, G. 2001. Dynamic alongwind fatigue of slender vertical structures. *Engineering Structures,* 23**,** 1622-1633.

REYNOLDS, T., BOLMSVIK, Å., VESSBY, J., CHANG, W.-S., HARRIS, R., BAWCOMBE, J. & BREGULLA, J. AMBIENT VIBRATION TESTING AND MODAL ANALYSIS OF MULTI-STOREY CROSS-LAMINATED TIMBER BUILDINGS. World conference on timber engineering, 2014 Canada.

REYNOLDS, T., CHANG, W. & HARRIS, R. Wind-induced vibration of tall timber buildings. 2011 IASS Annual Symposium: IABSE-IASS 2011: Taller, Longer, Lighter, 2011.

REYNOLDS, T. P. S. 2013. *Dynamic behaviour of dowel-type connections under in-service vibration.* University of Bath.

RIBERHOLT, H. 2007. *Performance of old glulam structures in Europe*, BYG. DTU.

RICE, S. O. 1944. Mathematical Analysis of Random Noise. 23**,** 282-332.

ROBERTSON, A. B., LAM, F. C. & COLE, R. J. J. B. 2012. A comparative cradle-to-gate life cycle assessment of mid-rise office building construction alternatives: Laminated timber or reinforced concrete. 2**,** 245-270.

ROBINSON, T., HALLOVA, A., SPIRITOS, J. & ROELOFS, M. J. C. J. 2016. New heights for renewables: The US tall wood building competition. 26-31.

RODI, W. 1997. Comparison of LES and RANS calculations of the flow around bluff bodies. *Journal of Wind Engineering and Industrial Aerodynamics,* 69-71**,** 55-75.

ROMANOWSKI, M. Reduced order unsteady aerodynamic and aeroelastic models using Karhunen-Loeve eigenmodes. 6th Symposium on Multidisciplinary Analysis and Optimization, 1996. 3981.

ROSSI, B., MARIQUE, A.-F., GLAUMANN, M. & REITER, S. 2012. Life-cycle assessment of residential buildings in three different European locations, basic tool. *Building and Environment,* 51**,** 395-401.

ROSSI, R., LAZZARI, M. & VITALIANI, R. 2004. Wind field simulation for structural engineering purposes. 61**,** 738-763.

RUUSKA, A. & HäKKINEN, T. J. B. 2014. Material efficiency of building construction. 4**,** 266-294.

SAGAUT, P. 2006. *Large eddy simulation for incompressible flows: an introduction*, Springer Science & Business Media.

SAHOO, K., BERGMAN, R., ALANYA-ROSENBAUM, S., GU, H. & LIANG, S. J. S. 2019. Life cycle assessment of forest-based products: A review. 11**,** 4722.

SANTERO, N., LOIJOS, A., AKBARIAN, M. & OCHSENDORF, J. 2011. Methods, impacts, and opportunities in the concrete pavement life cycle. MIT Concrete Sustainability Hub.

SARTORI, I. & HESTNES, A. G. 2007. Energy use in the life cycle of conventional and low-energy buildings: A review article. *Energy and Buildings,* 39**,** 249-257.

SCHEUER, C., KEOLEIAN, G. A., REPPE, P. J. E. & BUILDINGS 2003. Life cycle energy and environmental performance of a new university building: modeling challenges and design implications. 35**,** 1049-1064.

SCHMIDT, J., GRIFFIN, C. J. S. & ARCHITECTURE 2013. Barriers to the design and use of cross-laminated timber structures in high-rise multi-family housing in the United States. 2225-2231.

SCHNIEWIND, A. P. J. W. S. & TECHNOLOGY 1968. Recent progress in the study of the rheology of wood. 2**,** 188-206.

SERRANO, E., OSCARSSON, J., STERLEY, M. & ENQUIST, B. 2014. Green-glued products for structural applications. *Materials and Joints in Timber Structures.* Springer.

SHAHNEWAZ, M. 2018. *Performance of cross-laminated timber shear walls for platform construction under lateral loading.* University of British Columbia.

SHAHNEWAZ, M., ALAM, S. & TANNERT, T. 2018. In-Plane Strength and Stiffness of Cross-Laminated Timber Shear Walls. 8**,** 100.

SHAHNEWAZ, M., POPOVSKI, M. & TANNERT, T. J. J. O. S. E. 2019. Resistance of cross-laminated timber shear walls for platform-type construction. 145**,** 04019149.

SHAO, Y., GEYER, P., LANG, W. J. E. & BUILDINGS 2014. Integrating requirement analysis and multi-objective optimization for office building energy retrofit strategies. 82**,** 356-368.

SHEN, Y., SCHNEIDER, J., TESFAMARIAM, S., STIEMER, S. F. & CHEN, Z. 2021. Cyclic behavior of bracket connections for cross-laminated timber (CLT): Assessment and comparison of experimental and numerical models studies. *Journal of Building Engineering,* 39**,** 102197.

SHIRASAWA, T., TOMINAGA, T., YOSHIE, R., MOCHIDA, A., YOSHINO, H., KATAOKA, H., NOZU, T. J. A. J. O. T. & DESIGN 2003. Development of CFD method for predicting wind environment around a high-rise building part 2: the cross comparison of CFD results using various k-models for the flowfield around a building model with 4: 4: 1 shape. 18**,** 169-174.

SIMIU, E. & HECKERT, N. A. 1996. Extreme Wind Distribution Tails: A “Peaks over Threshold” Approach. 122**,** 539-547.

SIMIU, E. & SCANLAN, R. H. 1986. *Wind effects on structures: an introduction to wind engineering,* New York, Wiley.

SIMULIA, D. 2014. *ABAQUS 6.13 Analysis User's Guide* [Online]. [Accessed].

SKIDMORE, O. & MERRILL, L. J. S. C., IL, USA 2013. Timber tower research project: final report.

SKULLESTAD, J. L., BOHNE, R. A. & LOHNE, J. J. E. P. 2016. High-rise timber buildings as a climate change mitigation measure–A comparative LCA of structural system alternatives. 96**,** 112-123.

SMITH, I. & FRANGI, A. J. S. E. I. 2008. Overview of design issues for tall timber buildings. 18**,** 141-147.

SMITH, I., LANDIS, E. & GONG, M. 2003. *Fracture and fatigue in wood*, John Wiley & Sons.

SOCIETY, T. A. W. E. 2012. WIND LOADING HANDBOOK FOR AUSTRALIA & NEW ZEALAND – Background to AS/NZS 1170.2 Wind Actions. AWES.

SONSINO, C. M. J. I. J. O. F. 2007. Fatigue testing under variable amplitude loading. 29**,** 1080-1089.

SPALART, P. & ALLMARAS, S. A one-equation turbulence model for aerodynamic flows. 30th aerospace sciences meeting and exhibit, 1992. 439.

SPOSITO, C. & SCALISI, F. 2019. High-rise timber architecture: an opportunity for the sustainability of the built environment.

STA, S. T. A. 2003. Timber as a structural material: an introduction. [Accessed 06 Sep 2021].

STADLER, K., WOOD, R., BULAVSKAYA, T., SöDERSTEN, C. J., SIMAS, M., SCHMIDT, S., USUBIAGA, A., ACOSTA‐FERNáNDEZ, J., KUENEN, J. & BRUCKNER, M. J. J. O. I. E. 2018. EXIOBASE 3: Developing a time series of detailed environmentally extended multi‐regional input‐output tables. 22**,** 502-515.

STADLER, K. J. J. O. O. R. S. 2021. Pymrio–A Python Based Multi-Regional Input-Output Analysis Toolbox. 9.

STANDARDIZATION, I. O. F. 2009. Wind actions on structures. ISO international standard

STANIĆ, A., HUDOBIVNIK, B. & BRANK, B. 2016. Economic-design optimization of cross laminated timber plates with ribs. *Composite Structures,* 154**,** 527-537.

STAUB-FRENCH, S., PILON, A., POIRIER, E., FALLAHI, A., KASBAR, M., CALDERON, F., TESHNIZI, Z. & FROESE, T. J. C. I. 2021. Construction process innovation on brock commons Tallwood house.

STODDART, E. P. 2012. *DEVELOPMENT OF COMPONENT-BASED CONNECTION MODELLING FOR STEEL FRAMED STRUCTURES SUBJECTED TO BLAST OR PROGRESSIVE COLLAPSE.*

SU, S., LI, X., ZHU, Y., LIN, B. J. E. & BUILDINGS 2017. Dynamic LCA framework for environmental impact assessment of buildings. 149**,** 310-320.

SULLIVAN, T. 2012. Towards a direct displacement-based design procedure for cold-formed steel frame/wood panel shear walls.

SUN, X., HE, M., LI, Z. J. C. & MATERIALS, B. 2020. Novel engineered wood and bamboo composites for structural applications: State-of-art of manufacturing technology and mechanical performance evaluation. 249**,** 118751.

SUN, Z. 2007. *Computer Simulation and Analysis of Wind Loading of Structure (in chinese).* Master of Engineering, Nanjing University of Aeronautics and Astonautics

SUSTERSIC, I. & DUJIC, B. Seismic Strengthening of Existing Concrete and Masonry Buildings with Crosslam Timber Panels. 2014 Dordrecht. Springer Netherlands, 713-723.

SWADDIWUDHIPONG, S. & KHAN, M. S. 2002. DYNAMIC RESPONSE OF WIND-EXCITED BUILDING USING CFD. *Journal of Sound and Vibration,* 253**,** 735-754.

TAMURA, T. 2008. Towards practical use of LES in wind engineering. *Journal of Wind Engineering and Industrial Aerodynamics,* 96**,** 1451-1471.

TEDER, M. & WANG, X. Nondestructive evaluation of a 75-year old glulam arch. Proceedings: 18th International Nondestructive Testing and Evaluation of Wood Symposium. General Technical Report FPL-GTR-226. Madison, WI: US Department of Agriculture, Forest Service, Forest Products Laboratory. pg, 2013. 632.

TEH, S. H., WIEDMANN, T., SCHINABECK, J. & MOORE, S. J. P. E. 2017. Replacement scenarios for construction materials based on economy-wide hybrid LCA. 180**,** 179-189.

TESFAMARIAM, S., STIEMER, S., DICKOF, C. & BEZABEH, M. J. J. O. E. E. 2014. Seismic vulnerability assessment of hybrid steel-timber structure: Steel moment-resisting frames with CLT infill. 18**,** 929-944.

THELANDERSSON, S. & LARSEN, H. J. 2003. *Timber engineering*, John Wiley & Sons.

TIWARI, P. 2001. Energy efficiency and building construction in India. *Building and Environment,* 36**,** 1127-1135.

TOCHER, K. D. 1955. Statistical Theory of Extreme Values and Some Practical Applications; Probability Tables for the Analysis of Extreme Value Data. 118**,** 106-106.

TOMASI, R. & SMITH, I. J. J. O. M. I. C. E. 2015. Experimental characterization of monotonic and cyclic loading responses of CLT panel-to-foundation angle bracket connections. 27**,** 04014189.

TRADA 2009. Worked example. 12-storey building of cross-laminated timber (Eurocode 5).

TSAI, K. & ANSELL, M. P. J. J. O. M. S. 1990. The fatigue properties of wood in flexure. 25**,** 865-878.

TU, J., YEOH, G. H. & LIU, C. 2018. *Computational Fluid Dynamics : A Practical Approach,* Saint Louis, UNITED KINGDOM, Elsevier Science & Technology.

TUPENAITE, L., ZILENAITE, V., KANAPECKIENE, L., GECYS, T. & GEIPELE, I. J. S. 2021. Sustainability assessment of modern high-rise timber buildings. 13**,** 8719.

UIBEL, T. & BLAß, H. 2007. Edge Joints with Dowel Type Fasteners in Cross Laminated Timber.

UNE 2018. (UN Environment), Global Status Report 2018: Towards a zero-emission, efficient, and resilient building and construction sector. Global alliance for Building and construction, International Energy

agency.

.

UTAMA, A. & GHEEWALA, S. H. 2008. Life cycle energy of single landed houses in Indonesia. *Energy and Buildings,* 40**,** 1911-1916.

VAN DE KUILEN, J., CECCOTTI, A., XIA, Z. & HE, M. J. P. E. 2011. Very tall wooden buildings with cross laminated timber. 14**,** 1621-1628.

VAN STAALDUINEN, P. J. M., EDITOR. STRUCTURAL DYNAMICS, EURODYN & ET AL. 1993. Wind loading and fatigue of steel framed masts. 93**,** 1107-13.

VON MISES, R. 1936. La distribution de la plus grande de n valeurs. *Reprinted in Selected Papers, II, Amer. Math. Soc., Providence, RI (1954)***,** 271-294.

WALKER, G. 2010. A review of the impact of cyclone Tracy on building regulations and insurance. *Australian Meteorological and Oceanographic Journal,* 60**,** 199-206.

WALSHAW, D. 1994. GETTING THE MOST FROM YOUR EXTREME WIND DATA: A STEP BY STEP GUIDE. *Journal of Research of the National Institute of Standards Technology,* 99**,** 399-411.

WANG, X. & CUI, J. 2002. Formula of Coefficient K in Expression of Davenport Spectrum and Its Engineering Appl ication. *JOURNAL OF TONGJI UNIVERSITY,* 30**,** 849-852.

WANG, Z., FU, H., GONG, M., LUO, J., DONG, W., WANG, T. & CHUI, Y. H. 2017. Planar shear and bending properties of hybrid CLT fabricated with lumber and LVL. *Construction and Building Materials,* 151**,** 172-177.

WANG, Z., GONG, M. & CHUI, Y.-H. 2015. Mechanical properties of laminated strand lumber and hybrid cross-laminated timber. *Construction and Building Materials,* 101**,** 622-627.

WEIDEMA, B. P., BAUER, C., HISCHIER, R., MUTEL, C., NEMECEK, T., REINHARD, J., VADENBO, C. & WERNET, G. 2013. Overview and methodology: Data quality guideline for the ecoinvent database version 3.

WELLS, M. Stadthaus, London: raising the bar for timber buildings. Proceedings of the Institution of Civil Engineers-Civil Engineering, 2011. Thomas Telford Ltd, 122-128.

WHALE, L. R. J. 1989. DEFORMATION CHARACTERISTICS OF NAILED OR BOLTED TIMBER JOINTS SUBJECTED TO IRREGULAR SHORT OR MEDIUM TERM LATERAL LOADING.

WHITE, F. M. & CORFIELD, I. 2006. *Viscous fluid flow*, McGraw-Hill New York.

WILLIAMS, M. 2016. *Structural Dynamics,* Taylor and Francis, CRC Press.

WITHERDEN, F., JAMESON, A. & ZINGG, D. 2017. The design of steady state schemes for computational aerodynamics. *Handbook of Numerical Analysis.* Elsevier.

WOOD, L. W. 1960. Relation of strength of wood to duration of load.

WU, Q., HUO, L., ZHU, E., NIU, S. & WANG, H. 2021. An Investigation of the Duration of Load of Structural Timber and the Clear Wood. 12**,** 1148.

XIMENES, F. A. & GRANT, T. J. T. I. J. O. L. C. A. 2013. Quantifying the greenhouse benefits of the use of wood products in two popular house designs in Sydney, Australia. 18**,** 891-908.

XIONG YU, Z., SU XIN, R. & SABRI, O. J. V. U., VäXJö, SWEDEN 2009. Vertical Displacements in a Medium-rise Timber Building-Limnologen in Växjö, Sweden.

XU, H., HUANG, Q., LIU, G., ZHANG, Q. J. E. & BUILDINGS 2016. A quantitative study of the climate-responsive design strategies of ancient timber-frame halls in northern China based on field measurements. 133**,** 306-320.

XU, Y. L. 1995. Determination of Wind-Induced Fatigue Loading on Roof Cladding. 121**,** 956-963.

YANG, Y., HEIJUNGS, R. & BRANDãO, M. 2017. Hybrid life cycle assessment (LCA) does not necessarily yield more accurate results than process-based LCA. *Journal of Cleaner Production,* 150**,** 237-242.

YANG, Y. J. T. I. J. O. L. C. A. 2017. Does hybrid LCA with a complete system boundary yield adequate results for product promotion? 22**,** 456-460.

ZANGIáCOMO, A., BALANCO, G., CHRISTOFORO, A. & ROCCO LAHR, F. 2017. Glued Laminated Timber Produced with Tropical Brazilian Wood Species. *British Journal of Applied Science and Technology,* 23**,** 1-12.

ZHANG, X.-C., XUE, J.-Y., ZHAO, H.-T., SUI, Y. J. S. E. & MECHANICS 2011. Experimental study on Chinese ancient timber-frame building by shaking table test. 40**,** 453-469.

ZHANG, X., AZIM, M. R., BHAT, P., POPOVSKI, M. & TANNERT, T. J. C. J. O. C. E. 2017. Seismic performance of embedded steel beam connection in cross-laminated timber panels for tall-wood hybrid system. 44**,** 611-618.

ZHANG, X., FAIRHURST, M., KAUSHIK, K. & TANNERT, T. Ductility Estimation for a Novel Timber-Steel-Hybrid System with Consideration of Uncertainty. Structures Congress 2015, 2015. 2068-2077.

ZHANG, X., FAIRHURST, M. & TANNERT, T. J. J. O. S. E. 2016. Ductility estimation for a novel timber–steel hybrid system. 142**,** E4015001.

ZHANG, X., HU, X., GONG, H., ZHANG, J., LV, Z. & HONG, W. J. A. A. 2020. Experimental study on the impact sound insulation of cross laminated timber and timber-concrete composite floors. 161**,** 107173.

ZHOU, J., CHUI, Y. H., GONG, M. & HU, L. J. C. P. B. E. 2017. Elastic properties of full-size mass timber panels: Characterization using modal testing and comparison with model predictions. 112**,** 203-212.

ZHOU, Y., KAREEM, A. & GU, M. J. J. O. S. E. 2000. Equivalent static buffeting loads on structures. 126**,** 989-992.

ZIMMERMANN, M., ALTHAUS, H. J. & HAAS, A. 2005. Benchmarks for sustainable construction: A contribution to develop a standard. *Energy and Buildings,* 37**,** 1147-1157.

ZISIS, I., STATHOPOULOS, T., SMITH, I. & DOUDAK, G. 2011. Cladding pressures and primary structural system forces of a wood building exposed to strong winds1This paper is one of a selection of papers in this Special Issue in honour of Professor Davenport. *Canadian Journal of Civil Engineering,* 38**,** 974-983.

Zamanzad Gavidel, Saeed & Rickli, Jeremy. (2017). Quality assessment of used-products under uncertain age and usage conditions. International Journal of Production Research. 55. 1-15. 10.1080/00207543.2017.1349954.